



Defense Threat Reduction Agency  
8725 John J. Kingman Road, MS  
6201 Fort Belvoir, VA 22060-6201



DTRA-TR-18-8

# TECHNICAL REPORT

## Dust Cloud Combustion for Defeat of Airborne Bio-WMD

Distribution Statement A. Approved for public release; distribution is unlimited.

December 2017

HDTRA1-11-1-0014

David Frost

Prepared by:  
McGill University  
817 Sherbrooke St. W.,  
Montreal, Quebec  
Canada H3A OC3

DESTRUCTION NOTICE:

Destroy this report when it is no longer needed.  
Do not return to sender.

PLEASE NOTIFY THE DEFENSE THREAT REDUCTION  
AGENCY, ATTN: DTRIAC/ RD-NTF, 8725 JOHN J. KINGMAN ROAD,  
MS-6201, FT BELVOIR, VA 22060-6201, IF YOUR ADDRESS  
IS INCORRECT, IF YOU WISH IT DELETED FROM THE  
DISTRIBUTION LIST, OR IF THE ADDRESSEE IS NO  
LONGER EMPLOYED BY YOUR ORGANIZATION.

# REPORT DOCUMENTATION PAGE

Form Approved  
OMB No. 0704-0188

Public reporting burden for this collection of information is estimated to average 1 hour per response, including the time for reviewing instructions, searching existing data sources, gathering and maintaining the data needed, and completing and reviewing this collection of information. Send comments regarding this burden estimate or any other aspect of this collection of information, including suggestions for reducing this burden to Department of Defense, Washington Headquarters Services, Directorate for Information Operations and Reports (0704-0188), 1215 Jefferson Davis Highway, Suite 1204, Arlington, VA 22202-4302. Respondents should be aware that notwithstanding any other provision of law, no person shall be subject to any penalty for failing to comply with a collection of information if it does not display a currently valid OMB control number. **PLEASE DO NOT RETURN YOUR FORM TO THE ABOVE ADDRESS.**

<b>1. REPORT DATE (DD-MM-YYYY)</b>		<b>2. REPORT TYPE</b>	<b>3. DATES COVERED (From - To)</b>		
<b>4. TITLE AND SUBTITLE</b>			<b>5a. CONTRACT NUMBER</b>		
			<b>5b. GRANT NUMBER</b>		
			<b>5c. PROGRAM ELEMENT NUMBER</b>		
<b>6. AUTHOR(S)</b>			<b>5d. PROJECT NUMBER</b>		
			<b>5e. TASK NUMBER</b>		
			<b>5f. WORK UNIT NUMBER</b>		
<b>7. PERFORMING ORGANIZATION NAME(S) AND ADDRESS(ES)</b>			<b>8. PERFORMING ORGANIZATION REPORT NUMBER</b>		
<b>9. SPONSORING / MONITORING AGENCY NAME(S) AND ADDRESS(ES)</b>			<b>10. SPONSOR/MONITOR'S ACRONYM(S)</b>		
			<b>11. SPONSOR/MONITOR'S REPORT NUMBER(S)</b>		
<b>12. DISTRIBUTION / AVAILABILITY STATEMENT</b>					
<b>13. SUPPLEMENTARY NOTES</b>					
<b>14. ABSTRACT</b>					
<b>15. SUBJECT TERMS</b>					
<b>16. SECURITY CLASSIFICATION OF:</b>			<b>17. LIMITATION OF ABSTRACT</b>	<b>18. NUMBER OF PAGES</b>	<b>19a. NAME OF RESPONSIBLE PERSON</b>
<b>a. REPORT</b>	<b>b. ABSTRACT</b>	<b>c. THIS PAGE</b>			<b>19b. TELEPHONE NUMBER (include area code)</b>

## UNIT CONVERSION TABLE

### U.S. customary units to and from international units of measurement\*

U.S. Customary Units	Multiply by Divide by <sup>†</sup>	International Units
<b>Length/Area/Volume</b>		
inch (in)	2.54 × 10 <sup>-2</sup>	meter (m)
foot (ft)	3.048 × 10 <sup>-1</sup>	meter (m)
yard (yd)	9.144 × 10 <sup>-1</sup>	meter (m)
mile (mi, international)	1.609 344 × 10 <sup>3</sup>	meter (m)
mile (nmi, nautical, U.S.)	1.852 × 10 <sup>3</sup>	meter (m)
barn (b)	1 × 10 <sup>-28</sup>	square meter (m <sup>2</sup> )
gallon (gal, U.S. liquid)	3.785 412 × 10 <sup>-3</sup>	cubic meter (m <sup>3</sup> )
cubic foot (ft <sup>3</sup> )	2.831 685 × 10 <sup>-2</sup>	cubic meter (m <sup>3</sup> )
<b>Mass/Density</b>		
pound (lb)	4.535 924 × 10 <sup>-1</sup>	kilogram (kg)
unified atomic mass unit (amu)	1.660 539 × 10 <sup>-27</sup>	kilogram (kg)
pound-mass per cubic foot (lb ft <sup>-3</sup> )	1.601 846 × 10 <sup>1</sup>	kilogram per cubic meter (kg m <sup>-3</sup> )
pound-force (lbf avoirdupois)	4.448 222	newton (N)
<b>Energy/Work/Power</b>		
electron volt (eV)	1.602 177 × 10 <sup>-19</sup>	joule (J)
erg	1 × 10 <sup>-7</sup>	joule (J)
kiloton (kt) (TNT equivalent)	4.184 × 10 <sup>12</sup>	joule (J)
British thermal unit (Btu) (thermochemical)	1.054 350 × 10 <sup>3</sup>	joule (J)
foot-pound-force (ft lbf)	1.355 818	joule (J)
calorie (cal) (thermochemical)	4.184	joule (J)
<b>Pressure</b>		
atmosphere (atm)	1.013 250 × 10 <sup>5</sup>	pascal (Pa)
pound force per square inch (psi)	6.984 757 × 10 <sup>3</sup>	pascal (Pa)
<b>Temperature</b>		
degree Fahrenheit (°F)	[T(°F) - 32]/1.8	degree Celsius (°C)
degree Fahrenheit (°F)	[T(°F) + 459.67]/1.8	kelvin (K)
<b>Radiation</b>		
curie (Ci) [activity of radionuclides]	3.7 × 10 <sup>10</sup>	per second (s <sup>-1</sup> ) [becquerel (Bq)]
roentgen (R) [air exposure]	2.579 760 × 10 <sup>-4</sup>	coulomb per kilogram (C kg <sup>-1</sup> )
rad [absorbed dose]	1 × 10 <sup>-2</sup>	joule per kilogram (J kg <sup>-1</sup> ) [gray (Gy)]
rem [equivalent and effective dose]	1 × 10 <sup>-2</sup>	joule per kilogram (J kg <sup>-1</sup> ) [sievert (Sv)]

\* Specific details regarding the implementation of SI units may be viewed at <http://www.bipm.org/en/si/>.

<sup>†</sup> Multiply the U.S. customary unit by the factor to get the international unit. Divide the international unit by the factor to get the U.S. customary unit.

## Report Summary

The present document reports the results from a collaborative research project undertaken by David Frost at McGill University, and Nick Glumac at the University of Illinois, Urbana-Champaign, with the financial support of DTRA grant HDTRA1-11-1-0014. The objective consisted of performing fundamental studies on the dispersal and combustion of metal powders with the goal of determining the combustion properties of aluminum dust clouds. The ultimate goal of this research is to enable the development of a strategy aimed at defeating airborne biological weapons of mass destructions (bio-WMD).

The report is divided into 6 sections:

- 1) Flame propagation in aluminum dust clouds
- 2) Flames in hybrid mixtures of methane and metals
- 3) Optical diagnostics in dust flames
- 4) Modelling of flames in pure dust clouds and in hybrid mixtures of methane and dust
- 5) Explosive dispersal of metal powders
- 6) Biocidal agent dispersal

The study of flame propagation in aluminum clouds was performed with three different apparatus and geometrical scales: large-scale unconfined clouds in the field, freely-propagating flames contained within spherical balloons, and flat aluminum flames on a counter flow burner. The different studies investigated the flame propagation speed as a function of aluminum concentration for different oxidizers and inert diluents, the intrinsic instabilities in dust flames, the discrete flame propagation regime, the effect of initial temperature on the burning velocity, the influence of geometry on burning velocity, the effect of scale in flames propagating in aluminum dust clouds, and the effect of radiative heat transfer within aluminum clouds.

The studies on flames in hybrid mixtures were performed with a Bunsen dust burner, in tubes, and freely-propagating in balloons. The different results demonstrate the different regimes of flame propagations, the critical dust concentration, the quenching distances of different mixtures, and the role of the different oxidizers in the mixture.

Different optical diagnostics were developed to study the dust flames properties. The various diagnostic techniques allow the measurement of solid and gas phase temperature, aluminum suboxide AlO spectra, the regime of particle combustion, and burning velocity.

Two different models were developed to further extend our understanding of flames propagating in dust clouds. The first is an analytical model that addresses the different flame propagation behaviours observed in hybrid mixtures of aluminum and methane. The simple physical model intentionally omits complex chemical reaction schemes, yet is able to capture the essential physics of the different phenomena. The second model is a numerical model which is used to investigate the role of dust concentration on the different combustion properties of metal powders.

For some applications, it is necessary to rapidly generate a metal particle cloud. In this case, explosive dispersal of powders is a suitable technique. Experiments were performed to investigate the particle dynamics that result during explosive particle dispersal. Of

particular interest is the effect of the metal particle properties (such as particle material, density, and size) on the subsequent uniformity of the particle cloud and on the strength of the blast wave generated, which can interact with pre-existing airborne dust (such as a bio-agent in applications). For a wide range of particles, the explosive dispersal process leads to the formation of particle jets which results in general in a highly spatially non-uniform particle cloud. The acceleration of the powder reduces the peak blast overpressure generated in comparison to a bare explosive charge, although as the particles interact with the blast wave, the decay rate of the blast wave is reduced.

Finally, the last section reports experiments performed in the field with metal dust clouds containing the additive  $\text{CuCl}_2$ , a biocidal agent. The temperature and concentration of the agent was measured in the field at a scale that would be representative of a real-life application.

In conclusion, taken as a whole, the research undertaken in the context of this grant provides valuable information (such as the flame propagation speed, flame temperature, and radiative effects) that is useful for the design of devices targeting the defeat of airborne bio-agents.

# Table of Contents

<b>Section 1. Flames in pure aluminum clouds</b> .....	7
<b>Chapter 1. Freely-propagating aluminum flames in balloons</b> .....	7
1. INTRODUCTION .....	7
2. EXPERIMENTAL APPARATUS .....	8
3. RESULTS AND DISCUSSION .....	12
4. CONCLUSIONS .....	27
5. REFERENCES .....	27
<b>Chapter 2. Stabilized, flat aluminum flames on a counterflow burner</b> .....	30
1. INTRODUCTION .....	30
2. EXPERIMENTAL APPARATUS .....	31
3. RESULTS AND DISCUSSION .....	35
4. Conclusions .....	38
5. REFERENCES .....	39
<b>Chapter 3. Freely-propagating, large-scale aluminum flames in field tests</b> .....	42
1. INTRODUCTION .....	42
2. Experimental Apparatus .....	42
3. RESULTS AND DISCUSSION .....	45
4. Conclusions .....	51
5. References .....	51
<b>Chapter 4. Effect of initial temperature and radiation on burning velocity</b> .....	53
1. Introduction .....	53
2. Experimental Apparatus .....	56
3. Results and Discussion .....	59
4. Conclusions .....	64
5. References .....	64
<b>Section 2. Flames in hybrid mixtures of metal powders and methane</b> .....	66
<b>Chapter 1. Hybrid flames of aluminum and methane on a Bunsen burner</b> .....	66
1. Introduction .....	66

2. Experimental Apparatus .....	67
3. Results and Discussion .....	72
4. Conclusions .....	80
5. References .....	81
<b>Chapter 2. Hybrid flames of iron and methane on the Bunsen burner .....</b>	<b>84</b>
1. Introduction .....	84
2. Experimental Apparatus .....	85
3. Results and Discussion .....	86
4. Conclusions .....	93
5. References .....	94
<b>Chapter 3. Freely-propagating, hybrid flames of aluminum and methane in balloons.....</b>	<b>95</b>
1. Introduction .....	95
2. Experimental Apparatus .....	96
3. Results and Discussion .....	98
4. Conclusions .....	109
5. References .....	110
<b>Chapter 4. Hybrid flames of aluminum and methane in tubes.....</b>	<b>112</b>
1. Introduction .....	112
2. Experimental Apparatus .....	113
3. Results and Discussion .....	116
4. Conclusions .....	121
5. References .....	122
<b>Section 3. Optical diagnostics in dust flames .....</b>	<b>123</b>
<b>Chapter 1. Ultraviolet (UV) Absorption Spectroscopy in Optically Dense Fireballs Using Broadband Second Harmonic Generation of a Pulsed Modeless Dye Laser.....</b>	<b>123</b>
1. Introduction .....	123
2. Experimental Apparatus .....	125
3. Results and Discussion .....	129
4. Conclusions .....	135
5. References .....	136

<b>Section 4. Modelling of flames in metal suspensions and in hybrid suspensions of metals and hydrocarbons</b> .....	139
<b>Chapter 1. Flame Propagation and Quenching in Binary Fuel Mixtures</b> .....	139
1. Introduction .....	139
2. Experimental Apparatus .....	141
3. Results and Discussion .....	143
4. Conclusions .....	146
5. References .....	147
<b>Chapter 2. Reaction of a Particle Suspension in a Rapidly-Heated Oxidizing Gas</b> .....	149
Nomenclature.....	149
1. Introduction .....	149
2. Model and results.....	151
3. Conclusions .....	163
4. References .....	164
<b>Chapter 3. Thermal Structure of Flames in Non-Volatile Fuel Suspensions</b> .....	166
1. Introduction .....	166
2. Model formulation.....	167
3. Results and Discussion .....	172
4. Conclusions .....	177
5. References .....	177
<b>Section 5. Explosive Dispersal of powders</b> .....	180
<b>Chapter 1. Blast mitigation by granular materials and liquids in spherical geometry</b> .....	180
1. Introduction .....	180
2. Experimental Apparatus .....	182
3. Results and Discussion .....	188
4. Conclusions .....	200
5. References .....	200
<b>Section 6. Biocidal agent detection in field conditions</b> .....	203
<b>Chapter 1. CuCl Experiments</b> .....	203
1. Introduction .....	203

2. Experimental Apparatus .....	203
3. Results and Discussion .....	204

# SECTION 1. FLAMES IN PURE ALUMINUM CLOUDS

## Chapter 1. Freely-propagating aluminum flames in balloons

### 1. INTRODUCTION

Suspensions of combustible particles in an oxidizing media are ubiquitous in industry, agriculture, transportation and propulsion technology [1]–[6]. Though often amalgamated together under the term “combustible dusts”, solid fuels are very diverse, ranging from very volatile organic substances, such as plastics, flour, sugar or cornstarch, to refractory materials, such as carbon (graphite) or iron that do not volatilize or evaporate. Organic dusts have melting and volatilization temperatures well below their flame temperature, such that their combustion behavior differs little from the combustion of hydrocarbon droplets. The evaporation or decomposition of the organic volatile fuel and hydrocarbon sprays in the flame preheat zone might lead to the formation of a continuous flame sheet in the case of small particles and large fuel concentrations or, for large particles in fuel-lean mixtures, result in the combustion of particles surrounded by individual diffusion micro-flames [7]. Complex fuels, such as coal, contain both volatile and refractory substances and burn partially in the vapor phase by volatilization while leaving a charred core that burns heterogeneously.

Irrespective of the boiling temperature of the metal, the extremely fast and non-activated reaction kinetics of metal vapors with oxygen precludes formation of a premixed metal-vapor mixture in the flame preheat zone. [8], [9]. This excludes complex mixed heterogeneous/homogeneous flame regimes typical for combustion of solid and liquid hydrocarbon fuel suspensions which, combined with the fact that metals are pure elemental substances with well-defined properties, available in a wide range of particle sizes, makes flames in metal suspensions well-suited for the academic study of heterogeneous dust flames. Among all metals, aluminum is of special interest since it is often used as an energetic additive to propellants, explosives and pyrotechnics.

In contrast to hydrocarbon flames, the field of dust combustion remains vastly under-developed. This is partly due to the experimental difficulty of obtaining a laminar suspension of solid particles which is required to measure the fundamental combustion parameters, such as the burning velocity. Dust particles rapidly settle in a quiescent environment, and, in order to maintain the dust in suspension, an ascending laminar flow or some level of flow turbulence is required. For large particles that are tens of microns or more in size, the flow velocity that is required to counteract particle settling may even exceed the flame burning velocity. Thus, performing dust combustion experiments over a wide range of particle sizes ultimately requires a microgravity environment [10]. Furthermore, the combustion behavior of a dust suspension depends on the particle morphology and size distribution, which makes it difficult to compare experimental data obtained from different research groups using dissimilar powders.

The vast body of literature on dust combustion is mostly based on experiments in closed bombs with no visual access, where the pressure history within the vessel is the only parameter measured. This experimental technique is primarily used to empirically classify the explosivity of dusts based on the rate of pressure rise, in accordance with the explosion hazard scale, while leaving the scientific questions of the flame structure and flame propagation mechanism unresolved. Only a small number of experimental groups, using different techniques, have provided direct measurements of the flame propagation speeds from which the burning velocity can be extracted. For example, Cassel employed stabilized Bunsen-type flames [11], Ballal et al. [12] performed experiments with flat flames in a tube in microgravity, and Sun et al. [13]–[15] explored freely-propagating flames at very small scales. For the past 20 years, researchers at McGill University have systematically used visual observation of metal dust and hybrid hydrocarbon/metal-dust flames stabilized on Bunsen burners [16]–[19], propagating in tubes in normal and microgravity environments [20]–[23], and, more recently, spherically expanding in transparent latex balloons [24], to determine flame speeds and flame structure. The systematic use of the same batch of aluminum powder in the different experiments has facilitated the accumulation of a unique dataset of aluminum dust flame properties such as burning velocity, flame quenching distance, and flame spectral characteristics. This comprehensive compendium of data allows for the direct comparison of properties using different methods to fully characterize the combustion properties and flame structure.

## 2. EXPERIMENTAL APPARATUS

The transparent latex balloons have a diameter of about 30 cm and volume of about 14 L when inflated prior to injection of the powder (Fig. 1). As the flame propagates, the balloon expands, maintaining essentially isobaric conditions up until it bursts with a pressure rise that is less than 0.01 bar. The aluminum powder is initially placed in a hemispherical cup at the bottom of a cylindrical dispersion unit that has a maximum capacity of 8 g of powder. The powder is fluidized within the cylindrical chamber by an impinging pulse of high-pressure gas. The particles become entrained in the flow, and the aluminum-gas mixture travels upward through a hemispherical cap before entering the pre-inflated balloon. The cap is pierced with multiple holes to separate the two-phase flow into many particle-laden jets that move up through the center of the balloon. The suspended particles recirculate within the balloon, mixing with the gas mixture until a uniform gas-particle mixture is created within the balloon, as shown in Fig. 2. The powder suspension is then centrally ignited by a heated tungsten wire following a 4 s delay after the initial powder injection to allow the initial turbulence to decay, as described in a previous publication [24]. The dust dispersal and flame propagation processes are recorded using a high-speed Photron SA5 videocamera, operated at 4,000–7,500 frames per second. Neutral density filters are used to attenuate the light intensity of the intensely luminous flames at high dust concentrations. A photodiode and a microphone, installed near the balloon and synchronized with the camera, monitor the history of the flame brightness and the acoustic waves emitted by the flame, respectively. More details on the design and operation of the apparatus are given in a previous publication [24].

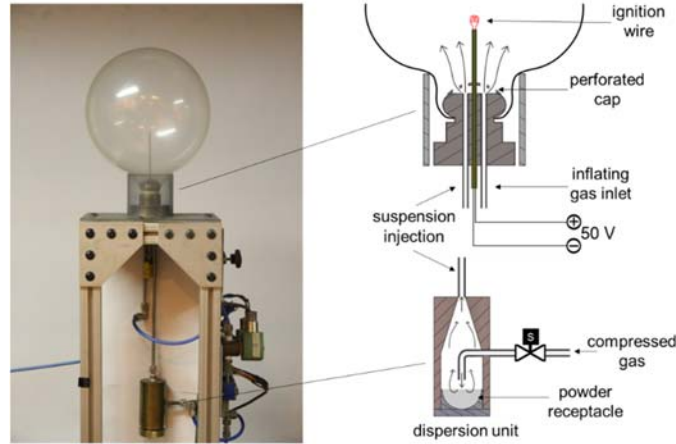


Figure 1. Schematics and photograph of the laboratory apparatus for observation of spherical dust flames in transparent latex balloons.

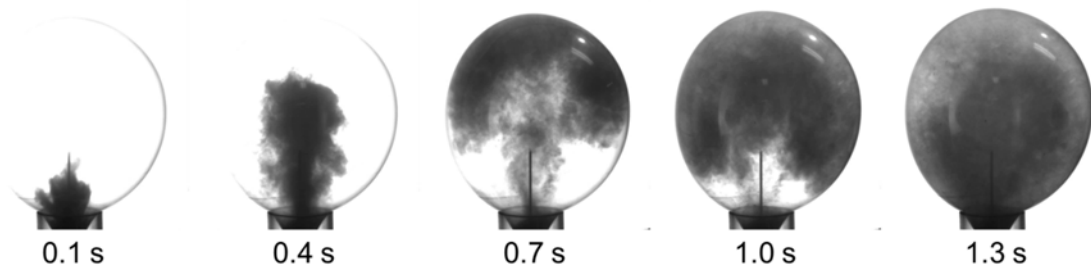


Figure 2. Still frames of the dispersion of 4g of aluminum powder in the latex balloon apparatus for a final concentration of approximately  $200 \text{ g/m}^3$ .

In most dust combustion experiments within closed vessels, it is usually assumed that the dust is uniformly dispersed throughout the vessel volume without any powder deposition, and hence the dust concentration is calculated by simply dividing the mass of the dust sample by the inner volume of the vessel. However, some portion of the powder does not remain in suspension but, rather, accumulates on the vessel wall or settles to the bottom of the chamber prior to ignition. In the present experiment, some degree of powder deposition also occurs, and hence a calibration is performed to correlate the mass of the dust sample initially within the dispersion unit with the actual amount of dust in suspension at the moment of ignition. A rigid acrylic sphere with a similar size and volume is used in place of the latex balloons in conjunction with a laser light-attenuation probe to calibrate the dust concentration [19], [16], [18], [17]. The probe consists of a 633 nm red laser and a photodiode with a narrow-bandpass filter corresponding to the wavelength of the laser. The powder is dispersed as usual but not ignited. The powder concentration is derived from the photodiode output signal using the Beer-Lambert law, which states that the logarithm of the light attenuation corresponds to the powder concentration multiplied by a constant. This constant, which depends on the distance traveled by the laser and the type of powder

used, has been determined in previous experiments using the same powder [19], [18]. Figure 3 shows a typical time history of the dust concentration determined within the suspension during and after the dust dispersal process. Figure 4 shows the concentration measured in the globe and the calculated concentration.

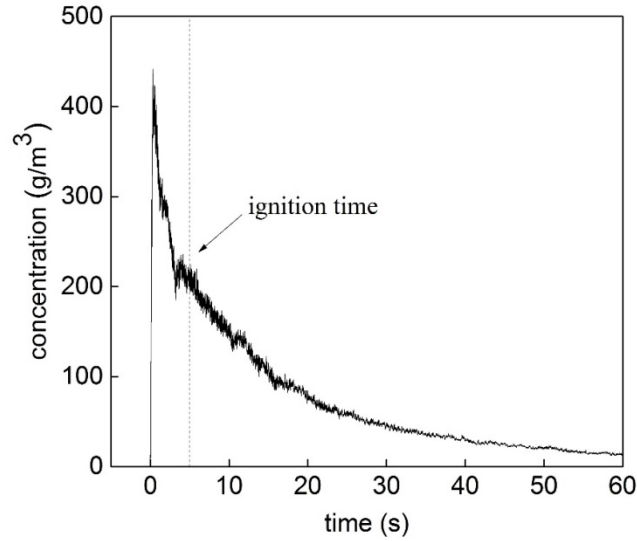


Figure 3. Time history of the aluminum dust concentration in the balloon measured by the laser light attenuation probe.

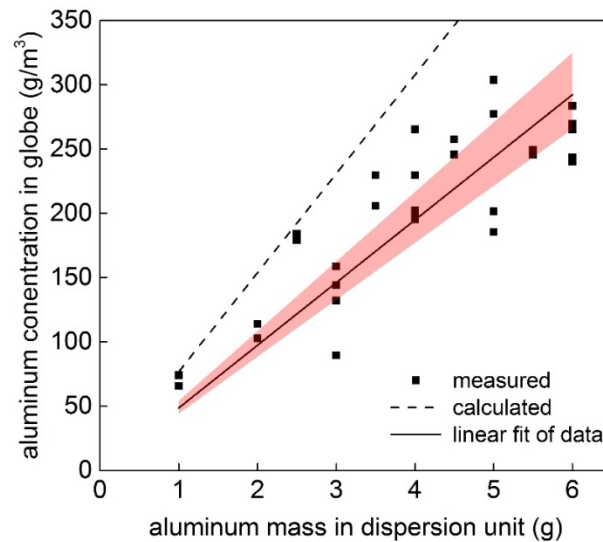


Figure 4. Experimentally measured concentration of the aluminum in suspension at the moment of ignition (4 s after the start of dispersion) as a function of the amount of aluminum dust initially placed in the dispersion unit. The shaded area represents the 95% confidence interval of the fit, the solid line the least-square fit and the dashed line is the estimate of the aluminum concentration obtained assuming that the entire dust sample remains in suspension.

The method of measuring flame speed is first validated using methane-air mixtures of various equivalence ratios. The contour of the flame on the high-speed movie is traced for every frame and the radius is taken to be the average distance between the contour and the center-of-mass. The flame speed is equal to the slope of the curve, which is found by linear regression. Conservation of mass allows the calculation of the 1D laminar burning velocity,  $S_L$  (Law, 2006) using  $S_L = S_f(\rho_b/\rho_u)$ , where  $S_f$  is the flame speed, and  $\rho_b$  and  $\rho_u$  are the burned and unburned gas densities, respectively. The density of the gas before and after combustion is found using the chemical equilibrium solver Cantera (Goodwin, 2003). As shown in Fig. 5, the burning velocities are in good agreement with other literature values measured with spherical flames (Gu, Haq, Lawes, & Wooller, 2000; Hassan, Aung, & Faeth, 1998; Qin, & Ju, 2005).

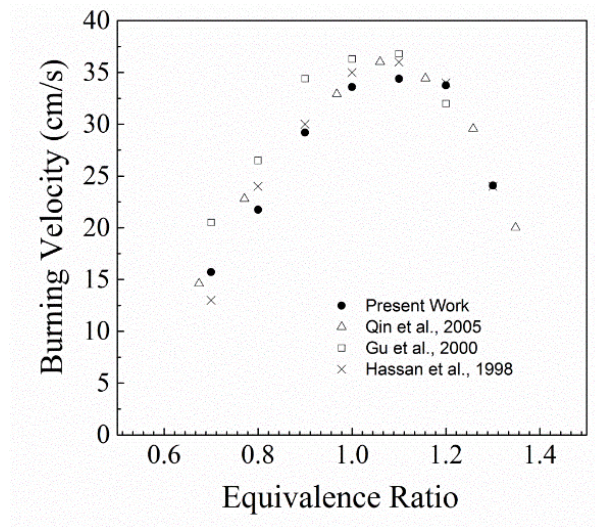


Figure 5: Burning velocity vs. equivalence ratio for methane-air mixtures compared to results from other freely-propagating spherical flames.

Tests with stoichiometric methane-air mixtures are performed to determine the minimum delay time required between the powder dispersal process and ignition. A pulse of pre-mixed methane-air instead of air is introduced into the balloon with no powder to study the effect of turbulence on the flame speed. The results are shown in Fig. 6 and the dashed line represents the laminar flame speed. It can be seen that approximately 5 seconds are required for the effect of turbulence to be negligible. This delay time is found to be a good compromise between the decay of turbulence and minimal settling of the powder.

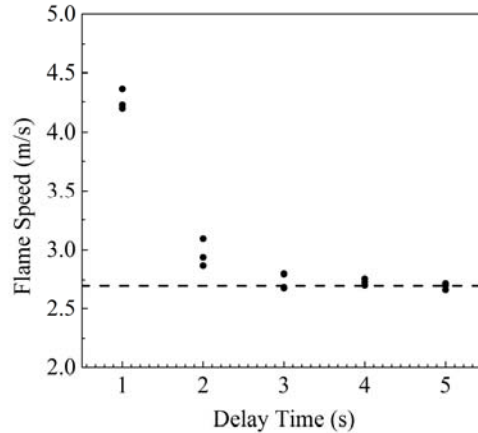


Figure 6: Methane flame speed as a function of ignition delay time. The dashed line represents the laminar flame speed.

The various test series within the balloons were performed with oxygen concentrations ranging from 15% to 100%. The oxygen is diluted with nitrogen, argon or helium to have different heat capacities and diffusivities while keeping the concentration of aluminum and oxygen constant. Oxidizing mixtures are prepared in a mixing tank by partial pressure. Tests were performed with Ampal aluminum powder, 637.

### 3. RESULTS AND DISCUSSION

#### *Regimes of flame propagation*

Figure 7 shows the flame propagation through an aluminum dust cloud with a concentration of about  $500 \text{ g/m}^3$ . The images are processed the same way as for the methane flames. A typical result for the average radius as a function of time is shown in Fig. 8, with the slope corresponding to the flame speed.

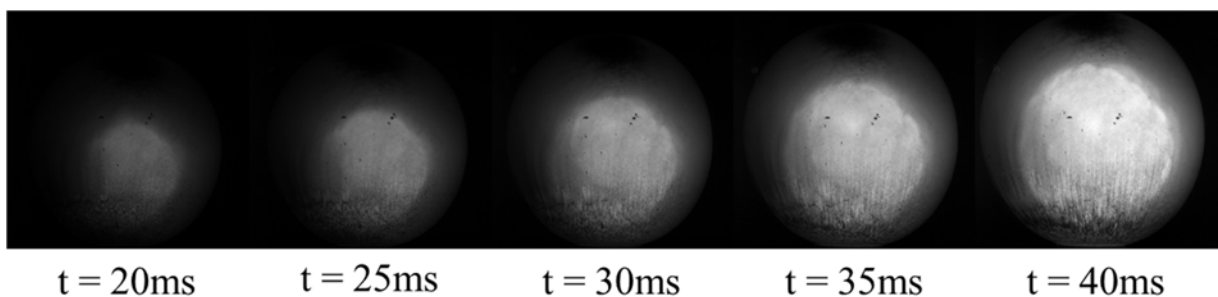


Figure 7: Characteristic aluminum flame propagation for a powder concentration of  $500 \text{ g/m}^3$ .

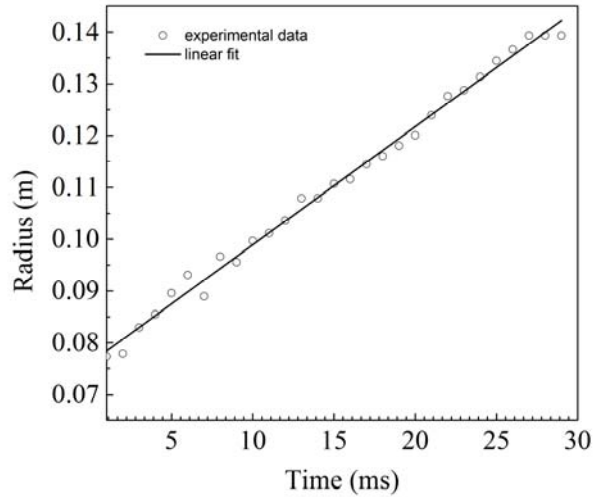


Figure 8: Flame front radius as a function of time for flame propagation in an aluminum-air mixture

Different regimes of flame propagation are observed in the present experiments, and the type of regime depends primarily on the fuel equivalence ratio, i.e., on the oxygen and aluminum concentrations. Mixtures in the vicinity of stoichiometric concentrations exhibit stable propagation of a smooth flame expanding radially outwards after central ignition. Figure 9 shows still frames from a stable flame experiment, with an aluminum concentration of about  $370 \text{ g/m}^3$  in air.

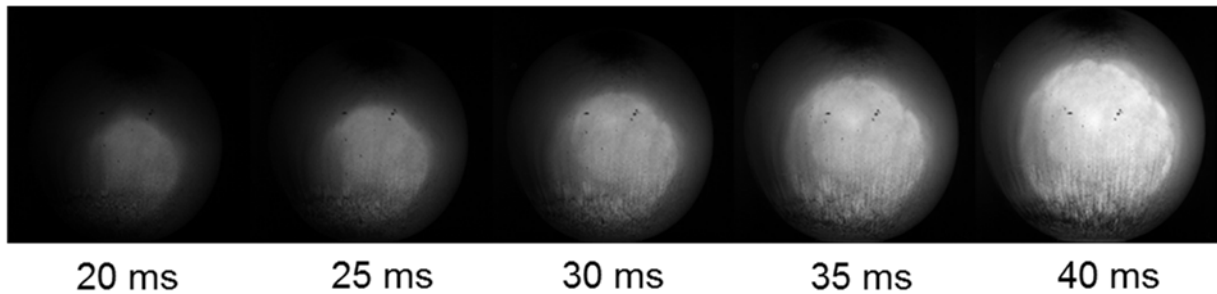


Figure 9. Flame front propagation in near-stoichiometric suspension in air at aluminum dust concentration of about  $370 \text{ g/m}^3$ . Stoichiometric concentration of aluminum in air is about  $320 \text{ g/m}^3$ .

Several unstable combustion regimes were observed in both very fuel-rich mixtures and fuel-lean mixtures. On the rich side, flames have exhibited cellular patterns on their surface. In fuel-lean suspensions, the flame instabilities are classified into the following four categories, listed in order of decreasing aluminum concentration starting from

stoichiometric conditions: i) decaying pulsating flames (pulsations with diminishing amplitude), ii) regular pulsating flames (pulsations with constant amplitude), iii) pulsating flames accompanied by spiral patterns formed on the flame surface, and iv) spiral flames.

Flames with decaying pulsations, followed immediately by pulsations, are the first forms of instabilities that are observed as the concentration of aluminum is decreased below the stoichiometric value. The first regime is referred to as “decaying pulsations” on the graph of Fig. 11 below. In both cases, pulsations start immediately after ignition and are characterized by brief periods of intense luminosity followed by an apparent extinguishing of the flame where the brightness of the flame is reduced by almost an order of magnitude. At aluminum concentrations only slightly below the stoichiometric value, the pulsations are weak, and the flame often starts to propagate steadily after only a few pulsating periods. As the aluminum concentration is decreased still further, the pulsations become more intense and persist until the flame reaches the balloon wall. Figure 10 shows still frames from two periods of such a pulsating flame.

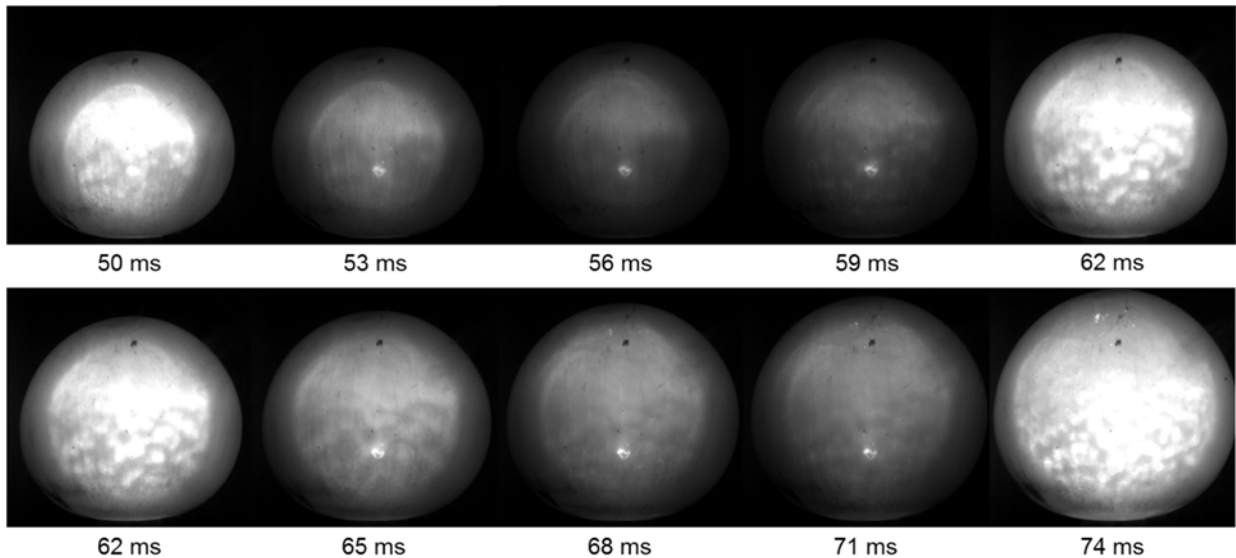


Figure 10. Still frames illustrating two periods of a pulsating aluminum flame in lean aluminum suspension in 60%O<sub>2</sub>/40% Ar gas mixture and aluminum concentration of about 280 g/m<sup>3</sup>.

At very low aluminum concentrations, near the lean flammability limit, a second type of thermo-diffusive instability is observed. Spiral waves, often referred to in the literature as *spin combustion*, can be clearly observed on the flame front. For extremely lean mixtures, when the flame speed becomes comparable to, or lower than, the flow speed induced by the buoyancy of the hot combustion products, the flame propagates upwards in the form of rotating spirals. The spirals appear to start and stop at different locations, and multiple rotating spirals can be observed simultaneously. A spiral flame is shown in a video in supplementary materials. When the mixture has an aluminum concentration between the values associated with the pulsation and spiral regimes, a combination of these two types of instabilities can be observed simultaneously. The flame pulsates, with the clear formation of spiral patterns on the flame surface during the burning phase.

Figure 11 presents the mapping of the different combustion regimes as a function of aluminum and oxygen concentrations in gaseous mixtures of oxygen with helium, nitrogen or argon. The horizontal dashed lines crossing the different columns indicate stoichiometric aluminum concentrations for each specific oxygen concentration. The present experimental set-up allows for a maximum aluminum concentration of about 550 g/m<sup>3</sup>, such that fuel-rich conditions are only possible in mixtures with oxygen concentration below 30%. As can be seen from Fig. 10, most fuel-rich mixtures, as well as fuel-lean mixtures with fuel equivalence ratios above 0.8, exhibit stable flame propagation. As the aluminum concentration is lowered below this value, the flame generally first starts propagating with decaying pulsations. As the concentration is decreased the pulsations grow stronger and persist until the flame front reaches the balloon wall. As the dust concentration is reduced even further, pulsations are followed by pulsations with spirals and, finally, purely spiral flames. It is interesting to note that spiral flames occur more frequently in nitrogen-oxygen mixtures while the combination of spirals and pulsations occurs more frequently in helium-oxygen mixtures.

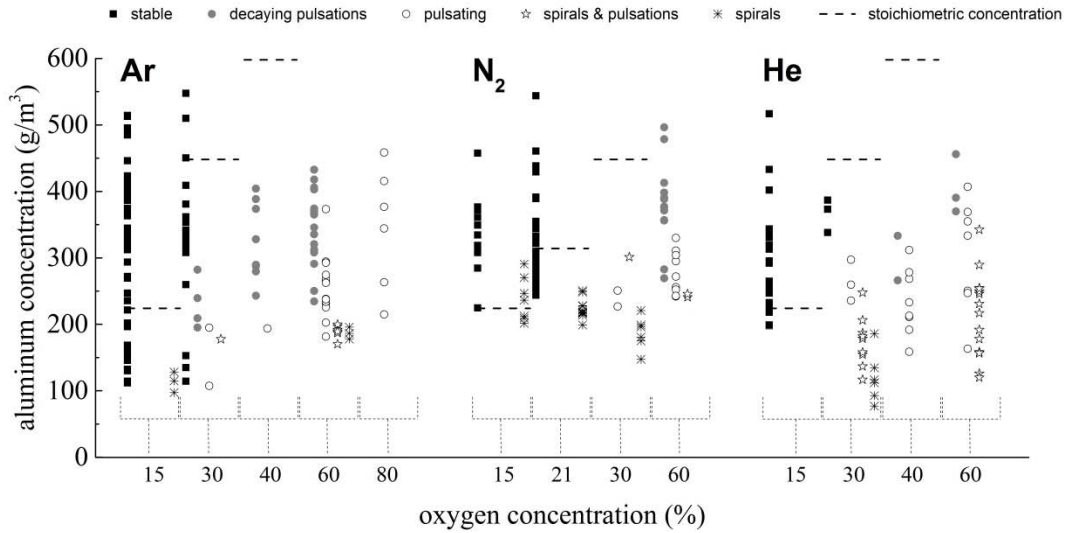


Figure 11. Map of the different regimes of combustion observed for variable oxygen and aluminum concentrations for several inert diluents.

### *Propagation speed of stable flames*

The propagation speed of stable flames is determined from the high-speed video records. As the flame is not always spherically symmetrical, the contour of the flame front on each frame was fit with an ellipse. The mean flame radius is then defined as the average distance from the edge of the ellipse to its center-of-mass. The flame radius is plotted as a function of time and a leastsquares fit to the data is used to find the slope of the line giving the flame speed,  $S_f = \frac{dr}{dt}$  [24]. The experimental data points of flame speed in air in the stable flame propagation regime are shown in Fig. 12 for different mass concentrations of

aluminum in suspension. As can be seen from Fig. 12, in fuel-lean mixtures, which corresponds to the portion of the curve left of the dashed line that represents stoichiometric conditions, the flame speed increases relatively sharply with an increase in aluminum concentration.

Figure 13 shows the measured flame speeds as a function of aluminum concentration in argon-oxygen mixtures at three different oxygen concentrations of 15, 20, and 30%. As can be seen, in fuel-lean mixtures the flame speed increases linearly with aluminum concentration, within the scatter, but is relatively insensitive to the oxygen concentration in the mixture. At all oxygen concentrations, the flame speed reaches an approximate plateau level in rich mixtures, and the average plateau value is larger for mixtures with larger oxygen content. This demonstrates a relatively strong dependence of the flame speed on oxygen concentration for fuel-rich mixtures.

The dependence of the flame speed on aluminum concentration in 15 % oxygen mixtures with different gaseous inert diluents ( $N_2$ , Ar, He) is shown in Fig. 14. At equal aluminum concentrations, the lowest flame speed is observed in oxygen-nitrogen mixtures followed by slightly higher speeds in mixtures with argon. In contrast, helium increases the flame speed more than three times in comparison to argon-diluted mixtures. The flame speeds are observed to be quite insensitive to the concentration of aluminum for rich mixtures, as observed previously [16].

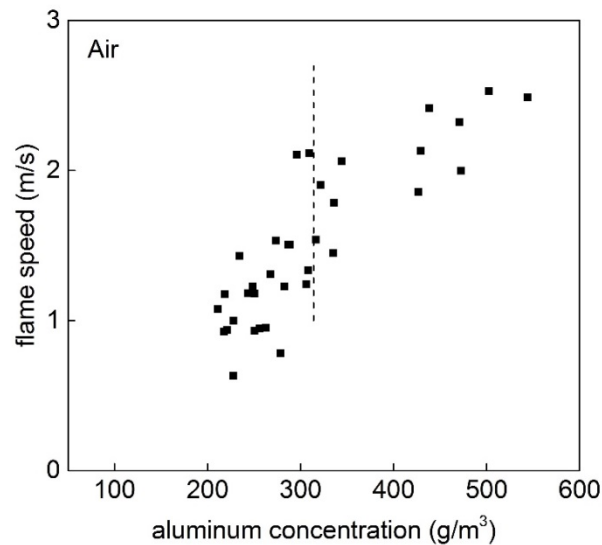


Figure 12. Flame speed at different aluminum concentrations in air for stable flames.

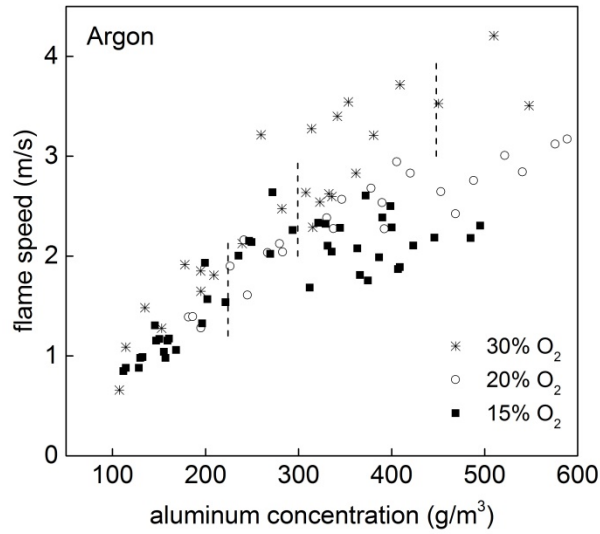


Figure 13. Flame speed versus aluminum concentration in argon mixtures with different oxygen content for stable flames.

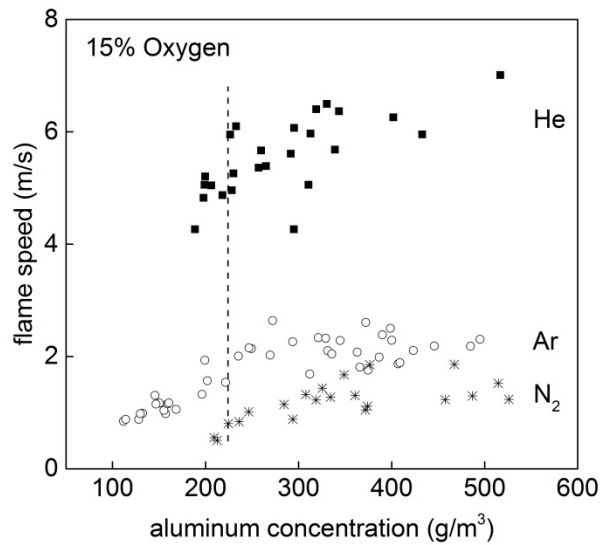


Figure 14. Flame speed versus aluminum concentration in 15% O<sub>2</sub> and 85% N<sub>2</sub>, Ar or He for stable flames.

### *Pulsation frequency and average flame speed of pulsating flames*

The flame front in the pulsating regime is also tracked by fitting an ellipse to the front on the images, and the radius is taken to be the average distance between the center of mass and the edge of the ellipse. Figure 15 shows an example of the flame radius tracked as a function of time for a pulsating flame. It can be seen that for very brief periods of time, the flame propagates at extremely high speeds separated by a longer phase where the flame radius effectively does not change with time. The average flame propagation speeds of the

pulsating flames, obtained from a linear fit to the data, are shown in Fig 16 for three different inert gas diluents with an oxygen concentration of 60%. The results demonstrate that the average flame propagation speed in the pulsating regime increases only with aluminum concentration and, surprisingly, is largely independent of the heat and mass diffusivity of the mixture, which differs by a factor slightly larger than two between helium and argon mixtures. This behavior is strikingly different from a stable flame propagation regime, where the flame speed strongly depends on the thermal diffusivity of the mixture increasing by almost factor of four when argon in mixture with oxygen is replaced by helium (Fig. 14) for flames in 15% oxygen.

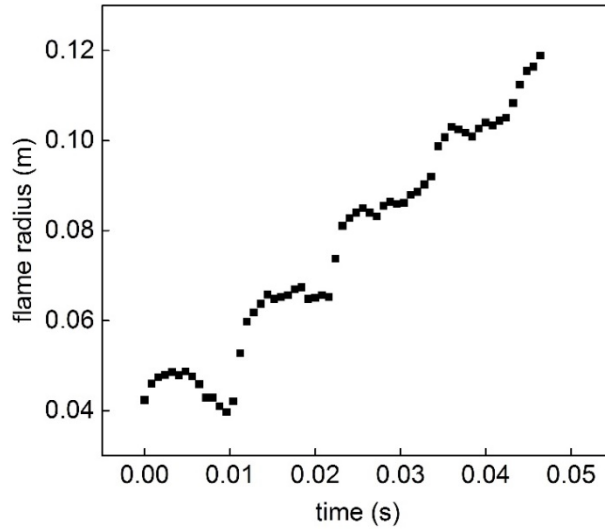


Figure 15. Time dependence of the radius of the pulsating flame in 60% O<sub>2</sub> and 40% Ar with an aluminum concentration around 280 g/m<sup>3</sup>.

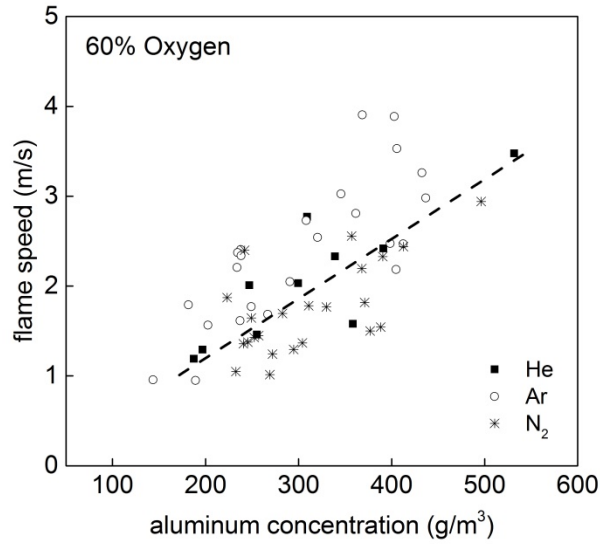


Figure 16. Average propagation velocity of the pulsating flame versus aluminum concentration in 60% O<sub>2</sub> and 40% N<sub>2</sub>, Ar or He.

A typical variation of the pulsating flame brightness recorded by the photodiode is shown in Fig. 17, superimposed with the acoustic pressure signal recorded by the microphone. It is evident that both traces coincide in frequency and are in-phase, indicating that acoustic pulsations are induced by the pulsating flame. Figure 18 presents an example of the light emitted from a flame with decaying pulsations undergoing transition from the pulsating mode to a stable flame propagation mode.

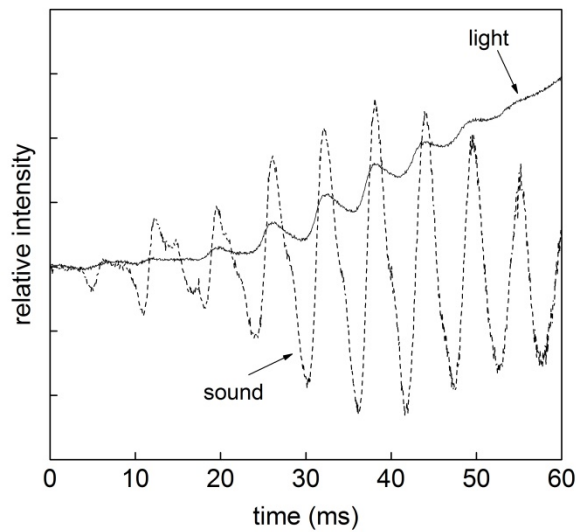


Figure 17. Typical light and sound pressure signals from pulsating flame (60% O<sub>2</sub> and 40% Ar mixture, aluminum concentration around 420 g/m<sup>3</sup>).

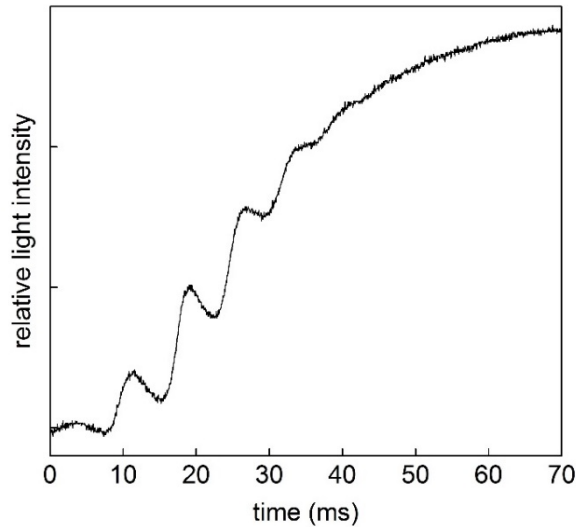


Figure 18. Typical light signal from a flame with decaying pulsations (42% O<sub>2</sub> and 58% Ar mixture, aluminum concentration about 450 g/m<sup>3</sup>).

Figure 19 illustrates the dependence of the frequency of flame oscillations on the aluminum concentration in fuel-lean mixtures of 80% oxygen diluted with either argon or helium. The dependence of the flame oscillation frequency on aluminum concentration under different concentrations of oxygen in argon-oxygen mixtures is illustrated in Fig. 20 for 42%, 60%, and 80% oxygen. As can be seen, in both cases, the frequency increases approximately linearly with aluminum concentration, while neither the oxygen concentration nor the type of inert gas exhibit any substantial influence on the oscillation frequency. Pulsation frequencies do not noticeably change in helium mixtures, which have much higher sound speed. Furthermore, experiments were performed for different balloon sizes, enclosure sizes and balloon thicknesses and yielded the same frequency for a given aluminum concentration.

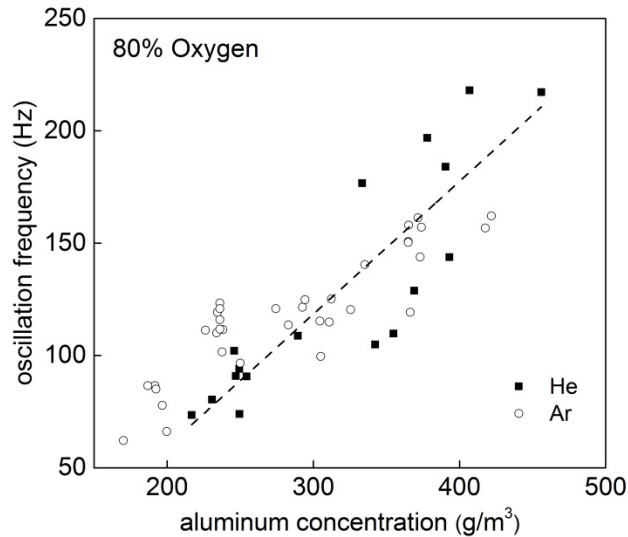


Figure 19. Dependence of the flame pulsation frequency on aluminum concentration in 80% O<sub>2</sub> and 20% Ar or He

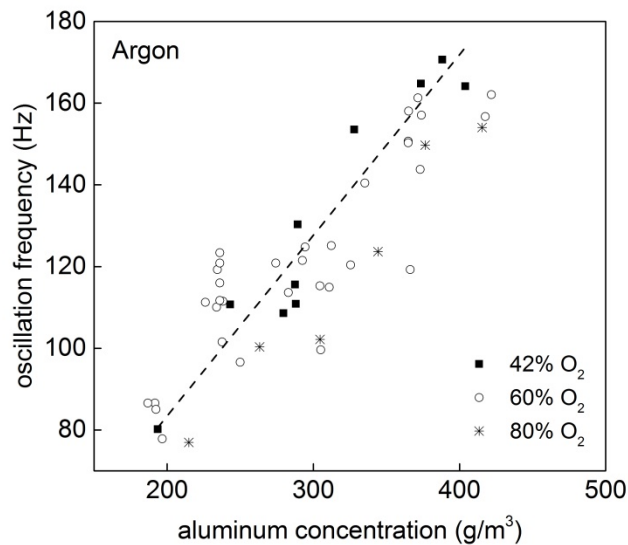


Figure 20. Dependence of the flame pulsation frequency on aluminum concentration in O<sub>2</sub>-Ar mixtures with varying O<sub>2</sub> concentrations of 42%, 60% and 80%.

Detailed modeling and quantitative numerical analysis must be performed to explain the various physical phenomena observed in the present work and will be the subject of a subsequent publication. However, some qualitative explanations of the observed phenomena and trends based on physical considerations can be discussed. The flame speed dependence on dust cloud parameters in the stable flame-propagation regime are interpreted using some of our previously-published qualitative dust-flame models. The physical interpretation of the observed unstable combustion regimes is based upon thermo-diffusive instability theory developed for the description of similar phenomena for gaseous

and condensed-phase mixtures. Large-scale tests are interpreted using a basic hydrodynamic model to obtain the burning velocity, and the effect of radiation is discussed in the context of pre-heating of reactants.

*Stable flame propagation*

*Flame speed and burning velocity*

Similarly to flames in gas mixtures, the burning velocity of a spherically-propagating, constant-pressure dust flame can be found by simply dividing the measured flame speed by the expansion coefficient, defined as the ratio of the density of unburned mixture to the density of combustion products [29]. For any given aluminum concentration, this ratio can be calculated using an equilibrium code, such as Chemical Equilibrium with Applications (CEA) developed by NASA [30], that calculates both equilibrium temperatures and the number of moles of gaseous combustion products. The burning velocities derived from the balloon experiments for mixtures in 20% oxygen diluted with argon are shown in Fig. 21 in comparison to the data obtained previously from experiments with Bunsen dust flames for the same batch of Ampal-637 aluminum powder [16] in argon and 21% oxygen. As can be seen from Fig. 21, the burning velocities obtained from the two different experiments are in agreement, as was shown for aluminum-air flames in a previous publication [24]. The agreement between two different experimental methods with different geometries implies that the notion of burning velocity as a fundamental physical-chemical parameter also applies for flames in metal suspensions, similar to gas flames.

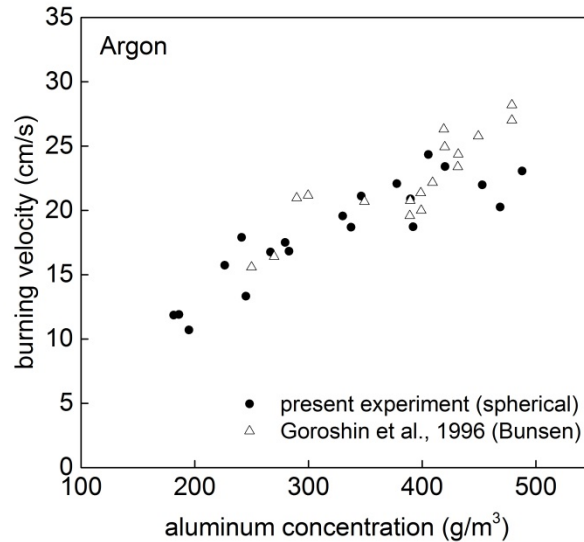


Figure 21. Comparison of the burning velocities derived from balloon experiments and Bunsen-type dust flames [16] in argon mixed with 20% O<sub>2</sub> for balloons and 21% O<sub>2</sub> for Bunsen flame.

### *Dependence of the burning velocity on aluminum and oxygen concentration*

The effect of aluminum concentration on the flame burning velocity at different levels of oxygen concentration is illustrated in Fig. 22 with argon being the inert diluent. Again, the burning velocities are obtained from the data of Fig. 13 by multiplying the flame speed by the expansion coefficient, which is also obtained with an equilibrium solver. The solid lines shown represent the trends of the flame speeds for the three different oxygen concentrations.

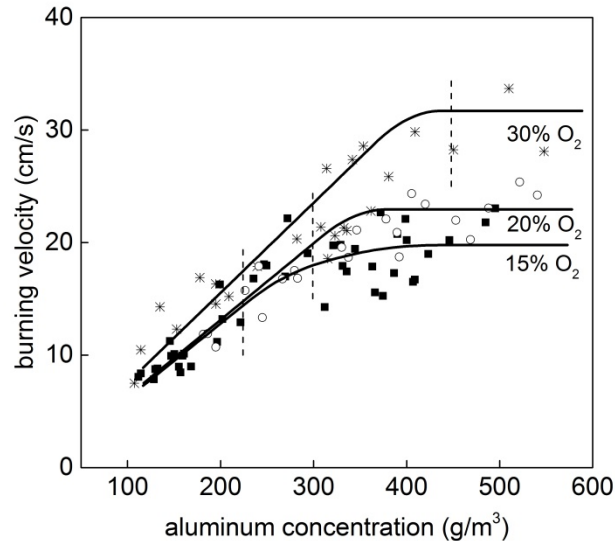


Figure 22. Dependence of burning velocity in aluminum suspensions on fuel concentration at different concentrations of oxygen diluted with argon.

As evident from Fig. 22, the dependence of the burning velocity with increasing aluminum concentration demonstrates the same qualitative behavior at all oxygen concentrations. The flame velocity increases with aluminum concentration in lean mixtures and then plateaus after crossing the stoichiometric value exhibiting very low sensitivity to dust concentration in fuel-rich mixtures. This behavior is different to flames in gaseous fuel mixtures where the dependence of the flame speed on the fuel equivalence ratio is more or less symmetrical around the stoichiometric value. There are two major reasons for this distinctive feature of dust flames. First of all, the flame temperature decreases less significantly with an increase of the fuel concentration in fuel-rich solid suspensions than in gases. This is because an increase in solid-fuel concentration only increases the specific heat of the mixture without diluting the oxygen concentration, since the solid particles occupy a negligible volume. Thus, the calorific value of a rich dust mixture is defined solely by the oxygen concentration and not the fuel. The second reason is that the rate of aluminum particle combustion in the diffusive-combustion regime is not very sensitive to the reduction in bulk flame temperature, due to the formation of micro-diffusion flames around each particle with each flame temperature at the stoichiometric value. In fact, a larger reaction surface area in rich mixtures actually leads to a faster

reaction rate, compensating for the decrease in flame temperature and, thus, keeping the value of flame speed relatively constant.

As can be seen from Fig. 22, the seemingly weak dependence of the burning velocity on oxygen concentration in fuel-lean mixtures is the most striking result observed in the present study for stable flames in aluminum suspensions. Regardless of the aluminum particle combustion regime, i.e., kinetic- or diffusion-limited, the particle reaction rate is proportional to the oxygen concentration. In accordance with the basic theory of diffusion-reaction waves in a reacting continuum [31], the propagation speed of the front is proportional to the square root of the reaction rate, which is equivalent to the square root of the oxygen concentration. The only reasonable explanation for the observed flame reduced sensitivity to oxygen concentration is the recently-developed theory of discrete flame propagation [32]–[34]. This theory predicts that in a system with fast-reacting, spatially-discrete heat sources, inter-source heat diffusion controls the flame propagation rate, resulting in a decrease in sensitivity of the flame speed on reaction time of the particles with oxygen. Based on this theory, the estimations provided in a previous publication [35] have actually predicted the results experimentally observed here. As the concentration of aluminum increases, the inter-particle spacing decreases and the discrete flame effects diminish. In fuel-rich mixtures, the amount of burned aluminum also rises proportionally to the oxygen content resulting in higher flame temperatures and, correspondingly, higher flame speeds for higher oxygen concentrations.

#### *Effect of the gas molecular transport coefficients on the burning velocity*

As in gaseous flames, the burning velocity in solid suspensions is roughly proportional to the square root of the heat diffusivity of the gas multiplied by the reaction rate. In addition, the rate of particle combustion in the diffusive combustion regime is proportional to the diffusivity of oxygen towards the micro-flames surrounding each particle. Combining these two factors gives the expression  $S_{L,He} / S_{L,Ar} = \sqrt{(\alpha D)_{He} / (\alpha D)_{Ar}}$  for the dependence of the burning velocity,  $S_L$ , in terms of the heat diffusivity  $\alpha$  and mass diffusivity of oxygen  $D$  for helium and argon as inert gases (they have equivalent heat capacities) [16]. This predicts a 3.9 fold flame speed increase for mixtures in 15% oxygen. As can be seen from the flame speed data in Fig 13, the ratio between the flame speeds in argon and helium is around 2.9. Perhaps this discrepancy could be explained by uncertainty in the measured values; however, a lower experimental ratio of burning velocities in helium-oxygen and argon-oxygen mixtures was also observed in experiments with stabilized aluminum Bunsen dust flames [16]. This trend of discrepancies points towards a different mode of particle combustion depending on whether oxygen is diluted with argon or helium. Particle combustion in argon mixtures is controlled by the diffusion of oxygen towards the diffusion micro-flame surrounding each particle and the experimental evidence indicates that a heterogeneous kinetically-controlled reaction at the surface might be the limiting reaction stage in helium mixtures due to their higher molecular heat and mass transfer coefficients [21]. In the asymptotic case of kinetically-controlled combustion, the flame speed depends on heat diffusivity only. Any intermediate (partial) dependence on oxygen diffusivity would indicate a transient particle combustion regime [36].

## *Unstable flames*

Contrary to acoustic oscillations previously observed in tubes [45], [46], pulsations in balloons are observed only in fuel-lean mixtures and are the strongest near the lean flame propagation limit indicating that their physical nature is very different from acoustic coupling. Similar pulsating flames in fuel suspensions have only been observed and reported once, for flames in suspensions of large PMMA particles in microgravity [47], [48]. Those authors considered the pulsations to be caused by periodical preheating of the fresh mixture by flame radiation. This, however, is an unlikely explanation since, as was discussed above, radiation cannot be sufficiently absorbed by the unburned mixture in small-scale dust clouds and primarily acts as a heat-loss mechanism. The effects of radiative heat transfer should also increase with fuel concentration, whereas pulsating flames are observed only in fuel-lean mixtures and are replaced by stable flame propagation when the fuel concentration approaches stoichiometric conditions. Thus, the observed pulsating and other unstable flame-propagation regimes are most probably the manifestation of thermo-diffusive instabilities, characteristic of flames with Lewis numbers deviating from unity [27], [49], [50].

Near stoichiometric concentrations, the diffusion of heat through the flame in the suspension is balanced by the diffusion of oxygen, resulting in Le numbers close to unity and steady flame propagation [51], [52]. According to flame stability theory, thermo-diffusive instabilities appear when this balance is broken, i.e., when the diffusion of either heat or mass begins to dominate over the other. For fuel-rich dust suspensions, the Lewis number is smaller than unity, which results in a cellular structure of the flame front [52]. Cellular flames have been observed in fuel-rich iron dust mixtures of small iron particle sizes during microgravity experiments by Tang *et al.* [20] as well as in the present balloon experiments when the aluminum concentration is above 500 g/m<sup>3</sup>. Increasing the dust concentration beyond the stoichiometric value does not change the heat conductivity of the mixture because the particles occupy a negligibly small volume. However, the heat diffusivity of the mixture does decrease with an increase in powder concentration due to the increase in heat capacity and density of the overall suspension. This effect yields Lewis numbers below unity for fuel-rich mixtures, causing the formation of cellular flames.

For fuel-lean dust mixtures, the gradient of oxygen concentration across the flame is small and the diffusion of oxygen does not substantially affect the flame structure. The Lewis number becomes very large due to the zero diffusivity of metal particles in suspension, and a different type of instability arises. These instabilities take the form of pulsations, target patterns, or spiral waves, and have been observed in numerous systems that support reaction-diffusion waves [53]–[55]. For combustion systems, the criterion for the onset of pulsating instabilities has been established by Joulin and Clavin and can be written as follows:  $\beta(Le - 1) > 16$ , with  $\beta$  being the Zeldovich number [42]. In other words, pulsating and spiral-wave instabilities are possible only for systems with sufficiently large Lewis numbers, high activation energy and low flame temperatures. These types of instabilities have been mostly observed in condensed systems [56]–[59] and rarely for gaseous flames due to the difficulty in creating combustible gaseous mixtures satisfying the instability criterion [28], [60]–[62].

A qualitative map of the different flame propagation regimes observed in the present experiments for aluminum suspensions as a function of the oxygen and aluminum concentrations is shown in Fig. 23.

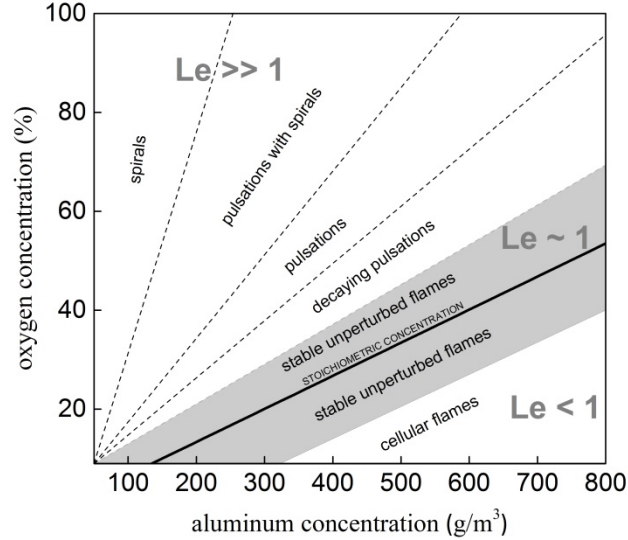


Figure 23. Map of the flame propagation regimes within fuel-oxygen concentration coordinates

As can be seen from Fig. 23, the structure of the map of the flame propagation regimes generally follows the criteria for stable/unstable flame propagation predicted by flame thermo-diffusive instability theory. However, a number of the phenomena observed in the present work still lack a clear physical explanation. For example, the flame trajectories in the pulsating regime shown in Fig. 15 indicate that brief periods of rapid flame movement are followed by comparatively-long periods of flame stagnation. The behavior within this flame propagation regime is difficult to rationalize with laminar flame theory. Also, the independence of the average flame propagation speed on the heat diffusivity of the gas mixture observed for pulsating flames and presented in Fig. 19 also seemingly contradicts the very nature of a flame driven by molecular heat diffusivity. One possible explanation may be that the observed pulsating phenomenon is closer to a series of consecutive thermal explosions, as described by the non-stationary thermal explosion theory developed first by Frank-Kamenetskii [63]. Each explosion is followed by a period of thermal relaxation, where the mixture burning rate falls effectively to zero. The combustion products after the explosion act like a hot wall, at a temperature close to the adiabatic value, that heats the reactants in the adjacent layer of the mixture until another thermal explosion event occurs inside the layer of unburned mixture bordering the combustion products from the previous explosion. Further work will be needed to clarify the physical mechanisms responsible for all of the flame propagation regimes shown in the regime map in Fig. 23.

## 4. CONCLUSIONS

The present work reports a large set of experimental data on isobaric, freely-propagating flames in aluminum dust clouds,

- Stable propagation of an unperturbed spherical flame was only observed in the vicinity of the stoichiometric concentration. Pulsating, spiral and combined spiral-pulsating flames were observed in fuel-lean mixtures and the formation of a cellular pattern on the flame front was evident in fuel-rich dust clouds. The appearance of unstable combustion generally follows the predictions of thermo-diffusive flame stability theory corresponding to pulsating flame instabilities at large  $Le$  numbers (fuel-lean dust suspensions) and cellular instabilities for  $Le$  numbers below unity (fuel-rich clouds).
- For the stable flame propagation regime in fuel-lean mixtures, the flame speed is quite insensitive to the oxygen concentration. For fuel-rich suspensions, the flame speed is insensitive to an increase in aluminum concentration. The first observation can be explained in terms of the discrete flame theory that takes into account inter-particle heat transfer. The latter observation is primarily a consequence of the insensitivity of the particle combustion rate to flame temperature in the diffusive regime.
- The burning velocity derived from flame propagation speeds in balloons correlates well with previously measured values from stabilized aluminum Bunsen flames.

## 5. REFERENCES

- [1] K. L. Cashdollar and M. Hertzberg, "Introduction to dust explosion," in *Industrial dust explosion*, K. L. Cashdollar and M. Hertzberg, Eds. ASTM 958, 1987, 5–32.
- [2] R. Eckhoff, *Dust explosions in the process industries: identification, assessment and control of dust hazards*. Gulf professional publishing, 2003.
- [3] I. Hartmann, J. Nagy, and M. Jacobson, *Recent studies on the explosibility of cornstarch*. US Dept. of the Interior, Bureau of Mines, 1950.
- [4] L. Meda, G. Marra, L. Galfetti, F. Severini, and L. De Luca, *Mater. Sci. Eng. C*, 27, (2007), 1393–1396.
- [5] O. F. Theimer, *Powder Technol.*, 8, (1973), 137–147.
- [6] M. Jacobson, A. R. Cooper, and J. Nagy, "Explosibility of metal powders," DTIC Document, Report, (1964).
- [7] J. H. Burgoyne and L. Cohen, *Proc. R. Soc. London. Ser. A. Math. Phys. Sci.*, 225, (1954), 375–392.
- [8] W. Felder and A. Fontijn, *J. Chem. Phys.*, 64, (1976), 1977–1980.
- [9] A. Fontijn, W. Felder, and J. J. Houghton, *Proc. Combust. Inst.*, 16, (1977), 871–879.
- [10] S. Goroshin, F.-D. Tang, A. J. Higgins, and J. H. S. Lee, *Acta Astronaut.*, 68,

(2011), 656–666.

- [11] H. M. Cassel, “Some fundamental aspects of dust flames,” US Dept. of the Interior, Bureau of Mines, Book, (1964).
- [12] D. R. Ballal, Proc. R. Soc. London. A. Math. Phys. Sci., 385, (1983), 21–51.
- [13] J. Sun, R. Dobashi, and T. Hirano, J. Loss Prev. Process Ind., 14, (2001), 463–467.
- [14] J.-H. Sun, R. Dobashi, and T. Hirano, Combust. Sci. Technol., 150, (2000), 99–114.
- [15] J. Sun, R. Dobashi, and T. Hirano, J. Loss Prev. Process Ind., 19, (2006), 769–773.
- [16] S. Goroshin, I. Fomenko, and J. H. S. Lee, Proc. Combust. Inst., 26, (1996), 1961–1967.
- [17] P. Julien, S. Whiteley, S. Goroshin, M. J. Soo, D. L. Frost, and J. M. Bergthorson, Proc. Combust. Inst., 35, (2015), 2431–2438.
- [18] P. Julien, M. Soo, S. Goroshin, D. L. Frost, J. M. Bergthorson, N. Glumac, and F. Zhang, J. Propuls. Power, 30, (2014), 1047–1054.
- [19] M. Soo, P. Julien, S. Goroshin, J. M. Bergthorson, and D. L. Frost, Proc. Combust. Inst., 34, (2013), 2213–2220.
- [20] F.-D. Tang, S. Goroshin, A. Higgins, and J. Lee, Proc. Combust. Inst., 32, (2009), 1905–1912.
- [21] F.-D. Tang, S. Goroshin, and A. J. Higgins, Proc. Combust. Inst., 33, (2011), 1975–1982.
- [22] S. Goroshin, M. Bidabadi, and J. H. S. Lee, Combust. Flame, 105, (1996), 147–160.
- [23] J. Palecka, P. Julien, S. Goroshin, J. M. Bergthorson, D. L. Frost, and A. J. Higgins, Proc. Combust. Inst., 35, (2015), 2463–2470.
- [24] P. Julien, J. Vickery, S. Whiteley, A. Wright, S. Goroshin, J. M. Bergthorson, and D. L. Frost, J. Loss Prev. Process Ind., 36, (2015), 230–236.
- [25] T. Skjold, K. L. Olsen, and D. Castellanos, J. Loss Prev. Process Ind.
- [26] E. W. Christiansen, C. K. Law, and C. J. Sung, Combust. Flame, 124, (2001), 35–49.
- [27] B. Matkowsky and G. Sivashinsky, SIAM J. Appl. Math., 35, (1978), 465–478.
- [28] G. Jomaas, J. K. Bechtold, and C. K. Law, Proc. Combust. Inst., 31, (2007), 1039–1046.
- [29] C. K. Law, *Combustion Physics*. Cambridge University Press, 2006.
- [30] G. E. Andrews and D. Bradley, Combust. Flame, 18, (1972), 133–153.

- [31] I. Glassman and R. Yetter, *Combustion*, 4th ed. Academic Press, 2008.
- [32] F. N. Egolfopoulos, N. Hansen, Y. Ju, K. Kohse-Höinghaus, C. K. Law, and F. Qi, *Prog. Energy Combust. Sci.*, 43, (2014), 36–67.
- [33] L. P. H. de Goey, A. van Maaren, and R. M. Quax, *Combust. Sci. Technol.*, 92, (1993), 201–207.
- [34] H. M. Cassel, A. K. Das Gupta, and S. Guruswamy, *Symp. Combust. Flame, Explos. Phenom.*, 3, (1949), 185–190.
- [35] L. V Boichuk, V. G. Shevchuk, and A. I. Shvets, *Combust. Explos. Shock Waves*, 38, (2002), 651–654.
- [36] P. Julien, J. Vickery, S. Goroshin, D. L. Frost, and J. M. Bergthorson, *Combust. Flame*, 162, (2015), 4241–4253.
- [37] J. M. Bergthorson, S. D. Salusbury, and P. E. Dimotakis, *J. Fluid Mech.*, 681, (2011), 340–369.
- [38] X. Qin and Y. Ju, *Proc. Combust. Inst.*, 30, (2005), 233–240.
- [39] S. D. Salusbury and J. M. Bergthorson, *Combust. Flame*, 162, (2015), 3324–3332.
- [40] L. J. Benezech, J. M. Bergthorson, and P. E. Dimotakis, *Proc. Combust. Inst.*, 32, (2009), 1301–1309.
- [41] R. Lockett, *Combust. Flame*, 119, (1999), 109–120.
- [42] C. M. Vagelopoulos and F. N. Egolfopoulos, *Proc. Combust. Inst.*, 27, (1998), 513–519.
- [43] J. D. Munzar, B. Akih-Kumgeh, B. M. Denman, A. Zia, and J. M. Bergthorson, *Fuel*, 113, (2013), 586–597.
- [44] J. M. Bergthorson and P. E. Dimotakis, *Exp. Fluids*, 41, (2006), 255–263.
- [45] D. B. Graves and J. O. L. Wendt, (1982), 1189–1196.
- [46] J. O. L. Wendt, B. M. Kram, M. M. Masteller, and B. D. Mccaslin, (1986), 419–426.
- [47] T. A. Milne and J. E. Beachey, *Combust. Sci. Technol.*, 16, (1977), 123–138.
- [48] T. A. Milne and J. E. Beachey, *Combust. Sci. Technol.*, 16, (1977), 139–152.
- [49] A. L. Sánchez, J. Urzay, and A. Liñán, *Proc. Combust. Inst.*, 35, (2015), 1549–1577.
- [50] N. Darabiha, F. Lacas, J. C. Rolon, and S. Candel, *Combust. Flame*, 95, (1993), 261–275.

## **Chapter 2. Stabilized, flat aluminum flames on a counterflow burner**

### **1. INTRODUCTION**

The burning velocity is a fundamental property of a mixture that reflects its reactivity and rate of heat transfer. It is defined as the speed at which an adiabatic, un-stretched, one-dimensional laminar flame propagates through a quiescent mixture of unburned reactants [1]–[3]. By definition, the burning velocity is an asymptotic approximation that is difficult to realize experimentally. Unavoidable complications, such as heat loss, flame stretch, and, in some experimental configurations, residual turbulence, all influence the flame speed observed in a given experiment that may differ significantly from the idealized laminar burning velocity. For gaseous and liquid fuels, these effects are generally understood and the laminar burning velocities obtained from different techniques, such as counterflow flames [4], spherically-expanding flames [1], [4], and flat-flame burners [5], can be reconciled [4]. The results from these different experimental geometries converge towards an accepted value of laminar burning velocity that can now be accurately calculated using advanced thermo-chemical models [4].

In contrast to gaseous and liquid fuels, attempts to measure burning velocity in particulate suspensions are scarce in the literature. Cassel first attempted to use the Bunsen flame technique to measure the burning velocity in aluminum suspensions [6], [7]. A similar technique, with a different dust dispersion system and an improved measurement technique for the dust concentration, was used by McGill researchers to measure flame speed in aluminum suspensions [8] and hybrid mixtures of aluminum with methane and air [9], [10]. Boichuk et al. [11] and Ballal [12] measured the flame speed in aluminum clouds within tubes under normal and micro-gravity conditions. Constant-pressure spherically-expanding flames propagating through aluminum suspensions, contained in latex balloons, were recently studied by McGill researchers [13]. This study enabled the measurement of the flame speed, and estimation of the laminar burning velocity, over a wide range of aluminum dust and oxygen concentrations [13]. Thermo-diffusive instabilities were also observed in flames propagating through lean particulate suspensions [13].

Although these recent studies on particulate-fuel flames have provided significant insight into the physics of flame propagation in such fuel clouds, the question remains as to whether the concept of burning velocity can be applied to flames propagating in particle suspensions. In comparison to a gas flame, dust flames are more sensitive to both scale and flow configuration. Creating a fuel suspension for flame studies requires a turbulent fuel-dispersion process, and maintaining large particles in suspension requires either a level of turbulence or an ascending laminar flow. The settling velocity of large particles can be comparable to or even exceed the burning velocity, and hence such particle sizes must be studied under microgravity conditions [14]. Solid fuel particles, unlike gases that are largely transparent to thermal radiation, can efficiently absorb the radiation emitted from the flame zone and post-combustion zone, effectively pre-heating the mixture [13], [15]. Dust flames are also more sensitive to flow gradients due to velocity slippage between solid and gas phases, as discussed in this paper. Furthermore, the comparison of results

obtained by different research groups is rendered difficult due to the unique nature of each powder used. Even powders with similar average diameters may have very different particle size distributions, which could affect the resulting flame speed. Powders also differ by purity, degree of initial particle oxidation, and particle shape, all of which increase the complexity of the problem.

To address this last issue, researchers at McGill University have performed a series of experiments, over a span of about 20 years, using different methodologies with the same batch of Ampal 637 aluminum powder hermetically stored in a container [8]–[10], [13], [15]–[17]. This unique dataset allows, for the first time, a comparison of burning velocities estimated from flame measurements in a variety of experimental configurations, including Bunsen dust flames [8], flames propagating in tubes [16], and freely-propagating spherical flames [13], [15]. In continuation of this effort, the present experimental paper describes the first time the burning velocity in aluminum suspensions is estimated using a counterflow flat-flame technique with a modified Particle Image Velocimetry (PIV) technique. The results from the present work are then compared with burning velocities obtained previously to assess whether the concept of laminar burning velocity can be applied to flames propagating through suspensions of particulate fuels.

## 2. EXPERIMENTAL APPARATUS

The experimental setup is based on the McGill Bunsen solid-fuel burner [8], which was also recently used in experiments in hybrid mixtures of methane and metal fuels [9], [10], [18]. The aluminum powder is initially loaded in a piston that is driven upwards by a mechanical actuator, allowing the solid particulate fuel to be dispersed at the top of the metal-powder charge using a concentric sonic air knife. The two-phase flow is entrained into air that ascends through a 60 cm-long laminarizing tube and exits through the bottom nozzle, with a diameter of 1.5 cm, surrounded by a co-flow of air. A second, inverted, nozzle is placed directly on top of, and concentric with, the bottom nozzle with a separation of two centimeters, which forces a jet of air against the aluminum-air mixture. This counterflow generates a stagnation point between the two nozzles, which produces a flat aluminum flame, as shown in Fig. 1.

The dust concentration is monitored at all times during the experiment using a laser-light attenuation probe that is synchronized with the other diagnostic techniques. The probe was calibrated using the dust Bunsen burner for this specific batch of aluminum powder [9], [10]. The aluminum powder used is Ampal 637 (Ampal, NJ) and has a mean Sauter diameter of about 5.6 microns. The powder is nodular in shape and the same batch has been used in previous experiments to measure the burning velocity in stabilized and propagating flames [8], [15].

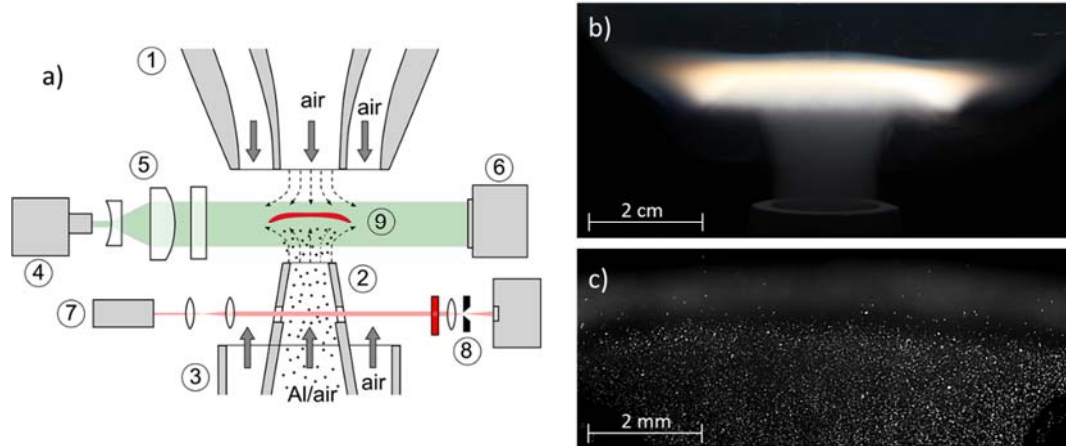


Figure 2. a) Counterflow apparatus and diagnostics. b) Flat aluminum flame obtained with a counterflow burner. c) Still frame from PIV image data showing the illuminated particles. The diffuse area of light at the top corresponds to the flame. The aluminum concentration is around  $400 \text{ g/m}^3$  for both b) and c). The numbered parts are 1) top nozzle with air co-flow 2) bottom nozzle 3) bottom co-flow 4) 5 W green laser 5) beam expansion optics 6) Photron SA-5 high-speed camera 7) 5 mW red laser 8) photo-diode 9) flat aluminum flame.

Previous studies of flame speeds, and inference of burning velocities, in metal-particulate flames have relied on imaging of the flame surface location. The present study improves upon these past techniques and uses a particle image velocimetry (PIV) diagnostic technique. A 5 W, 532 nm green laser is used to illuminate the aluminum particles ahead of the flame. As shown in Fig. 1, the light beam is expanded with the use of beam-shaping optics, which consists of an  $f = -25 \text{ mm}$  planoconcave lens followed by an  $f = 50 \text{ mm}$  planoconvex lens. A thin light sheet is formed, passing through the centerline of the nozzle, by horizontally focusing the expanded beam using a  $f = 300 \text{ mm}$  cylindrical lens.

The flame and the illuminated particles in the pre-heat zone are imaged using a Photron SA-5 video camera operating at 4000 frames per second and an exposure time of  $10^{-6} \text{ s}$ . The particle velocity in the flow is estimated using the commercial PIV software, DAVIS, produced by LaVision. Figure 1 shows the bottom and top nozzle along with the optical diagnostics. It also shows a stabilized aluminum flame with a concentration of roughly  $400 \text{ g/m}^3$ . The particles in the flow below the flame are illuminated by the light emitted from the flame and the bottom nozzle is visible. Fig. 1c shows the aluminum particles illuminated by the green laser. The diffuse area of light at the top of the image is the aluminum flame, which has an observed thickness of approximately 3 mm.

Counterflow [4] or stagnation-flow experiments [19] are widely used in the study of gas-phase combustible mixtures, where the fluid velocity profile is typically visualized using small, micron-sized, inert tracer particles, such as aluminum oxide, with a narrow size distribution. The seeded particles are illuminated with a laser sheet and particle image velocimetry [4], [20], particle-tracking velocimetry [21], [22], or laser-Doppler velocimetry [23], [24] are used to track the motion of particles. The small size of the inert tracer particles allows them to accurately follow the motion of the gas molecules, and the deviations in the high-gradient regions of the flow can be estimated [21], [25], [26]. The

reference flame speed and the stretch rate are deduced from the measured velocity profiles and this information can be used to extrapolate the burning velocity to un-stretched conditions using linear [1], or non-linear [4], [19], methodologies.

The problem becomes more complicated with two-phase flames, where the combustible particles now play both the role of fuel and tracer. In these flames, it is not possible to distinguish between micron-sized inert tracers and the larger fuel particles when performing the laser diagnostic techniques, complicating the interpretation of the resulting measurements.

Counterflow coal flames have been stabilized, but diagnostics have been limited to the sampling of gases at different locations, as well as temperature measurements obtained with thermocouples, without any attempt to track the motion of coal particles or assess the flame speed [27], [28]. Burning velocities from flat coal flames come only from porous plug burners [29], [30] and no previous attempt has been made to use particle image velocimetry on dust flames, to the authors' knowledge.

Sanchez et al. recently discussed counterflow flames in liquid-fuel sprays in their review on spray combustion [31]. The authors highlight the difficulty in obtaining the fluid velocity from the particle motion due to inertia of the particles. The motion of spray droplets, as well as solid aluminum particles, depends on the Stokes number or the ratio of the accommodation time to the characteristic flow time [31]. The particle tracers used in gas-phase flames have very low Stokes numbers, hence the particles closely follow the gas flow [26]. The accurate knowledge of the particle size and the physics of particle motion in such flames has enabled very accurate estimates of the measured particle velocity profiles in stagnation flames using the results of one-dimensional stagnation-flame simulations [19], [26]. Such estimates involve the prediction of the particle motion as it responds to the Stokes drag and thermophoretic forces, as well as the particle inertia, through the various velocity and temperature gradients within these flames [22], [26].

The aluminum powder used in the present experiments has a wide distribution in size that ranges from 1 micron to around 15 microns, mixed with a small fraction of agglomerates. The Stokes number, or accommodation time, depends on the particle size and mass and, thus, the current fuel does not have a unique Stokes number. Droplet experiments can be conceived using monodisperse droplets [32], which simplifies the problem. Unfortunately, such a technique is not currently possible for metal-particulate fuel suspensions. Furthermore, agglomerates and larger particles, although small in number, will individually scatter more laser light due to their larger scattering cross-sections and will, therefore, be over-represented in the signal captured by the high-speed camera sensor. The measured signal is, therefore, not representative of the average particle size, 6 microns, that composes most of the powder in the mixture.

This inherent complexity related to the measurement of particle velocities in particulate-fuel suspensions with a finite particle size distribution prevents the estimation of the Stokes time from first principles and necessitates a new approach to estimate the *effective* Stokes time. In counterflow flame measurements, the reference flame speed and stretch rate are traditionally taken as the values within the fluid. Assuming a viscous fluid with a low Reynolds number, since the particles only deviate by relatively small values from the

nominal gas flow, the fluid velocity,  $U_f$ , can be estimated from the measured particle velocity profile with the following equation

$$U_f = U_p + \tau_s U_p \frac{dU_p}{dx} \quad (1)$$

where  $\tau_s$  is the effective Stokes time, which depends on the fluid velocity, particle diameter, and particle density. Since the signal is biased towards larger particles and agglomerates and particles have a distribution in size, the effective Stokes time has to be found experimentally. The equation was used to calibrate the effective Stokes time of the Ampal powder using a cold unreacted impinging-jet flow in the same counterflow configuration. The flow conditions were kept constant between the two experiments, one of which used 1 micron alumina particles with a narrow size distribution, and the second used the Ampal 637 aluminum fuel. Figure 2 shows the particle velocity profile in the two cold flow cases, where the fluid flow is maintained constant in both experiments. Assuming alumina particles perfectly follow the flow, the alumina profile can be considered to be a measurement of  $U_f(x)$ . For the same flow, the effect of the larger particle sizes within the Ampal powder leads to a significant lag of the measured velocity profile relative to that of the alumina powder. With the measured  $U_p(x)$  from the aluminum fuel,  $\tau_s$  is estimated for Ampal powder using Eq. 1. The estimated effective Stokes time from the measured velocity profile with the Ampal powder is 1 ms, while a value of 11.9  $\mu$ s is estimated using the nominal particle diameter of 6 microns.

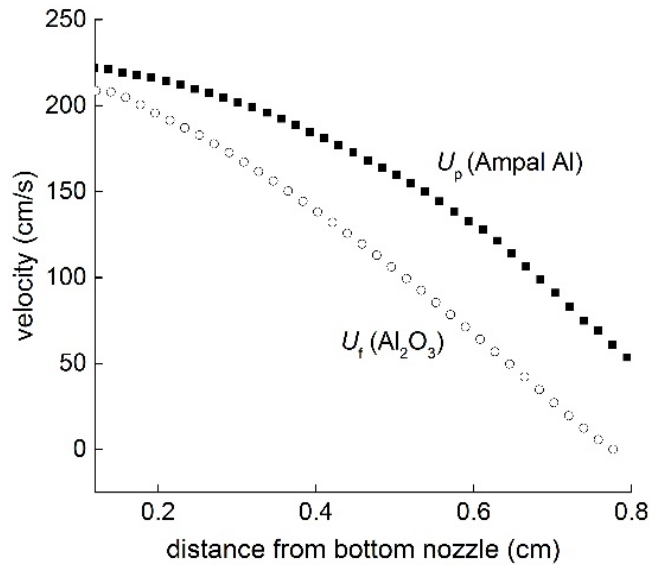


Figure 3. Cold impinging-jet flow profiles for aluminum Ampal powder and 1 micron alumina, which is assumed to follow perfectly fluid velocity, for the same jet flow conditions.

### 3. RESULTS AND DISCUSSION

Aluminum flames were stabilized at various fuel concentrations on the counterflow burner with constant flow rates, corresponding to a stretch rate of approximately  $K \approx 180 \text{ s}^{-1}$ . The stoichiometric concentration for an aluminum-air flame corresponds to a mass loading of about  $314 \text{ g/m}^3$ . The flow fields are obtained from 2 consecutive images and the velocity profile is measured along the center line of the flame. Figure 2 shows an example of a typical flow profile for a flame with an aluminum concentration of about  $400 \text{ g/m}^3$ . It shows the measured velocity obtained from the particles and the calculated flow profile of the gas, estimated using the Stokes correction given by Eq. (1). The flow decelerates as soon as it leaves the bottom nozzle due to the opposing flow and accelerates after the flame due to thermal expansion, consistent with typical flow profiles from such stagnation flames [22].

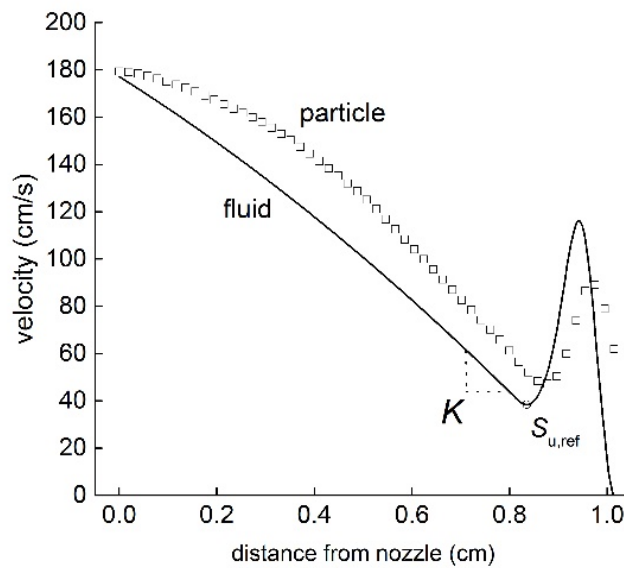


Figure 4 Measured particle, and estimated fluid, velocity profiles for a typical counterflow aluminum flame. The value of  $S_{u,ref}$  is taken from the fluid profile as the minimum of the profile upstream of the flame and the strain rate,  $K$ , is taken as the slope of the cold-flow velocity profile upstream of  $S_{u,ref}$ .

The reference flame speed is taken as the minimum of the estimated fluid velocity curve upstream of the flame, as for gaseous and liquid fuel flames [4], [21], [25]. The reference flame speeds obtained from each PIV profile are then averaged from a set of approximately 500 PIV vector fields at each concentration. Flames can only be successfully stabilized for fuel rich mixtures in air. As can be seen in Fig. 4, the measured flame speed does not depend on aluminum concentration within the uncertainty. The scatter in the data is caused by the PIV measurement uncertainty, which is amplified by the need to estimate the fluid velocity using the Stokes correction, and the inherent fluctuations in the dust concentration during the experiments.

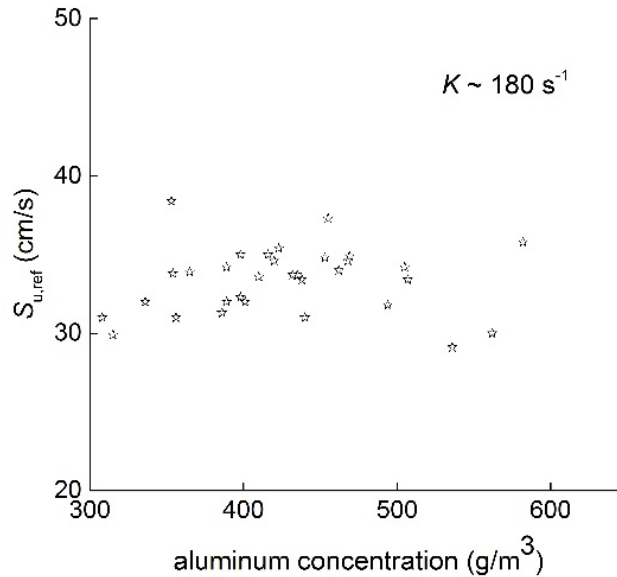


Figure 5. Flame speed obtained on counterflow apparatus as a function of aluminum concentration for rich aluminum-air flames.

## Discussion

### Concept and measurement of burning velocity

Researchers have developed a wide array of experimental techniques to measure the laminar burning velocity of gas-phase flames. Early studies used more rudimentary techniques, such as Bunsen burners, to measure the burning velocity, despite inherent problems such as heat loss at the nozzle and negative stretch and curvature at the tip of the flame [2], [4]. To improve the accuracy of the measurements, alternative methodologies were developed, such as spherically-propagating flames and flames in tubes, but these were also found to have inherent experimental uncertainties. This led to the development of more sophisticated techniques, such as flat flames through the use of stagnation [4], [19] or counterflow burners [33], which, with the help of particle tracking techniques and an improved understanding of the effect of hydrodynamic stretch on the resulting flame speed, led to increasing precision in the measurement of the burning velocity. Despite all these efforts, there still remains a discrepancy between the various values for burning velocity reported for gaseous mixtures.

This paper poses the question as to whether the notion of burning velocity can also be applied to flames in particulate suspensions of nonvolatile fuels, such as aluminum. The burning velocity is defined in a premixed gaseous fuel where the mixture is homogeneous. In heterogenous flames, the oxidizer is uniform in space, but the fuel is localized in particles with large inter-particle spacing when compared to the diameter of the particle. It was proposed by Bradley and Lee [34], and later by Dahoe et al. [35], that the concept of burning velocity can be applied to organic dusts that volatilize in the flame pre-heat zone and sustain an effectively gas-phase combustion, as discussed by Seshadri et al. [36]. The reaction rates of aluminum vapor with various oxidizers has an extremely low activation

energy [37], [38], which prevents the accumulation of aluminum vapor where oxidizers are present and, therefore, forces the reaction zone close to the particle surface in either a heterogeneous reaction or through lifted micro-diffusion flames [39].

*Burning velocity in aluminum suspensions*

The present work reports the first flat aluminum stagnation flame stabilized using a counterflow apparatus. The new experimental measurements of flame speed in fuel-rich aluminum suspensions obtained in the counterflow aluminum flames discussed in this paper can now be compared to previous data from a range of apparatus. Each of these different approaches has the same inherent systematic experimental uncertainty as for gas-phase flames, along with the additional complexity associated with the multi-phase nature of the fuel-oxidizer suspension. Thus, a similar or greater spread in the data is expected.

Figure 5 shows the reference flame speed obtained with the present counterflow apparatus in comparison to the burning velocities estimated with different techniques. As can be seen, burning velocities from Bunsen flames and spherically-expanding flames are in relatively good agreement and are about 30% lower than the reference flame speed obtained from the present counterflow apparatus. The burning velocities obtained from the tube method [16] are also presented but the factor that relates the measured flame speed to the fundamental burning velocity is unknown and these values are, therefore, associated with large uncertainties.

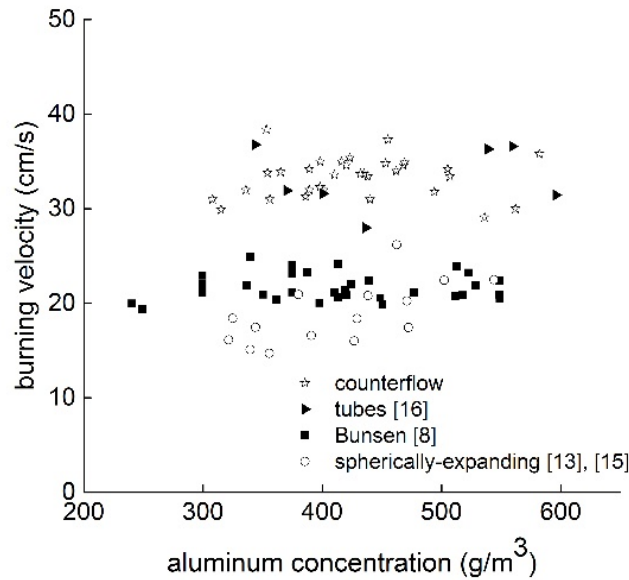


Figure 6 Burning velocity as a function of aluminum concentration for different measurement techniques that include Bunsen burner [8], spherically-expanding flames [13], present work from counterflow burner, and flames propagating in tubes [16].

The discrepancy obtained in the present results is of similar order to those that can be seen for gas-phase flames [4]. Aluminum Bunsen flames [8] have an even stronger curvature at the tip than a typical methane flame and, thus, have greater experimental uncertainty.

These flames also lose heat to the cold burner rim, lowering the effective burning rates. The flame speed estimated from spherically-expanding flames is obtained by tracking the radius as a function of time using high-speed imaging. The hot combustion products act as a piston displacing the flame outwards and, thus, the burning velocity is estimated by multiplying the flame speed by the ratio of densities from the burnt and unburnt gases. The density of the hot products cannot be measured in situ and is estimated using thermodynamic values. The actual temperature of the combustion products in the experiments must, by necessity, be lower than the adiabatic flame temperature. The difference in final product temperature, and therefore density, from thermodynamic predictions results from both heat losses due to radiation, as well as from incomplete combustion of the particles inside the flame. If the actual final flame temperature was measured, the resulting burning velocities would be greater than those estimated assuming adiabatic combustion.

Flames propagating in tubes towards the closed end propagate at a speed that depends on the flame curvature. The value of the measured speed can go from that of the burning velocity for a flat, smooth horizontal flame front to three to four times the burning velocity if the flame is slanted [40]. The knowledge of this factor is important in order to accurately estimate the burning velocity from this technique and is the main source of systematic experimental uncertainty. The flames in tubes were reported to be smooth and curved, with a parabolic shape, such that the values were estimated assuming a value of flame speed over burning velocity of 2. The systematic-uncertainty range for the flames in tubes shown in Fig. 5 range from 1.5 times to 3 times the burning velocity.

The wide scatter in burning-velocity estimates for gas-phase fuels was only reconciled with improved theories for the effect of flame stretch and curvature on the burning rates of these flames [1], [4]. In all cases, the measured reference flame speed in the counterflow or stagnation-flow geometries is higher than the laminar burning velocity, due to the fact that the flame preheat zone acts as a low pass filter that increases the reference flame speed even in cases where the flame speed at the reaction-zone surface is decreasing [19], [21].

More research, both experimental and theoretical, is needed to properly assess the effects of flame stretch on the observed flame speeds in a variety of flame geometries in nonvolatile particulate-fuel suspensions in a variety of oxidizing gases. The counterflow heterogeneous flame apparatus used in the present work is a convenient system for assessing these effects, as has been done in the past for gaseous and liquid fuels.

#### 4. CONCLUSIONS

This paper has demonstrated, for the first time, that flames of nonvolatile fuels, such as aluminum, can be stabilized in the counterflow flame geometry. The stabilization of steady flames in this new geometry enabled the measurement of the velocity profile through the cold flow and flame zones using an effective Stokes time to compensate for the large particle inertia. The ability to stabilize flat, essentially one-dimensional, counterflow flames in nonvolatile fuel suspensions allows improved measurements of the flame structure and burning rates in such flames.

The measured reference flame speeds from the rich aluminum flames investigated in this paper are compared to those estimated from previous studies using Bunsen flames,

spherically-propagating flames, and flames propagating in tubes. Each of these experimental approaches has a degree of uncertainty associated with it, related to the effect of flame stretch and curvature, as well as the effects of incomplete fuel combustion and radiative heat loss. Given these various uncertainties, the reasonable agreement between the reference flame speeds measured in the counterflow flames and the other techniques suggests that the concept of a laminar burning velocity may, indeed, be applicable to flames propagating through suspensions of nonvolatile fuels. More work is needed to assess how such flames respond to hydrodynamic stretch and curvature. Not only is the Lewis number not well defined for such heterogeneous fuel-air mixtures, but additional effects, such as particle lag, are inherent to these flames and must be accounted for in any predictive model.

## 5. REFERENCES

- [1] C. K. Law, *Combustion Physics*. Cambridge University Press, 2006.
- [2] G. E. Andrews and D. Bradley, *Combust. Flame*, 18, (1972), 133–153.
- [3] I. Glassman and R. Yetter, *Combustion*, 4th ed. Academic Press, 2008.
- [4] F. N. Egolfopoulos, N. Hansen, Y. Ju, K. Kohse-Höinghaus, C. K. Law, and F. Qi, *Prog. Energy Combust. Sci.*, 43, (2014), 36–67.
- [5] L. P. H. de Goey, A. van Maaren, and R. M. Quax, *Combust. Sci. Technol.*, 92, (1993), 201–207.
- [6] H. M. Cassel, “Some fundamental aspects of dust flames,” US Dept. of the Interior, Bureau of Mines, Book, (1964).
- [7] H. M. Cassel, A. K. Das Gupta, and S. Guruswamy, *Symp. Combust. Flame, Explos. Phenom.*, 3, (1949), 185–190.
- [8] S. Goroshin, I. Fomenko, and J. H. S. Lee, *Proc. Combust. Inst.*, 26, (1996), 1961–1967.
- [9] M. Soo, P. Julien, S. Goroshin, J. M. Bergthorson, and D. L. Frost, *Proc. Combust. Inst.*, 34, (2013), 2213–2220.
- [10] P. Julien, M. Soo, S. Goroshin, D. L. Frost, J. M. Bergthorson, N. Glumac, and F. Zhang, *J. Propuls. Power*, 30, (2014), 1047–1054.
- [11] L. V Boichuk, V. G. Shevchuk, and A. I. Shvets, *Combust. Explos. Shock Waves*, 38, (2002), 651–654.
- [12] D. R. Ballal, *Proc. R. Soc. London. A. Math. Phys. Sci.*, 385, (1983), 21–51.
- [13] P. Julien, J. Vickery, S. Goroshin, D. L. Frost, and J. M. Bergthorson, *Combust. Flame*, 162, (2015), 4241–4253.
- [14] S. Goroshin, F.-D. Tang, A. J. Higgins, and J. H. S. Lee, *Acta Astronaut.*, 68, (2011), 656–666.
- [15] P. Julien, J. Vickery, S. Whiteley, A. Wright, S. Goroshin, J. M. Bergthorson, and

- D. L. Frost, *J. Loss Prev. Process Ind.*, 36, (2015), 230–236.
- [16] S. Goroshin, M. Bidabadi, and J. H. S. Lee, *Combust. Flame*, 105, (1996), 147–160.
- [17] J. Palecka, P. Julien, S. Goroshin, J. M. Bergthorson, D. L. Frost, and A. J. Higgins, *Proc. Combust. Inst.*, 35, (2015), 2463–2470.
- [18] P. Julien, S. Whiteley, S. Goroshin, M. J. Soo, D. L. Frost, and J. M. Bergthorson, *Proc. Combust. Inst.*, 35, (2015), 2431–2438.
- [19] J. M. Bergthorson, S. D. Salusbury, and P. E. Dimotakis, *J. Fluid Mech.*, 681, (2011), 340–369.
- [20] X. Qin and Y. Ju, *Proc. Combust. Inst.*, 30, (2005), 233–240.
- [21] S. D. Salusbury and J. M. Bergthorson, *Combust. Flame*, 162, (2015), 3324–3332.
- [22] L. J. Benezech, J. M. Bergthorson, and P. E. Dimotakis, *Proc. Combust. Inst.*, 32, (2009), 1301–1309.
- [23] R. Lockett, *Combust. Flame*, 119, (1999), 109–120.
- [24] C. M. Vagelopoulos and F. N. Egolfopoulos, *Proc. Combust. Inst.*, 27, (1998), 513–519.
- [25] J. D. Munzar, B. Akih-Kumgeh, B. M. Denman, A. Zia, and J. M. Bergthorson, *Fuel*, 113, (2013), 586–597.
- [26] J. M. Bergthorson and P. E. Dimotakis, *Exp. Fluids*, 41, (2006), 255–263.
- [27] D. B. Graves and J. O. L. Wendt, (1982), 1189–1196.
- [28] J. O. L. Wendt, B. M. Kram, M. M. Masteller, and B. D. Mccaslin, (1986), 419–426.
- [29] T. A. Milne and J. E. Beachey, *Combust. Sci. Technol.*, 16, (1977), 123–138.
- [30] T. A. Milne and J. E. Beachey, *Combust. Sci. Technol.*, 16, (1977), 139–152.
- [31] A. L. Sánchez, J. Urzay, and A. Liñán, *Proc. Combust. Inst.*, 35, (2015), 1549–1577.
- [32] N. Darabiha, F. Lacas, J. C. Rolon, and S. Candel, *Combust. Flame*, 95, (1993), 261–275.
- [33] F. N. Egolfopoulos, P. Cho, and C. K. Law, *Combust. Flame*, 76, (1989), 375–391.
- [34] D. Bradley and J. H. S. Lee, *Proc. First Int. Colloq. Explos. Ind. Dusts*, 2, (1984), 220–223.
- [35] A. E. Dahoe, K. Hanjalic, and B. Scarlett, *Powder Technol.*, 122, (2002), 222–238.
- [36] K. Seshadri, A. L. Berlad, and V. Tangirala, *Combust. Flame*, 89, (1992), 333–342.

- [37] A. Fontijn, W. Felder, and J. J. Houghton, *Proc. Combust. Inst.*, 16, (1977), 871–879.
- [38] W. Felder and A. Fontijn, *J. Chem. Phys.*, 64, (1976), 1977–1980.
- [39] J. M. Bergthorson, S. Goroshin, M. J. Soo, P. Julien, J. Palecka, D. L. Frost, and D. J. Jarvis, *Appl. Energy*, 160, (2015), 368–382.
- [40] C. Almarcha, B. Denet, and J. Quinard, *Combust. Flame*, 162, (2015), 1225–1233.

## **Chapter 3. Freely-propagating, large-scale aluminum flames in field tests**

### **1. INTRODUCTION**

The ever increasing role of modern technologies based on metal powders, such as powder metallurgy, chemical processing, plasma spraying, etc., and the rapidly increasing scale of metal powder production are overshadowed by the increased human and material cost of accidents caused by metal dust explosions [1]. In spite of the strong impetus to implement state-of-the-art preventive measures to mitigate accidents, the progress in this field has been relatively slow in comparison to other branches of preventive science. The slow progress in prevention of metal dust explosions reflects the relatively underdeveloped state of combustion science in this field in contrast to the impressive progress achieved in understanding the physics and chemistry of homogeneous gas flames.

The primary reason for the slow progress in dust combustion science is rooted in the difficulties of extracting the fundamental combustion parameters, such as ignition temperature, burning velocity, flame quenching distance and flame structure, from laboratory experiments with metal dust clouds. Traditionally, most dust combustion tests are performed in constant volume vessels. Though convenient for empirical testing, constant-volume bombs have limited or no optical access, and the pressure rise is the only parameter typically measured in most experiments. The pressure history provides limited insight into the dust flame propagation since the deduction of the flame speed from the rate of pressure rise is neither accurate nor representative if the flame propagation deviates from the ideal picture of a spherically symmetric laminar flame[2], [3]. Some experiments have demonstrated that the residual turbulence induced in the mixture during the dust dispersal phase may have a considerable influence on flames ignited with short delay times after dispersal [4], [5]. Furthermore, the implementation of modern flame diagnostic techniques, such as emission and laser-absorption spectroscopy, is required to elucidate the flame structure and verify equilibrium calculations of flame temperatures against experimental values, which is difficult to accomplish in constant volume bombs.

The current paper presents a new apparatus that permits the creation of unconfined dust clouds with a total volume in the range of 5-10 m<sup>3</sup>.

### **2. EXPERIMENTAL APPARATUS**

Combustion experiments in large-scale aluminum dust clouds are performed using the dust dispersal device previously developed [6] and shown in Fig. 1 below. The apparatus is essentially a scaled-up version of the dust dispersal unit used with our laboratory Bunsen burner, as described by Soo et al. [7] and Julien et al. [8], and can create a large uniform column of suspended powder. Up to 1 kg of aluminum powder is initially loaded into the cylindrical cartridge having an inner diameter of about 5 cm and length of 30 cm. During the dispersal process, the powder column is displaced upwards at constant speed by a pneumatic piston and is progressively de-agglomerated and entrained into the

vertical air flow generated by an impinging sonic annular air jet (or air-knife) at the top of the cartridge. All of the powder within the cartridge is dispersed within a time of less than 1 second, as shown in Fig. 2, creating a vertical dust cloud about 4 m tall and 2 m wide near the top.

Initial tests were performed at an outdoor test site [6], but it was necessary to initiate the flame propagation promptly during the latter stages of the dispersal process to avoid the displacement of the dust cloud by the ambient wind conditions. To provide a sufficient delay time between powder dispersal and ignition to allow the turbulence within the multiphase cloud to decay, quiescent ambient conditions are required. Hence, the present experiments were performed indoors in the large-scale fire tower at the Fire Research Laboratory of the National Research Council of Canada (Mississippi Mills, Ontario, Canada). The tower is approximately 10 stories (35 m) high and has about 200 m<sup>2</sup> of floor area. Two large, variable-area openings at the tower base allow the intake of outside air for ventilation and prevent any pressure build up during the flame propagation. The combustion products are vented through openings in the ceiling connected to a powerful ventilation system, which is operated only after the combustion event is completed to avoid disturbing the cloud formation and flame propagation.

Cloud ignition is achieved with a small 2 g charge of black powder placed at the cloud base, which is initiated by an electrically-heated bridge wire. The ignition charge is placed on a mast to vary the height as the ignition delay times are adjusted. Another mast with two rows of bare junction K-type thermocouples with three different bead sizes (0.075, 0.0125 and 0.25 mm) is placed close to the dispersal unit, with the thermocouple arms extending into the dust cloud axis to record the temperature history within the cloud during the passage of the flame. A Photron SA5 videocamera was used to record the flame propagation at 2,000 frames per second. The camera record and temperature measurements were synchronized using a photodiode signal from the ignition event.

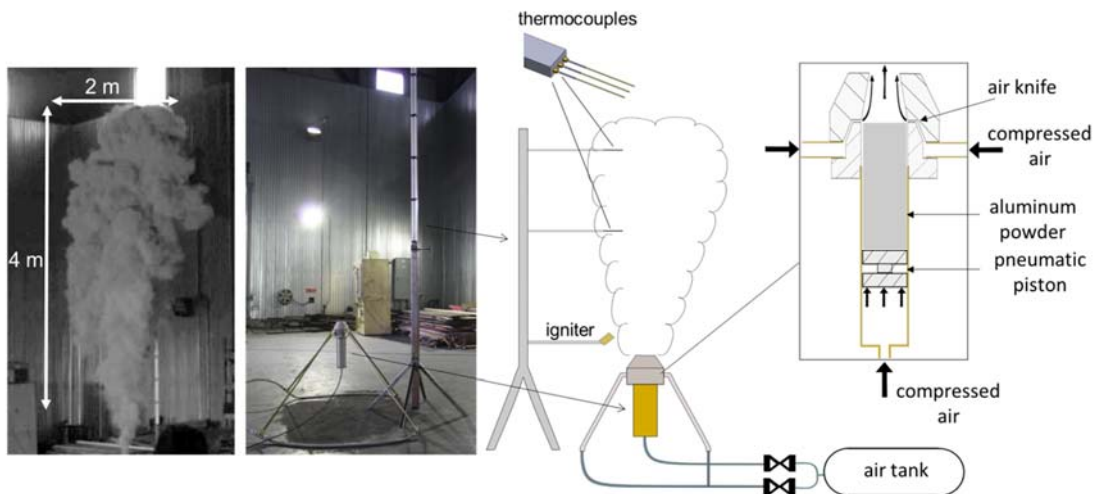


Figure 1. Schematics and photograph of the experimental rig for the large-scale dust cloud combustion tests.

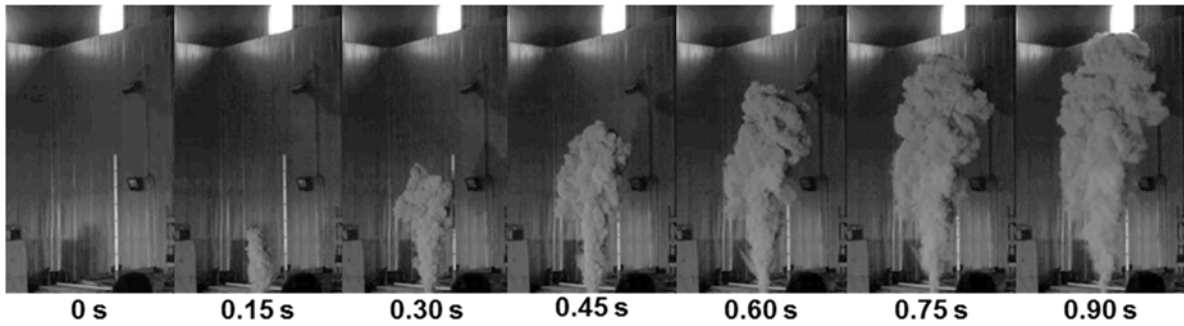


Figure 2. Still frames of dust dispersion process for large-scale tests.

Three different types of aluminum powders were used in the present investigation. The large-scale experiments were performed using either H-5 or H-10 aluminum powder manufactured by Valimet Inc. (Stockton, CA), which have a relatively spherical morphology as shown in Fig. 3. The large-scale experiments required large quantities of powders, such that the amount of Ampal 637 available was insufficient. The particle size distributions of Valimet H-5 and H-10 powders were obtained using a Malvern Mastersizer 2000 are shown in Fig. 7, and have considerable overlap with the particle size distribution of Ampal 637 powder.

The various test series within the balloons were performed with oxygen concentrations ranging from 15% to 100%. The oxygen is diluted with nitrogen, argon or helium to have different heat capacities and diffusivities while keeping the concentration of aluminum and oxygen constant. Oxidizing mixtures are prepared in a mixing tank by partial pressure.

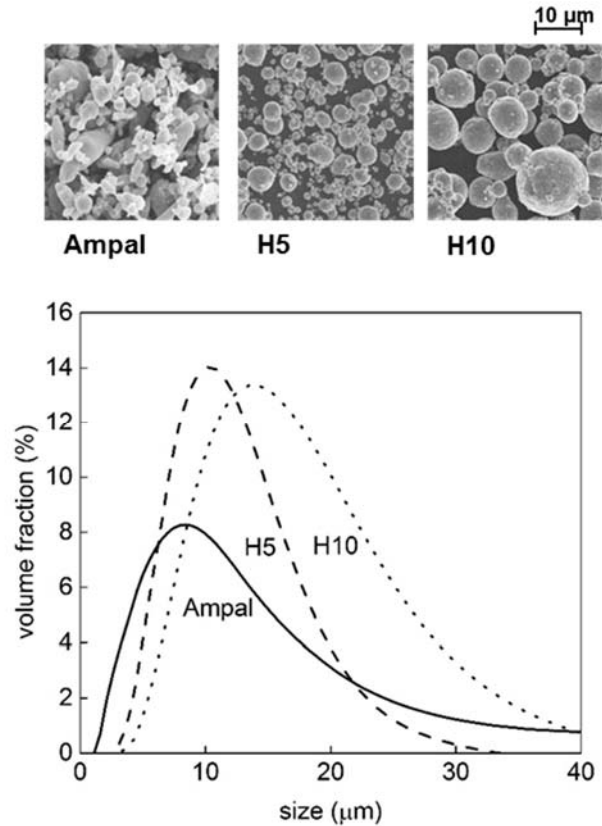


Figure 3. Electron microscope photographs and particle size distributions of Ampal 637 and Valimet H5 and H10 aluminum powders.

### 3. RESULTS AND DISCUSSION

The progression of the flame front can be determined by tracing the location of the leading edge of the flame. Light scattered from the aluminum particles ahead of the flame makes it difficult to precisely determine the front boundary and this issue is accounted for in the experimental uncertainty. Figure 4 shows the vertical progression of the flame front. Figure 5 shows the position of the flame front as a function of height for a vertical cross-section. The flame speed is found by a linear fit through these data points. As shown in Fig. 6, the average flame speed at different horizontal positions across the cloud varies by an insignificant amount.

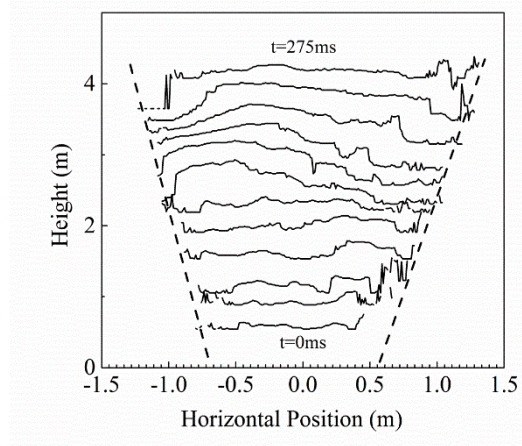


Figure 4: Flame front progression over time.

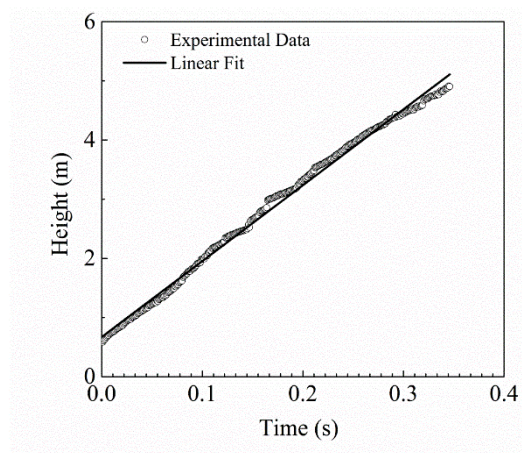


Figure 5: Flame front progression for a vertical section of the flame

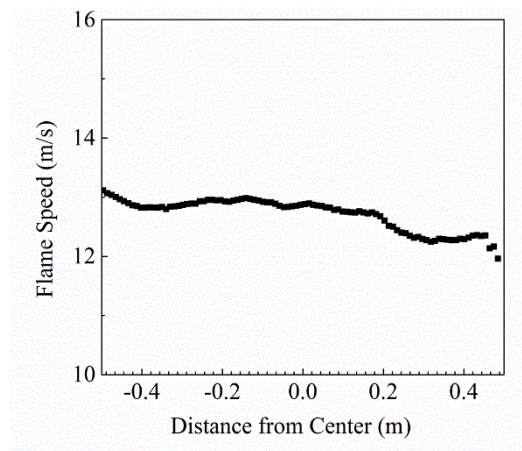


Figure 6: Calculated flame speed along the horizontal front

In total, six successful trials were performed in the field when the flame propagated without interruption from the bottom to the top of the cloud. The tests were performed with the spherical industrial aluminium powders H-5 and H-10 (Valimet Inc, CA) having median particle diameters  $d_{50}$  of 8.0  $\mu\text{m}$  and 12.0  $\mu\text{m}$ , respectively. The average residual vertical velocity of the powder jet after flow cut-off and ignition can be easily deduced from the video images and is found to be around 0.2 m/s. This value has already been subtracted from the measured flame speeds shown in Table 1.

Table 1: Flame speed in large-scale aluminum dust clouds

<b>Trial Number</b>	<b>Flame Speed(m/s)</b>	<b>Aluminum Powder</b>
1	13	H-5
2	12	H-5
3	13	H-5
4	10	H-5
5	14	H-10
6	10	H-10

Experiments were also performed indoors, to prevent wind from interfering with the experiment. In total, 18 successful trials were performed indoors. Selected still frames from high-speed movies of the flame propagation event through the dust cloud are shown in Fig. 7. The top row shows images of the flame initiated with zero ignition delay time after dispersion. The bottom row shows a flame propagation event initiated with a 0.4 second delay following the end of the dust dispersion process. Because the cloud continues to move upwards after the powder dispersal stops, the position of the ignition charge for the longest ignition delays is raised to 1 m above the dispersion nozzle, while, for zero-delay ignition, the igniter was positioned next to the dispersion nozzle exit. Attempts to increase the ignition delay time beyond 0.4 seconds were unsuccessful as the flame either did not propagate through the whole length of the cloud or was increasingly asymmetrical, indicating the development of strong fuel concentration gradients. The average aluminum concentration in the cloud is estimated by dividing the mass of the dispersed powder by the volume of the cloud at the end of dispersal process, derived from video images, and is found to be close to stoichiometric conditions for all large-scale tests.

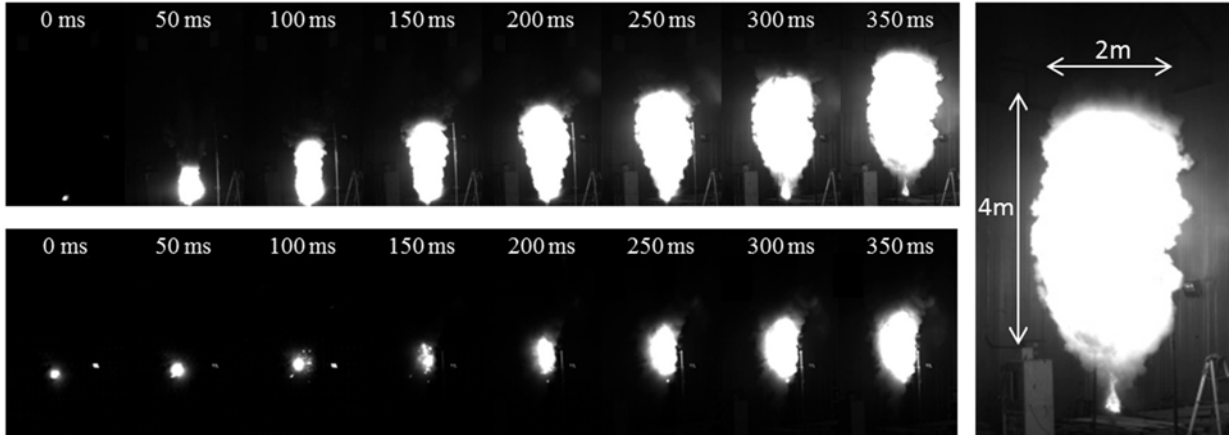


Figure 7. Still frames of flames ignited without delay (top) and with 0.4 seconds delay (bottom) after the end of the dust dispersion process for Valimet H-5 powder and a concentration around stoichiometry.

The procedure for obtaining the flame propagation speed from the high-speed movies is described in detail in and is based on tracking and averaging the flame movement through individual columns of vertical pixels of the images. Some fraction of the observed flame propagation velocity is induced by the buoyancy forces lifting the combustion products upwards. The buoyancy-induced flame speed is estimated by tracking the upward movement of the combustion products after the flame reaches the top of the cloud, which was found to be in the range of  $2.5 \pm 1$  m/s. The average flame speed values measured in H-5 and H-10 aluminum dust clouds at different ignition delay times, reduced by the speed induced by buoyancy, are shown in Fig. 8. The error bars are the sum of the standard deviations of the flame measurements and the buoyancy-induced speeds. As in the balloon experiments, the flame propagation in large dust clouds is strongly influenced by the initial turbulence induced by the dust dispersal process. However, as can be seen from Fig. 8, the influence of turbulence is significantly reduced with a delay time between the end of the powder dispersal and the ignition event of 0.3-0.4 seconds.

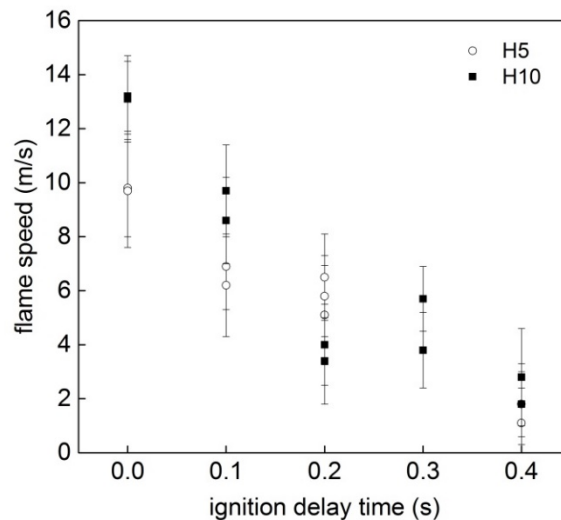


Figure 8. Flame speed as a function of mixture ignition delay time in dust clouds of H-5 and H-10 Valimet aluminum powders for aluminum concentrations around stoichiometry.

### *Mixture pre-heating by radiation*

A typical result illustrating the temperature history in the dust cloud prior to the arrival of the flame front, recorded by the array of three thermocouples of different sizes, is shown in Fig. 9. Starting from the bottom curve to the top, the three temperature traces represent the output signals from thermocouples with junction diameters of 0.25, 0.125 and 0.075 mm, respectively. The top temperature trace is derived by extrapolating the temperature signals from thermocouples at each moment in time to the signal that would be produced by a “zero-sized junction” thermocouple with no thermal inertia, indicative of the gas-phase temperature. The two different slopes of the gas temperature curve indicate preheating of the reactants by the absorbed radiative flux emitted by the flame and the combustion products, followed by the rapid heating via molecular heat diffusion with the arrival of the flame front. The maximum temperature attained by the mixture due to radiative heating is indicated in Fig. 9 by a dashed line and was below 200 °C in all experiments. The test facility was not heated and, therefore, the initial temperature of 0 °C corresponds to the room temperature during the tests.

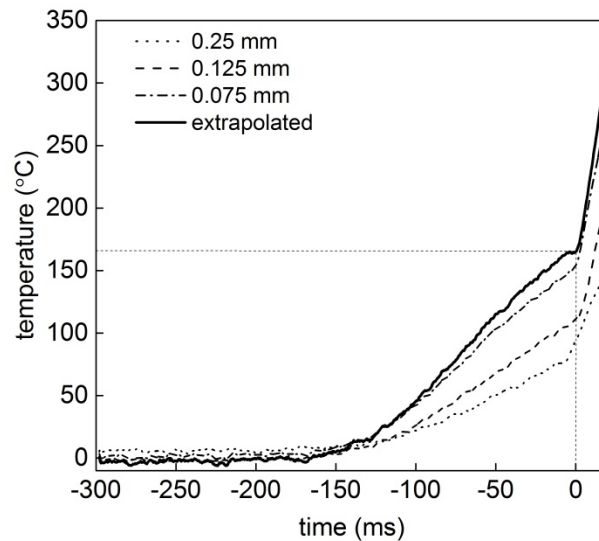


Figure 9 Temperature traces as a function of time for different size thermocouples ahead of the flame front (dashed lines). The solid line represents signal extrapolation to “zero-size” thermocouple. Powder H-5, 0.3 sec ignition delay time and an aluminum concentration around stoichiometry.

As mentioned above, the good agreement between the burning velocities derived from experiments with small-scale aluminium clouds having characteristic sizes from cm’s (Bunsen dust flames) to tens of cm’s (balloon experiments) confirms the applicability of the burning velocity notion towards small-scale dust flames. The absence of an increase in velocity with an increase in the scale of the flame over this range indicates that the effects of radiative heat transfer are negligible for small-scale dust clouds. Indeed, estimations show that the free path length of radiation in a stoichiometric aluminium dust cloud with Ampal aluminium powder is around 10 cm and that the absorption length is probably even larger, so that the absorption of radiation emitted by the flame and

combustion products in the laboratory-scale dust clouds is effectively negligible. The radiation in such clouds acts essentially as a heat loss mechanism, similar to gas flames and, thus, can only lead to a decrease in flame speed.

However, the characteristic size of the dust cloud in the field experiments is much larger than the effective radiation absorption length, thereby ensuring that the radiation emitted by the aluminium flame front and the hot condensed combustion products will be absorbed by the fresh unburnt dust suspension. Thus, at first glance, the observed six-fold increase in flame speed in the field tests in comparison to the laboratory experiments might be considered as evidence that the flame is driven by radiative heat transfer. Simple estimations shown below, however, clearly demonstrate that the radiation alone is insufficient to explain the observed difference in flame speeds. Recent calculations [9] of the integral emissivity coefficient  $\varepsilon$  from an infinite optically-thick layer of 0.5 micron aluminium oxide particles, which are the primary radiation emitters in aluminium flames, estimates its value at about 0.3 at 3000 K. The flame at this temperature can then emit a maximum radiation flux  $W = \varepsilon\sigma T^4$  of about  $W = 1.4 \times 10^6$  W/m<sup>2</sup>. Because the particle residence time within the radiation heating zone  $t_r = l/V$  (where  $l$  is radiation absorption length and  $V$  is the flame speed) is at least an order of magnitude longer than the characteristic time of the heat exchange between 5 micron particles and the gas, the suspension is uniformly heated by the absorbed radiation as a whole. Thus the maximum temperature increase of the aluminium suspension due to radiation absorption can be estimated from the energy balance between the enthalpy of the incoming dust flow and radiation flux, ie.,  $\Delta T = \frac{\varepsilon\sigma T^4}{(C_g\rho_g + C_s\rho_s)V}$ . The estimations show that at the observed flame speeds of 10-12 m/s, the radiation preheating of the mixture would not exceed 100 K. Such a small preheating is unable to provide a sufficient increase in the aluminium flame burning rate, irrespective of whether the particles burn in a kinetic or diffusive mode. This suggests that some other mechanism(s) besides radiative heating may be responsible for the observed high-speed flames in the field tests.

One possible mechanism is associated with the residual large-scale eddy turbulence within the dust cloud. The high-speed videos of the dust dispersal process in the field tests provide clear evidence of the formation of large-scale eddies generated by the high-speed submerged dust dispersal jet. Unlike the small-scale turbulence that quickly dissipates after the termination of the dispersal flow due to viscous momentum losses within two-phase media, the large eddy turbulence is more persistent. The motion of the eddies continues for several seconds after the powder is dispersed albeit with diminishing flow speeds. As was demonstrated in the theoretical work by Kagan and Sivashinsky [10], even low-speed large-eddy turbulence is capable of more than an order of magnitude increase in the flame speed largely due to the increase of the flame surface area.

Another process that might lead to the increase of the flame propagation speed is specific to dust combustion and may be referred to as a “frozen turbulence” effect. Large eddies created during the dust dispersal process with a submerged jet are accompanied by the entrainment of large amounts of surrounding air into the resulting dust cloud [11]. This leads to a stratification of the dust concentration within the jet with alternating areas of high and low dust concentration. Such stratification persists long after the decay of any

turbulence due to the effectively zero diffusivity of the particulate fuel. A complex pattern of dust concentration fluctuations results in a spatially fluctuating burning interface which may lead to the appearance of a corrugated flame having an average flame speed greater than that of a freely propagating flat flame.

#### 4. CONCLUSIONS

Of course, without direct experimental verification the proposed explanations of the effect of “live” and “frozen” large-scale eddy turbulence as a possible cause for the observed flame speed increase are unsubstantiated. One possible verification procedure would be to introduce longer delay times from the end of dust dispersal to the time of ignition of the cloud, giving the dynamic or “live” large-eddy turbulence additional time to decay. This would, however, require performing the experiments with unconfined dust clouds within a large-scale enclosure that would eliminate the influence of the weather (in particular the wind) on the stability of the dust cloud. Direct measurements of the temperature history at various locations within the cloud are also required to confirm estimations of the absence of a noticeable radiative preheating in the flame. Such experiments are already under preparation stage and will be performed in the near future.

#### 5. REFERENCES

- [1] K. L. Cashdollar and M. Hertzberg, “Introduction to dust explosion,” in *Industrial dust explosion*, K. L. Cashdollar and M. Hertzberg, Eds. ASTM 958, 1987, 5–32.
- [2] M. Hertzberg, K. L. Cashdollar, and I. A. Zlochower, *Proc. Combust. Inst.*, 21, (1988), 303–313.
- [3] Y. K. Pu, F. Jia, S. F. Wang, and T. Skjold, *J. Loss Prev. Process Ind.*, 20, (2007), 462–469.
- [4] A. E. Dahoe, R. S. Cant, and B. Scarlett, *Flow, Turbul. Combust.*, 67, (2002), 159–184.
- [5] Y. Kang Pu, J. Jarosinski, C. Sheng Tai, C. William Kauffman, and M. Sichel, *Proc. Combust. Inst.*, 22, (1989), 1777–1787.
- [6] P. Julien, J. Vickery, S. Whiteley, A. Wright, S. Goroshin, J. M. Bergthorson, and D. L. Frost, *J. Loss Prev. Process Ind.*, 36, (2015), 230–236.
- [7] M. Soo, P. Julien, S. Goroshin, J. M. Bergthorson, and D. L. Frost, *Proc. Combust. Inst.*, 34, (2013), 2213–2220.
- [8] P. Julien, M. Soo, S. Goroshin, D. L. Frost, J. M. Bergthorson, N. Glumac, and F. Zhang, *J. Propuls. Power*, 30, (2014), 1047–1054.
- [9] L. A. Dombrovsky, “Emissivity of two-phase combustion products in a solid-propellant rocket engine,” 2011. [Online]. Available: <http://thermopedia.com/content/179/>.
- [10] L. Kagan and G. Sivashinsky, *Combust. Flame*, 120, (2000), 222–232.

[11] A. J. Yule, *J. Fluid Mech.*, 89, (1978), 413–432.

## Chapter 4. Effect of initial temperature and radiation on burning velocity

### 1. INTRODUCTION

Clear cold gases are generally transparent to thermal radiation and the radiation emitted by gaseous flames is thus not absorbed by the gas mixture ahead of the flame and results in heat loss. However, if the combustible gas is seeded with solid particles or a flame propagates in a cloud of a combustible solid fuel particles, the radiation emitted by the flame can be potentially re-absorbed by the upstream gas-particle mixture. The radiative heat transfer, which is in addition to molecular conductive heat transfer, may influence the flame propagation mechanism. This was first realized almost a century ago by Nusselt [1], who estimated the speed of a radiation-driven flame in a coal dust suspension by simply equalizing the black body radiation emitted by the flame with the heat flux required to heat the mixture to some postulated “ignition” temperature. His estimations predicted that radiation would have a dominant role for flames in coal dust clouds and that the corresponding flame speeds would be very high. Several efforts to model the propagation of dust flames including radiative heat transfer were attempted during the 1970’s and 1980’s. Todes et al. [2] departed from Nusselt’s black body assumption by introducing a dependence of the flame optical thickness, and therefore its emissivity, on flame speed and particle size. They also considered a temperature difference between particles heated by the absorbed radiation and the gas in the flame preheat zone. This model predicted that the speed of a radiation-driven flame increases with particle size reaching values above 10 m/s with a flame thickness of several meters in suspensions of very large particles (~100’s microns in size). More realistic numerical models for the flame propagation including both radiative and molecular heat transfer were developed by Ozerova and Stepanov [3] and Krazinski [4] and predicted moderate flame speeds in the range of 0.3 – 1.5 m/s in coal dust clouds which the authors attempted to correlate with some limited experimental observations. Joulin and Deshaies [5], Yoshio et al. [6], and Joulin and Eudier [7] have modeled the energy transfer in flames propagating through gases seeded with inert particles and in combustible dust suspensions by considering both molecular heat conductivity and radiation. They emphasized that radiative heat transfer actually leads to an accumulation of excess enthalpy within the combustion zone leading to super-adiabatic flame temperatures that may extend the flame propagation limits.

#### *Previous experimental work on radiative effects in dust-air flames*

In spite of the large amount of effort carried out to investigate dust-air flames, direct evidence of the effects of radiation, let alone a systematic comparison of model predictions with experimental results for dust flames, has been, until recently, practically absent from the literature. With the lack of direct evidence of the role of radiative heat transfer in dust flames, some authors have ironically viewed the observed departure of the dust flame behavior from predictions by some simplified models based only on molecular conductivity, as evidence of the effects of radiation while ignoring possible alternative explanations. For example, Cassel [8] regarded the low ratio of flame speeds in aluminum-air mixtures with argon and helium diluants, in comparison with predictions from models based on molecular conductivity, as evidence for the role of radiative heat transfer. This

effect, however, was recently attributed to the change of the particle combustion mode from a predominantly diffusive-controlled mode with argon to a primarily kinetically-controlled particle combustion mode in helium mixtures [9]. The increase of the flame speed with particle size in magnesium mixtures burning in tubes observed in [10] was also regarded as evidence of the dominant role of radiation heating while, in fact, it is caused, as shown in [11], by the appearance of convective recirculation cells driven by gravitational settling of large dust particles through the gas in the tube. Similarly, elevated flame speeds propagating through coal dust clouds in small enclosures in comparison to burners were regarded in [4] as a manifestation of radiation effects.

The common error of the work cited above, as well as in many other studies present throughout the relevant literature, is a disregard for the fact that the scale of the experimental apparatus used in the dust combustion experiments has been, in general, too small to exhibit augmented flames speeds from radiation effects. Indeed, in order for the radiation emitted by the flame to be absorbed by the cold mixture, the characteristic size of the dust cloud ahead of the flame needs to be larger than the characteristic length for radiation absorption. The characteristic size for flame in tubes is the tube radius (not the tube length!) and for different types of burners it is usually the nozzle diameter. Elementary estimations show that the tube diameters and burner sizes in the work cited above are much smaller even than the radiation free-path-length, i.e., the distance travelled by a photon before it is absorbed or scattered by the particles within the medium. Due to elastic photon scattering and diffraction around small particles, the absorption cross section of small micron-sized particles (i.e., the ratio of the radiation absorption coefficient to the geometrical cross section of the particle) is much smaller than unity in the near-infrared wavelength region typical of radiation at flame temperatures. Consequently, the effective absorption length of the thermal radiation can be several times longer than the photon free-path-length [12], making the suspensions in the work cited above, and as a matter of fact in the majority of laboratory-scale dust combustion experiments known in the literature, effectively transparent to radiation. Only recently has the radiation preheating ahead of the propagating flame been unambiguously documented in recent field experiments with large-scale aluminum dust clouds [12]. The relationship between molecular conduction and radiative heat transfer in flames propagating in large-scale metal dust clouds and a possible simplified approach for modeling such flames is discussed below.

#### *Separation of radiation and molecular heat transfer scales in metal dust flames*

As described in previous work [12], [13], the aluminum dust clouds created in field experiments are typically about 4 m tall and 1.5 – 2 m wide which allows complete capture of the thermal radiation emitted by the flame front within the fresh mixture upstream of the flame. Indeed, a simple geometrical estimation of the radiation free-path-length, based on the assumption that the extinction cross section of the particle (i.e., the sum of the absorption and scattering cross sections) is close to one, gives a value for the photon free-path-length of about 7 cm, based on the estimated dust cloud parameters, i.e., an aluminum concentration of about 300 g/m<sup>3</sup> and an average particle size for Valimet H-10 Al powder of about 12 μm. As indicated by the temperature traces for a thermocouple array positioned in a dust cloud ahead of the flame front (see Fig.1), the noticeable temperature rise starts about 0.12 s prior to the arrival of the flame. Taking into account the average flame speed relative to the stationary thermocouple of about 2 m/s [12], this corresponds to a radiation

heating length of about 25 cm, i.e., more than three times longer than the radiation free-path-length derived from geometrical assumptions for the blackbody particles. This not surprising as data found in the literature indicate very small absorption cross sections for micron-sized metal particles in the IR region [14].

The scale of the flame molecular heat conductivity in the flame is on the order of  $\alpha/S_u$ , where  $\alpha$  [cm<sup>2</sup>/s] is the gas heat diffusivity and  $S_u$  [cm/s] is the flame burning velocity. Burning velocities in aluminum dust suspensions of similar size measured with aluminum Bunsen flames [15] are in the range of 18 – 25 cm/s. Thus the width of the molecular heat conductivity zone can be estimated to be on the order of 0.1 cm. Due to the more than two orders of magnitude difference in the characteristic length scales, the problems of radiation and conductive heating thus become spatially separated, i.e., molecular heat conductivity is negligible within the radiation heating zone whereas radiative heat transfer can be considered negligible within the molecular heating zone. Estimations also show that in spite of the nanosized oxide particles formed during aluminum combustion, the aluminum reaction zone is also largely transparent to radiation due to its small thickness (2 – 5 mm [15]) and the extremely low radiation absorption cross section of aluminum oxide particles ([16], [17] and see below). The separation of the radiation and heat conductivity scales is schematically illustrated in Fig. 2. Since radiative heat flux can propagate irrespective of the sign of the temperature gradient, the flame temperature  $T_f$  as shown in [5], [7] can be higher than adiabatic flame temperature  $T_{ad}$ .

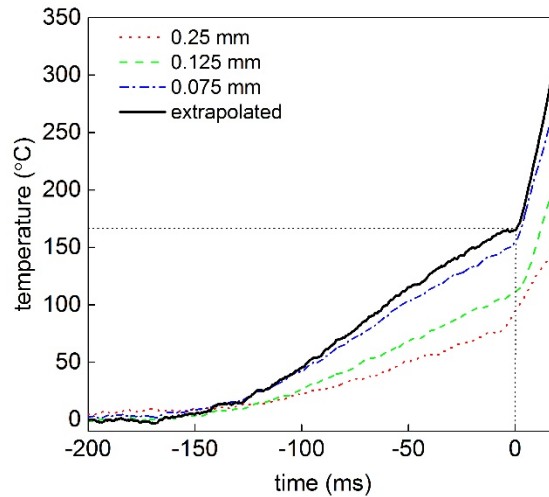


Fig. 7: Radiative preheating of gas ahead of flame in large-scale dust flames.

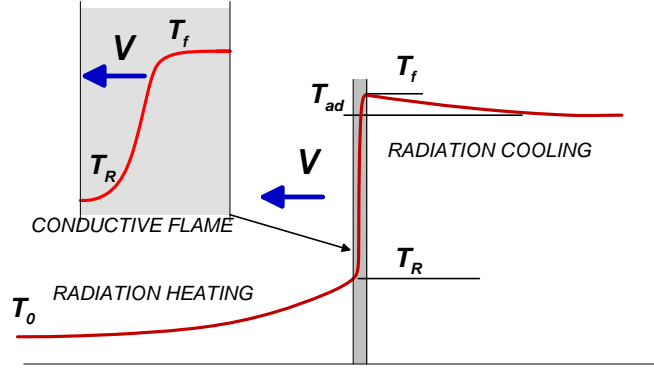


Fig. 2: Schematic of thermal structure of dust flame illustrating radiative heating and cooling.

Separation of the spatial scales of radiation and molecular heat transfer means that the role of radiation in flame propagation can be reduced to the problem of the response of the inner flame driven by molecular heat conductivity to the change of the mixture temperature due to radiation preheating. Although the preheating by about 170 K measured in the above-mentioned field experiments might be considered small in relation to the aluminum flame combustion temperature which is in the range of 3000 – 3500 K [18], it considerably affects the flame speed due to the strong sensitivity of the flame to preheating, as shown below. Information regarding the influence of the initial suspension temperature on the flame burning velocity in aluminum dust clouds, and as a matter of fact for dust flames in general, is practically nonexistent in the literature, with the notable exception of the unpublished data cited in earlier publications [19]. The dependence of burning velocity on the initial temperature of an aluminum-air suspension was determined experimentally using a modified dust burner apparatus permitting stabilization of Bunsen-type dust flames [15], [20]–[22]. In-situ measurements were also performed to measure the effective flame radiation temperature and estimate the effective flame emissivity. This, together with a knowledge of the effect of initial mixture temperature on the flame propagation speed allows the estimation of the radiation effects on flame speed in experimental configurations different from above.

## 2. EXPERIMENTAL APPARATUS

### *Experimental apparatus and aluminum powder*

Measurements of the burning velocity at different initial temperatures of the aluminum-air suspension were performed with a modified version of the “dust burner” apparatus described in detail in previous publications [15], [20]–[22]. The aluminum suspension was preheated by passing the two-phase flow, as shown in Fig. 3, through an 80 cm long, 2.5 cm OD stainless steel tube heated by two tubular electrical heaters with a total power of about 600 W.

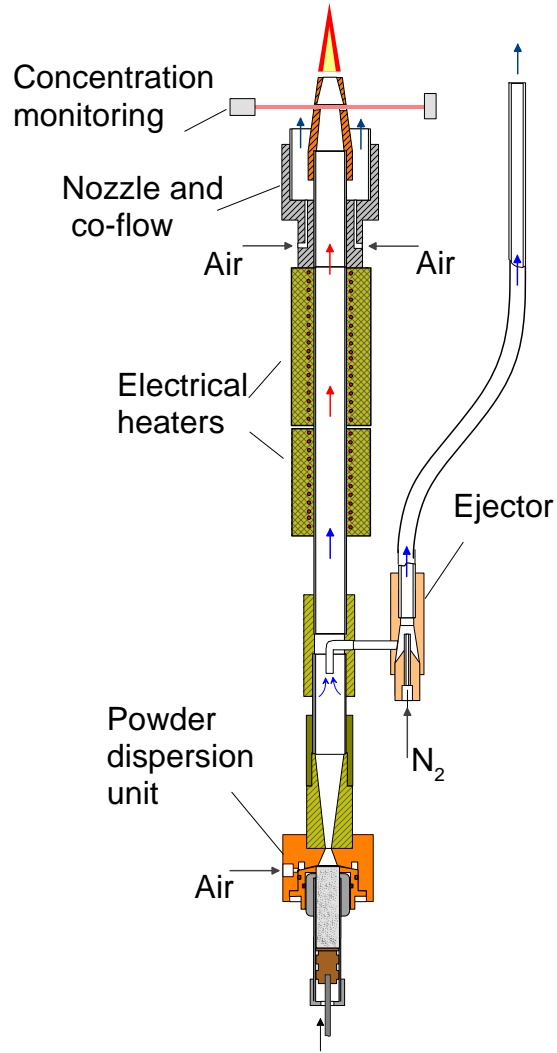


Fig. 3: Schematic of experimental dust flame apparatus showing preheat section and nozzle.

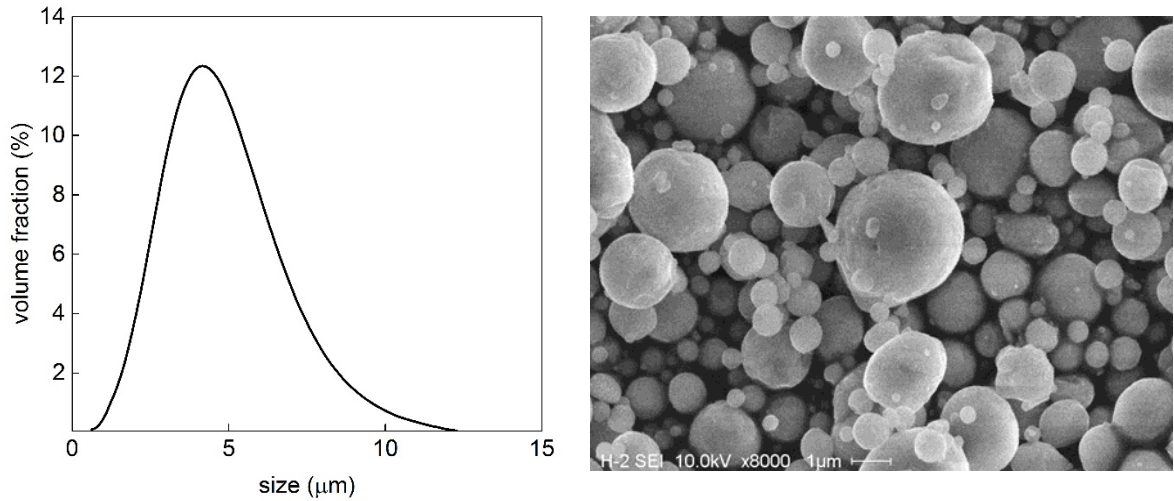


Fig. 4: Particle size distribution and scanning electron micrograph of Valimet H-2 Al powder.

The measurement of the temperature profile across the exit nozzle diameter ( $D=18$  cm) by a thermocouple indicated that the temperature profile was nearly flat with the temperature starting to drop only about 7-8 mm from the nozzle centerline. The spherical H-2 aluminum powder produced by Valimet Inc. (Stockton, CA) used in the experiments has a reported purity of 99.7% and a particle size distribution as shown in Fig. 4.

#### *Validating the method with methane-air flames*

In order to validate the method and verify its accuracy, benchmark experiments were performed with stoichiometric methane-air mixtures whose burning velocity dependence on preheating is well documented in the literature [23]–[25]. The burning velocity was determined by dividing the known flow rate of the mixture through the nozzle by the surface area of the inner Bunsen flame cone. The surface area of the Bunsen flame was determined from digital images of the flame processed with custom routines using MATLAB. The results of the experimental measurements are shown in Fig. 5 in comparison with data from the literature and calculations of the burning velocity performed with the Cantera software using the reduced dr<sub>m</sub>-19 mechanism developed by Kazakov and Frenklach (Kazakov and Frenklach).

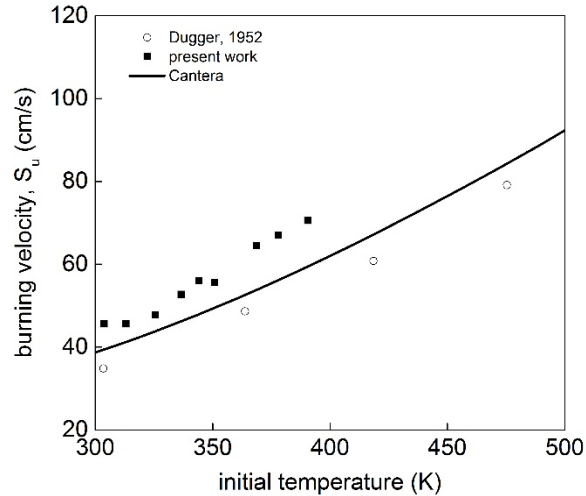


Fig. 5: Burning velocity as a function of upstream gas temperature.

The observed correlation between experimental data from the literature, Cantera calculations and the current experimental data can be considered satisfactory taking into account the lower accuracy of the Bunsen flame method in comparison with the flat flame burners used for more accurate measurements [27], [28]. The obtained dependence can be interpolated with good accuracy by the power law function  $v = v_0 (T/T_0)^{1.6}$ , where  $v_0$  is the burning velocity at the room temperature  $T_0$ . There is general agreement in the literature [27], [28] that the flame speed in gases increases with preheating mostly due to the corresponding increase of the flame temperature that has a strong influence on the burning velocity because of the high activation energies of the Arrhenius reactions controlling the combustion in hydrocarbon gas flames [28].

### 3. RESULTS AND DISCUSSION

Fig. 6 shows photographs of conical Bunsen-type flames in aluminum-air mixtures stabilized with approximately equal mass flow rates but at different gas temperatures. The reduction in the size of the flame cones (and hence the flame surface area) unambiguously indicates that dependence of the burning velocity on the initial mixture temperature is stronger than a linear function (increase in temperature resulting in decreased density), for which the cone size would not change.

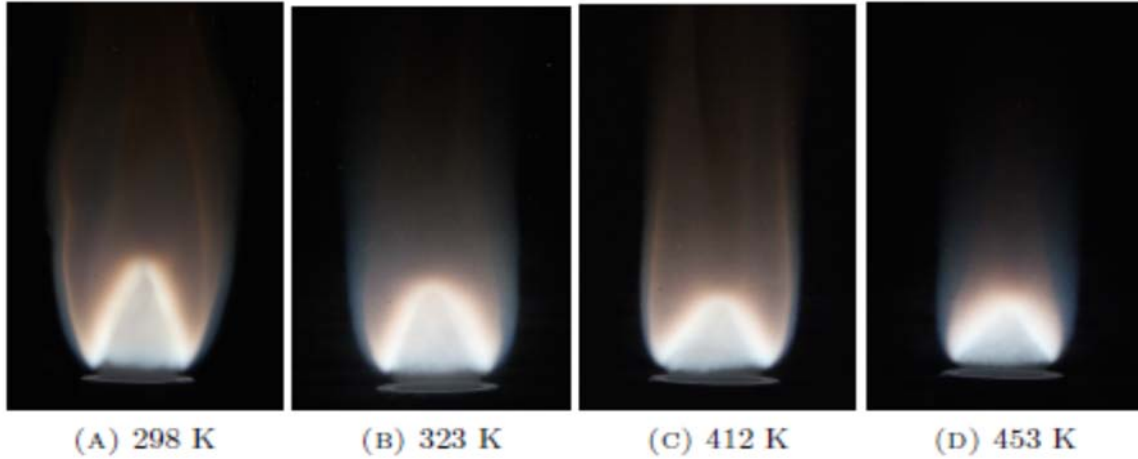


Fig. 6: Stabilized aluminum-air dust flames as a function of upstream gas temperature.

Indeed, experimental results from this work, as well as results that were cited in [19] from unpublished sources show, as can be seen from Fig. 7, that the dependence of burning velocity on mixture temperature is as strong as, if not stronger than, for methane-air mixtures. The large scatter in the results is due to difficulties in properly defining the borders of the inner flame because of light scattering by aluminum particles as well as asymmetry of the flames.

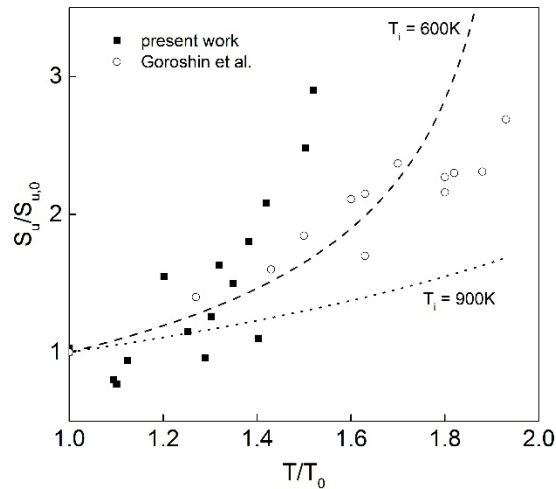


Fig. 7: Normalized flame speed as a function of normalized temperature for Al-air flames.

The strong influence of the relatively low levels of pre-heating on flame speeds in the aluminum-air suspensions is surprising as, unlike for methane-air flames, preheating has practically no influence on the adiabatic flame temperature in the aluminum mixture (see

Fig. 7). The independence of the aluminum flame temperature on preheating is due to the formation of the solid aluminum oxide whose evaporation/decomposition effectively stabilizes the temperature of the flame [29].

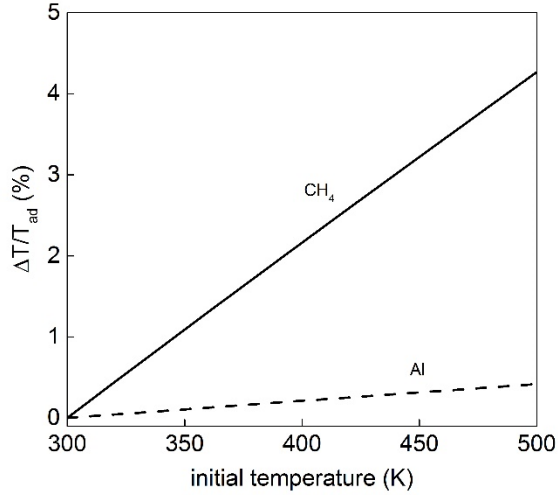


Fig. 8: Effect of initial gas temperature on adiabatic flame temperature for methane-air and Al-air flames.

With the lack of change in the aluminum flame temperature, reaction kinetics may be ruled out as an explanation of the observed strong effect of the mixture preheating on flame speed. Estimations show that for the case in which aluminum particles ignite and subsequently burn in the combustion regime controlled by oxygen diffusion, the expected dependence is, however, expected to be stronger than for kinetically-limited combustion.

Indeed, the estimation of the flame speed in case of particle ignition<sup>1</sup> can be derived from the energy balance between the preheat and combustion zones by assuming a linear temperature profile in the combustion zone [8]:

$$\overline{vc\rho} (T_i - T_0) = \lambda \frac{(T_{ad} - T_i)}{v\tau_c}, \quad v \approx \sqrt{\frac{\lambda (T_{ad} - T_i)}{\overline{c\rho} (T_i - T_0)}} \quad (1)$$

Here  $\overline{c\rho}$  is the total mixture heat capacity,  $\tau_c$  is the particle combustion time and  $\lambda$  is the heat conductivity of the gas in the combustion zone. From (1) the estimation of the relative

<sup>1</sup> The notion of ignition temperature can be used only for purposes of rough estimations. More properly named as a reaction onset temperature in flame it, in general, is not only a function of particles concentration but also the flame speed [31].

flame speed increase with preheating gives:  $v/v_0 = \sqrt{(T_i - T_0)/(T_i - T)}$ . The corresponding estimated dependence plotted on Fig. 7 shows that only very low values of  $T_i$  of about 600 K may explain the strong dependence found experimentally. Reaction onset temperatures as low as 1000 K were recorded in experiments of clouds of small aluminum particles behind shock waves [30] and are attributed to a cooperative heating effect [31].

On the basis of the experimental data, the relative increase of the burning velocity with a mixture preheating of about 170°C gives a factor of about 2 – 2.4. This estimate correlates with present Bunsen flame measurement of the burning velocity of about 22 cm/s at room temperature and a propagation velocity of the flame front relatively to unburned mixture estimated from field experiments of about 50 – 60 cm/s.

*In situ measurements of the flame temperature and estimation of its effective emissivity*

Flame temperature measurements were performed during large-scale field experiments, as described in Julien et al. (2015a, 2015b). The aluminum cloud measures roughly 2m in width and 4m in height and Fig. 9 shows still-frames from the fireball resulting from the aluminum combustion.



Fig. 9: Visible radiation from a flame propagating through a large-scale aluminium (12  $\mu\text{m}$  Valimet H-10 powder)-air dust cloud. Time between frames is 125 ms.

The temperature of the aluminum flame was derived from AlO molecular spectra. Light from three equidistant locations 0.5 m apart, perpendicular to the incoming flame front, was transmitted by multimode fibers (0.4 mm dia) to the entrance slit of a customized f/5 imaging, Czerny-Turner spectrometer. The fibers were coupled along the slit such that the light from each fiber was spatially separated on the spectrometer image plane. The spectrometer was coupled to a high speed SA-5 Photron digital videocamera filming spectra at 2000 frames/s. Using a 300 gr/mm grating, the spectrometer resolution was about 0.15 nm with a spectral range of about 130 nm covering the entire AlO emission band. The resulting integrated spectrum signal from a fiber and the corresponding theoretically calculated spectrum corresponding to a temperature for several different frames is shown in Fig. 10.

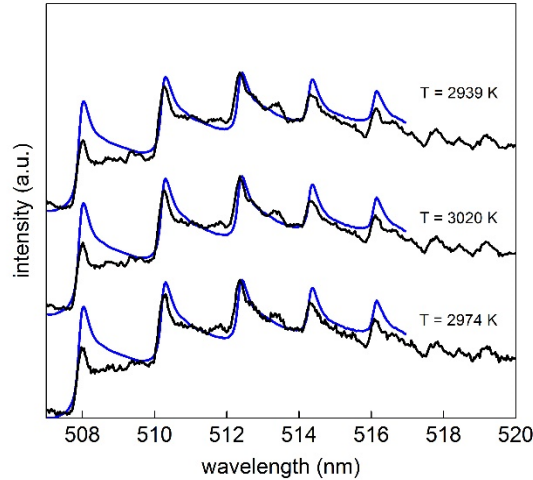


Fig. 10: Experimental and fitted theoretical AlO spectra at a single temperature from a single fiber for different points in time after dispersion, each 5 ms apart.

The measured flame temperatures are in the range of 2900 – 3000 K which is about 300 K lower than temperatures measured from a Bunsen aluminum flame by the same method. The difference can be attributed to the experimental uncertainty of the measurement, which is on the order of a few hundred Kelvin.

The effective flame radiation emissivity  $\epsilon$  can be estimated by equating the radiation heat flux emitted by the flame with the increase of the flow enthalpy due to preheating by radiation  $\overline{c\rho v\Delta T} = \epsilon\sigma T^4$ . Here we assume that all radiation is completely absorbed by the incoming reactant mixture and neglect back-and-forth radiation reflections between the aluminum cloud and combustion products. We also assume that the particles and gas have the same temperature since the characteristic time for radiative heating is on the order of about hundred milliseconds, which is much longer than the characteristic time for heat exchange between the micron-sized particles and gas of a few milliseconds. The estimations give a very low value of the flame emissivity of about 0.03. This is about an order of magnitude smaller than the recent theoretical calculations performed by Dombrovsky [32] for the emissivity of an infinite cloud of 1 $\mu$ m molten alumina particles at 3000 K. The difference can be attributed to the actual size of the nanoscale aluminum oxide particles typically generated in an aluminum dust flame ( $\sim$ 100 nm according to Plass (1965, 1964)), which hence corresponds to much smaller individual absorption cross sections. The other factor is the generally non-isothermal character of the post-flame region due to the forward radiation heat loss and convective cooling.

In spite of the approximate nature of the above estimate of flame emissivity, the estimated value, together with the known sensitivity of the conductive flame to the mixture preheat, can be used to estimate flame speeds in aluminum dust clouds for experimental configurations that differ from the field experiments cited in this work. We have to note, however, that because of the long range of radiative heat transfer, the problem of radiation heating generally cannot be decoupled from the flow problem. Thus 1-D flame

formulations calculating a flame “burning velocity” as well as the very notion of a fundamental “burning velocity” have little practical merit for flames with strong radiation heat transfer effects.

#### 4. CONCLUSIONS

The radiation emissivity of the aluminum dust flame is estimated using in-situ measurements of the flame front temperatures and mixture preheating by the thermocouple array. In spite of low flame emissivity estimated to be on the order of  $5 \times 10^{-2}$  resulting in mixture heating by radiation to only 150 °C it practically doubles the flame burning velocity due to its strong sensitivity to the initial mixture temperature as is demonstrated in laboratory experiments with stationary Bunsen type aluminum dust flames.

#### 5. REFERENCES

- [1] W. Nusselt, *Der Verbrennungsvorgang in der Kohlenstaubfeuerung*. 1924.
- [2] O. M. Todes, A. D. Gol'tsiker, and K. K. Ionushas, *Combust. Explos. Shock Waves*, 10, (1974), 71–75.
- [3] G. Ozerova and A. Stepanov, *Combust. Explos. Shock Waves*, 9, (1973), 543–549.
- [4] J. L. Krazinski, R. O. Buckius, and H. Krier, *Prog. Energy Combust. Sci.*, 5, (1979), 31–71.
- [5] G. Joulin and B. Deshaies, *Combust. Sci. Technol.*, 47, (1986), 299–315.
- [6] Y. Yoshio, S. Kiyoshi, and E. Ryoza, *Int. J. Heat Mass Transf.*, 31, (1988), 311–319.
- [7] G. Joulin and M. Eudier, *Proc. Combust. Inst.*, 22, (1989), 1579–1585.
- [8] H. M. Cassel, “Some fundamental aspects of dust flames,” US Dept. of the Interior, Bureau of Mines, Book, (1964).
- [9] F.-D. Tang, S. Goroshin, and A. J. Higgins, *Proc. Combust. Inst.*, 33, (2011), 1975–1982.
- [10] V. Shevchuk, S. Goroshin, L. Klyachko, N. Ageev, K. EN, and A. Zolotko, *Combust. Explos. Shock Waves*, 16, (1980), 52–58.
- [11] F. T. Green and J. E. O'Donnell, “The quenching behavior of coal dust air mixtures, Final Report,” (1980).
- [12] P. Julien, J. Vickery, S. Goroshin, D. L. Frost, and J. M. Bergthorson, *Combust. Flame*, 162, (2015), 4241–4253.
- [13] P. Julien, J. Vickery, S. Whiteley, A. Wright, S. Goroshin, J. M. Bergthorson, and D. L. Frost, *J. Loss Prev. Process Ind.*, 36, (2015), 230–236.
- [14] J. R. Howell, R. Siegel, and M. P. Mengüç, *Thermal Radiation Heat Transfer*, 5th ed. CRC Press, 2011.

- [15] S. Goroshin, I. Fomenko, and J. H. S. Lee, *Proc. Combust. Inst.*, 26, (1996), 1961–1967.
- [16] G. N. Plass, *Appl. Opt.*, 3, (1964), 867.
- [17] G. N. Plass, *Appl. Opt.*, 4, (1965), 1616–1619.
- [18] S. Goroshin, J. Mamen, A. Higgins, T. Bazyn, N. Glumac, and H. Krier, *Proc. Combust. Inst.*, 31, (2007), 2011–2019.
- [19] S. Goroshin, A. Higgins, and M. Kamel, *AIAA*, (2001), 2001–3919.
- [20] M. Soo, P. Julien, S. Goroshin, J. M. Bergthorson, and D. L. Frost, *Proc. Combust. Inst.*, 34, (2013), 2213–2220.
- [21] P. Julien, M. Soo, S. Goroshin, D. L. Frost, J. M. Bergthorson, N. Glumac, and F. Zhang, *J. Propuls. Power*, 30, (2014), 1047–1054.
- [22] P. Julien, S. Whiteley, S. Goroshin, M. J. Soo, D. L. Frost, and J. M. Bergthorson, *Proc. Combust. Inst.*, 35, (2015), 2431–2438.
- [23] G. L. Dugger, “Effect of initial mixture temperature on flame speed of methane-air, propane-air, and ethylene-air mixtures,” (1952).
- [24] F. W. Stevens, “A constant pressure bomb,” (1923).
- [25] R. A. Strehlow and J. G. Stuart, *Proc. Combust. Inst.*, 4, (1953), 329–336.
- [26] A. Kazakov and M. Frenklach, “No Title.” [Online]. Available: <http://www.me.berkeley.edu/drm/>. [Accessed: 01-Jan-2015].
- [27] F. N. Egolfopoulos, N. Hansen, Y. Ju, K. Kohse-Höinghaus, C. K. Law, and F. Qi, *Prog. Energy Combust. Sci.*, 43, (2014), 36–67.
- [28] C. K. Law, *Combustion Physics*. Cambridge University Press, 2006.
- [29] I. Glassman and R. Yetter, *Combustion*, 4th ed. Academic Press, 2008.
- [30] A. L. Kuhl and V. M. Boiko, “Ignition of aluminum particles and clouds,” in *Energetic Materials: High Performance, Insensitive Munitions and Zero Pollution, Proc. of the 41st Int. Annu. Conf. of ICT*, 2010.
- [31] M. Soo, S. Goroshin, J. M. Bergthorson, and D. L. Frost, *Propellants, Explos. Pyrotech.*, 40, (2015), 604–612.
- [32] L. A. Dombrovsky, “Emissivity of two-phase combustion products in a solid-propellant rocket engine,” 2011. [Online]. Available: <http://thermopedia.com/content/179/>.

## **Section 2. Flames in hybrid mixtures of metal powders and methane**

### **Chapter 1. Hybrid flames of aluminum and methane on a Bunsen burner**

#### **1. INTRODUCTION**

Combustion of metal particulate suspensions in the products of hydrocarbon flames occurs in metalized slurry fuels [1], metalized propellants [2, 3], solid and fuel-air metalized explosives [4, 5], in technological processes including reactive particle spray deposition [6] and the synthesis of nano-oxides [7], as well as in industrial accidents. The extensive literature accumulated over more than fifty years of research on metal combustion is primarily dedicated to the experimental study and theoretical modeling of the ignition and combustion of a single isolated metal particle, including the effect of different pressures, temperatures and oxidizing environments [8]. Due to experimental limitations, the majority of studies were performed with relatively large particles, ranging from tens to even hundreds of microns in size; whereas, in practical applications, the size of particles is often in the micron-size range. Recent work has pointed out that the extrapolation of results obtained for large particles to particles of smaller size might not always be appropriate due to a possible change in the combustion regime with a reduction in particle size; that is, a transition from combustion controlled by the diffusion of oxygen or other oxidizing gases to a combustion mode limited by the reaction kinetics [9].

The present study investigates yet another factor that impedes the application of the isolated single particle approach for the prediction of metal combustion characteristics in real systems with large metal content. The combustion of metal particles in such systems occurs within relatively-dense dust clouds and, therefore, can be a frontal phenomenon analogous to a gas flame. The experimental results presented in this paper demonstrate that the formation of a flame front within a metal particle cloud and the subsequent characteristics of the combustion front cannot be predicted by direct extrapolation of data obtained with isolated single particles. The generation of heat within the dust flame front and the consumption of the oxidizer not only continuously modify the combustion environment around the burning particles, but also influence the flow conditions upstream of the metal flame front via molecular or turbulent diffusion of heat and gaseous species. Due to heat transfer to the flow upstream of the metal dust combustion front, the conditions for particle combustion may be sustained without relying solely on the heat provided by the hydrocarbon flame, as would be the case for a single particle. In fact, metal dust flames in micron-sized suspensions can self-stabilize in a cold flow, without any hydrocarbon fuel source, with flame speeds comparable to those of hydrocarbon fuels. This technique was first demonstrated by Cassel [10] and reproduced in more recent work [11, 12].

In the current investigation, the formation of a stabilized, aluminum dust-cloud flame in the products of a hydrocarbon flame is studied experimentally by seeding premixed methane Bunsen flames with micron-sized aluminum particles. The first results of this

investigation unambiguously demonstrated that, as the concentration of aluminum particles increases, an aluminum dust flame forms rapidly above some critical value of metal mass loading [13]. In the present work, the combustion characteristics of the metal dust flame are studied for flames with and without excess oxygen, and are investigated with the use of more accurate and detailed flame diagnostics. In particular, spatially-resolved emission spectroscopy is synchronized with optical dust concentration monitoring, allowing the direct correlation between flame temperature and aluminum mass concentration. In addition to the condensed phase temperature derived from the continuous spectra, a temperature is also obtained by fitting the emission spectrum of AlO, a gas phase intermediate, to a simulated spectrum. Comparison of the solid phase and AlO temperatures is used to shed light on the combustion mechanism. The dependence of the burning velocity, or laminar flame speed, of the mixture as a function of aluminum particle concentration is compared with similar measurements with inert silicon carbide (SiC) particles to determine the concentration at which the heat release from the aluminum combustion significantly influences the flame speed. The condensed flame products are also collected at different aluminum loadings, corresponding to different combustion regimes, before and after the formation of an aluminum flame front. Products are chemically analyzed to determine the fraction of aluminum remaining and transmission electron microscopy (TEM) is used to determine the particle morphology. Finally, a simplified theoretical estimation, based on the Frank-Kamenetskii approach, is presented to describe the conditions under which the methane and aluminum flames may be coupled. The aluminum particle concentration for which coupling is predicted to occur is consistent with the experimental results. A key characteristic of the new theoretical estimation is that the aluminum combustion

## 2. EXPERIMENTAL APPARATUS

A schematic of the hybrid gaseous-dust fuel burner is shown in Fig. 1. The burner was specifically assembled for the current experiments on methane-aluminum mixtures and has several new design elements compared to the previous dust burner that was used to study stabilized pure aluminum dust flames [11]. The new apparatus has the capability of dispersing a variety of micron-sized powders in any gaseous mixture. The premixed methane-air flow is seeded with aluminum particles using a dust dispersion system described previously [11, 14]. The powder is continuously fed via a syringe-type feeder and dispersed using a supersonic jet from an annular 50 micron slot. The initially highly-turbulent flow is expanded in a low angle conical diffuser and laminarized in a 60 cm long, 2.2 cm inner diameter flow tube before exiting through a conical nozzle with an exit diameter of 12 mm. The co-flow assembly surrounding the nozzle provides a coaxial flow of air or inert gases at the same speed as the combustible mixture. The flow rate through the nozzle is regulated by diverting part of the flow through a side tube using an ejector system (see Fig. 1). The ejector was calibrated using pure oxygen as the main flow and nitrogen as an ejecting flow and measuring the oxygen concentration at the exit of the bypass tube. The combustible flow is ignited at the nozzle exit by a remotely-operated propane-oxygen torch.

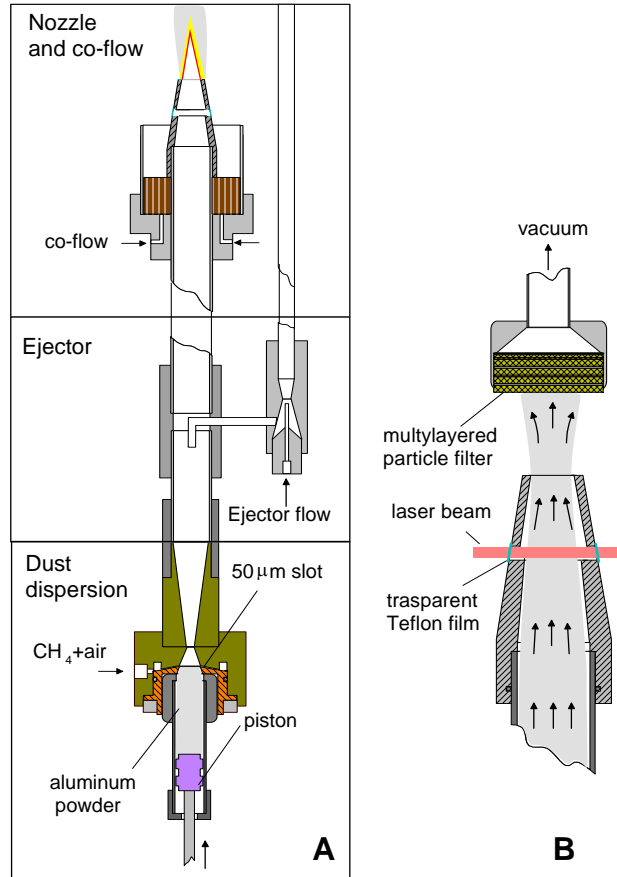


Fig. 8 Schematics of the dust burner (left) and set up for calibrating the light attenuation probe (right).

### *Aluminum Powder*

The Ampal 637 micron-sized aluminum powder used in the present experiments is composed of spheroidal or nodular aluminum particles having a Sauter mean diameter ( $d_{32}$ ) of about 6.5  $\mu\text{m}$ . This powder came from the same large batch that was used in previous experiments with aluminum dust cloud flames [11, 12, 14]. The consistent use of the same powder allows the results for the hybrid mixtures obtained in the current paper to be quantitatively compared to the previous results for pure aluminum-air flames. The scanning electron microscope (SEM) image of the powder shown in Fig. 2 illustrates the size and morphology of the particles. Fig. 2 also shows the particle size distribution obtained with a Malvern Mastersizer 2000.

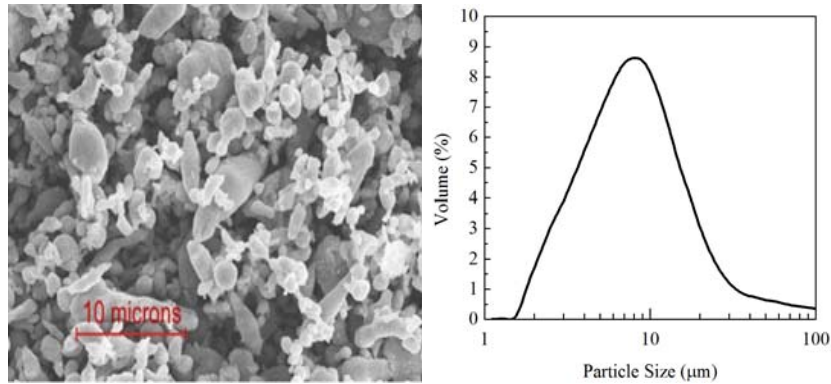


Fig. 9 SEM photograph (left) and volumetric particle size distribution (right) of Ampal-637 aluminum powder.

### *Dust concentration measurements and monitoring*

The concentration of aluminum particles in the flow is continuously monitored by a laser light attenuation probe. A 5 mW diode laser emits a beam that is expanded through cylindrical lenses and collimated to a 3x6 mm rectangular-shaped laser sheet before being transmitted directly through the burner nozzle, as shown in Fig. 1B. The rectangular slits on the nozzle walls are covered with transparent, high-temperature, optically-clear Teflon tape and the special nozzle geometry, which includes a wider cone angle above the slit, prevents dust deposition on the inner side of the tape. After attenuation from the dust flow, the laser beam is focused onto a photodiode, which is protected from the intense flame illumination by a narrow bandpass filter of the same wavelength as the laser light (633 nm) and a spatial filter. The signal from the photodiode is recorded by a data acquisition system.

The laser-light-attenuation probe is calibrated by pulling the two-phase flow through a stack of several fine particulate filters using a vacuum, and collecting the dust for approximately 5 seconds. The dust concentration in the flow is calculated by dividing the mass of aluminum by the total volume of the gas that passed through the nozzle for the same period of time. The light attenuation probe calibration for the aluminum powder used in the present experiments is shown in Fig. 3, which also includes the two-sigma prediction band for measurements (dash lines) and the uncertainty band for the resulting calibration curve (shaded area).

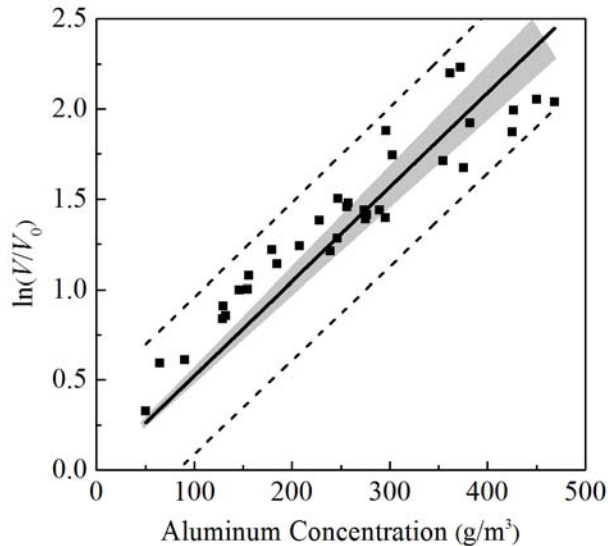


Fig. 10 Calibration of the light attenuation probe versus dust concentration. Dash lines show the prediction band for new measurements and the shaded area indicates the uncertainty (3 standard deviations) for the resulting calibration.

### *Flame Photography and Spectroscopy*

A high-resolution digital camera equipped with a macro lens and a variable neutral density filter is used to image the flames. The camera hot-shoe adapter is connected to a battery to generate a signal at the time of the photograph that can be correlated, on the data acquisition record, with a particular value of aluminum dust concentration. A high-speed digital video camera allows the flame behaviour in the transition regime to be monitored with a framing rate of 300 frames per second.

Spatially-resolved flame emission spectra are obtained using an opto-mechanical scanning system similar to the one used in our previous work for the study of aluminum dust flames [11]. The telescopic system focuses the magnified flame image on the film plane of a SLR camera with a magnification ratio of 1:1.5. The fiber optic cable installed in the center of the image plane of the SLR camera transmits the optical signal to a miniature diffraction spectrometer. The scanning of the flame image across the entrance of the telescopic system is performed by a rotating flat mirror and a step motor. The step signal driving the motor triggers the spectrometer acquisition and allows the spectrum acquired at each step to be correlated with the instantaneous aluminum mass concentration. The spatial resolution of the system varies between 0.15 mm and 0.6 mm to accommodate the different flame luminosities and different spectrometers used. Two Ocean Optics Inc. miniature spectrometers with fiber optic inlets are used. The first, an Ocean Optics USB-4000 spectrometer, with a spectral resolution of 2.5 nm and a spectral range from 350 nm to 1100 nm, has no entrance slit and is coupled to a 100  $\mu\text{m}$  fiber optic cable. Data from this spectrometer is analyzed to derive the flame temperature from the continuous part of the spectrum. The second spectrometer, an Ocean Optics HR-4000, with a spectral resolution of up to 0.02 nm in the range of 200 nm-1100 nm (depending on the grating installed), has an entrance slit of about 8 microns and is coupled to a 600  $\mu\text{m}$  optical fiber. This

spectrometer provides the necessary spectral resolution to fit an AIO vibrational band to a temperature. . The top view of the optical diagnostic set up is shown in Fig. 4.

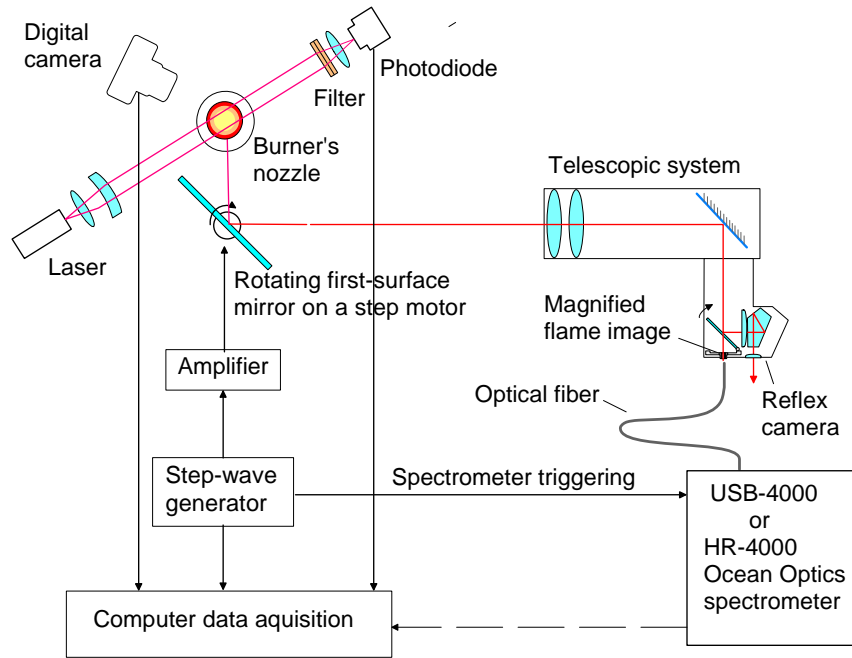


Fig. 11 Schematic of the optical diagnostic apparatus.

The position of the flame front is located by the maximum intensity of the spectral signal determined from each set of scans across the flame cone. The temperature of the condensed emitters in the flame front is derived by fitting the continuous part of the spectra to Planck's law of blackbody radiation. As in Ref. [12], it is assumed that the prime emitters of the continuous spectra are aluminum oxide particles whose spectral emissivity is assumed to be proportional to the inverse of the square of the wavelength  $(1/\lambda)^2$ . The estimated accuracy of the method is approximately  $\pm 50$  K at low flame temperatures and about  $\pm 150$  K at high temperatures.

Temperatures of the gaseous aluminum sub-oxide, AIO, are derived by fitting the spectrum of the AIO  $\Delta v = -1$  band obtained with the high-resolution spectrometer to a theoretically calculated spectrum as described in detail in Ref. [15]. This particular band of AIO is chosen due to the sensitivity of its shape to temperatures typically encountered in aluminum combustion. The AIO temperature derived is close to the peak temperature in the system [16].

#### *Gas flow and oxygen concentration*

The gas flow through the system is controlled using needle valves and rotameters that are calibrated with a digital flow meter within 2% accuracy. For the ejector calibration, the

oxygen concentration in the flow is measured with an oxygen analyzer having an accuracy of roughly 0.2%. Two different gas compositions are used in the present experiments. The first gas mixture is a stoichiometric methane-air mixture. The second mixture has identical flow rates of oxidizer and methane, but the air is replaced by a mixture of 26% oxygen and 74% nitrogen. Thus, after methane combustion, the first composition produced a flow of combustion products without any free oxygen, whereas the second composition generated a product flow with 5% of remaining free oxygen. This allows the effect of free oxygen on the combustion of aluminum in hydrocarbon combustion products to be determined. This enriched oxygen mixture is used to keep the flow rates identical (required for consistent dust dispersion) and to maintain similar methane flame temperatures.

### 3. RESULTS AND DISCUSSION

The qualitative behaviour and structure of the flame in the hybrid methane-aluminum mixture at different aluminum concentrations is analyzed using digital high-resolution images and high-speed movies synchronized with the dust concentration monitoring system. Figure 5 contains images of the different flame structures observed as a function of aluminum concentrations. As seen from the images in Fig. 5, the flame structure changes drastically with an increase in aluminum concentration. A 3.0 neutral density filter was employed at high aluminum concentrations to distinguish the flame structure, such that the actual changes in the flame appearance are greater than what is depicted by the images in Fig. 5. At low mass concentrations, below  $100 \text{ g/m}^3$ , the flame appears yellow in color, with no cone arising from the aluminum combustion zone. The appearance of the methane-aluminum flame at this aluminum concentration range is not different from the flame seeded with inert SiC powder. As the concentration of aluminum particles increases to roughly  $120\text{--}140 \text{ g/m}^3$ , a bright white spot emerges first at the tip of the flame and, as the concentration increases further to about  $180 \text{ g/m}^3$ , a very bright front with a well-defined outer border indicating aluminum combustion moves down along the flame cone, eventually stabilizing just a few millimetres above the rim of the methane flame. This process is illustrated with the still frames shown in Fig. 5 (bottom). A similar aluminum front formation behaviour is observed in methane mixtures containing 5% of free oxygen. In this case, the appearance of the aluminum flame front can be seen at somewhat lower dust concentrations.

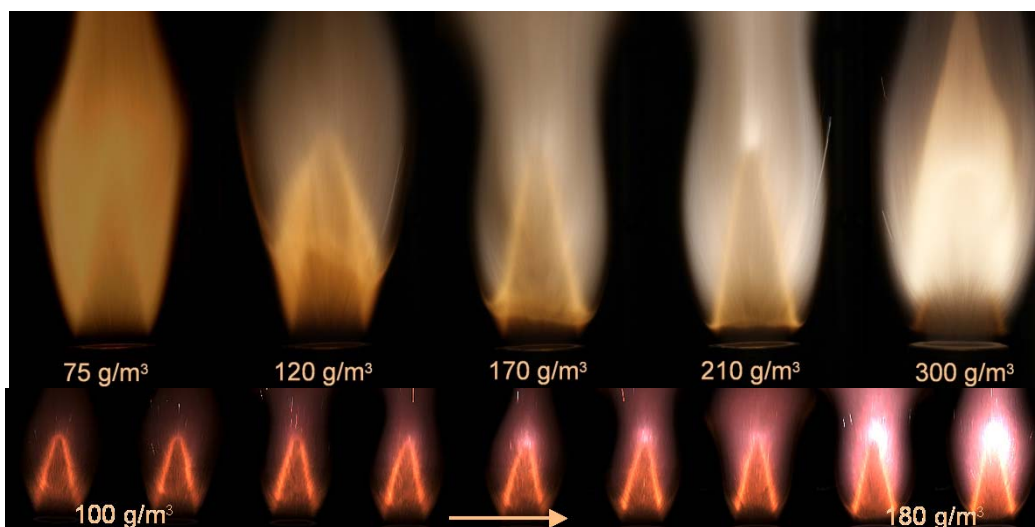


Fig. 12 Flame images at different concentration of aluminum (top) and still frames from high-speed recording of aluminum front formation process (bottom).

### *Flame spectra and temperature*

Typical flame spectra acquired before and after the formation of the aluminum dust flame front (at low and high aluminum concentrations) are presented in Fig. 6. As can be seen from Fig. 6, the flame demonstrates a weak signal of the AIO band sequence at low aluminum concentrations. In contrast, after the formation of the aluminum combustion front at higher aluminum concentrations, the AIO molecular bands are strong in emission and are similar to spectra from pure aluminum dust-air flames [12]. At concentrations above  $200 \text{ g/m}^3$ , strong non-ionized aluminum vapor atomic lines can be seen at  $394.40 \text{ nm}$  and  $396.15 \text{ nm}$  [17].

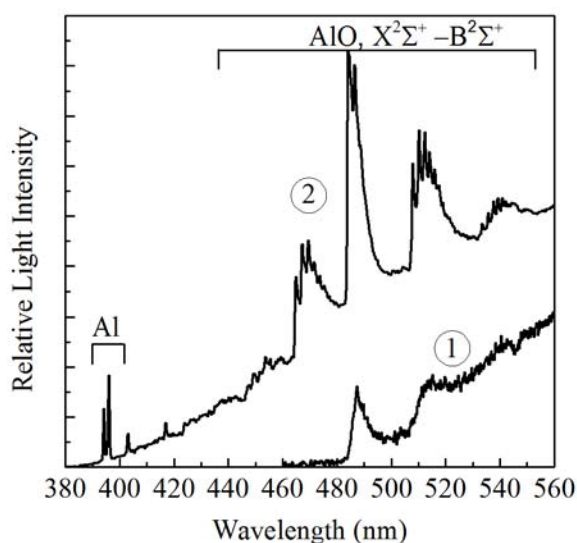


Fig. 13 Flame spectra before (low aluminum concentration,  $80 \text{ g/m}^3$ , number 1) and after the formation of aluminum flame front (high aluminum concentration,  $250 \text{ g/m}^3$ , number 2), in products of methane combustion containing 5% of free oxygen content.

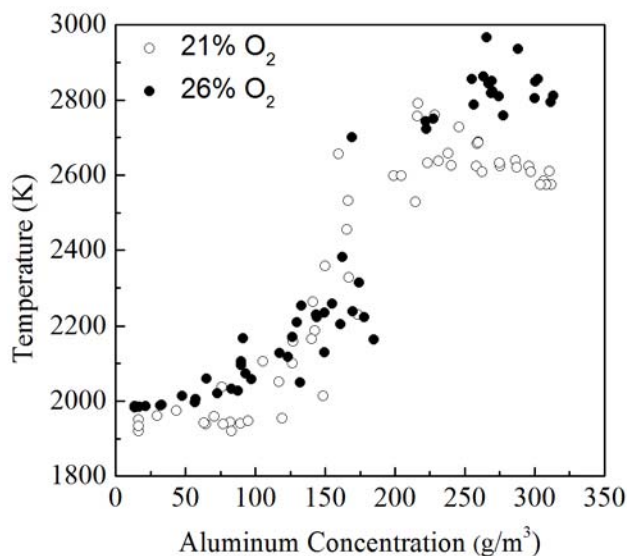


Fig. 14 Temperature of condensed emitters in methane-aluminum flames with (26% O<sub>2</sub>), and without (21% O<sub>2</sub>), free oxygen in the combustion products.

The results of the temperature measurements for condensed-phase emitters as a function of aluminum concentrations in a stoichiometric methane-air flame and in the methane mixture with 5% of free oxygen) are presented in Fig. 7. The temperature measurements confirm the observed qualitative behavior of both flames as the aluminum concentration is increased. There is a sharp rise in the flame temperature at concentrations around 150–175 g/m<sup>3</sup>, which corresponds to the observed formation of the aluminum flame front. As shown in Fig. 8, the flame temperature changes from a temperature typical of a methane flame loaded with inert particles to a flame temperature close to temperatures predicted by equilibrium calculations with aluminum as a reactant. From the photographic video evidence illustrated in Fig. 5, it is apparent that, for every particular point on the Bunsen-flame cone, there is a rapid bifurcation-type transition associated with the formation of the aluminum dust combustion flame front. In spite of this sudden, step-wise flame-front formation, measurements within a narrow range of aluminum concentration produce intermediate flame temperatures situated between the two combustion modes. However, these temperatures are not associated, as high-speed videos show, with any transitional phenomenon. Rather, they arise from spectra acquired over a long integration time, during which the two combustion regimes were both present during the measurement interval.

Measurement of the characteristic AIO temperatures can only be performed for high-temperature flames that have strong enough AIO emission so that the  $\Delta v = -1$  band (see Fig. 6) can be resolved. The results are presented in Fig. 8 together with the condensed-phase temperature and thermodynamic calculations of the adiabatic flame temperature. Figure 8 demonstrates that, before the formation of the aluminum flame front, the heat released from the relatively-slowly oxidizing aluminum has little effect on the flame temperature, which remains close to that of the methane flame. Only after the formation of the aluminum flame front does the flame temperature approach the predicted

thermodynamic equilibrium value. The gaseous and condensed-phase temperatures are effectively equivalent considering the accuracy of the temperature measurements, which are estimated to be  $\pm 120$  K for the condensed phase temperature and  $\pm 100$  K for the AlO temperatures.

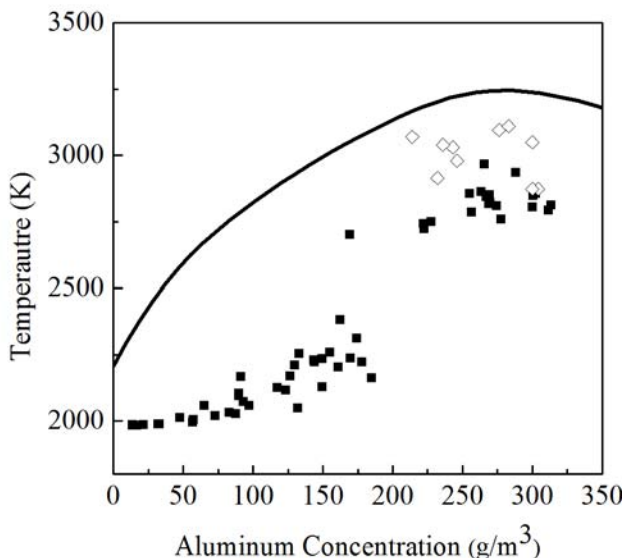


Fig. 15 Temperature of the condensed emitters (solid squares) and the gas phase temperature (open diamonds) derived from AlO molecular spectra in comparison to the temperature obtained from the constant-pressure thermodynamic calculations (solid line).

#### *Analysis of condensed combustion products*

Condensed combustion products from the methane-aluminum flame are collected on a thick horizontal copper plate positioned at about 20 mm above the flame tip for approximately 5-15 seconds. The cold metal surface is a relatively efficient collector of particles from the hot combustion flow due to a strong thermophoretic force moving particles along the temperature gradient towards the plate surface [18]. From 5 to 10 exposures (plates) were required to collect a sample mass sufficient for chemical analysis. Due to the relatively long collection time, product samples cannot be linked to a particular value of aluminum concentration but only to some concentration range, as identified in Table 1, corresponding to slow aluminum oxidation (50–100 g/m<sup>3</sup>), establishment of the aluminum flame front (150–200 g/m<sup>3</sup>) and aluminum-rich flames (200–300 g/m<sup>3</sup>). The product samples were analyzed for metallic aluminum content via the NaOH digestion method. The results of the analysis are presented in Table 1 for the two different oxygen concentrations, with theoretical values obtained from the equilibrium calculation (in parentheses).

**Table 2. Product Analysis.**

Sample/concentration range	Aluminum Content	
	21% Oxygen	26% Oxygen
Original Powder	98.9	98.9
50-100 g/m <sup>3</sup>	25.6 (0.0)*	0.5 (0.0)*
150-200 g/m <sup>3</sup>	0.9 (0.0)*	0.2 (0.0)*
200-300 g/m <sup>3</sup>	7.4 (4.1)*	2.9 (1.3)*

\* Values calculated using an equilibrium solver

The original sample contains 98.9% aluminum, indicating a very thin oxide layer on its surface. As can be seen from Table 1, even in the case with no free oxygen (21% O<sub>2</sub>), the degree of conversion of aluminum to oxide reaches 75% even without the formation of the aluminum flame front. It is practically complete for mixtures with 5% of free oxygen (26% O<sub>2</sub>). The slow, non-frontal oxidizing reaction stretches over a long downstream distance and contributes little, as mentioned before, to the flame temperature. The TEM photographs of the collected products in this concentration range reveal that they are dominated by the heavily oxidized aluminum particles with traces of submicron spherical aluminum oxide present. In contrast, the product composition of aluminum combustion in the frontal regime is dominated by submicron ( $d < 0.1 \mu\text{m}$ ) aluminum oxide particles and the degree of aluminum conversion to oxide is close to 100%. Metallic aluminum can again be found in aluminum-rich mixtures above the stoichiometric concentration in accordance with thermodynamic predictions [13]. The presence of unburned metallic aluminum in the collected condensed flame products also indicates that the reaction of aluminum with oxygen in the ambient air is minimal during the collection process.

#### *Burning velocities of aluminum-methane mixtures*

The total flame surface area method is used to obtain flame burning velocities in aluminum-methane-air mixtures. Hence, the known volumetric flow rate through the nozzle is divided by the surface area of the inner flame cone to obtain the burning velocity [11]. Each flame image is linked to a particular value of dust concentration using timing marks produced by the camera output on the data acquisition system record. The procedure is first tested by comparing data obtained for pure methane-air and aluminum-air mixtures with results published in literature. The burning velocity of the stoichiometric methane-air mixture is found to be about  $36 \pm 2$  cm/s, in good agreement with data in the literature obtained with the same method [19]. The burning velocity in a pure aluminum flame is found to be  $20 \pm 3$  cm/s at an aluminum concentration of roughly 400 g/m<sup>3</sup>, in agreement with previous measurements performed for the same aluminum powder but on a different burner [11]. The burning velocities in stoichiometric methane-air ( $0.095\text{CH}_4 + 0.190\text{O}_2 + 0.715\text{N}_2$ ) and methane mixture with 26% of oxygen ( $0.095\text{CH}_4 + 0.235\text{O}_2 + 0.670\text{N}_2$ ) seeded with aluminum and inert silicon carbide powders at different concentrations are presented in Fig. 9 (the data from the plot on the left was first published in [13]).

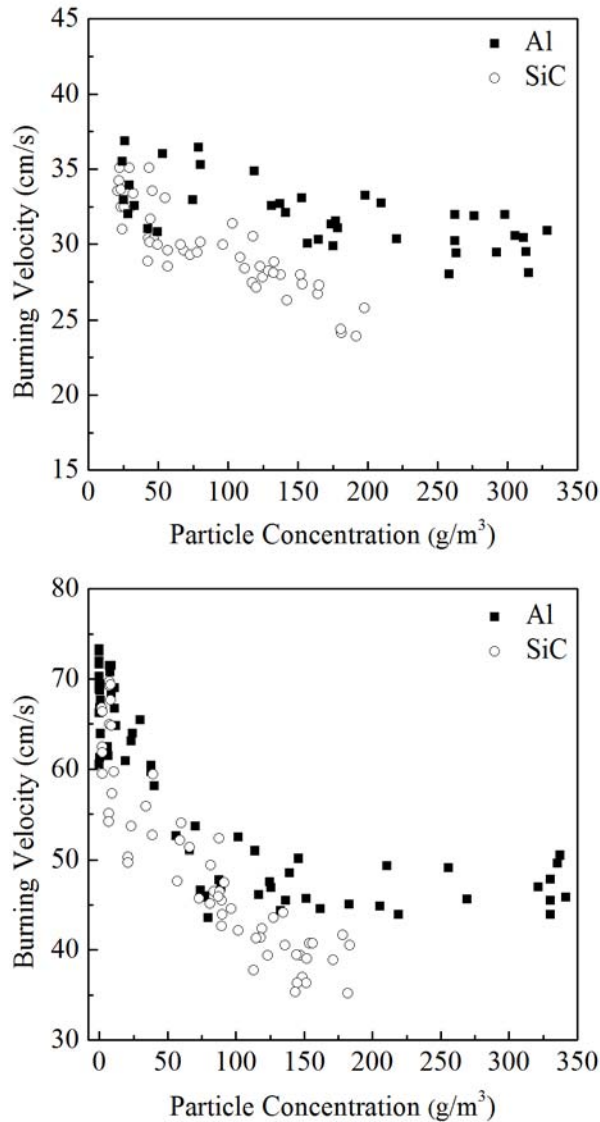


Fig. 16 Burning velocities of methane flames seeded with different concentrations of aluminum and silicon carbide (SiC) powders. Top: 21% O<sub>2</sub>, Bottom: 26% O<sub>2</sub>.

As can be seen, both aluminum and silicon carbide suspensions in either gaseous mixture first exhibit a decrease in the flame speed with increasing solid phase concentration. The obvious explanation for the lower methane flame speed when it is seeded with inert particles is that the specific heat of the gas-solid mixture increases, resulting in lower flame temperatures. The somewhat stronger decline of the burning velocity in silicon carbide suspensions can be attributed to the smaller SiC particles (1–5  $\mu\text{m}$ ) in comparison to aluminum and, as a consequence, a smaller difference between the particle and gas temperatures within the reaction zone. At silicon carbide concentrations above 170  $\text{g/m}^3$ , the flame starts to extinguish in both gaseous mixtures. The flame quenching starts with the opening of the flame tip. The opening progressively widens with the increase of the SiC concentration until a value of approximately 250  $\text{g/m}^3$ , at which point most of the mixture escapes unburned. In contrast, in mixtures with aluminum

particles, the flame burning velocity stops decreasing after the aluminum flame front is formed and the tip of the flame remains closed even at aluminum concentrations up to 400 g/m<sup>3</sup>. The observed plateau of the burning velocity with respect to aluminum concentration indicates a coupling between the methane and aluminum combustion fronts. Upon coupling, heat is transferred from the aluminum flame front to the methane flame front, which promotes the methane flame propagation. Without this heat transfer, the methane flame speed would keep decreasing until the flame quenches, as it occurs when inert particles are seeded in the flames. The coupled flames may be analogous to a so-called control regime, discussed in previous studies of binary dust mixtures, in which the slower burning, but more energetically potent, component defines the burning velocity of the linked fronts, even though it is positioned behind the faster primary flame front [20].

#### *Theoretical estimation of the required aluminum concentration for flame coupling*

Due to the complexity of the flame in a hybrid mixture consisting of two interacting methane and aluminum combustion fronts, development of a complete non-steady theoretical model of the combustion process is beyond the scope of the present paper. Instead, here we develop a simple theoretical estimation of the minimal concentration of aluminum in suspension for which the methane and aluminum combustion fronts may be coupled into a single flame structure. The obvious criteria for such a linkage would be the ability of the aluminum dust flame front to propagate in the methane combustion products with a speed equal to or exceeding the speed of the product flow from the primary methane flame front. In this estimation, the methane and aluminum dust combustion fronts will be assumed to be independent, and not interacting, thus neglecting the experimental observation that the joint methane-aluminum front has a somewhat greater speed than a pure methane flame seeded with inert particles. Such an approximation is acceptable for determining the mechanism and concentration at which coupling occurs, but cannot predict the resulting flame speed of the hybrid flame front.

The burning velocity of the methane-air mixture seeded with inert aluminum particles and the flow speed of the products are calculated with the open-source combustion software Cantera [21] using the reduced mechanism *drm-19* developed by Kazakov and Frenklach<sup>2</sup>. In these calculations, the particles and gas are assumed to be in thermal equilibrium. The flow speed of the methane combustion products with inert aluminum particles,  $S_{b,\text{methane}}$ , is shown in Fig. 11, denoted by a solid line, and decreases with higher particle loading, as expected.

The burning velocity of the aluminum dust flame is estimated assuming that the small aluminum particles used in the present experiments burn in the methane combustion products in the kinetic mode, i.e., the burning rate is limited by some reaction kinetics, rather than diffusion of the oxidizers towards the particle surface, as indicated in a previous study [9]. This assumption is based on the set of observations of these flames that indicates that the transition from slow-burning to frontal combustion of the aluminum front happens at a critical concentration where the kinetic rate of reaction becomes fast enough to enable flame coupling. The nature of the kinetic resistance in the high-temperature aluminum flames encountered in the present work remains open for discussion. The calculated adiabatic flame temperature of the linked methane-aluminum flame is close to, or even exceeds, the aluminum boiling point (2792 K). The experimentally-measured flame

---

<sup>2</sup> <http://www.me.berkeley.edu/drm/>

temperatures, although somewhat lower, are also close to the aluminum boiling point. Estimates show that, near the boiling point, the evaporation rate of an aluminum droplet considerably exceeds the rate of heterogeneous reactions published in the literature [22]. Moreover, aluminum evaporation likely occurs in the kinetic regime because of the small particle size and the fact that the very rapid non-activated nature of the reaction of aluminum vapor with oxidizers [23] prevents accumulation of the aluminum vapor at the droplet surface. Thus, it is assumed that the effective aluminum reaction rate,  $\dot{\omega}$ , corresponds to the kinetic evaporation mass flux from the total surface area of aluminum particles per unit volume. The evaporation rate,  $R_e$ , per unit surface area in the kinetic regime is given by:

$$R_e = \alpha_e \sqrt{\frac{m_{Al,atomic}}{2\pi k_B T_b}} P_v \quad (1)$$

where  $T_b$  is the droplet temperature,  $\alpha_e$  is the coefficient of evaporation,  $m_{Al,atomic}$  is the atomic mass of aluminum and  $k_B$  is the Boltzmann constant [24]. For a pure aluminum droplet, the coefficient of evaporation should be close to unity, as aluminum is composed of single atoms which makes the liquid easier to evaporate than, for example, a polar molecule like water [25]. However, part of the aluminum droplet surface does not participate in the evaporation as it is covered by a liquid aluminum oxide cap, as was observed in previous work [8]. Thus, estimates provided in the present paper consider  $\alpha_e$  as an unknown parameter in the range, for sake of argument, from 0.2–1. The vapor pressure,  $P_v$ , can be found using the Clausius-Clapeyron relationship:

$$P_v = A e^{\frac{-h_v}{RT_b}} \quad (2)$$

where the activation energy,  $h_v = 294$  kJ/mol, is the latent heat of aluminum vaporization,  $A = 3.1 \times 10^{10}$  Pa is the pre-exponential factor and  $R$  is the universal gas constant [26]. The total reaction rate,  $\dot{\omega}$ , can then be obtained by multiplying the expression (1) by the total surface area of aluminum droplets per unit volume:

$$\dot{\omega} = \frac{3B\alpha_e A}{r_0 \rho_{Al,s}} \sqrt{\frac{m_{Al,atomic}}{2\pi k_B T_b}} e^{\frac{-h_v}{RT_b}}, \quad (3)$$

where  $r_0$  is the initial radius of the aluminum particle,  $B$  ( $\text{g/m}^3$ ) is the mass concentration of aluminum suspension in methane combustion products and  $\rho_{Al,s}$  is the solid aluminum density. In the present formulation, the flame in the aluminum suspension with the burning rate controlled by the kinetics of aluminum evaporation is no different from a gaseous flame with a one-step first-order Arrhenius-type reaction. Thus, a known Zel'dovich-Frank-Kamenetskii type analytical expression [27] can be derived for estimating the burning velocity of an aluminum flame in methane combustion products. The present analysis was done assuming that the fuel (aluminum particles) had zero diffusivity which leads to the temperature dependence in the expression below:

$$S_u = \sqrt{\frac{3\sqrt{2\pi}}{Ze} \left(\frac{T_u}{T_b}\right)^2 \left(\frac{\lambda_b}{\rho_b C_{p,b}}\right) \frac{A\alpha_e}{r_0 \rho_{Al,s}} \sqrt{\frac{m_{Al,atomic}}{2\pi k_B T_b}} e^{\frac{-h_v}{RT_b}}} \quad (4)$$

where the Zel'dovich number,  $Ze$ , is given by the expression:

$$Ze = \frac{h_v(T_b - T_u)}{RT_b^2} \quad (5)$$

the heat conductivity,  $\lambda_b$ , the density,  $\rho_b$ , the heat capacity,  $C_{p,b}$ , and the flame temperature,  $T_b$ , in the expression (4) are all obtained from Cantera using an equilibrium calculation.

The initial temperature,  $T_i$ , is obtained from the flame speed calculation for the methane flame loaded with inert aluminum particles. The results obtained for different values of evaporation coefficient  $\alpha_e$  are plotted in Fig. 10 with dash lines.

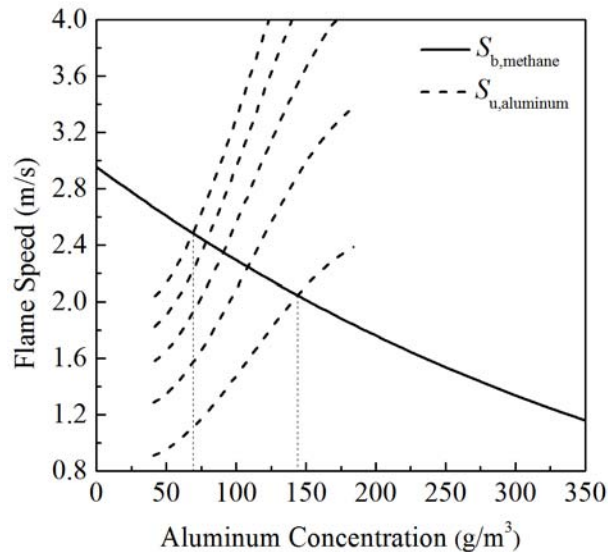


Fig. 17 Calculated flow speed of methane products from Cantera (solid lines) and estimated burning velocity of aluminum dust flame (dashed line, from bottom to top,  $\alpha_e = 0.2, 0.4, 0.6, 0.8, 1.0$ ) controlled by aluminum evaporation rate.

As discussed above, the aluminum concentration value corresponding to the intersection of the methane products flow speed with the predicted speed of an aluminum flame can be interpreted as the minimal concentration at which the methane and aluminum flame fronts became coupled. The estimated concentration changes from around  $70 \text{ g/m}^3$  to  $150 \text{ g/m}^3$  with a change in the evaporation coefficient from 1 (top curve) to 0.2 (bottom curve). The simple theoretical approach used here predicts the observed coupling of the aluminum and methane flame fronts within a concentration range consistent with the experiments and, therefore, supports the assumption that the aluminum burning rate is controlled by the aluminum vaporization rate.

#### 4. CONCLUSIONS

Historically, the reaction dynamics of metal particles in hot oxidizing flows, produced by the combustion of hydrocarbons in various energetic systems including metalized solid and liquid propellants and explosives, has been studied and modeled as a combustion process involving isolated individual particles. The implicit assumption behind this approach is that the transition from individual-particle combustion towards combustion of a metal suspension, or ensemble of particles, characteristic of real systems would not significantly change the underlying combustion physics. The present work has demonstrated that this approach is inadequate for heavily-metalized systems that rely on the metal for the bulk of the energy output and, thus, require relatively dense dust clouds. Thus, knowledge of the ignition temperature and combustion times of individual aluminum particles is insufficient for the prediction of the combustion dynamics of aluminum suspensions at high dust concentrations. For example, aluminum particles large enough to

burn in the diffusive mode might be unable to ignite at the relatively low temperatures of some hydrocarbon combustion products but effective aluminum combustion might be established if the conditions are right for the formation of an aluminum flame front. Similarly, the combustion time for the kinetically-reacting small aluminum particles, which is controlled by relatively slow surface reactions at temperatures characteristic of hydrocarbon combustion, will be replaced by the much faster kinetics of aluminum evaporation at the high dust-flame temperatures that are produced by burning the aluminum itself.

Modeling of metal combustion in heavily-metalized energetic systems must consider the possibility of laminar or turbulent frontal combustion in the metal suspensions generated by the burning, or detonating, energetic system. The present work has demonstrated that, for a flame in a hybrid methane-aluminum mixture, the dust-combustion front may also influence the hydrocarbon flame; thus, a proper theoretical model has to analyze these two fronts as a coupled flame structure.

The main results of the present work are highlighted in the points below:

- It is observed that, at some critical aluminum concentration, the aluminum flame front becomes coupled to the hydrocarbon flame, corresponding to a change in the aluminum reaction mode from relatively-slow oxidation to a fast combustion process.
- The temperature of the aluminum flame, derived from the continuous part of the spectrum and from AlO molecular bands, is close to the thermodynamically-predicted values with aluminum as a reactant; whereas, before the formation of the aluminum front, the temperature derived from the continuous spectra is close to the temperature of the methane flame with aluminum as an inert additive.
- The burning velocity of the methane-aluminum flame decreases with an increase in aluminum concentration prior to the formation of the aluminum flame front and attains a plateau value thereafter. In comparison, the flame speed of a methane flame seeded with inert SiC particles similarly decreases, but then extinguishes at high particle concentrations.
- A theoretical estimate for the propagation speed of an aluminum flame propagating in methane combustion products, with the reaction rate controlled by the kinetic evaporation of aluminum, can adequately predict the minimal concentration at which the methane and aluminum flames become linked.

## 5. REFERENCES

[1] Choudhury, P. R., "Slurry Fuels," *Progress in Energy and Combustion Science*, Vol. 18, No. 5, 1992, pp. 409-427.

doi: [10.1016/0360-1285\(92\)90008-O](https://doi.org/10.1016/0360-1285(92)90008-O)

[2] Natan, B., and Rahimi, S., "The Status of Gel Propellants in Year 2000," *International Journal of Energetic Materials and Chemical Propulsion*, Vol. 5, 2001, pp. 172-194.

doi: 10.1615/IntJEnergeticMaterialsChemProp.v5.i1-6.200

- [3] Geisler, R. L., Frederick, R. A., and Giarra, M., "Historical Overview and Solid Rocket Motor Fundamentals," *Encyclopedia of Aerospace Engineering*, John Wiley & Sons, Ltd, 2010.  
doi: 10.1002/9780470686652.eae101
- [4] Zhang, F., "Detonation in Reactive Solid Particle-Gas Flow," *Journal of Propulsion and Power*, Vol. 22, No. 6, 2006, pp. 1289-1309.  
doi: 10.2514/1.18210
- [5] Maranda, A., "Research on the Process of Detonation of Explosive Mixtures of the Oxidizer Fuel Type Containing Aluminium Powder," *Propellants, Explosives, Pyrotechnics*, Vol. 15, No. 4, 1990, pp. 161-165.  
doi: 10.1002/prop.19900150408
- [6] Li, Z., Liu, C., Huang, J., and Yin, S. "Synthesis and Deposition of TiC-Fe Coatings by Oxygen-acetylene Flame Spraying," *Journal of Materials Science and Technology*, Vol. 19, No. 2, 2003, pp. 161-163.
- [7] Zolotko, A. N., Vovchuk, Y. I., Poletayev, N. I., Florko, A. V., and Al'tman, I. S., "Synthesis of Nanooxides in Two-phase Laminar Flames," *Combustion, Explosion and Shock Waves*, Vol. 32, No. 3, 1996, pp. 262-269.  
doi: 10.1007/BF01998454
- [8] Yetter, R. A., and Dryer, F. L., "Metal Particle Combustion and Classification," *Microgravity combustion: fire in free fall*, Academic Press, 2001, pp. 419-478
- [9] Bazyn, T., Krier, H., and Glumac, N., "Evidence for the Transition from the Diffusion-Limit in Aluminum Particle Combustion," *Proceedings of the Combustion Institute*, Vol. 31, No. 2, 2007, pp. 2021-2028.  
doi: 10.1016/j.proci.2006.07.161
- [10] Cassel, H. M., *Some fundamental aspects of dust flames*, US Department of the Interior, Bureau of Mines, 6551, 1964.
- [11] Goroshin, S., Fomenko, I., and Lee, J. H. S., "Burning Velocities in Fuel-Rich Aluminum Dust Clouds," *Proceedings of the Combustion Institute*, Vol. 26, No. 2, 1996, pp. 1961-1967.  
doi: 10.1016/s0082-0784(96)80019-1
- [12] Goroshin, S., Mamen, J., Higgins, A., Bazyn, T., Glumac, N., and Krier, H., "Emission Spectroscopy of Flame Fronts in Aluminum Suspensions," *Proceedings of the Combustion Institute*, Vol. 31, No. 2, 2007, pp. 2011-2019.  
doi: 10.1016/j.proci.2006.07.175
- [13] Soo, M., Julien, P., Goroshin, S., Berghthorson, J. M., and Frost, D. L., "Stabilized Flames in Hybrid Aluminum-Methane-Air Mixtures," *Proceedings of the Combustion Institute*, Vol. 34, No. 2, 2013, pp. 2213-2220.  
doi: [10.1016/j.proci.2012.05.044](https://doi.org/10.1016/j.proci.2012.05.044)
- [14] Goroshin, S., Bidabadi, M., and Lee, J. H. S., "Quenching Distance of Laminar Flame in Aluminum Dust Clouds," *Combustion and Flame*, Vol. 105, No. 1-2, 1996, pp. 147-160.  
doi: 10.1016/0010-2180(95)00183-2
- [15] Glumac, N., Krier, H., Bazyn, T. I. M., and Eyer, R., "Temperature Measurements of Aluminum Particles Burning in Carbon Dioxide," *Combustion Science and Technology*, Vol. 177, No. 3, 2005, pp. 485-511.  
doi: 10.1080/00102200590909030

- [16] Peucker, J. M., Lynch, P., Krier, H., and Glumac, N., "On AlO Emission Spectroscopy as a Diagnostic in Energetic Materials Testing," *Propellants, Explosives, Pyrotechnics*, 2013. (to be published)  
doi: 10.1002/prop.201200144
- [17] Kelleher, D. E., Mohr, P., Martin, W., Wiese, W., Sugar, J., Fuhr, J., Olsen, K., Musgrove, A., Reader, J., and Sansonetti, C. J., "New NIST Atomic Spectra Database," *SPIE's International Symposium on Optical Science, Engineering, and Instrumentation*, International Society for Optics and Photonics, 1999, pp. 170-179.  
doi: 10.1117/12.364152
- [18] He, C., and Ahmadi, G., "Particle Deposition with Thermophoresis in Laminar and Turbulent Duct Flows," *Aerosol Science and Technology*, Vol. 29, No. 6, 1998, pp. 525-546.  
doi: 10.1080/02786829808965588
- [19] Lewis, B., and von Elbe, G., *Combustion, Flames, and Explosions of Gases*. New York: Academic Press, 1961.
- [20] Goroshin, S., Kolbe, M., and Lee, J. H. S., "Flame Speed in a Binary Suspension of Solid Fuel Particles," *Proceedings of the Combustion Institute*, Vol. 28, No. 2, 2000, pp. 2811-2817.  
doi: 10.1016/s0082-0784(00)80703-1
- [21] Goodwin, D. "An open-source, extensible software suite for CVD process simulation," *Chemical Vapor Deposition XVI and EuroCVD*, Electrochemical Society, Vol. 14, No. 2003, 2003, p. 08.
- [22] Servaites, J., Krier, H., Melcher, J. C., and Burton, R. L., "Ignition and Combustion of Aluminum Particles in Shocked H<sub>2</sub>O/O<sub>2</sub>/Ar and CO<sub>2</sub>/O<sub>2</sub>/Ar Mixtures," *Combustion and Flame*, Vol. 125, No. 1-2, 2001, pp. 1040-1054.  
doi: 10.1016/s0010-2180(01)00225-5
- [23] Fontijn, A., Felder, W., and Houghton, J. J., "Hiff Kinetics Studies. Temperature Dependence of Al/O<sub>2</sub> and AlO/O<sub>2</sub> Kinetics from 300 to 1700/1400 K," *Proceedings of the Combustion Institute*, Vol. 16, No. 1, 1977, pp. 871-879.  
doi: 10.1016/S0082-0784(77)80380-9
- [24] Langmuir, I., "The Evaporation, Condensation and Reflection of Molecules and the Mechanism of Adsorption," *Physical Review*, Vol. 8, No. 2, 1916, pp. 149-176.
- [25] Eames, I. W., Marr, N. J., and Sabir, H., "The Evaporation Coefficient of Water: a review," *International Journal of Heat and Mass Transfer* Vol. 40, No. 12, 1997, pp. 2963-2973.  
doi: 10.1016/S0017-9310(96)00339-0
- [26] Haynes, W.H., *CRC handbook of chemistry and physics*, 93rd edition, Boca Raton, Florida: CRC Press, 2012.
- [27] Zeldovich, I. B., Barenblatt, G. I., Librovich, V. B., and Makhviladze, G. M., *Mathematical theory of combustion and explosions*, New York: Consultant Bureau, 1985

## Chapter 2. Hybrid flames of iron and methane on the Bunsen burner

### 1. INTRODUCTION

Multi-front reactive waves are complex phenomena that are known to occur in a variety of different systems. Two or more reactive fronts can interact by different physical mechanisms, including diffusion and convection of either heat or active species, and through radiative heat transfer. Double detonation fronts have been studied for reactive particle-laden gases [1, 2]. Similar phenomena have been observed in systems undergoing self-propagating high-temperature synthesis [3], metalized propellants [4] and also figure into proposed novel nuclear reactor concepts [5]. A simple system to study multi-front phenomena consists of mixtures containing two fuels that have very different activation energies and reaction mechanisms. Deflagrations in such mixtures have been studied theoretically [6, 7] and experimentally for  $\text{CH}_4\text{-NO}_2\text{-O}_2$  mixtures [8] and hybrid aluminum-methane mixtures [9].

For aluminum-methane-air mixtures, previous studies have demonstrated that an aluminum flame front may form in the products of the methane combustion with micron-sized aluminum particles reacting in a kinetically-controlled regime [9]. In this case, the aluminum flame front forms only above a critical particle concentration and is believed to be coupled to the methane flame front. However, due to the intense luminosity of the aluminum flame it is not possible to directly observe the methane flame front once the aluminum flame has formed. In addition, aluminum typically burns in the vapor phase and produces a large quantity of sub-oxides which increases the complexity of the problem by introducing other potential limiting factors, such as the rate of evaporation [10]. For these reasons, a different particulate fuel is selected to simplify the investigation of multi-front reactive waves. Iron is a suitable candidate as it burns purely heterogeneously by surface reactions. The iron-air adiabatic flame temperature is on the order of the methane flame temperature, which allows the observation of both flames simultaneously. It has also been shown that iron can burn in either a diffusion-controlled or a kinetically-controlled regime can depend on, among other things, the oxidizing environment [11].

The present study investigates stabilized flames with a double-front structure in hybrid mixtures of iron and methane and focuses on the effect of the particle combustion mode on this flame structure and its propagation speed with different oxidizing mixtures. The kinetically-controlled regime is observed in the products of methane-air combustion, whereas the diffusion regime is observed when the mixture contains excess oxygen. The gases are seeded with micron-sized iron powder with a particle concentration varying from zero to  $350 \text{ g/m}^3$ . Flames are directly observed with high-speed imaging and burning velocities are obtained using an estimate of the flame surface area from the flame photographs. Emission spectroscopy is used to determine the temperature of the condensed-phase species in the flame. The results are then compared to that of a methane flame seeded with inert silicon carbide (SiC) particles. In the kinetically-controlled regime, an iron flame front forms above a critical concentration and couples to the methane flame, even though the particles do not ignite. In the case of the diffusion-controlled regime single

particles do ignite, even at the lowest concentrations, but again form a distinct iron flame front above a critical concentration.

## 2. EXPERIMENTAL APPARATUS

### *Iron Powder and Gaseous Mixtures*

The iron powder used in the present investigation was produced by Alfa Aesar. The Sauter mean diameter of the particles is  $d_{32} = 2.20 \mu\text{m}$  with a volume-weighted size distribution obtained from a Malvern Mastersizer shown in Fig. 1. Figure 2 shows an SEM photograph of the powder, indicating the spherical morphology of the powder.

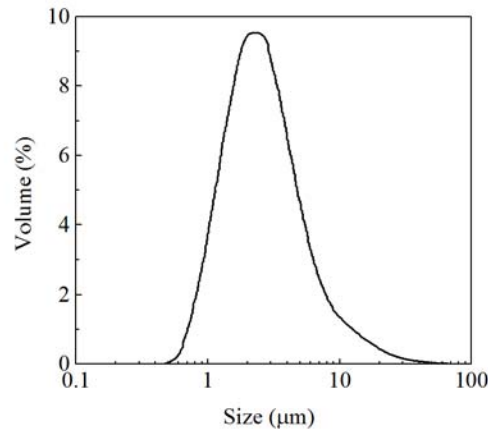


Figure 1. Iron particle size distribution.

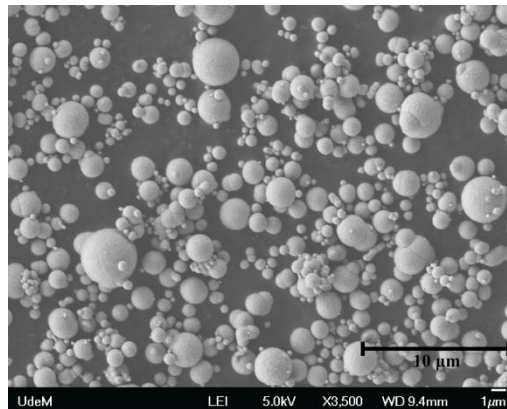


Figure 2. Scanning electron micrograph of iron powder.

Two different gaseous mixtures are used: the first is a stoichiometric methane-air mixture in which, after the methane flame, there is no excess oxygen; in the second case, all flow rates are kept identical but the air is replaced with the modified mixture made up of 26% oxygen and the balance nitrogen, which has little effect on the flame temperature and the operation of the dust dispersion system. The resulting mixture corresponds to an

equivalence ratio of 0.8, which leaves approximately 5% excess oxygen after the methane has been fully consumed.

### *Dust Burner and Diagnostics*

Experiments are performed with a Bunsen burner designed to operate with gaseous and dust fuels. Detailed schematics of the apparatus can be found in previous publications [9]. The powder is fed from a reservoir to the burner by a piston and is dispersed by the gas mixture through an air-knife. The resulting two-phase flow is laminarized in a 60-cm-long tube and ignited at the exit of the nozzle.

The dust concentration is monitored by laser attenuation. A beam passes through the two-phase mixture through a slit in the nozzle covered with high-temperature, high-optical clarity tape. The Beer-Lambert law is used to correlate the laser attenuation with the dust concentration. The system is calibrated separately for every type of powder [12].

An Ocean Optics USB 4000 spectrometer coupled with a 100-micron optical fiber is used to obtain emission spectra from the dust flame. Spatial resolution is achieved in one dimension by coupling the optical fiber to a telescope focused on a rotating mirror reflecting the image of the flame. The Bunsen cone is scanned with a step motor attached to the mirror. The flame front is located by the point of maximum emission intensity [13]. Flame images and videos are acquired with a high-resolution digital camera and a high-speed video camera operating at 300 frames per second. A variable neutral-density filter is used to reduce the intensity of the light emitted by the flame [9]. The intensity of the filter is changed according to the luminosity while keeping the exposure time and f-number the same. All optical systems are linked to the particle concentration monitor to correlate the time of the picture, video or spectrum with its corresponding dust concentration.

## 3. RESULTS AND DISCUSSION

### *Flame spectra and temperature*

Flame emission spectra are acquired over the range of particle concentrations in both types of methane flames. The integration time varies with the dust concentration and temperature. Shorter integration times are required for high particle loadings due to the greater number of emitters. The two oxidizing environments produce distinctively different spectra, as illustrated in Fig. 3.

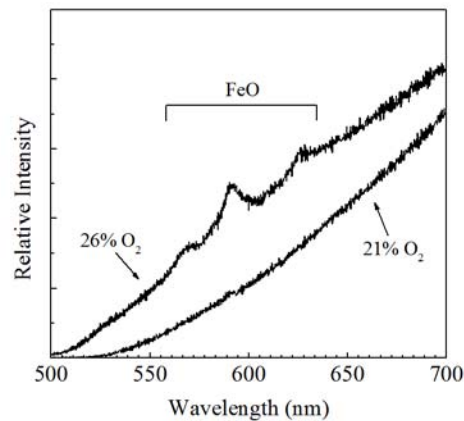


Figure 3. Emission spectra for both stoichiometric methane-air and enriched-oxygen-methane cases at an iron concentration of approximately  $200 \text{ g/m}^3$ .

The lower spectrum in Fig. 3 is obtained from iron particles in the stoichiometric methane-air flame. The spectrum is composed solely of continuous blackbody radiation, without any atomic lines or molecular bands. By contrast, the top spectrum, from the methane-lean mixture, exhibits molecular bands between  $550 \text{ nm}$  and  $650 \text{ nm}$  on top of the continuous spectrum. Those bands are present even at low iron concentration and are thought to be attributed to an electronic transition of iron oxide,  $\text{FeO}$ , identified from the spectrum produced by West and Broida [14]. The temperature is obtained by fitting the continuous part of the spectra to Planck's law of blackbody radiation [13], assuming that iron particles behave as grey bodies. The accuracy of the temperature measurements are estimated to be  $\pm 120 \text{ K}$ . Measurements are taken in the middle of the flame and the temperature can vary over the height of the cone, with the tip being the hottest part. Results are shown in Fig. 4, with the open squares reflecting the stoichiometric case and closed squares the enriched-oxygen case.

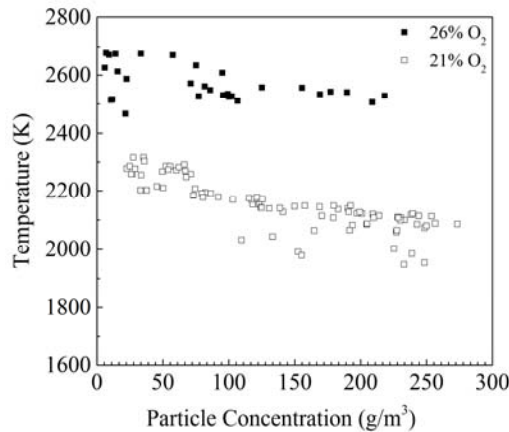


Figure 4. Iron particle temperatures as a function of iron concentration in both oxidizing environments.

There is a significant difference in particle temperature depending on the oxidizing environment. The methane flame temperature without iron loading in both cases is approximately  $2200 \text{ K}$ . The particle temperature in the methane-air flame is close to the methane-flame temperature at low particle concentration and slowly decreases with increasing concentration. The particle temperature in the oxygen-enriched mixture, however, has a relatively constant value near  $2600 \text{ K}$ , even at low particle concentration, which is about  $400 \text{ K}$  greater than the methane adiabatic-flame temperature.

### *Burning velocities*

The burning velocities are obtained from photographs of the flame. The contour of the Bunsen cone is traced on a touch-sensitive screen, fitted with a seventh-order polynomial and rotated to obtain the total surface area,  $A$ . The volumetric flow rate,  $\dot{V}$ , is then divided

by  $A$  to obtain the burning velocity,  $S_L$  [15]. The burning velocity as a function of particle concentration is shown in Figs. 5 and 6.

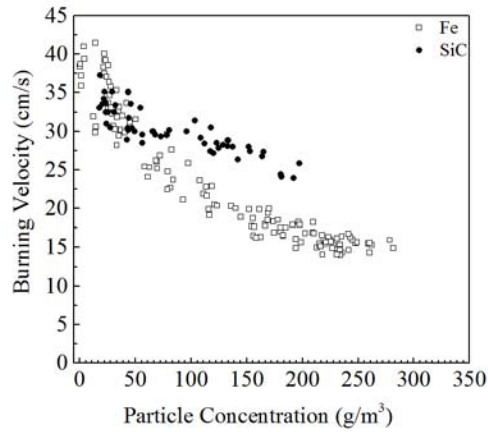


Figure 5. Burning velocities as a function of dust concentration. The gaseous mixture is stoichiometric methane-air.

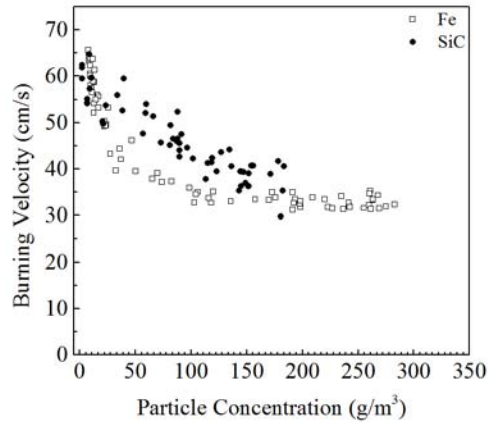


Figure 6. Burning velocities as a function of dust concentration. The gaseous mixture has 5% excess oxygen.

Figure 5 shows the results in air and Fig. 6 shows the result in enriched-oxygen. The results are also compared with the values obtained with silicon carbide particles. The stoichiometric methane-air burning velocity is about 35 cm/s, which agrees with literature values [16]. The burning velocity when calculated with the GRI-30 mechanism [17] in Cantera [18] gives a value 51 cm/s in the excess oxygen case, which agrees with the experimental results.

Silicon carbide particles are used as a heat sink in the methane flame, increasing its effective heat capacity. This decreases the flame temperature and, in turn, decreases the

burning velocity. This trend can be observed in both gaseous environments. In small quantities, iron particles behave in a similar fashion and reduce the burning velocity. In the stoichiometric case, the flame speed appears to plateau at a particle concentration of about  $250 \text{ g/m}^3$ , near the maximum value for which the flame was stable, as discussed below. The plateau appears to occur sooner for the excess-oxygen flame, at a concentration of about  $100 \text{ g/m}^3$ . It is suspected that the steepness of the burning velocity is due to the discrepancy of particle size. The iron particles range from 1 to 3  $\mu\text{m}$  whereas the average SiC particle is 6  $\mu\text{m}$ . This difference in size implies that the SiC particles do not reach thermal equilibrium within the methane reaction zone and thus have a reduced impact on the methane flame, compared to iron, for the same particle loading.

*Stoichiometric methane-air flame: No excess oxygen*

The flame temperatures indicate that the iron burns in a kinetically-controlled regime when introduced into the stoichiometric methane-air flame. The absence of oxygen after the methane flame means that the iron particles must react with the combustion products of methane: water vapor and carbon dioxide. Water molecules diffuse quicker than oxygen molecules yet the reaction rate is most likely slower than with oxygen, which would explain why the chemical reaction rates control the combustion. The particle temperature at low iron concentrations is very close to the adiabatic flame temperature of 2220 K. This does not necessarily imply that the particles burn in a kinetically-controlled regime since the predicted thermodynamic equilibrium iron-air temperature (without methane) is comparable at about 2250 K [11]. In a diffusion-controlled regime, the particle temperature is independent of the particle loading and does not follow the gas-phase temperature. However, as can be seen in Fig. 7, the particle temperature follows the thermodynamic prediction (solid line) for the methane-air mixture including iron particles, further indicating that the particle and bulk gas temperatures are equal and that the particles are reacting in the kinetically-controlled regime.

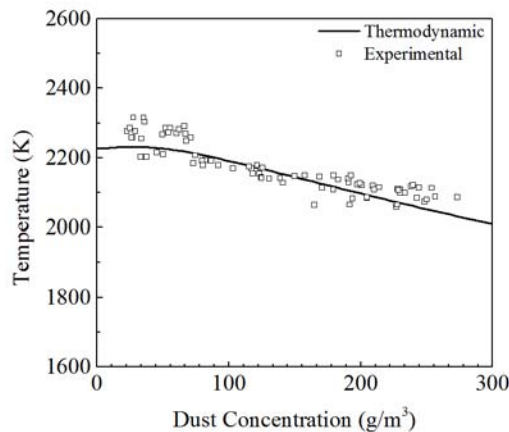


Figure 7. Measured iron-particle temperature and calculated equilibrium temperature for the stoichiometric methane-air case.

Figure 8 shows images of iron-methane-air flames at three different iron concentrations. Depending on the concentration, the stabilized flame has one of three different

appearances. Flame A has a low concentration of about  $80 \text{ g/m}^3$  and only one Bunsen cone is visible. The light observed comes from the blackbody radiation emitted by hot iron particles in the flame. This alone is not a sign of combustion. At these low concentrations, particles will oxidize in the hot environment but neither ignition nor flame front formation is observed. Flame B has an intermediate iron concentration of about  $200 \text{ g/m}^3$  and two distinct Bunsen cones are visible. The thin inner cone is the methane flame and the thick outer one is the iron flame. The two cones are separated by a dark zone, in which there is no flame. After leaving the first flame, the gas expands causing the local iron concentration to decrease, which is why less light is observed in that region. The second cone is the iron flame front, which causes the particles to heat up again and emit more light. This double-front structure happens only above a certain critical concentration, which coincides with the point of the iron flame front formation. This critical concentration, found from the flame speed data and high-speed videos, is situated at around  $200 \text{ g/m}^3$ . The dust flame front is separated from the methane flame front, which means that the particles still absorb heat from the methane reaction zone. However, a leveling off of the burning velocity is observed at this point (see Fig. 5), which implies that enough heat is transferred from the iron flame to the methane flame to compensate for the heat absorbed and the flames must be coupled. Furthermore, a methane flame loaded with a similar concentration of SiC particles quenches, which indicates that the methane flame could not exist at these particle loadings without being supported by the energy released from the iron flame.

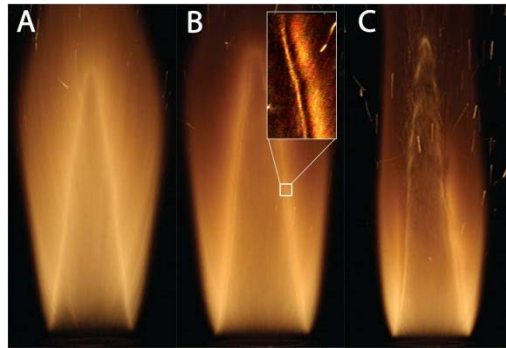


Figure 8. Iron-methane-air flames: (a) Low particle concentration ( $\sim 80 \text{ g/m}^3$ ) showing no iron flame front formation; (b) intermediate particle concentration ( $\sim 150 \text{ g/m}^3$ ) showing a double flame front; (c) high iron concentration ( $\sim 325 \text{ g/m}^3$ ) showing flame instabilities.

Finally, Fig. 8c is taken in the high concentration range of about  $325 \text{ g/m}^3$ . The flame becomes unstable and cellular due to thermo-diffusive instabilities. These instabilities occur when the flame is deficient in the more mobile reactant, changing the Lewis number of the mixture [15]. Increasing the particle concentration will not vary the amount of gaseous reactants since the gas flow rates are unchanged and the particles occupy an insignificant volume compared to the gases. Thus, an increase in particle concentration will not decrease the concentration of oxidizers, the species actually diffusing in the mixture. An increase in particle concentration will increase the overall heat capacity of the mixture,

which in turn affects the heat diffusivity and decreases the Lewis number. When the Lewis number is sufficiently small, the structure becomes cellular [15]. A similar cellular structure has been observed for pure iron flames in microgravity [11].

*Enriched-oxygen-methane Flame: 5% Excess Oxygen*

The experimental results suggest that, with 5% excess oxygen in the methane flame, iron particles ignite and burn in a diffusion-controlled regime. The particle temperature, even at low concentrations, is about 400 K above the methane adiabatic flame temperature. Furthermore, the temperature remains constant across the concentration range, further indication that the particles ignite and that the particle and bulk-gas temperatures separate. The gas-phase temperature cannot be measured directly by emission spectroscopy, but the iron particles can be replaced with inert SiC particles. The temperature results are shown in Fig. 9. As expected, the temperature at low SiC concentrations is close to 2220 K and decreases with an increase in particle loading. This figure also shows equilibrium thermodynamic calculations performed for different iron concentrations. The solid line is the calculation performed for the enriched-oxygen-methane mixture including iron. The measured particle temperature is always above that of the calculated equilibrium temperature of the iron-methane-oxygen mixture.

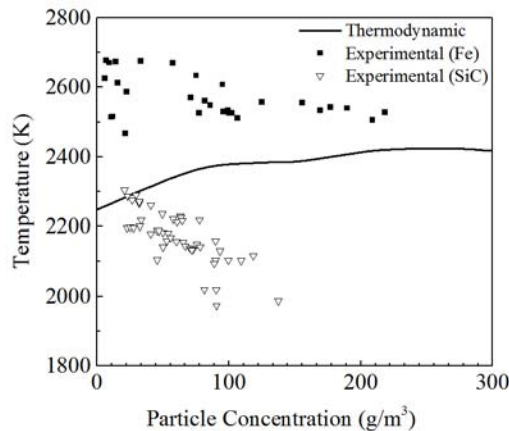


Figure 9. Emission temperature measurements for iron and silicon carbide particles in enriched-oxygen-methane mixture and comparison to thermodynamic equilibrium predictions.

Figure 10 shows two flame images taken at two different concentrations for the enriched oxygen case. Image A has a low iron concentration and only the methane flame is visible. It is also possible to see single iron particles burning, after ignition, including the characteristic micro-explosion at the end of the particle track. The heat required to bring the particle up to the ignition temperature comes from the methane flame and the particles may react with the 5% excess oxygen, in addition to the water vapor and carbon dioxide. Image B is taken at a concentration of about 150 g/m<sup>3</sup>. In this image, only one Bunsen cone is visible in the diffusion regime, which is the coupled combustion front consuming both methane and iron. The formation of the iron flame front coincides with the levelling off of the burning velocity, which occurs at lower concentrations than in the methane-air case.

Furthermore, the formation of the dust flame front is clearly visible in high-speed images and is a distinct phenomenon from a mere increase of igniting particles in the flow.

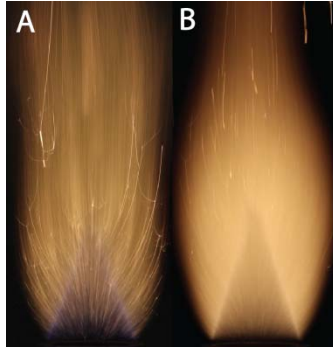


Figure 10. Iron-methane-enriched-oxygen flames: (a) low concentration ( $\sim 25 \text{ g/m}^3$ ) with no dust flame front; (b) high concentration ( $\sim 140 \text{ g/m}^3$ ) with a coupled flame and one visible Bunsen cone.

### *Flame front formation*

These experiments have shown that the formation of a dust flame front in the hydrocarbon-air flame products is independent of the regime of particle combustion and is analogous to what can be observed in a gas phase mixture. A minimum concentration of iron particles is required for the heat-release rate to be sufficient to sustain the propagation of the iron flame. In this respect, single particle models are insufficient to completely describe the observed results, as they ignore the effect of feedback from the reaction of neighboring particles on increasing the local temperature above the methane product temperature. This description of flame front formation applies to any reactive particulate system, whether it is a pure dust cloud [12] or for hybrid mixtures of gaseous and solid fuels [9].

In the kinetically-controlled regime, iron particles at low concentration will oxidize in the flame but the reaction rate will be too slow to form a flame front. The iron flame will form only when there is at least a critical number of iron particles, such that the overall heat released from the dust cloud is sufficient to propagate a flame at a speed that matches the speed of the methane-flame products. For the structure to be stable, the two fronts must be coupled, which can only happen through the exchange of heat between the two reaction zones, which is reflected, among other things, in the leveling off of the flame speed [10]. This situation is illustrated with Fig. 11a, where the two heat release zones are separated from each other and the temperature plateau between reaction zones corresponds to the dark region. This phenomenon has been previously discussed for flames in hybrid mixtures of aluminum and methane in air. This regime has been denoted a *control* regime [19], where the second flame front effectively controls the speed of the first flame, observed by the levelling off of the flame speed. It has also been discussed in the case of binary mixtures of dusts [20].

It is important to distinguish between particle ignition and flame front formation. Particle ignition refers to a specific phenomenon: the particle transitioning from kinetic-oxidation to diffusion-controlled combustion, causing a separation of the particle from the bulk-gas temperature. When introduced into the excess-oxygen flame, iron particles heat up and ignite after an induction time, which depends on the particle size. At low concentrations, this ignition occurs after the methane flame and the particles act merely as heat sinks within

the reaction zone, decreasing the pure gas flame temperature, without contributing to the flame propagation. This is represented by Fig. 11b, where the heat release from the ignited iron particles happens far from the flame and is spread over a large distance, reflecting the range in particle-induction and burn time for the variable particle sizes in the iron powder. As the dust concentration increases, increased heat release from surrounding particles leads to a feedback mechanism, and locally higher temperatures than in the low-concentration case, which causes the particles to ignite closer to the methane flame. At the critical concentration, the heat released by the iron particles will be enough to form a flame front. In such a case, the iron reaction zone is small and must overlap with the methane reaction zone; hence only one flame is visible. This is denoted a *merging* flame regime [19] and is represented by Fig. 11c.

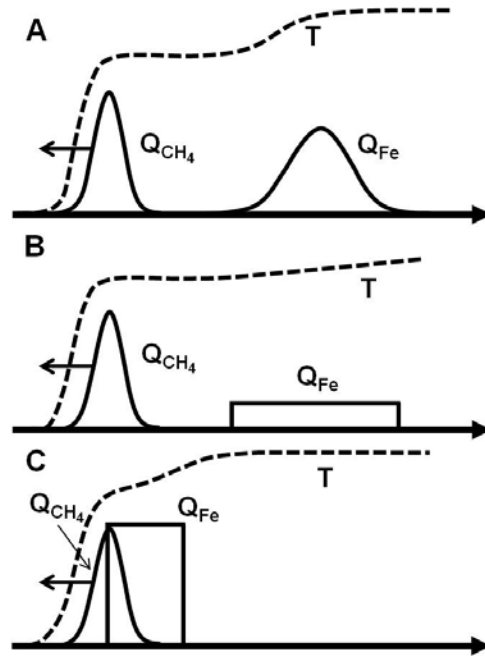


Figure 11. Different combustion regimes observed in this study: (a) kinetic regime with iron flame front; (b) diffusion regime with no flame front; (c) diffusion regime with flame front.

#### 4. CONCLUSIONS

The flame structure of methane-iron-air flames is investigated for particles reacting in the diffusion-controlled or kinetically-controlled regimes through the use of different oxidizing mixtures. In the kinetic regime at low particle concentrations, iron slowly oxidizes in the hot combustion products of methane and an iron flame front only forms above a critical concentration and couples to the methane flame. Finally, at high concentrations, the flame structure exhibits instabilities due to thermo-diffusive effects caused by the increase in the overall heat capacity of the mixture. The second case, with diffusion-controlled particle combustion, where single iron particles ignite in the hot combustion products and burn with a temperature close to their own adiabatic flame temperature, an iron flame front is also seen to form and merge with the leading methane flame above a critical particle concentration. Detailed modeling of the phenomena

observed requires further knowledge of high-temperature iron kinetics with oxygen, water and carbon dioxide. These rates are currently unknown and determination of these reaction rates should be the focus of future studies.

These results demonstrate that it is possible to form a stabilized flame front in a reactive-particle suspension whether the particles are reacting in a kinetically-controlled or diffusion-controlled regime or, likely, even in a regime where both kinetics and diffusion play equal roles. For a flame front to form, the rate of heat release by the particles must be sufficient to stabilize the reaction wave within the dust suspension, which requires that the resulting flame speed of the metal front in the local oxidizing environment be equal to the local flow velocity. These metal-hydrocarbon-air flames provide a relatively clean and simple system in which to study the stability and physics of multi-front reactive waves.

## 5. REFERENCES

- [1] B.A. Khasainov, B. Veyssiere, *Shock Waves* 6 (1) (1996) 9-15.
- [2] F. Zhang, *J. Propul. Power* 22 (6) (2006) 1289-1309.
- [3] A.G. Merzhanov, in: Z.A. Munir, J.B. Holt (Eds.), *Combustion and Plasma Synthesis of High-Temperature Materials*. 1990, VCH. p. 1-53.
- [4] R.L. Geisler, R.A. Frederick, M. Giarra, in: *Encyclopedia of Aerospace Engineering*. 2010, John Wiley & Sons, Ltd.
- [5] R.P.T. Ellis, P. Hejzlar, G. Zimmerman, D. McAlees, C. Whitmer, J.H. Touran, K. Weaver, J. C. Walter, J. McWhirter, C. Ahlfeld, T. Burke, R.H. Odedra, J. Gilleland, Y. Ishikawa, L. Wood, N. Myhrvold, W. H. Gates, *Traveling-Wave Reactors: A Truly Sustainable and Full-Scale Resource for Global Energy Needs*, International Congress on Advances in Nuclear Power Plants 2010, San Diego, CA, 2010
- [6] B. Khaikin, A. Filonenko, S. Khudyaev, *Combust., Explos. Shock Waves* 4 (4) (1968) 343-348.
- [7] S. Goroshin, M. Bidabadi, J.H.S. Lee, *Combust. Flame* 105 (1-2) (1996) 147-160.
- [8] M.C. Branch, M.E. Sadequ, A.A. Alfarayedhi, P.J. Van Tiggelen, *Combust. Flame* 83 (3-4) (1991) 228-239.
- [9] M. Soo, P. Julien, S. Goroshin, J.M. Bergthorson, D.L. Frost, *Proc. Combust. Inst.* 34 (2) (2013) 2213-2220.
- [10] P. Julien, M. Soo, S. Goroshin, D.L. Frost, J.M. Bergthorson, N. Glumac, F. Zhang, *J. Propul. Power*, *in press*
- [11] F.-D. Tang, S. Goroshin, A.J. Higgins, *Proc. Combust. Inst.* 33 (2) (2011) 1975-1982.
- [12] S. Goroshin, I. Fomenko, J.H.S. Lee, *Proc. Combust. Inst.* 26 (2) (1996) 1961-1967.
- [13] S. Goroshin, J. Mamen, A. Higgins, T. Bazyn, N. Glumac, H. Krier, *Proc. Combust. Inst.* 31 (2) (2007) 2011-2019.
- [14] J.B. West, H.P. Broida, *J. Chem. Phys.* 62 (7) (1975) 2566-2574.
- [15] C.K. Law, *Combustion Physics*, Cambridge University Press, New York, 2006
- [16] B. Lewis, G. Von Elbe, *Combustion, Flames and Explosions of Gases*, Vol. 3. Cambridge University Press, 1961
- [17] G.P. Smith, D.M. Golden, M. Frenklach, N.W. Moriarty, B. Eiteneer, M. Goldenberg, C.T. Bowman, R.K. Hanson, S. Song, W.C. Gardiner, V.V. Lissianski, Z. Qin, available at <[http://www.me.berkeley.edu/gri\\_mech/](http://www.me.berkeley.edu/gri_mech/)>
- [18] D.G. Goodwin, An open-source, extensible software suite for CVD process simulation, in: *Proceedings of CVD XVI and EuroCVD Fourteen*. 2003. p. 155-162
- [19] I. Zeldovich, G.I. Barenblatt, V. Librovich, G. Makhviladze, *Mathematical theory of combustion and explosions*, Consultants Bureau, New York, 1985
- [20] S. Goroshin, M. Kolbe, J.H.S. Lee, *Proc. Combust. Inst.* 28 (2) (2000) 2811-2817.

## **Chapter 3. Freely-propagating, hybrid flames of aluminum and methane in balloons**

### **1. INTRODUCTION**

Hybrid mixtures of combustible dust and gas-phase fuel pose a serious risk of accidental explosions in many industrial settings [1]. Examples of such hybrid mixtures include pulverized coal and methane in coal mines [2], pharmaceutical dust and solvent vapors [3], organic dust with fermentation gases [4], paint pigments and solvents [5], plastic powders and solvents [6] or even metal particles with hydrogen, natural gas or other vapors in various industries [7-9]. In addition to the dangers they present in industrial settings, hybrid mixtures of metal particles and energetic materials are frequently encountered in condensed high explosives [10], fuel-air explosives [11], propellants [12], slurry fuels [13] and synthesis of nano-scale oxides [14]. Aluminum is the most widely used additive in these energetic materials due to its high energy density and capacity to burn in water vapor and carbon dioxide, the main combustion products of high explosives and hydrocarbon fuels.

Plastic dust particles, unlike metal particles, have low melting and boiling temperatures compared to hydrocarbon flame temperatures, hence evaporation of the particles occurs in the flame pre-heat zone and the plastic fuel vapor mixes with the surrounding oxidizers [15], similar to droplet combustion [16]. Organic dusts and coal particles will significantly volatilize in the flame pre-heat zone, while the solid residue will burn heterogeneously [17]. Since plastic and organic dusts are competing for the same oxidizers as hydrocarbons, the addition of these dusts has little effect on the severity of explosions and energy content of fuel-rich hydrocarbon mixtures [18].

Conversely, metals have much higher melting and boiling temperatures relative to their flame temperature, and the fast kinetic reaction rates of metal vapors with oxidizers prevents the accumulation of metal vapors such that they must burn in a heterogeneous mode [19-20]. Metals can also react with the products of hydrocarbon flames, including steam and carbon dioxide, possibly allowing them to enhance the burning of hybrid metal-hydrocarbon mixtures. Recent studies [21-23] with aluminum-methane-air and iron-methane-air hybrid mixtures using a modified Bunsen dust burner found that the solid fuel particles did not react at low metal mass loadings and acted solely as heat sinks, which resulted in lower methane flame temperatures and, thus, flame speeds. Above a certain critical metal concentration, however, the particles reacted by forming a flame front which coupled to the hydrocarbon flame. A study by Palecka et al. [24] on quenching distances in hybrid mixtures of aluminum and methane confirmed that aluminum behaved like inert particles at low metal loadings and that a critical concentration is required for the formation of the metal flame front. The Bunsen burner experimental configuration can only accommodate stabilized flames, such that only the presence or absence of a metal front can be observed, which is not entirely representative of the transient phenomena in freely-propagating flames that can occur in accidental explosions [25].

Other experimental efforts have investigated freely-propagating flames in hybrid mixtures of hydrogen-air with aluminum, tungsten or carbon dust in a 20 L constant volume

combustion bombs [7-9]. The experiments showed that, at low hydrogen concentrations (i.e., low flame temperatures), the dust did not react and only the hydrogen flame propagated. When the hydrogen concentration was increased, the pressure traces showed two distinct peaks, indicating the formation and propagation of a solid-fuel flame behind the hydrogen flame. While the results from the combustion bomb experiments provide insight into the different combustion regimes possible in these hybrid mixtures, the pressure traces only provide information about the flame when it arrives at the wall of the vessel, and thus any unsteady propagation within the vessel cannot be detected.

The present experimental work introduces an experimental method in which the transient history of the freely propagating flame in hybrid mixtures is observed visually. Clear latex balloons are used to contain aluminum-methane-oxidizer mixtures, providing an isobaric combustion environment to study spherically-expanding, freely-propagating flames. High-speed cameras are used to record the dust dispersal and flame propagation processes within the balloon. Mixtures with and without excess oxygen in the methane flame combustion products are studied. Results for mixtures without excess oxygen in the methane flame products are found to be consistent with previous studies on the Bunsen burner, while a specific transient phenomenon is also observed for mixtures with excess oxygen.

## 2. EXPERIMENTAL APPARATUS

Experiments are performed in transparent latex balloons measuring approximately 30 cm in diameter. The balloon is initially inflated without dust with a specific gas mixture. The dust is then dispersed within the balloon by a 0.8 s pulsed flow of the same gaseous mixture. There is a 4 s delay between the beginning of the dust dispersal process and ignition to allow turbulence within the balloon to decay. The mixture is ignited by a capacitor discharging through a tungsten wire located at the center of the balloon. As the flame propagates outward, the balloon expands, maintaining an approximately isobaric combustion environment, and bursts when the flame reaches the balloon surface. Figure 1 shows a picture of the apparatus along with several still frames showing the dust dispersal and flame propagation within the balloon. The aluminum powder used is Ampal 637 (Ampal, NJ), with a Sauter mean diameter of about 6.5 microns. The same batch of Ampal 637 has been used in all of our previous experiments with dust and hybrid mixtures [21,22,24]. Scanning electron micrographs of the powder samples and particle size distribution can be found in [21], [22] and [26]. Detailed schematics of the apparatus is given in [26] and [27].

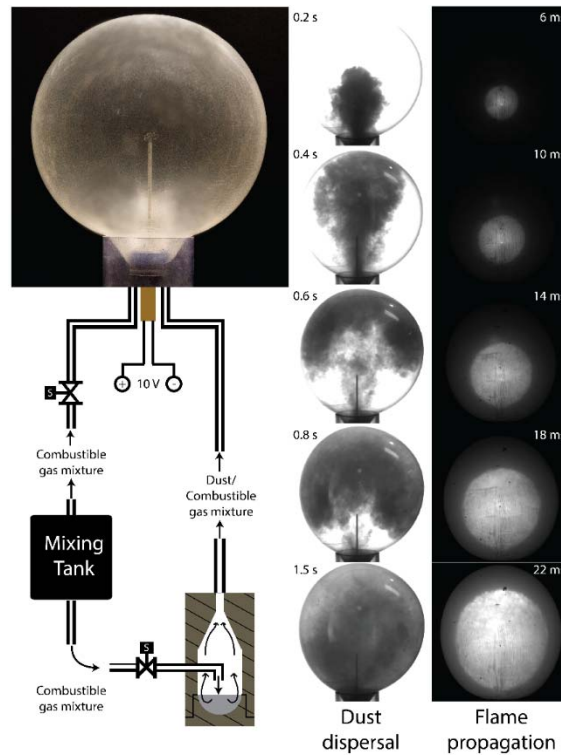


Figure 1: The left side of the figure shows the experimental apparatus with an actual picture of the balloon inflated with only the combustible gas mixture before dust dispersion on top with a schematic of the key components below. The right side of the figure shows both the dust dispersion and flame propagation processes.

### *Gas Mixtures*

In the present work, three different gas mixtures are studied. The first gas mixture is methane-air with an equivalence ratio of 1.1, meaning there is no excess oxygen in the post-methane flame zone (0% excess  $O_2$ ). The next two gas mixtures have varying amount of excess oxygen. In these mixtures, different amounts of nitrogen in the air is replaced with oxygen while keeping the methane concentration constant. Consequently, all of the mixtures to have the same flame temperature and thermal diffusivity which allows us to isolate the effect of oxygen concentration. Simply changing the equivalence ratio of the methane-air mixture to increase the excess oxygen would result in a lower flame temperature, making comparison between the mixtures difficult to interpret. The first mixture with excess oxygen is an oxidizing mixture of 26% oxygen/74% nitrogen and methane with an equivalence ratio of 0.8 (5% excess oxygen). The third is an oxidizing mixture of 30% oxygen/70% nitrogen and methane with an equivalence ratio of 0.7 (8% excess oxygen).

### *Dust concentration and flame speed measurements*

An initial estimation of the dust concentration is found by dividing the initial mass of aluminum in the dispersion unit by the volume of the balloon. This value is then corrected to find actual dust concentration in suspension at the time of ignition by using data from a light attenuation probe obtained in previous dispersion experiments [27]. In the

previous work, a known amount of aluminum dust was dispersed within an acrylic sphere of a known volume. Use a laser-light attenuation probe which had previously been calibrated for this powder [], a relationship between the mass placed in the powder dispersion unit and the actual concentration of aluminum powder in suspension at was determined. It was found that actual aluminum concentration in suspension is about 40 % less than the initial estimate due to particles depositing on the surface of the balloon or settling before the mixture is ignited.

The flame propagation is recorded at 5,000–7,500 frames per second using a Photron SA-5 video camera. The position of the flame front is tracked in every frame by fitting the front contour to an ellipse. The radius of the flame is taken to be the average distance from the flame contour to the center-of-mass of the ellipse. To obtain the flame speed, the radius-time data are interpolated by the first-order polynomial and the speed is taken as the derivative. The data are also fit to a second-order polynomial, and the acceleration is taken as the second derivative of the expression. The flames are analyzed over an approximate radial range of 3 cm to 10 cm.

### 3. RESULTS AND DISCUSSION

#### *Flame propagation within the balloon*

Figure 2 shows examples of radius-time flame trajectories measured experimentally. The markers denote the measured experimental values, and the lines are second-order polynomial fits to the data. Two distinct types of the flame propagations events are observed. In some cases, the flames propagate with a constant speed throughout the balloon, whereas in other cases, the flame speed increases during the observed propagation.

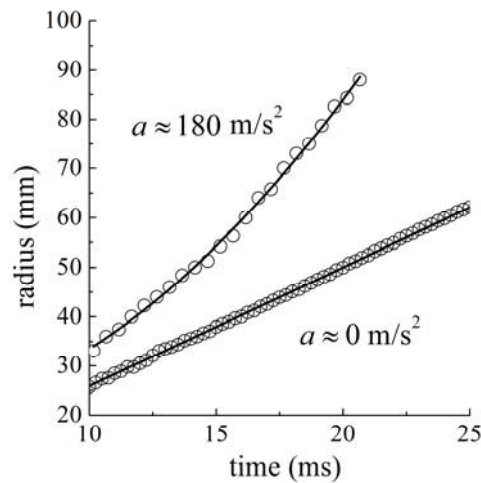


Figure 2: Radius-time flame trajectories illustrating both steady ( $a \approx 0$ ) and unsteady ( $a > 0$ ) propagation.

#### *Effect of Excess Oxygen on Flame Topology at Low Concentrations*

The effect of oxygen concentration on the flame surface is investigated using the high speed videos filming the flame propagation. Using a home-made Matlab script, the

high speed videos can be manipulated for mixtures at low concentrations to analyze the surface of the flame. The light scattering nature of dust suspensions make it impossible to make any claims about the surface of the flames at high concentrations; however, at low concentrations, the particles help illuminate the flame front in the current experimental set-up. By subtracting subsequent flames in Matlab, changes in the flame's surface during its propagation can be identified. Figure 3 shows sample images for this technique for the gas mixtures 0% excess oxygen and with 8% excess oxygen both with aluminum concentrations of about  $15 \text{ g/m}^3$ .

In the case where there is no excess oxygen, the flame surface remains relatively smooth during its propagation. A few large cells can be seen, most likely from some residual turbulence in the flow at the time of ignition; however, the cells do not appear to grow much during the observed propagation. In contrast, the flame in the mixture with 8% excess oxygen has a very clearly wrinkled surface during the majority of its propagation within the balloon. Similar results not shown here were found with the 5% excess oxygen case. Furthermore, these results were also seen (for both no excess oxygen and excess oxygen cases) when aluminum was replaced with inert alumina, indicating that the surface instabilities are related to the excess oxygen in the mixture.

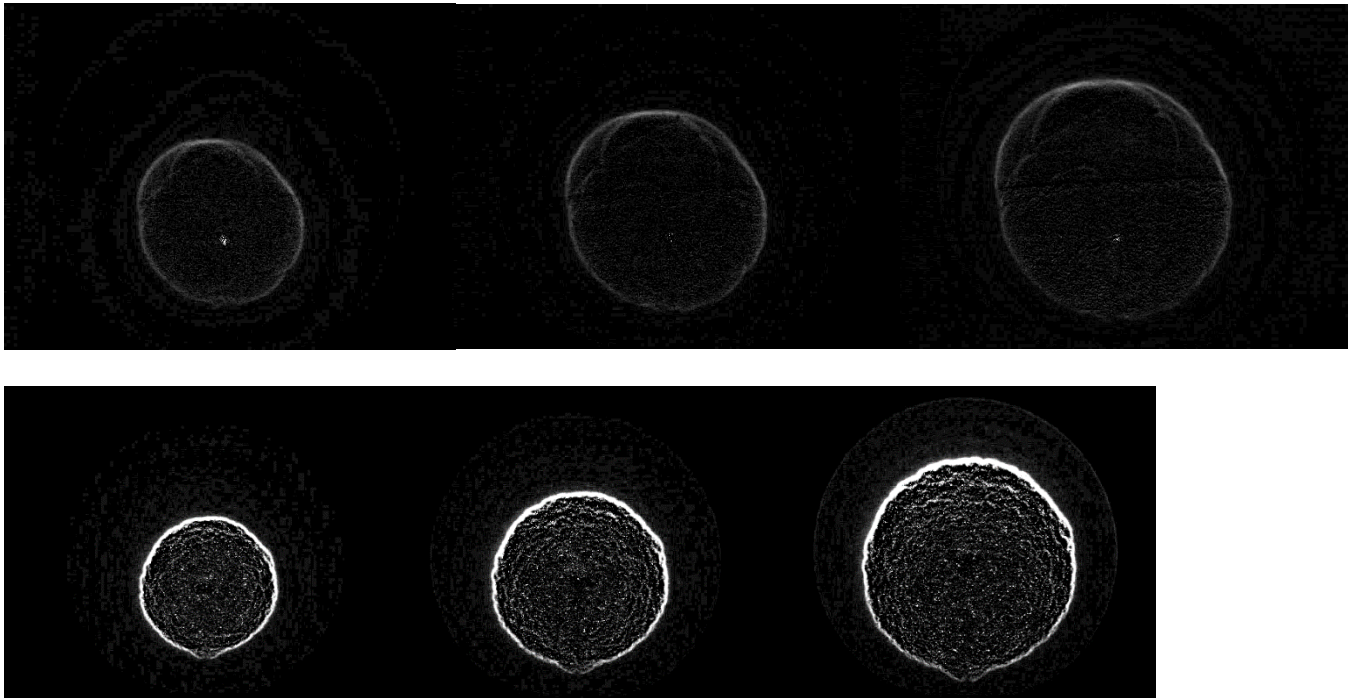


Figure 3: The top sequence of images shows the flame surface in the gas mixtures with no excess oxygen. The bottom sequence of images shows the flame surface for gas mixture with 8% excess oxygen. Both mixtures have aluminum concentrations of approximately  $15 \text{ g/m}^3$ .

### *The Effect Excess Oxygen and Dust Concentration on Flame Acceleration*

In this section, the acceleration of the the flames is analyzed. The rate of acceleration is determined by fitting a second order polynomial to the radius vs time data and taking acceleration as the second derivative, as discussed above. In order to isolate of the effect of aluminum particles burning, experiments were also conducted with inert alumina ( $\text{Al}_2\text{O}_3$ ) powder to serve as a benchmark for comparison. Figure 4 shows the acceleration vs dust concentration for all three gas mixtures for both inert alumina and aluminum powder (note: different y-axis scales\*). From the plots, it can be seen that mixtures without any excess oxygen for both alumina and aluminum powders have very small values of acceleration, indicating that the flames are propagating at a constant velocity within the balloon. The flames in mixtures with excess oxygen are accelerating during their propagating for both aluminum and alumina. For the inert alumina case, the flames appear to be accelerating the most at low concentrations; however, as more alumina is added, the rate of acceleration decreases. With aluminum powder, the acceleration values are similar to the alumina case at low concentrations with values around  $75\text{-}125\text{ m/s}^2$ . In contrast to the alumina case, the rate of acceleration increases as more aluminum is added. Peak acceleration values appear at  $100\text{-}150\text{ g/m}^3$  and  $150\text{-}200\text{ g/m}^3$  for the 8% and 5% excess oxygen cases, respectively, before decreasing with additional aluminum concentration.

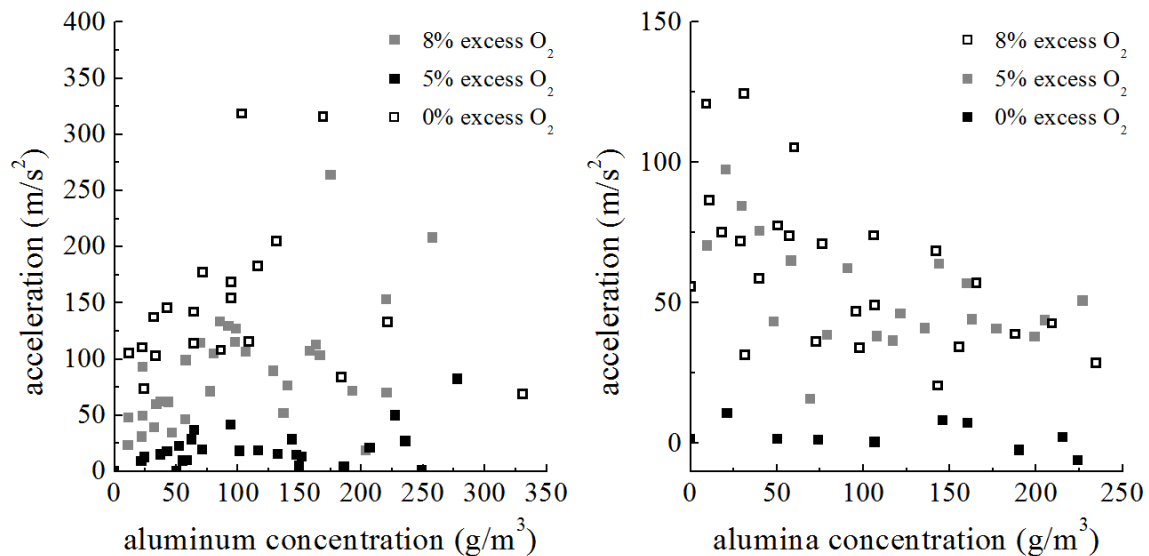


Figure 4: Acceleration vs dust concentration for a) alumina (left) and b) aluminum (right) powders in different gaseous mixtures.

### *Effect of dust concentration on flame propagation speed*

The effect of dust concentration on the flame propagation speed is analyzed in this section. Figure 4 shows the flame speed vs concentration again for both alumina and aluminum powders. For the accelerating flames, a first-order polynomial is fit to the radius vs. time data, and the flame speed is taken as the slope. Since the flame is accelerating, the linear fit to the data, denoted as average flame speed, does not represent an actual flame

speed, but instead is indicative of the total time of the event within the balloon, with higher average flame speeds corresponding to shorter event times. The dashed lines on the graph represent the theoretical flame speeds calculated using the equilibrium software Cantera []. The effect of dust concentration is modelled simply by increasing the heat capacity of the inert gas (i.e.  $N_2$ ) in the mixture by amount proportional to the dust concentration. By this method, the dash lines represent how the flame is expected to behave if the powder is non-reactive. These theoretical flame speeds decrease with dust concentration since the increased heat capacity decreases the flame temperature, and thus its propagation speed.

The results for the alumina powder show that the flame speeds decrease with alumina concentration. The mixtures with 0% excess oxygen which propagate at a constant velocity show good agreement with the line predicted by Cantera. For the mixtures with 5% and 8% excess oxygen which were previously shown to be accelerating, the average flame speeds generally lie slightly above the line predicted by Cantera but still follow the general trend.

The results for the mixtures with aluminum show different trends depending on whether or not there is excess oxygen in the post-methane flame zone. When there is no excess oxygen, the flame speed initially *decreases* with increasing aluminum concentrations, following the dashed line. At a critical concentration of about  $100\text{ g/m}^3$ , the flame speed breaks from the dashed line and remains constant with increasing aluminum concentration. When there is excess oxygen, the flame speed initially *increases* with increasing aluminum concentration before also reaching a plateau in flame speed. The plateau occurs at lower aluminum concentrations for larger amounts of excess oxygen in the mixture. The increase of flame speed with aluminum concentration (i.e., the slope of the flame speed vs. aluminum concentration) is proportional to the excess oxygen in the mixture.

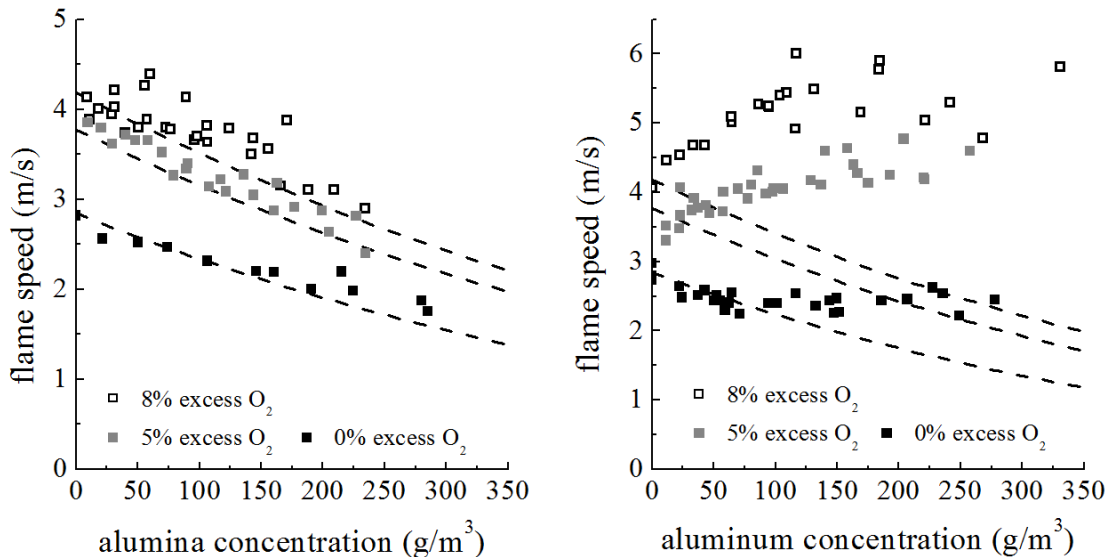


Figure 5: Flame speed measurements for A) inert alumina powder (left) and B) aluminum powder (right) in different gaseous mixtures

### *Discussion*

The present experimental configuration presents many advantages over combustion bombs for the study of spherically-expanding, freely-propagating flames. The transparent latex balloon expands along with the flame propagation, producing isobaric conditions during the entire event, while also providing full visual access that allows the assessment of the uniformity of the dust dispersion and flame symmetry. The experimental set-up also allows for the dust concentration measurements to be calibrated, accounting for the loss of powder to the balloon walls and settling, to increase the accuracy of the concentration measurements. The transient flame can be imaged from soon after ignition until the balloon bursts, which allows for a long event and imaging time in comparison to dust bombs where the pressure rise is only observed when the flame arrives close to the walls of the vessel and therefore cannot detect any transient or unsteady behavior which may occur during the flame's propagation.

Due to the optical thickness of the dispersed dust cloud, it is only possible to observe the leading flame front. Hot particles will emit blackbody radiation and, thus, light emission from the particles cannot be used as a marker for metal combustion. The igniter in this work is chosen to be only energetic enough to ignite the methane mixture and fails to ignite a pure aluminum cloud. Consequently, the leading front is always initially a methane flame, which is supported by the spherical shape of the initial flame, a geometry that is difficult to obtain in a pure aluminum dust cloud [27]. As the results demonstrate, both inert alumina and potentially reactive aluminum particles can affect the flame propagating in different ways, depending on both dust and excess oxygen concentrations.

### *No excess oxygen – Stable flame propagation*

As can be seen in Fig. 4b, the flame speed of the leading front in fuel-rich methane-air mixtures initially decreases with an increase in aluminum concentration, a behavior also observed when methane flames are seeded with inert alumina particles (Fig. 4a). When the aluminum concentration reaches approximately  $100 \text{ g/m}^3$ , the behavior diverges from the one predicted for inert particles, represented by the dashed lines in Fig. 4, and the flame speed remains constant with an increase in aluminum concentration.

The behavior has been observed previously in experiments also performed at McGill on a modified Bunsen burner with hybrid aluminum-methane-oxidizer flames. In the experiment, the methane-oxidizer Bunsen flame was seeded with increasing amounts of aluminum powder. At low concentrations, the aluminum acted only as a heat sink, decreasing the flame temperature and reducing the burning velocity of the methane flame. At a critical concentration, an aluminum flame front formed and coupled to the methane flame. After the formation of the aluminum flame front, the burning velocity of the coupled flame remained approximately constant with increasing aluminum concentration. Upon coupling, heat from the aluminum flame diffuses upstream and increases the temperature of the methane flame, compensating for the increased heat capacity from the aluminum in suspension. This allows the flame to propagate at a higher speed than it would if the aluminum was inert.

A follow up investigation studied hybrid iron-methane-oxidizer flames and found the same flame coupling behavior past a critical concentration of iron in the flow.

Furthermore, the behavior was also observed while studying similar hybrid aluminum-methane-oxidizer mixtures propagating in tubes []. At low concentrations only a methane flame would propagate; however, after a critical concentration, an aluminum flame front would form, and the coupled aluminum-methane flame would propagate down the tube.

Although the second aluminum flame front cannot be directly observed in the balloon configuration, the results clearly suggest its existence above a critical concentration. The present findings indicate that this flame coupling is not unique to the geometric configuration of a Bunsen burner or propagating in tubes, but is an intrinsic phenomenon associated with flames propagating in hybrid metal-hydrocarbon mixtures.

### *Excess Oxygen*

The hybrid aluminum-methane-oxidizer mixtures with excess oxygen show a generally different behavior than the mixtures without excess oxygen. From Fig. 5b, the average flame speeds in mixtures with excess oxygen increase with increasing aluminum concentration for relatively low (0-100 g/m<sup>3</sup>) aluminum concentrations, which is in direct contrast to the mixtures without excess oxygen where the flame speed initially decreases with increasing aluminum concentration in this concentration range. Furthermore, Fig. 4b shows that the flames in mixtures with excess oxygen accelerate during their propagation, which is also starkly different from the flames in mixtures without excess oxygen which propagate at a constant speed.

### *Flame Instabilities and Acceleration at Low Dust Concentrations*

Fig. 4 shows average acceleration of the flames during their propagation, and the mixtures with excess oxygen are clearly accelerating compared to the mixtures without excess oxygen, regardless of the powders used. Although the rate of acceleration increases with aluminum concentration and decreases with inert alumina concentration, there are similar and quite significant rates of acceleration at very low concentrations (<15 g/m<sup>3</sup>) with both powders, indicating that the acceleration at these low concentrations is controlled primarily by instabilities in the methane flame.

Figure 3 shows images of the flame surfaces in mixtures with and without excess oxygen. For mixtures without excess oxygen, the flame surface remains smooth during its propagation, but in mixtures with excess oxygen, the flame surface is clearly cellular. The formation and growth of these cells increases the surface area of the flame available for reactions, which allows the flame to propagate at a faster speed than if the flame remained smooth. As the cells grow, the surface area further increases, causing the flame to accelerate.

Whether or not the observed flame becomes cellular depends several factors which can act to either stabilize or de-stabilize the flame. The work of Darrius [] and Landau showed that all propagating flames were hydro-dynamically unstable due to the density discontinuity across the flame, and perturbations of all wavelengths had positive growth rates. A positive growth rate, however, is not enough to observe these instabilities. The growth rate must be greater than the stabilizing effects on the flame.

For a spherically-expanding flames, stretch is the most dominant stabilizing effect. If the stretch rate is greater than the disturbance growth rate, then the flame is growing faster than the instability, and the flame surface will remain smooth. The stretch rate for spherically-expanding flames is  $K = \frac{2}{R} \frac{dR}{dt}$ . Stretch dominates when the flame is small, damping the growth of most instabilities, but at some critical radius, the growth rate of the disturbances over takes the stretch rate, and the flame becomes unstable. Consequently, large-scale facilities are typically used to study instabilities.

In their initial analysis, Darrius and Landau assumed an infinitely thin flame, and their work predicted that the growth rate of instabilities would go to infinity as the size of the disturbance approached zero; however, more recent studies have shown that disturbances with wavelengths on the same of magnitude or smaller than the flame thickness are damped out by the system. Nevertheless, flame thickness plays an important role in the onset of instabilities, with thinner flames resulting the appearance of cells at a smaller critical radius. Some researchers have taken advantage of this and use high-pressure systems to study this instability at smaller scales. The high pressure reduces the flame thickness, allowing for earlier onset of instabilities.

Thermo-diffusive imbalances can also act to stabilize or destabilize the flame. An apartment parameter for assessing thermo-diffusive stability is the Lewis number, defined as:  $Le = \frac{\alpha}{D}$  where  $\alpha$  is the thermal diffusivity of the mixture and  $D$  is the mass diffusivity of the limiting reactant. When the Lewis number is less than unity, the deficient reactant can diffuse towards the flame at a faster rate than the heat is diffusing away, which promotes the growth of cells. Conversely, when the Lewis number is greater than one, the growth of cells damped.

Betchold and Matalon combined all of these effects and found the critical radius for the onset of instabilities depends on:  $R_{cr} \sim \delta_T E_a \frac{Le - Le^*}{\sigma^2}$  where  $\delta_T$  is the flame thickness,  $E_a$  is the activation energy of the reaction,  $Le$  is the Lewis number of the mixture,  $Le^*$  is a critical Lewis number at which cells appear from ignition, and  $\sigma$  is the expansion ratio across the flame []. In the current experimental investigation, the expansion ratios and the activation energies between the different gas mixtures are the same; however, the flame thickness and Lewis number are affected.

The critical radius for onset of instabilities in methane-air flames is found to be around  $R_{cr} \approx 25$  cm, which is consistent with our results which showed the slightly fuel-rich methane-air flame to be smooth and stable in our radial viewing range of approximately  $3 < R < 10$  cm. In the excess oxygen mixtures, when oxygen replaces nitrogen in the mixture, the increased oxygen concentration at the same flame temperature increases the reaction rates. Since the flame thickness scales with the reaction rate by  $\delta_T \sim \frac{1}{\sqrt{\dot{\omega}}}$  where  $\dot{\omega}$  is the reaction rate, faster reaction rates lead to thinner flames and reduce the critical radius at which cells appear. Furthermore, when the mixtures go from slightly fuel-rich (0% excess oxygen) to fuel-lean, the limiting reactant changes from oxygen, which is slightly heavier than the average molecular weight of the mixture, to methane,

which is slightly lighter than the average molecular weight of the mixture. Consequently, the Lewis number changes from greater than unity to less than unity. The combined effects of reduced flame thickness and Lewis number less than unity in the mixtures with excess oxygen result accelerating cellular flames.

#### Effect Inert Dust Concentration

As inert alumina is added to the flames, the average flame speed and the rate of acceleration decrease. Once the flames become cellular, the growth of the flames are typically assumed to grow in a self-similar manner according to the expression:  $R = R_{cr} + At^\alpha$ .  $\alpha$  is related to the growth rate of the cells with a higher  $\alpha$  indicating larger amplitude of cells.  $A$  is related expansion ratio and burning velocity. If the flame were stable, then  $\alpha = 1$ , and  $R = R_{cr} + At^\alpha = At = \sigma S_L t$  where  $\sigma$  is the expansion ratio across the flame and  $S_L$  is the laminar burning velocity. Therefore,  $A \sim \sigma S_L$ . In the present work, the constants  $R_{cr}$ ,  $A$ , and  $\alpha$  are found using matlab least squares fit to the data.  $R_{cr}$  was found to be consistently at or below the smallest observable flame. The results for  $A$  and  $\alpha$  are shown in Fig.

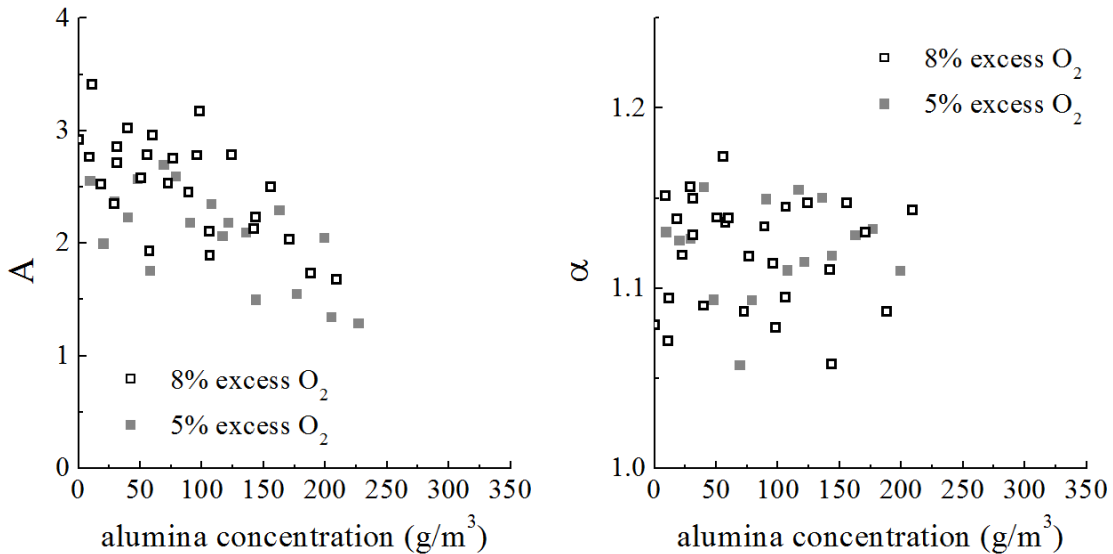


Figure 6: Values of  $\alpha$  and  $A$  found by fitting the radius vs time data to the equation:

$$R = R_{cr} + At^\alpha$$

The results show that  $\alpha$  remains approximately constant, indicating that the flame is still cellular and growing with similar cellular characteristics. However,  $A$  decreases as more inert alumina is added. This is to be expected since addition of inert alumina increases the heat capacity of the mixture which decreases both the expansion ratio,  $\sigma$ , and the burning velocity,  $S_L$ . This increased heat capacity effect results in both lower flame speeds and lower rates of acceleration.

### *Effect of Aluminum Concentration Low concentrations*

As aluminum is added to the mixtures, the average flame speeds and the rates of acceleration increase, which is in contrast to the above results where both of those quantities decreased with the addition of inert alumina. This means that the aluminum must be reacting in order to contribute to the methane flame propagation, even at small concentrations.

There are two ways the aluminum can influence the flame propagation. The first way, as discussed above, is for an aluminum flame front to form and couple to the methane flame. When the flames are coupled, the pre-heat zone of the aluminum flame overlaps with the reaction zone of the methane flame, increasing the temperature of the methane flame and thus the burning velocity of the methane flame. This explanation, however, is unlikely for very small concentrations of aluminum where the collective heating effects are small.

The second way is for aluminum to react at some distance behind the methane flame. In this case, the heat released by the reacting aluminum does not increase the temperature of the methane flame, but instead causes the gases behind the methane flame to expand and push on the flame. For spherically-expanding flames, the observed flame is  $S_F = \sigma S_L$  where  $\sigma$  is the expansion ratio across the flame and  $S_L$  is the laminar burning velocity. Therefore, aluminum reacting at some distance behind the methane flame can increase the volumetrically averaged expansion ratio across the flame:  $\sigma_{avg} = \frac{R_{Al}^3 T_{Al} + (R_{CH_4} - R_{Al})^3 T_{CH_4}}{R_{CH_4}^3 T_u}$  where  $R_{Al}$  is the radius of the aluminum reaction,  $T_{Al}$  is the temperature after the aluminum reaction,  $R_{CH_4}$  is the radius of the leading methane flame,  $T_{CH_4}$  is the temperature of the methane flame, and  $T_u$  is the temperature of the unburned mixture.

If aluminum reacts at some constant distance behind the methane flame,  $\sigma_{avg}$  will be changing in time; as the flame propagates, a larger portion of the post flame zone will be at the aluminum flame temperature. This explains both the acceleration and increase of flame speed at low concentrations. This also explains the continuing increase in flame speed and acceleration with aluminum concentration. As more aluminum is added, the temperature of the aluminum reaction increases which leads to higher  $\sigma_{avg}$  at any given time during the propagation which increases the average flame speed. Furthermore, an increase in the aluminum flame temperature increases the difference in temperature between the methane and aluminum reaction zones, leading to higher rates of acceleration.

### *High Concentrations*

At high concentrations of aluminum, the flame speed reaches a plateau with increasing aluminum concentration, and the acceleration decreases. Based on the observed plateau in flame speed and findings from previous experimental investigations, it is logical to conclude that the flames are coupled in this region. When the flames are coupled, the expansion ratio across the flame does not change with time, resulting in lower rates of acceleration. The rates of acceleration, however, do not go to zero in the plateau region. This is most likely due to the fact that the coupled flame is still cellular.

Similar to what was done before for alumina, the data for the mixtures with aluminum was fit to the function  $R = R_{cr} + At^\alpha$ . As discussed above,  $\alpha$  is related to the growth rate of cells, and  $A$  is related to the expansion ratio. In this formulation,  $A$  is considered be a constant, so any transient behavior of the expansion will result in larger  $\alpha$ . Therefor, the results for low concentrations ( $<150 \text{ g/m}^3$ ) do not have any physical meaning. The results do provide some important insight. At high concentrations (where the flames are believed to be coupled), the value of  $\alpha$  drops to near its value for very low concentrations. This indicates that the cellular structure on the flame surface still causes the flame to accelerate even after it is coupled.

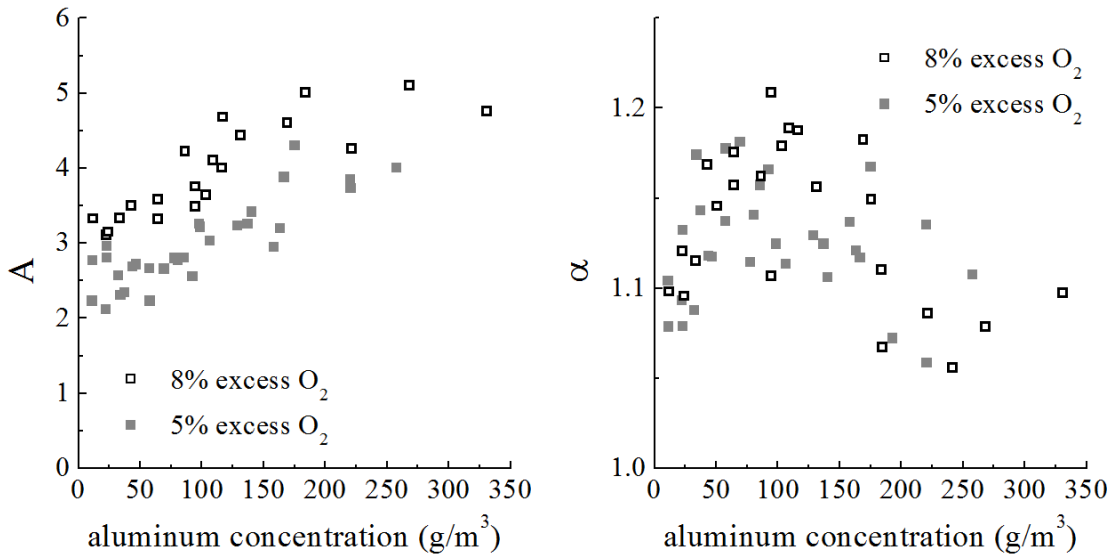


Figure 7: Values of  $\alpha$  and  $A$  found by fitting the radius vs time data to the equation:  

$$R = R_{cr} + At^\alpha$$

#### Moderate Concentrations

At concentrations near where the plateau in flame speed occurs (100-175  $\text{g/m}^3$ ), there is also a spike in acceleration for a few cases. This may be due to a *transient coupling* phenomenon. In the previous cases, the aluminum either burned at some distance behind the methane flame, or the aluminum and methane flames were coupled from the outset of the flame propagation. At concentrations near where the flames become coupled, the aluminum reaction front may form at some distance behind the methane flame and then catch up to and couple to the methane flame during the observed flame propagation. As the aluminum front approaches, the average expansion ratio,  $\sigma_{avg}$ , across the flame will rapidly increase, causing large acceleration rates.

Figure 8 shows schematics of the different interactions between the aluminum and methane.

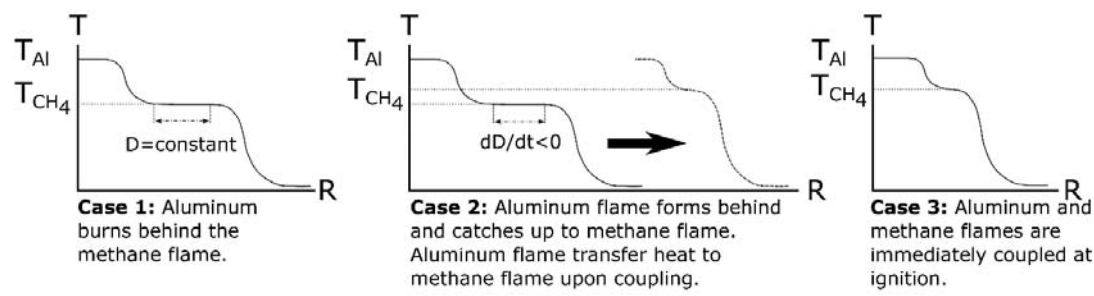
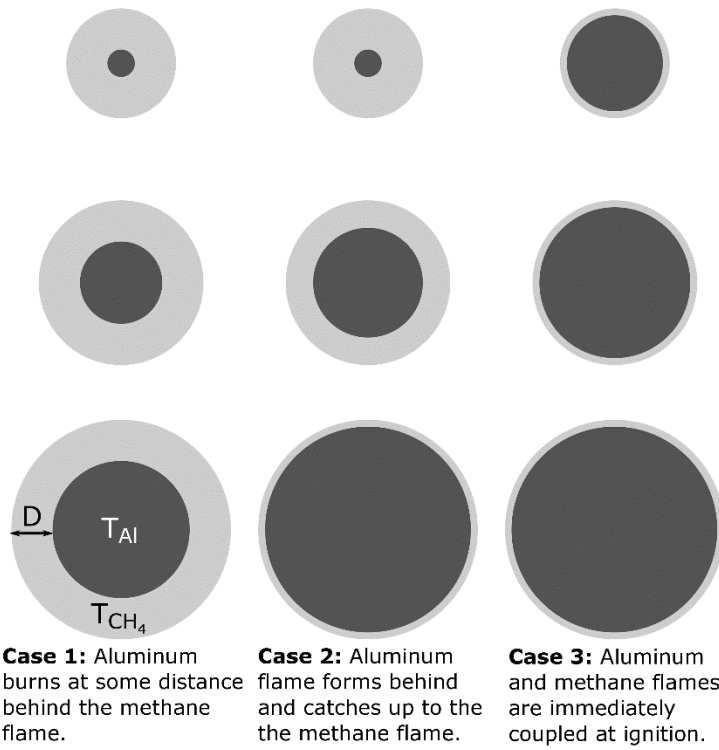


Figure 8: Diagrams showing the different ways that aluminum can influence the methane flame propagation.

*Effect of Oxidizer and Particle Mode of Combustion*

In present investigation, the gas mixtures are made such that the flame temperature and thermal diffusivity remain constant, and the only difference is the amount of free oxygen in the methane flame combustion products. In the mixtures without excess oxygen, the aluminum behaves as an inert for low concentration before coupling to the methane flame at a critical concentration. In the mixtures with excess oxygen, the aluminum reacts behind the methane flame even at very small concentrations. This difference in behavior may be due to differences in particle mode of combustion with the different oxidizers.

The critical concentration behavior in mixtures without excess oxygen suggests the particles are burning in the kinetic regime. Particles burning in the kinetic regime are limited by reaction kinetics, which are governed by Arrhenius kinetics where the reaction rates depend strongly on the ambient temperature. Consequently, the concentration of particles plays a crucial role. If the concentration is too small, the heat released from slowly oxidizing particles will not be sufficient to transition to thermal runaway. As the critical concentration is increased, the collective heating of the reacting particles will allow the mixture to transition from slow oxidation to rapid combustion.

The fact that aluminum can react at such low concentrations in mixtures with excess oxygen indicates that the particles may be burning in the diffusion limit regime. When particles ignite and transition to diffusion limited combustion, the oxidizers are consumed more quickly than they can diffuse to the particle. Aluminum-oxygen kinetic reaction rates are much faster than aluminum-water and aluminum-carbon dioxide kinetic reaction rates, and the addition of free oxygen in the methane-post flame zone can cause the particle to switch from kinetically limited to diffusion limited. In this case, the rate of reaction is determined by the rate that new oxidizers can diffuse to the aluminum, which is a weak function of ambient temperature. This explains how even small concentrations can still burn fast enough to influence the methane flame.

#### *Effect of Geometry*

Previous work studied the same hybrid aluminum-methane-oxidizers on a modified Bunsen burner. This work used the exact same 0% excess oxygen and 5% excess oxygen gas mixtures studied in the present work. In this previous work, both mixtures with and without excess oxygen displayed the same behavior. At low concentrations, the aluminum acted as an inert additive to the methane flame, and past a critical concentration, an aluminum flame front formed and coupled the methane flame. In the present work, this critical concentration behavior is only observed in mixtures without excess oxygen.

In mixtures with excess oxygen, the low concentrations of aluminum burn behind the methane flame, increasing the flame speed and causing the flame to accelerate. The geometry of the flame plays an important role in how the aluminum affects the flame. In the stabilized configuration, particles reacting behind the methane flame simply flow away downstream. In the spherically-expanding flame, the particles are trapped in the hot combustion products behind the flame, and particles reacting behind the methane flame after some induction time can cause the gas to expand and push on the flame.

## 4. CONCLUSIONS

Flame propagation through hybrid mixtures of hydrocarbon and metal fuels is a complex process that involves the formation and coupling of multiple flame fronts. These flames are inherently transient and must be studied using an apparatus that allows the observation of freely-propagating flames. The duration of the experimental event must be sufficient to observe the phenomena, which depends on many conditions, including the type of gaseous and solid fuels, their concentrations, and the oxidizer composition. The present experiment makes use of transparent latex balloons to maintain isobaric conditions while allowing imaging of the spherically-expanding flames throughout the event. The use

of balloons enables the gaseous mixtures and aluminum concentration to be varied in order to observe a variety of propagation regimes.

The key scientific findings of this work are:

- An aluminum flame front forms above a critical concentration and couples to the primary hydrocarbon flame. This behavior appears to be intrinsic to flames propagating in hybrid mixtures of hydrocarbon and metal fuels and is independent of the flame geometry.
- With a lack of oxygen in the methane combustion products, the aluminum particles are thought to burn in a kinetic regime. The flame speed decreases before a critical concentration, after which it remains constant, consistent with previous data.
- With excess oxygen in the methane combustion products, the aluminum particles are thought to ignite and burn in a diffusion-limited regime. Addition of increasing aluminum allows higher net flame temperatures that enables higher flame propagation speeds.
- The observed flame propagation in mixtures with excess-oxygen in the methane combustion products is unsteady and the speed can increase for quite low aluminum concentrations. The unsteady flame propagation is explained by a combination of cellular instabilities in the methane flame along with aluminum particles burning behind the methane flame, which causes the average density ratio across the flame to increase with time.

The results of these recent studies show that flame propagation and coupling in hybrid hydrocarbon-metal mixtures contains a rich set of physics that deserves significantly more attention than it has received to date.

## 5. REFERENCES

- [1] R. Eckhoff, Dust explosions in the process industries: identification, assessment, and control of dust hazards. Gulf professional publishing, 2003.
- [2] Y. Liu, J. Sun, and D. Chen, *J. Loss Prev. Ind.*, 20, (2007), 691-697
- [3] O. Dufaud, L. Perrin, M. Traore, S. Chazelet, and D. Thomas, *Powder Tech.*, 190, (2009), 269-273.
- [4] R. Pilão, E. Ramalho, and C. Pinho, *J. Loss Prev. Ind.*, 19, (2006), 27-23.
- [5] O. Dufaud, L. Perrin, M. Traorè, S. Chazelet, and D. Thomas, Hybrid mixtures explosions: when vapours met dusts. International Chemical Engineering Symposium, 2007.
- [6] P. Amyotte, M. Lindsay, R. Domaratzki, N. Marchand, A. Di Benedetto, and P. Russo, *AIChE J.*, 29, (2009), 17-21.
- [7] A. Denkevitz, *J. Loss. Prev. Industries*, 20, (2007), 698-707.
- [8] A. Denkevitz, *Fusion Eng. Des.*, 85, (2010), 1059-1063.
- [9] A. Denkevitz, and B. Hoess, *J. Loss Prev. Ind.*, 26, (2014), 509-521.
- [10] A. Maranda, *Propellants Explos. Pyrotech.*, 15, (1990), 161-165.
- [11] F. Zhang, *J. Propul. Power*, 22, (2006), 1289-1309.
- [12] R. L. Geisler, R. A. Frederick, and M. Giarra, *Encyclopedia of Aerospace Engineering*, John Wiley & Sons, Ltd, 2010.
- [13] P. R Choudhury, *Prog. Energy Combust. Sci.*, 18, (1992), 409-427.

- [14] A. N. Zolotko, Y. I Vovchuk, N. I. Poletayev, A. V. Floriko, and I. S. Al'tman, *Combust. Explos. Shock Waves*, 32, (1996), 262-269.
- [15] K. Seshadri, A. L. Berlad, and V. Tangilara, *Combust. Flame*, 89, (1992), 333-342.
- [16] J. H. Burgoyne, and L. Cohen, *Proc. Roy. Soc. London Ser. A. Math. Phys. Sci.*, 225, (1954), 375-392.
- [17] K. Zygourakis, *Mechanisms and Optimization of Coal Combustion, Department of Energy*, 2000.
- [18] R. Sanchirico, A. Di Benedetto, A. Garcia-Agredo, P. Russo, *J. Loss. Prev. Ind.*, 24, (2011), 648-655.
- [19] W. Felder and A. Fontijn, *J. Chem. Phys.*, 64, (1976), 1977-1980.
- [20] A. Fontijn, W. Felder, and J. J. Houghton, *Proc. Combust. Inst.*, 16, (1977), 871-879.
- [21] M. Soo, P. Julien, S. Goroshin, J. M. Bergthorson, and D. L. Frost, *Proc. Comb. Inst.*, 34, (2013), 2213-2220.
- [22] P. Julien, M. Soo, S. Goroshin, D. L. Frost, J. M. Bergthorson, N. Glumac, and F. Zhang, *J. Propul. Power*, (2014), 1-8.
- [23] P. Julien, S. Whiteley, S. Goroshin, M. J. Soo, D. L. Frost, and J. M. Bergthorson, *Proc. Combust. Inst.*, 35, (2015), 2431-2438.
- [24] J. Pakecka, P. Julien, S. Goroshin, J.M. Bergthorson, D. L. Frost, and A. J. Higgins, *Proc. Combust. Inst.*, 35, (2015), 2463-2470.
- [25] J. Servaites, H. Krier, J. C. Melcher, and R. L. Burton, *Combust. Flame*, 125, (2001), 1040-1054.
- [26] P. Julien, J. Vickery, S. Whiteley, A. Wright, S. Goroshin, J. M. Bergthorson, and D. L. Frost, *J. Loss Prev. Ind.*, 36, (2014), 230-236.
- [27] P. Julien, J. Vickery, S. Goroshin, D. L. Frost, and J. M. Bergthorson, *Combust. Flame*, 162, (2015), 4241-4253.
- [28] D. Goodwin, *Electrochem. Soc.*, 14, (2003), 8.
- [29] S. Goroshin, F. Tang, A. J. Higgins, J. H. S. Lee, *Acta Astronaut.*, 68, (2011), 656-666.

## Chapter 4. Hybrid flames of aluminum and methane in tubes

### 1. INTRODUCTION

Combustion of a hybrid multiphase fuel mixture, i.e., a suspension of micron-size solid fuel particles in a combustible gas mixture, is encountered in many practical applications such as propulsion (e.g., metalized solid propellants), industrial processes (e.g., reactive spray deposition), and fire safety (e.g., methane-coal dust explosions in mines). In spite of the practical importance of such multiphase flames, few investigators have experimentally studied the combustion of hybrid mixtures, with the majority of studies performed in standard constant volume closed vessels [1] that do not permit observation of the flame structure or allow accurate measurements of fundamental flame parameters, such as the burning velocity.

Flame-structure measurements in stabilized Bunsen-type flames in suspensions of hybrid premixed aluminum-methane-air mixtures were first carried out in our recent work [2, 3]. The experiments show that the transition from relatively slow oxidation to fast aluminum combustion is associated with the appearance of a double-front structure, where the aluminum dust flame front is coupled to the gas flame. It was also found that the formation of this coupled gas-dust flame front is a critical phenomenon that occurs rapidly at some minimum concentration of aluminum fuel. The flame structure and the interaction mechanisms between the gas and dust combustion fronts are complex and are not yet well understood.

In the present work, combustion in hybrid methane-aluminum mixtures is investigated by probing the response of the flame to heat losses. This was accomplished by propagating flames into channels formed from a set of parallel plates. Reducing the spacing between plates eventually leads to flame quenching. Together with burning velocity, the quenching distance of a flame in a narrow channel, i.e., the minimum channel width through which a flame can propagate, is a fundamental flame characteristic that reflects both the flame propagation mode and its structure.

Quenching distance is also an important technical parameter that is widely used in the design and safety validation of various industrial equipment and processes. Numerous experimental data on flame quenching distances in gases have been obtained and can be correlated with the burning velocities of the fuel mixture and compared with predictions of various theoretical flame models [4]. Measuring quenching distance in suspensions of solid fuels is experimentally more challenging than in gases and requires a relatively complex setup. Different modifications of an apparatus permitting measurement of flame quenching distances in dust clouds have been developed at McGill University over the past two decades. The quenching distances in aluminum and iron suspensions were measured in laboratory settings [5] and microgravity experiments aboard a parabolic flight aircraft [6]. The current paper presents experimental results on flame quenching in hybrid methane-aluminum fuel mixtures obtained with a new apparatus with an improved design that incorporated the majority of technical solutions developed previously for quenching experiments in dust clouds [5,6]. In order to provide a baseline, quenching distance

measurements were also performed in gas-solid fuel suspensions where the reactive aluminum powder was replaced with an inert silicon carbide (SiC) powder with a similar particle size that does not react with the methane combustion products. The results obtained are qualitatively interpreted using a simple model of the double-flame front structure developed previously for the analysis of flame propagation in binary dust suspensions [7].

## 2. EXPERIMENTAL APPARATUS

### *Aluminum and silicon carbide powders*

The same batch of atomized aluminum powder (Ampal 637, Ampal NJ) was used in the present work as in all our previous experiments with stabilized dust flames and aluminum flames in tubes [2,3,5,6]. Ampal aluminum particles have a spheroidal or nodular shape. The Sauter mean diameter,  $d_{32}$ , derived from the particle distribution obtained from SEM images of the powder, is about 5.6  $\mu\text{m}$ , which compares well with the value of 6.9  $\mu\text{m}$  obtained using the light scattering technique with a Malvern Mastersizer 2000. Detailed information on the particle size distribution of the powder is given in [2]. The inert silicon carbide powder has an irregular particle shape with a Sauter mean diameter obtained with the Malvern instrument of about 4.2  $\mu\text{m}$ .

### *Apparatus*

The new experimental apparatus constructed to measure quenching distances in hybrid solid-gaseous fuel mixtures combines the basic features of our earlier designs for flame quenching experiments in dust clouds [5], together with a number of novel features for the dust flow and flame diagnostics developed for the stabilized flame burner apparatus [2]. In particular, it uses a modified design of our generic dust dispersion system [5, 6] that permits the creation of a uniform dust flow with micron-size powders below 20  $\mu\text{m}$ . The system employs a piston feeder and provides powder dispersal via impingement of a concentric supersonic “air knife” jet issuing from a 50  $\mu\text{m}$  annular slot. The initially turbulent flow is expanded and laminarized in a long 8° angle conical diffuser before flowing into the flame tube (see Fig. 1B).

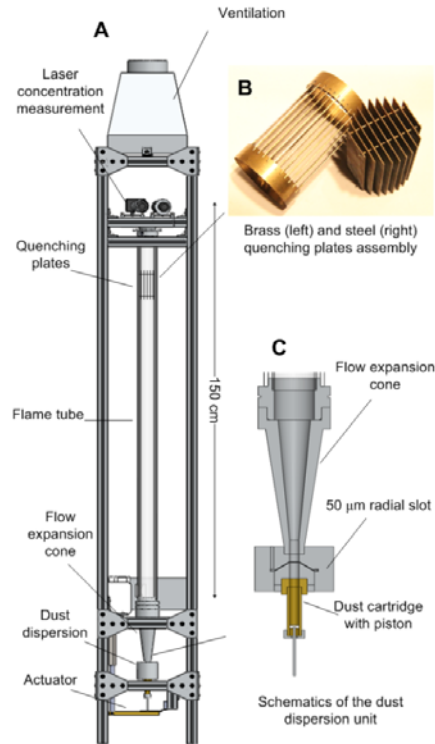


Figure 18 Overall schematics of the apparatus (a), photo of quenching channels assembly (b), and schematics of the dust dispersion unit (c)

A 48-mm-inner-diameter, 1.5-m-long vertical Pyrex flame tube (see Fig. 1(a)) is encased inside a larger diameter acrylic tube for safety. The upper end of the flame tube is equipped with a short aluminum conical nozzle with an opening of about 25 mm. The nozzle produces a dust jet flow with well-defined boundaries needed to minimize noise from the dust concentration monitoring system as well as minimizing disturbances to the flow inside the tube that otherwise are induced by the ventilation flow. A miniature remotely-operated propane-oxygen torch or an electrically-heated tungsten filament, stretched across the flow at the upper open end of the tube, ignites the mixture. Immediately after ignition, the flow in the tube is stopped by closing the solenoid valve in the gas supply line and the flame propagates down to the closed end of the tube in the quiescent two-phase fuel-air mixture. Flame quenching distance measurements were made by observing flames propagating through assemblies of equally-spaced steel or brass plates (see Fig. 1(b)) positioned in the upper part of the tube at about 50 cm from the upper end of the flame tube. The quenching channel assembly is supported inside the glass tube by resting on a loop of spring wire. The positioning of the quenching channels at a relatively short distance from the point of the dust concentration monitoring (laser beam) minimizes both the error in estimating the dust concentration inside the quenching channels and the influence of the flame acoustic oscillations on flame propagation and quenching. The quenching-plate assemblies had equal spacing between 0.5-mm-thick and 52-mm-long brass or steel plates, while the spacing varies from 4 to 20 mm for steel assemblies and 2 to 5 mm for brass assemblies. The steel quenching plates are soldered together by four thin rods, whereas the brass plates

are held together between lower and upper brass rings having precision-milled 0.5 mm slots (see Fig. 1(b)).

#### *Dust concentration measurement and monitoring*

The dust concentration in the flow is monitored with a laser-light-attenuation probe consisting of a diode laser, cylindrical lenses forming a rectangular  $10 \times 2$  mm beam, a narrow band-pass filter and spatial filters, and lenses to focus the laser beam onto a photodiode sensor. The laser beam traverses the dusty flow along the flow jet diameter right above the nozzle exit at the upper end of the tube. The output of the photodiode is constantly recorded by a data acquisition system and is also displayed on the monitor for real-time observation. The dust concentration probe is calibrated by aspiration of the dusty flow through a set of fine multilayered filters with a vacuum pump for about 5 seconds. The average dust concentration during the measurement time is then determined by dividing the total mass of the collected dust by the flow volume, i.e., the volume of gas fed through the dispersion system during the same time [2].

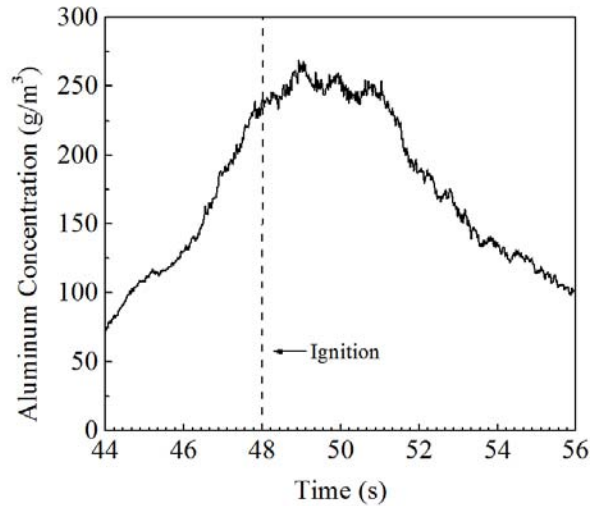


Figure 19 Typical time history of the dust concentration in the fuel flow measured with laser light attenuation probe at the exit of the flame tube

#### *Experimental procedure*

After the start of the dust dispersion, the concentration of aluminum in the laminar stream of the hybrid fuel mixture ascending the tube is transient. It reaches an approximate plateau after about 45-50 seconds as indicated by the concentration monitoring system at the exit of the tube (see Fig. 2). The duration of the plateau is usually about 3-5 second. With the speed of the ascending dust flow of about 25 cm/s, this means that the dust concentration is uniform over about 75-100 cm of the upper tube length. The flow is cut and the mixture is ignited by the operator as soon as the concentration-monitoring system indicates the plateau has been reached. As a result, the flame propagates down through the quiescent

mixture with a sufficiently uniform dust concentration before, within, and after the quenching channels.

Upon reaching the plate assembly, the flame either extinguishes or separates into flamelets, propagating through individual channels of the quenching plate assembly. The flame propagation in the tube and through the quenching plate assembly is recorded by a high-speed camera at a rate from 300 to 600 frames/s.

### 3. RESULTS AND DISCUSSION

Initial experiments were performed with inert silicon carbide (SiC) powder in order to provide benchmark data for the quenching distance of methane flames seeded with an inert powder. In our recent experiments with methane-air-SiC flames on the Bunsen dust burner [2, 3], we have confirmed that SiC does not noticeably react in the methane-flame products. The oxygen concentration in stoichiometric methane-oxygen-nitrogen fuel mixtures was reduced to about 16.3% O<sub>2</sub> in the present experiments in order to increase the quenching distance of pure gaseous flames. This was required to improve the resolution of the quenching measurements and ensure flame propagation through the minimal available quenching-plate spacing of 2 mm. The results on quenching experiments with methane flames seeded with SiC powders are presented in Fig. 3.

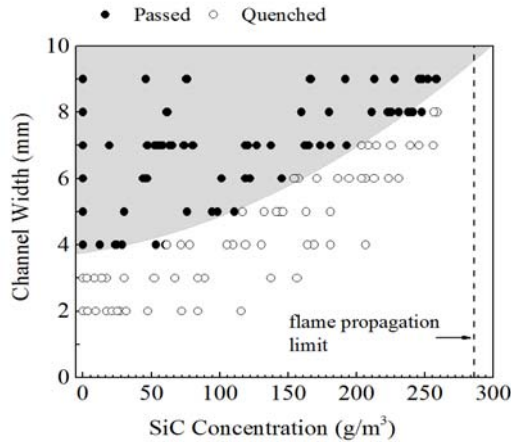


Figure 20 Results of flame quenching experiments at different concentrations of the silicon carbide dust in 16.3% O<sub>2</sub>/8.1% CH<sub>4</sub>/75.6% N<sub>2</sub>/SiC mixtures.

As can be seen from Fig. 3, the quenching distances obtained for pure gaseous methane flames are in the range of 3–3.5 mm. This is consistent with the reported value of 2–2.5 mm for a stoichiometric methane-air flame quenching within rectangular channels at the normal oxygen content of 21% [8]. The increase in quenching distance for methane mixtures with reduced oxygen content also correlates well with the known dependence of the flame speed in methane-air mixtures on oxygen concentration [9]. In the event of flame propagation through the plate assembly, the speed of individual flamelets propagating in each channel was usually different, reflecting local fluctuations in dust concentration. As can be seen from Fig. 3, the quenching distance increases with the increase of SiC content from about 3.5 mm for an unseeded flame to about 9.5 mm for concentrations around 270 g/m<sup>3</sup> for which flame propagation in the tube is still possible. At higher concentrations of

SiC powder above  $270 \text{ g/m}^3$ , the seeded flame fails to propagate down the tube. This correlates with our previous observation of the influence of SiC seeding on quenching of the stabilized stoichiometric methane-air flame [2], where it was observed that the tip of the Bunsen methane flame seeded with SiC starts to be open at dust concentrations of about  $200 \text{ g/m}^3$  and the flame quenches at SiC concentrations above  $300 \text{ g/m}^3$ .

*Quenching of the flame in methane-oxygen-nitrogen mixture seeded with Al powder*

As in the case of stabilized Bunsen methane-aluminum flames studied earlier [2, 3], the freely-propagating flames within the tube demonstrate two significantly different flame modes below and above some critical concentration of aluminum in suspension. At aluminum concentrations below the critical value, which was about  $300 \text{ g/m}^3$  in the present experiments, the aluminum oxidizes relatively slowly in the products of the methane flame over a long distance without substantially raising the flame temperature [2, 3]. The flame appearance and color are very similar to the appearance of the flame seeded with inert SiC powder, and the flame quenching distance, as shown in Fig. 4, similarly increases with an increase of powder loading. The somewhat higher quenching distance of the flame seeded with SiC, in comparison to aluminum, can be explained by the smaller size of the SiC particles that are in closer thermal equilibrium with the gas than aluminum and, therefore, provide a more effective heat sink.

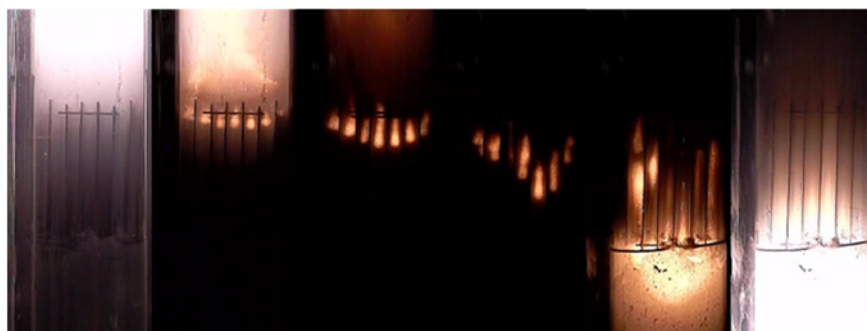


Figure 21 Results of flame quenching experiments at different concentrations of aluminum dust in  $16.3\% \text{ O}_2/8.1\% \text{ CH}_4/75.6\% \text{ N}_2/\text{Al}$  mixtures.

At some critical concentration of aluminum, the rapid transformation of the flame appearance is observed. This occurs around  $150\text{--}200 \text{ g/m}^3$  for the stationary Bunsen flame in methane-air mixtures studied in [3] and at about  $300 \text{ g/m}^3$  in the present experiments performed with freely-propagating flames at reduced oxygen concentration. This qualitative transformation, as was shown in [2, 3], is associated with the formation of an aluminum dust-flame front that becomes coupled to the methane flame. In contrast to a slow aluminum oxidation below the critical concentration, the width of the aluminum combustion zone reduces to 1–2 mm and the completeness of aluminum combustion increases from about 50–70% to 100%. The flame temperature also jumps from values characteristic of the methane flame with aluminum as an inert additive to temperatures predicted by thermodynamic calculations with aluminum as a fuel capable of reacting with water and  $\text{CO}_2$  in the methane combustion products [2].

Due to the heat input from aluminum combustion, the coupled methane-aluminum flame can propagate at much larger dust concentrations than for inert SiC-powder loading, as shown in Fig. 4. Thus, while the methane flame could not propagate at all for SiC concentrations exceeding  $300 \text{ g/m}^3$ , it propagated without difficulty at Al concentrations up to  $600 \text{ g/m}^3$ , which is the highest concentration that the current dust dispersion system can reliably provide. The coupled methane-aluminum flame exhibits two different types of quenching behavior depending on the aluminum concentration and the width of the channel. At aluminum concentrations below  $450 \text{ g/m}^3$ , the aluminum flame becomes decoupled from the methane flame when entering the channels and quenches. In this case, only methane flamelets propagate through the quenching channels, as observed in the video frame sequence in Fig 5 (notice the color change of the flamelets compared to the aluminum-methane flame entering the plates). The coupled aluminum flame, however, re-establishes itself in less than a tube diameter after the flame emerges from the quenching channels (see Fig. 5).

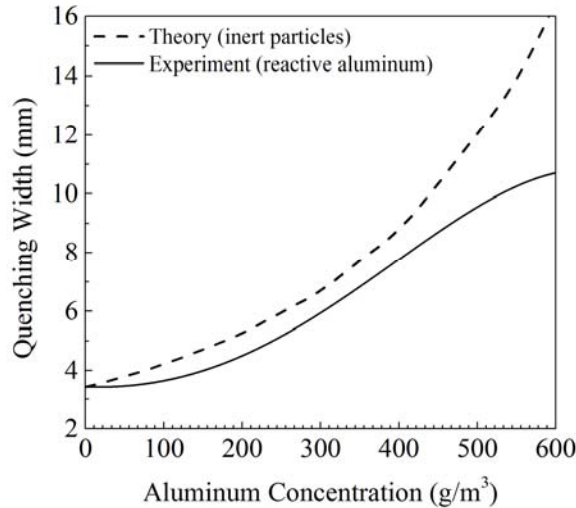


Figure 22 Frame sequence of the hybrid  $\text{CH}_4\text{-Al}$  flame propagating through the quenching plate assembly at aluminum concentration of about  $400 \text{ g/m}^3$ . Upon entering channels, the aluminum flame quenches and only methane flame propagates through.

At aluminum dust concentrations above  $450 \text{ g/m}^3$ , the flame can only propagate through the channel as a coupled methane–aluminum flame without changing its appearance (brightness). It continues to propagate as a coupled flame upon emerging from the quenching plate assembly. It is also interesting to note that the coupled flame inside the channel seems to demonstrate a much weaker dependence of the quenching distance on concentration than the decoupled methane-aluminum flames (see Fig. 4).

## Discussion

In order to understand the role of the heat release from reactive aluminum particles on the quenching of flames in hybrid fuel mixtures, an analysis of how inert-particle loading, with the same physical properties as aluminum, would affect the methane flame was performed using the simple Spalding model of a one-dimensional flame with heat loss [10]. The particles were considered to be in complete thermal and mechanical equilibrium with the gas. The overall effective methane kinetics and molecular transfer coefficients were determined by the Cantera software [11] with the reduced DRM-19 kinetic mechanism [12]. The heat loss term in the Spalding model was estimated for the slot formed by the two parallel plates of infinite width. The results of calculations of the flame quenching with non-reactive aluminum particles are shown in Fig. 6 and are compared to experimental results on aluminum-methane flame quenching. The experimental quenching curve in Fig. 6 is the boundary of the shaded area shown in Fig. 4 that separates flame-quenching and propagation events as a function of aluminum concentration.

As can be seen from Fig. 6, the quenching distances calculated with the assumption of inert non-reacting aluminum particles agree reasonably well with experimental data up to aluminum concentrations of about  $400 \text{ g/m}^3$ . The small and increasing deviation between experiment and theory in this concentration range can be the result of the temperature lag between particles and gas that was not taken into account in the calculations. The lack of thermal equilibrium between particles and gas effectively reduces the heat capacity of the suspension that leads to a higher flame temperature than the model predicts. Naturally, the difference between the calculated and measured quenching diameter progressively rises with the increase of solid fuel concentration because of the larger influence of the increasing heat capacity.

The appearance of the aluminum dust-flame front coupled to the methane flame at dust concentrations around  $300 \text{ g/m}^3$  does not immediately reduce the value of quenching distance or the rate of its rise with an increase in aluminum concentration. This behavior, as observed in the high-speed movies, is understandable since the aluminum flame quenches within the narrow channels at concentrations below  $400 \text{ g/m}^3$ . Thus, in spite of burning in the large diameter flame tube, aluminum plays the role of inert particles for the flame inside the channels. Only at concentrations above  $400 \text{ g/m}^3$ , when the coupled methane and aluminum flame fronts propagate and quench within narrow channels as a whole, does the difference between inert and reactive particulate suspensions become pronounced. Thus, while the theoretically predicted quenching distance for inert particles increases with dust concentration almost exponentially, the rise of the quenching distance for coupled aluminum-methane flames tapers off and is linear for concentrations above  $400 \text{ g/m}^3$ . Comparison of the flame extinction results, obtained with inert SiC (Fig. 3) and reactive Al (Fig. 4) particulate suspensions, demonstrates that flame propagation beyond a certain solid suspension concentration becomes impossible without assistance from the dust flame not only in narrow channels but, eventually, also in the wide flame tube. Thus, the flame propagation limits for flames seeded with reactive powders are, in general, much wider than for suspensions with inert particles, as could be expected.

The qualitative change of the hybrid flame quenching behavior with an increase of solid fuel concentration becomes more understandable if we consider various flame structures,

obtained with different proportions of reactive phases in a binary fuel mixture. Such analysis was first performed in our earlier work [7] in the framework of a simple analytical model that considers a flame in a suspension of two chemically different dust fuels. The model developed in [7] can be used for a qualitative analysis of the methane-aluminum flame, even though it was constructed using the assumption of a diffusive-combustion regime with two well-defined ignition temperatures for the particles in both fuel fractions. In the methane-aluminum flames studied here, both fuels burn in the kinetic mode [3], but similar behavior of the coupled fronts will be observed whether the model uses the ignition temperature and burning time, or is based on successive kinetic reactions of Arrhenius form.

The model predicts the occurrence of three different types of flame structure, shown in Fig. 7, which appear consecutively with an increase of the concentration of the second fuel (the concentration of the first fuel being assumed fixed).

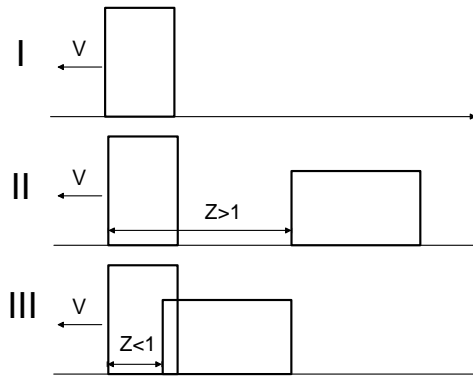


Figure 23 Schematic representation of different possible front structures in a binary fuel mixture: I, below threshold concentration of the second fraction when only first fuel burns frontally; II, double-front structure in the “control” flame mode; III, flame structure in the “merged” fronts mode.

The type I structure consists of a single combustion front burning the first fuel while the second fuel plays the role of an inert additive that merely decreases the flame speed. The second flame front appears only above some critical threshold concentration of the second fuel when the flame speed through the second fraction, preheated by the combustion of the first, becomes able to match the flame speed of the first flame front. The double-front flame structure (type II structure) has two well-defined preheat zones and is stable due to the thermal interaction between fronts through molecular heat transfer. Thus, as the separation distance ( $Z$ ) between the two fronts increases, the heat flow from the second front to the first one decreases, and the first flame speed drops. The shrinkage of  $Z$  correspondingly raises the heat input from the second front and, consequently, increases the flame speed. Such a binary flame structure is known in the literature as the “control” propagation mode [13, 14] because the second combustion front controls the total flame speed through the aforementioned thermal interaction mechanism with the first flame. However, due to large separation distances between the flames, the “control” combustion mode is vulnerable to heat loss and, thus, the second flame can be more easily extinguished in the quenching

channels. Evidently, the first flame structure type with a single flame front is realized in our case at aluminum concentrations below  $300 \text{ g/m}^3$  while the second double-front flame structure in the “control” flame mode occurs between 300 and  $400 \text{ g/m}^3$  in the flame tube outside the quenching channels. Because of the sensitivity of the double flame structure to heat loss, aluminum combustion extinguishes, and the flame converts to the type I single-front structure where aluminum is inert, as soon as the flame enters the narrow channels.

The third type of flame structure is the so-called “merged”-front propagation mode (type III in Fig. 7) [13, 14] which eventually appears at large concentrations of the second fraction when it starts to dominate the total heat production in the flame. In type III flames, the flame speed through the second fraction increases to a point where the stable structure can only be formed with overlapping combustion zones of the two fractions. Having only a single preheat zone, type III flames are more compact than type II flames and thus are more resistant to heat losses. Such flames can only be extinguished as a whole, since the first flame front cannot exist alone with an inert second fraction due to the effect of its very large heat capacity (see SiC results in Fig. 3). Clearly, the third “merged”-front mode is realized in our case at aluminum fuel concentrations above  $400 \text{ g/m}^3$ , where the coupled aluminum-methane flame is seen to propagate and quench as a single front.

#### 4. CONCLUSIONS

The main findings from this investigation can be summarized as follows:

Seeding of a stoichiometric premixed methane-air mixture with both inert SiC and reactive Al particles increases the flame quenching distance. At 16.3% reduced oxygen concentration in the mixture, the quenching distance increases from about 3.5 mm for an unseeded methane flame to about 9.5 mm for a flame seeded with  $270 \text{ g/m}^3$  of inert SiC powder. It increases to about 10 mm for mixtures with Al concentrations of  $600 \text{ g/m}^3$ .

Coupled aluminum-methane flame fronts only appear above a threshold aluminum concentration around  $300 \text{ g/m}^3$ . Below this concentration, the appearance and quenching behaviors of the methane flame seeded with reactive aluminum and inert SiC dusts are similar. The coupled aluminum-methane flame demonstrates two quenching modes. At concentrations below  $400 \text{ g/m}^3$ , the aluminum flame decouples from the methane flame and quenches in the narrow channel while the methane flame still propagates. The quenching of a decoupled methane flame in a narrow channel resembles the quenching behavior of the inert powder-seeded flame. At concentrations above  $400 \text{ g/m}^3$ , the coupled aluminum-methane flame can only propagate, or be extinguished, as a whole and exhibits a weaker dependence of the quenching distance on aluminum concentration.

The structure and quenching behavior of the methane-aluminum flame is qualitatively interpreted using a previously-developed simple analytical model for the description of flames in binary dust suspensions. The model correctly predicts the existence of a threshold concentration above which the linked methane-flame structure appears, as well as indicates the existence of the so-called “control” and “merged” flame propagation modes in hybrid mixtures which aid the interpretation of the flame quenching behavior.

## 5. REFERENCES

1. P.R. Amyotte, K.J. Mintz, M.J. Pegg, Y.H. Sun, *Fuel* 72 (5) (1993) 671-679.
2. M. Soo, P. Julien, S. Goroshin, J.M. Bergthorson, D.L. Frost, *Proc. Combust. Inst.* 34 (2) (2013) 2213-2220.
3. P. Julien, M. Soo, S. Goroshin, D.L. Frost, J.M. Bergthorson, N. Glumac, F. Zhang, *J. Propul. Power* (2013), *in press*.
4. J. Jarosinski, *Prog. En. Comb. Sci.*, 12 (2) (1986) 81-116.
5. S. Goroshin, M. Bidabadi, J.H.S. Lee, *Combust. Flame* 105 (1-2) (1996) 147-160.
6. S. Goroshin, F.-D. Tang, A.J. Higgins, J.H.S. Lee, *Acta Astron.* 68 (7) (2011) 656-666.
7. S. Goroshin, M. Kolbe, J.H.S. Lee, *Proc. Combust. Inst.* 28 (2) (2000) 2811-2817.
8. M. Maekawa, *Combust. Sci. Tech.* 11 (3-4) (1975) 141-145.
9. B. Lewis, G. Von Elbe, *Combustion, flames and explosions of gases*, Academic Press, New York, U.S., 1987
10. D.B. Spalding, *Proc. R. Soc. A.* 240 (1220) (1957) 83-100.
11. D. G. Goodwin, *Proceed. of CVD XVI and EUROCVI*, (14) (2003)
12. A. Kazakov, M. Frenklach, available at <<http://www.me.berkeley.edu/drm/>>.
13. B. I. Khaikin, A. K. Filonenko, S. I. Khudyaev, *Combust., Explos. Shock Waves* 4 (4) (1968) 343-348.
14. Y.B. Zeldovich, G.I. Barenblatt, V. Librovich, G. Makhviladze, *Mathematical Theory of Combustion and Explosions*, Consultants Bureau, New York, U.S., 1985, p. 402-415

# SECTION 3. OPTICAL DIAGNOSTICS IN DUST FLAMES

## Chapter 1. Ultraviolet (UV) Absorption Spectroscopy in Optically Dense Fireballs Using Broadband Second Harmonic Generation of a Pulsed Modeless Dye Laser

### 1. INTRODUCTION

Combustion measurements within the fireballs generated by explosives and other energetic materials have several diagnostic hurdles owing to the multiphase dynamics, the high temperatures, short time scales, and high optical depths of the combustion event. Explosives are often enhanced by the addition of solid phase fuels like metal particles which create high temperature environments of particulate and gas phases within the fireball. The relevant diagnostic time scales within explosives systems are typically on the order of several microseconds necessitating diagnostics which can be performed with this time resolution.

One of the key diagnostic capabilities is the characterization of temperatures within the fireball and the ability to monitor chemical species that evolve during the combustion. Optical techniques are more robust within the high temperature, multiphase environments where mechanical probes methods are difficult to implement due to temperature limitations and slow response time. In fireballs containing reactive particles, it is possible that the temperatures of the solid phase and gas phase may be different due to kinetically limited and diffusion limited particle reactions. Spectroscopic diagnostics may be able to analyze the possible separation of particle and gas temperatures by examining the gas phase components of the flame thereby demonstrating the regimes of particle combustion.

The high luminosities of fireballs of energetic materials lend to the prevalence of emission based diagnostics. The condensed phase temperature is often determined by using optical pyrometry or by fitting the continuum from the condensed phase to a Planck distribution, and this technique has been used as a temperature diagnostic in energetic materials in many studies.<sup>1, 2</sup> There is also precedent for using metal salt tracers to introduce vaporized atomic species into flames to determine electronic excitation temperatures which can be extended to diagnostics of explosives.<sup>3</sup> Lewis et al. have shown that by using atomic tracer elements seeded into explosives that a gas phase temperature can be measured from the relative intensities of the resulting atomic lines in the emission spectrum of the fireball.<sup>4</sup> Emission from the diatomic species present in the combustion of energetic materials (e.g. AlO) can also be fit to theoretical transitions to determine temperatures and concentrations.<sup>5</sup>

Emission spectroscopy measurements probe upper (excited) electronic states, and, in many cases, especially when the upper state is strongly populated by exothermic reactions, the population distribution in the upper state is not representative of the more abundant ground state molecules.<sup>3</sup> In general, a temperature derived from an emission

measurement should be checked for rotational/vibrational equilibrium or by comparing to an absorption measurement. In the particular case of optically thick fireballs, it has been shown that the detonation products of gram scale and higher experiments that the attenuation lengths are on the order of a few centimeters implying that the temperatures derived from the emission measurements may be only representative of the outer edge of the fireball.<sup>6</sup>

The preferred measurement, in these cases, would be to probe the ground state in absorption which provides quantifiable information on species concentration and temperature, though the measurements are path averaged. However, absorption measurements in fireballs are difficult owing to the intense luminosity of the fireball and the high intensity and coherence required from a broadband source to penetrate the fireball in order to perform the measurement.

The limitations of emission spectroscopy have prompted several experiments to probe of the inside of explosive fireballs. Lewis et al. found no significant difference in apparent temperatures measured by emission spectroscopy of the interior and the outer edge of an RDX explosive cloud revealing the possibility of temperature uniformity throughout the fireball at certain times during the combustion.<sup>7</sup> Carney et al. demonstrated the use of a booster optical amplifier to measure the absorption of water vapor in the near-infrared (NIR) and obtained a line-of-sight temperature measurement in a high explosive.<sup>8</sup>

In previous work, Glumac was able to show proof-of-concept experiments using a modeless dye laser as a spectral source for absorption spectroscopy measurements in optically thick fireballs.<sup>9</sup> Modeless dye lasers offer a widely tunable, relatively high bandwidth (~1-10 nm) coherent source and have moderate divergence and high power. In optically thick regions, there is difficulty in passing sufficient signal to detector from other broadband sources due to the scattering of the light. The dye laser offers an intense, directional beam allowing the strong rejection of the fireball luminosity and sufficient signal at the detector even at 98% attenuation.

Dye beam wavelengths are limited to above the near-ultraviolet (UV) due to the nature of the available dyes. A great number of important diatomic and atomic transitions occur below these wavelengths necessitating broadband UV spectral sources that can access the transitions. The advantage of dye lasers is that almost any visible wavelength can be reached by the appropriate selection of dye. By utilizing broadband second harmonic generation (SHG) of the dye laser beam using a nonlinear crystal, the wavelength range can be extended into the deep UV. Absorption measurements of several more atomic and diatomic species become possible for diagnostics ranging from the transitions found in hydrocarbon flames (e.g. OH, CN, NO) to those associated with the combustion of energetic materials (e.g. Ni, Fe, BO, AlCl). In this work, energetic systems are examined, and a stationary gas of NO is used to calibrate the diagnostic. Time resolution of the diagnostic is demonstrated by probing Al atomic line absorptions in exploding bridge wires (EBW). Finally, the diagnostic is used to obtain spectra from diatomic species of metal-fluorocarbon reactions (MgF and AlF) in dispersed flash powders which are of recent interest to enhance combustion performance in energetic materials.<sup>10, 11</sup> Spectra are fit to a model in order to confirm the species and yield path averaged temperatures.

## 2. EXPERIMENTAL APPARATUS

### *Dye laser configuration*

The schematic of the entire setup is shown in Figure 1. A frequency tripled, compact neodymium-doped yttrium aluminum garnet (Nd:YAG) laser (Quantel) at 355 nm with 5 ns pulses at 20 Hz is used as the pump for the dye laser. The maximum power available from the laser is approximately 60 mJ per pulse. The built in flash-lamp/Q-switch delay on the laser is used to adjust the power to pump the dye with 2-4 mJ per pulse which produces sufficient dye laser energy for the experimental setup.

The custom dye laser configuration is demonstrated in previous work by Glumac to produce a modeless beam with about 5% efficiency.<sup>9</sup> The 355 nm Nd:YAG beam is passed through a cylindrical lens to produce a horizontally spread beam and then focused down in the vertical direction by a second cylindrical lens onto a quartz dye cuvette 40 mm in length. The cuvette is tilted at a 20 degree angle to minimize etaloning effects. A full reflecting mirror is placed at one end of the laser cavity approximately 10 cm from the cuvette, though for a modeless laser this distance may vary without much consequence. The laser has no output coupler, and the front end is empty aside from an iris to prevent stray light and an achromatic collimating lens with a focal length of 175 mm to counteract the moderate divergence of the beam.

In cases where higher power and better beam shape is desired, Glumac shows that a partially reflecting mirror may be used at the front end of the cavity as long as the cavity is designed with very low finesse.<sup>9</sup> Modeless dye lasers designed for broadband coherent anti-Stokes Raman spectroscopy (CARS) utilize Bethune dye cells and pass the initial dye beam through an amplifier to change the beam shape and divergence.<sup>12</sup> The power of the pump beam may be increased by using a flowing dye cell since stationary dyes tend to degrade quickly under high pump powers. The advantage of the modeless configuration is the broadband character which is found to have a much smoother spectral distribution of intensity.<sup>13</sup> The power of the dye beam produced by an empty cavity front end and a stationary dye cell is found to be sufficient for the systems examined in this work. The Coumarin 450, 460, and 540 (Exciton) dye laser pulse energies are measured to be 0.1-0.2 mJ per pulse for a pump beam energy of 2-4 mJ.

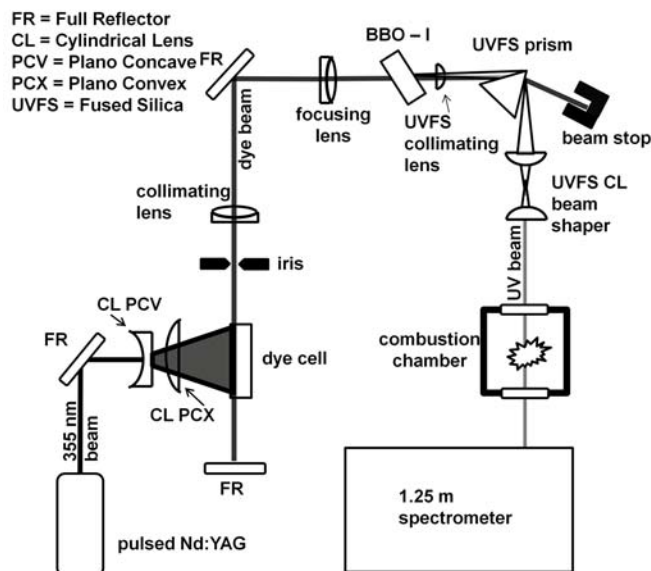


Figure 24. Schematic of the entire setup for the absorption measurement. A pulsed Nd:YAG (355 nm) pumps a dye cell in a grazing incidence configuration. The modeless dye beam is then focused onto a BBO-I crystal, and the resulting UV beam is collimated and separated from fundamental and passed through the combustion chamber.

### *Second harmonic generation*

The wavelengths produced by dye lasers are limited to wavelengths above 330 nm for Nd:YAG pumped dyes. To extend deeper into UV spectrum to access a much greater number of species, the beam can be passed through a non-linear crystal for SHG. Critical phase matching to the non-linear crystal allows for efficient SHG of a monochromatic beam by simply rotating the crystal to the optimum angle determined by the crystal cut. Wavelengths in a broadband beam which are outside the phase-matching bandwidth, determined by the thickness of the crystal and the diameter of the beam incident on the crystal, will typically have very low SHG efficiencies. The beta barium borate (BBO) type I, 7mm crystal with a cut-angle of 52 degrees (Radiant Dyes) used in this study theoretically has less than 0.1 nm of phase matching bandwidth at the desired wavelengths for NO absorption. Shorter crystals will theoretically provide higher spectral bandwidth at the expense of conversion efficiency.

The broadband nature of ultra-short laser pulses has led to the development of several techniques for increasing the phase matching bandwidth in crystals using chromatic dispersion of the fundamental beam.<sup>14-17</sup> Due to the relatively low power of the dye beam in this experimental setup, the use of any method of increasing the bandwidth which requires a significant loss in power is generally not desired. Dispersive elements can cause significant losses due to reflections of the required polarization for SHG in the nonlinear crystal at the surfaces of the dispersive element.

Unlike the large bandwidth of ultra-short pulses (typically around 100 nm), the bandwidth of the second harmonic pulse in the present experiments is only few nanometers in wavelength since the bandwidth of the fundamental dye beam has only around 10 nm of bandwidth at maximum. Previous studies indicate that by simply creating a strong focusing

condition of the fundamental beam into the crystal, a significant bandwidth in the frequency doubled beam can be achieved at a fraction of the signal loss compared to dispersive methods.<sup>18, 19</sup> To demonstrate this in the current experiment, the spectral bandwidth of the SHG of a Coumarin 540 dye beam under different focusing conditions is plotted in Figure 25. The crystal is first rotated to the central phase matching angle of the dye beam, and the lenses are varied without changing the crystal angle. The tight focus decreases the effective interaction length thereby increasing the spectral bandwidth.

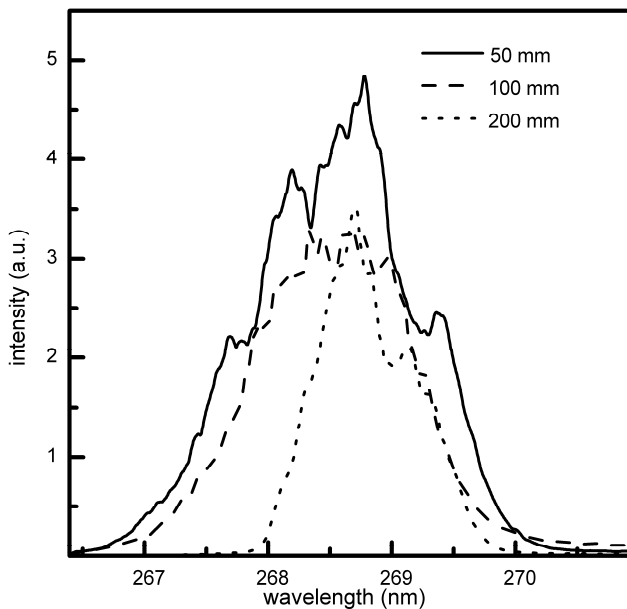


Figure 25. Spectral bandwidth of the second harmonic for different focal lengths of the lens used to focus the fundamental beam onto the nonlinear crystal.

Without spectral dispersion, the fundamental dye beam is focused onto the crystal with a 50 mm focal length achromatic lens. The crystal is then rotated until the second harmonic appears and adjusted to the desired spectral position. The combined fundamental and second harmonic beams are then re-collimated using a UV fused silica (UVFS) 25 mm focal length plano-concave lens. It is found in previous studies under strong focusing condition, the UV beam emerges nearly collimated in the horizontal direction.<sup>15</sup> The re-collimating lens allows the collimation of the beam in the vertical direction but causes divergence in the horizontal direction necessitating cylindrical correction optics to shape the beam in the horizontal direction (see Figure 24). The combined fundamental and second harmonic emerging from the crystal are first passed through a UVFS dispersion prism with an apex angle of 60 degrees to separate the fundamental from the second harmonic and then shaped with a UVFS cylindrical inverse telescope consisting of a 75 mm and 25 mm focal length UVFS plano-convex cylindrical lens. The resulting beam is approximately 5 mm in diameter as seen on a UV viewing card. The spectral profiles of an example dye beam (Courmarin 450 at 920  $\mu\text{mol/L}$  concentration in ethanol) and the second harmonic

are shown in Figure 26. The pulse energy from the second harmonic of the Coumarin 450, 460, and 540 dye beam is determined to be 1-5  $\mu\text{J}$  per pulse.

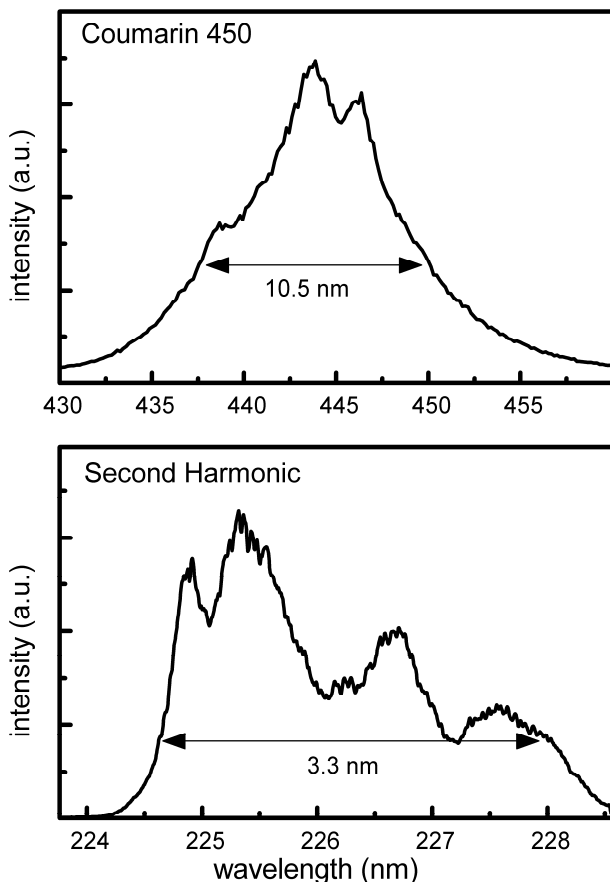


Figure 26. (top) Spectral bandwidth of modeless dye beam with Coumarin 450 as the dye averaged over several pulses. (below) The spectral profile of the second harmonic.

After passing through the combustion chamber, the UV beam is focused onto the 50  $\mu\text{m}$  slit of a customized 1260 mm focal length Czerny-Turner SPEX 1250 spectrometer with deviation angle of 11 degrees and a 3600 grooves/mm UV holographic grating (Optometrics). The detector used for NO absorption is a GARRY 3000 which is a CCD line array of 3000 pixels each  $7 \times 200 \mu\text{m}$ . The approximate resolution achieved by this spectrometer is approximately 0.01 nm full-width-half-maximum (FWHM) determined by the FWHM of an elemental calibration line over a range of about 4 nm on the detector. The detector used in flash powder tests is a Hamamatsu C7041 CCD array with  $1044 \times 255$  pixels each  $25 \mu\text{m} \times 25 \mu\text{m}$  with an approximate resolution of 0.013 nm FWHM over about a 4 nm range. The spectrum is binned over the entire chip. Even at low dye beam powers, the generated SHG UV beam is sufficient to saturate the spectrometer detectors with a single pulse.

### 3. RESULTS AND DISCUSSION

#### *Stationary NO gas*

The diagnostic is first calibrated with the NO  $A^2\Sigma^+ \leftarrow X^2\Pi$  (0,0) transition in the 226 nm to 227 nm range, the fundamental dye beam is created by pumping a solution of Coumarin 460 (Exciton) in ethanol at 0.005 mol/L. The resulting spectral bandwidth of the UV beam generated from the strong focusing of the dye beam onto the crystal is approximately 1.5 nm at FWHM. The spectral position on the detector is calibrated using a Ni-Ne hollow cathode lamp (Azzota) and checked against the position of the strong NO transitions.

A test system of NO is generated in a sealed chamber with fused silica windows using a continuous electric arc discharge in air. The electrodes are mounted within a 5 cm wide sealed chamber with quartz windows. The amount of NO produced in the chamber is correlated to the duration of the arc.

The laser is set to pulse continuously (20 Hz), and integration time is set to one second on the detector in order to obtain an averaged spectrum over the 20 pulses. A reference spectrum is first taken in the empty chamber. An optically thin spectrum of NO is obtained by producing an arc for five seconds or until only a slight absorption feature is qualitatively observed in the raw spectrum. The resulting spectrum and comparison to the LIFBASE simulation<sup>20</sup> is shown in Figure 4. Good agreement is shown between the simulation and resulting averaged spectrum from several laser shots in the optically thin limit.

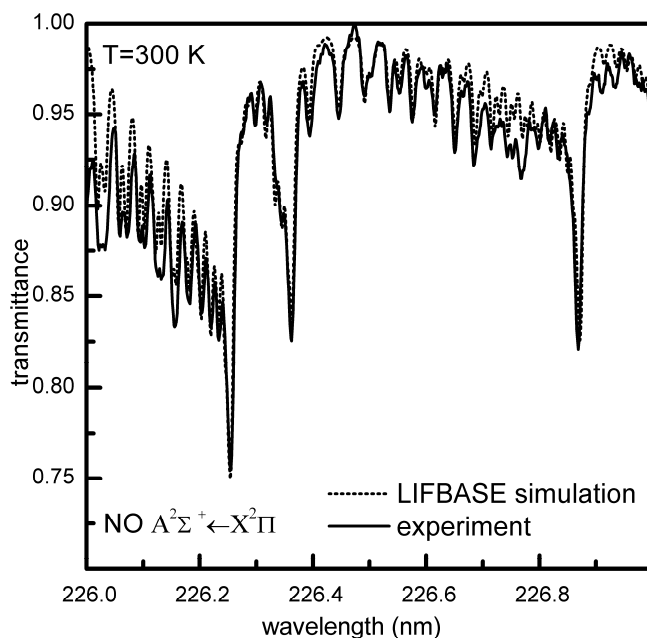


Figure 27. NO spectrum at low concentration from continuously pulsed laser (20Hz) integrated over 1 second compared to spectrum simulated by LIFBASE at T=300K.

A single pulse measurement is then taken in a high concentration of NO to simulate conditions in an optically dense fireball medium. The detector is set to a two second integration time and a reference pulse averaged over ten pulses taken in the empty chamber. An arc is then produced in the chamber for 30 seconds until the absorption signal is noticeably visible over the noise from the laser, and a second pulse is recorded. The transmittance from the single pulse measurement is plotted in Figure 28. A simulation of the NO absorption spectrum is provided by LIFBASE for comparison using the resolution of 0.013 nm obtained by spectrometer calibration and set to room temperature at 300 K. The single pulse absorption measurement produces a high signal to noise spectrum across a 1 nm region with approximately 30 well resolved rotational lines. A comparison of the optically thick with an optically thin LIFBASE spectrum shows clearly the effects of optical depth in the spectrum, which enhance weaker lines at the expense of stronger ones.

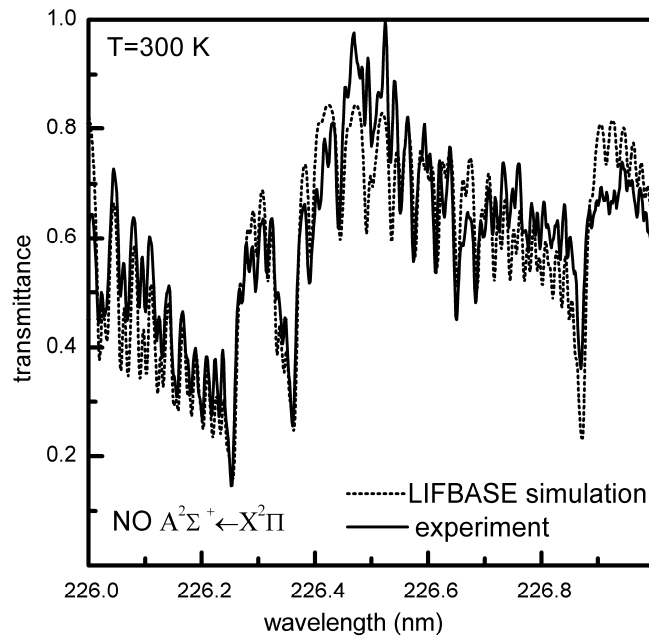


Figure 28. NO spectrum under optically thick conditions from a single pulse compared to spectrum simulated by LIFBASE at T=300K.

### *Time resolution in exploding bridge wires*

The ability to time resolve species absorption in the UV is demonstrated in the vapor cloud produced by an aluminum EBW. Previous work<sup>9</sup> showed that Al concentration in an exploding bridgewire cloud varies strongly over the first millisecond after breakdown. The same dye mixture used in the stationary NO gas measurement is used to probe the spectral range from 226 nm to 227 nm. To create aluminum bridge wires, aluminum foil is cut into thin strips approximately 0.5 mm wide  $\times$  25  $\mu$ m thick. The thin strips are then clamped between two electrodes set approximately 1 cm apart. The center of the UV beam is then positioned approximately 1 cm above the bridgewire. The electrodes are then connected to a Teledyne RISI FS-43 fireset synchronized to the

laser pulse output by a delay generator (Quantum) to allow for measurements at different times after the bridgewire initiation. An optical beam shutter (Thor Labs) is placed in front of the combustion chamber and connected to the pulse generator. Several single shot experiments are conducted with the absorption probe beam passing through the cloud at different times after breakdown. Before each wire is initiated, a reference pulse averaged over ten pulses is taken.

The resulting spectra for aluminum absorption lines at 200  $\mu\text{s}$  increments after the initiation of the bridge wire are shown in Figure 29. Two atomic absorption lines, the Al I ( $^2P^{\circ}_{1/2} \rightarrow ^2D_{3/2}$ ) transition at the lower wavelength and the Al I ( $^2P^{\circ}_{3/2} \rightarrow ^2D_{5/2}$ ) transition at the upper wavelength,<sup>21</sup> are apparent in the spectrum. It is seen initially that after the explosion, the absorption lines are extremely broad while gradually thinning out at later times. The broadening is attributed to the increase in equivalent width due to the optically thick spectrum. The observed linewidth far exceeds the expected pressure, Doppler, and Stark broadened linewidths in the bridgewire environment.

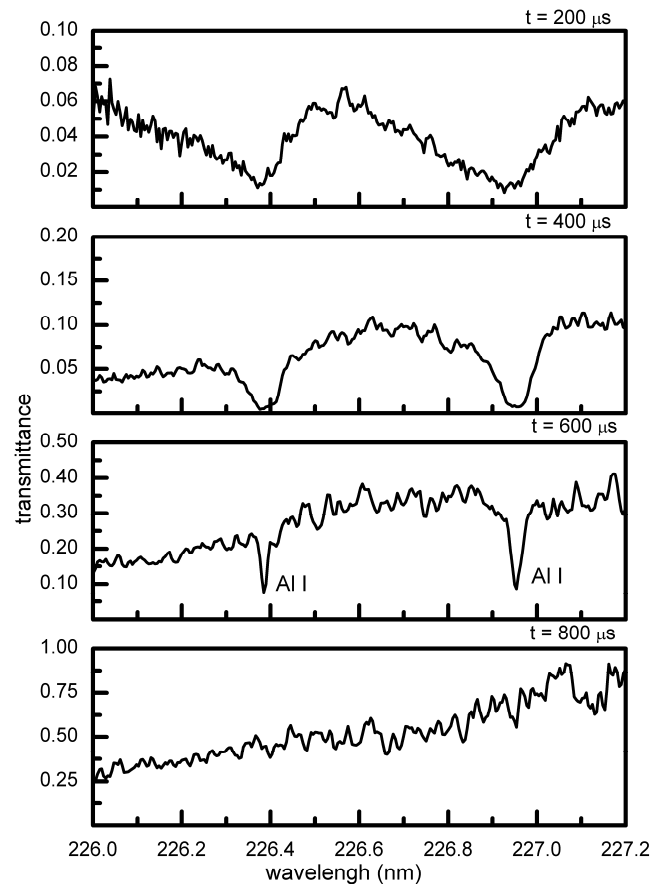


Figure 29. Al atomic line absorption in EBWs taken in a series of experiments at different times after bridge wire initiation.

### *Metal-Teflon Flash Powders*

Flash powders mixed with PTFE powder are used to examine fluorinated metal species in absorption in a solid fuel combustion environment. The spectrum of AlF is examined in a flash powder a powder of containing KClO<sub>4</sub>/PTFE/Al (57/10/33 by wt %). The spectrum of MgF is examined in a flash powder containing KClO<sub>4</sub>/PTFE/Mg (40/10/50 by wt%). An EBW is used to disperse and ignite the powders. A tungsten bridgewire with 0.005 cm diameter (McMaster Carr) is attached between the electrodes in the combustion chamber. Testing the tungsten wire in the same manner as described in the previous section revealed no absorption features in the regions of interest at any time after the initiation of the bridgewire making it an ideal candidate for dispersing powders. A piece of non-conductive tape is placed directly under the bridgewire to support a small pile of flash powder (5 mg) that rests on top of the wire. The bridge wires are initiated and spectrum recorded in the same manner as described in the previous section.

### *Spectroscopic Model for AlF and MgF*

The procedure for calculation of line positions and intensities used in this study is outlined in Arnold et al. utilizing the approximation to the Voigt profile provided in the reference.<sup>22</sup> The spectroscopic constants for the aluminum AlF  $A^1\Pi \leftarrow X^1\Sigma^+$  transition are taken from Rowlinson and Barrow.<sup>23</sup> The Franck-Condon factors for the first five vibrational levels of the  $\Delta v=0$  transitions are taken from Liszt and Smith.<sup>24</sup> Due to the nearly vertical nature of the transition, factors for five subsequent vibrational levels are estimated to be unity. Spectroscopic constants for the magnesium MgF  $B^2\Sigma^+ \leftarrow X^2\Sigma^+$  transition are taken from Huber and Herzberg.<sup>25</sup> Frank-Condon Factors for the first five levels of the the  $\Delta v=0$  transition were taken from Maheshwari et al..<sup>26</sup> Expressions for Hönl-London factors for both molecules are taken from Kovacs.<sup>27</sup> The calculation of the absorption coefficients is outlined by Luque.<sup>20</sup>

The classical Beer's law expression is used to describe the absorption. There are five adjustable parameters for the simulation of absorption spectrum taking into account the optical thickness: the temperature, a factor of non-resonant absorption/ scattering, a factor of the amount of light that passes through the absorbers, an effective product of the number density and path length, and the effective resolution. The slit function of the spectrometer setup is approximated as a Lorentzian function. The transmittance is plotted as a function of the wavelength. The fitting parameters are the same as described in previous work in modeling the AlO absorption spectrum.<sup>28</sup> The model is meant to be primarily used to verify the species being probed. The quantitative accuracy of the temperature measurement is not assessed in this work.

### *MgF detection in dispersed flash powder combustion*

The MgF  $B^2\Sigma^+ \leftarrow X^2\Sigma^+$   $\Delta v=0$  bandhead is observed at 268.85 nm. In order to reach this transition, a Coumarin 540 dye at 0.0035 mol/L concentration is used to produce the fundamental beam. The UV pulse energy is measured to be 3  $\mu$ J. The spectral position on the detector is calibrated using the atomic lines produced by a Fe-Ne hollow cathode lamp (Analyte). The spectral bandwidth after doubling is approximately 2 nm with a profile

similar to the bandwidth in Figure 25. The combustion of the dispersed magnesium flash powder provides moderate optical thickness of the MgF spectrum at times 500-600  $\mu\text{s}$  after the initiation of the tungsten EBW. The resulting spectrum is shown in Figure 30 along with the simulation at 3000 K with an effective resolution of 0.015 nm. Despite the path averaged nature of the measurement, a fair fit to the spectrum is obtained using a single temperature.

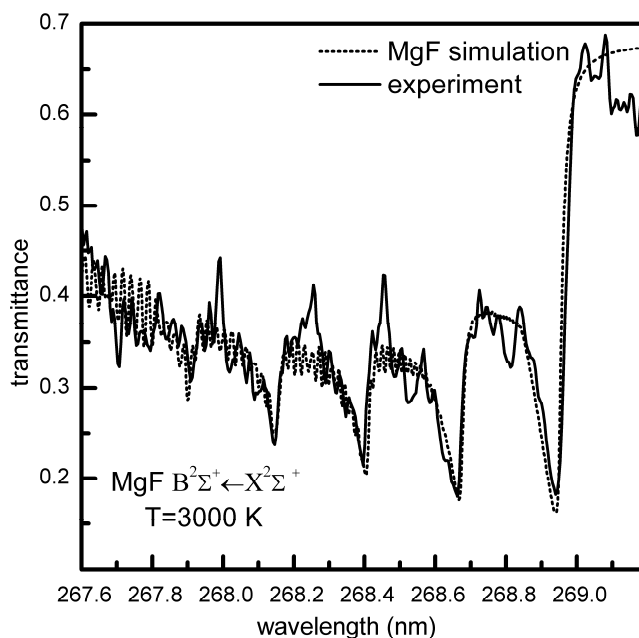


Figure 30. The absorption spectrum of MgF in flash powder combustion fit with a 3000 K simulation.

#### *AIF detection in dispersed flash powder combustion*

The AIF  $A^1\Pi \leftarrow X^1\Sigma^+$   $\Delta v=0$  transition is observed with a strong absorption feature with a peak at 227.4 nm. The same Courmarin 460 dye used for the aluminum bridge wire tests is used to produce the fundamental beam. The crystal is angle adjusted to center the beam in the 227 to 228 nm region of interest for AIF. The resulting pulse energy is approximately 1  $\mu\text{J}$ . The spectral position is calibrated by the Ni-Ne hollow cathode lamp. Measurements of AIF are taken approximately 800-1000  $\mu\text{s}$  after the initiation of the EBW, and produce noticeably optically thick spectrum. There is considerable difficulty in obtaining an optically thin spectrum since the highly optically thick signal rapidly decays to negligible signal. An example spectrum of the AIF transition is shown in Figure 31 with a simulation at 2800 K with an effective resolution of 0.015 nm. There is disparity of the model in the blue-degraded absorption feature at 227.4 nm possibly due to an unaccounted source of broadening or from the relative uncertainty of the spectroscopic constants in the literature.

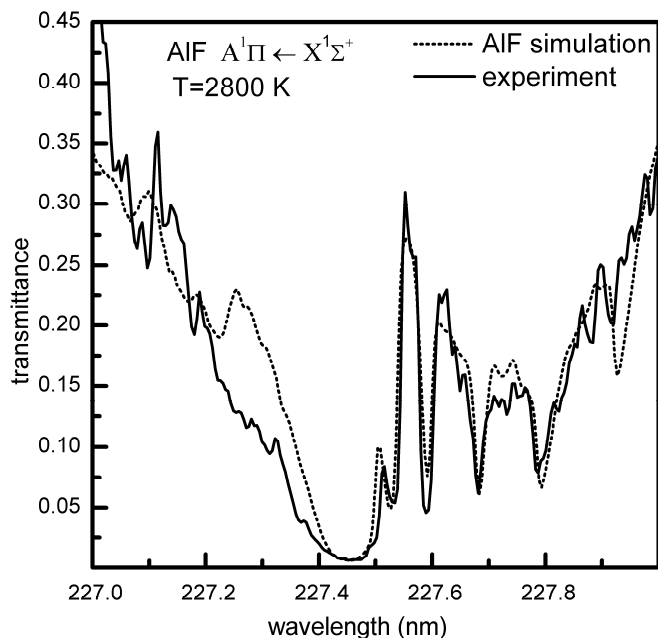


Figure 31. The absorption spectrum of AIF in flash powder combustion fit with a 2800 K simulation.

The intensity and coherence of the UV beam allows for easy alignment of the spectrometer in the second order of the grating. In the second order, the dispersion and resolution are more than doubled. The theoretical instrument resolution becomes 0.0026 nm with a range of 1.4 nm. The second order spectrum is shown in Figure 32. It is observed that pulse noise is increased. Although the majority of the rotational lines are too closely spaced to be resolved, a new feature appears in the main spectrum at about 227.5 nm which also appears in the simulated spectrum. The second order spectrum is again fit to a temperature of 2800 K.

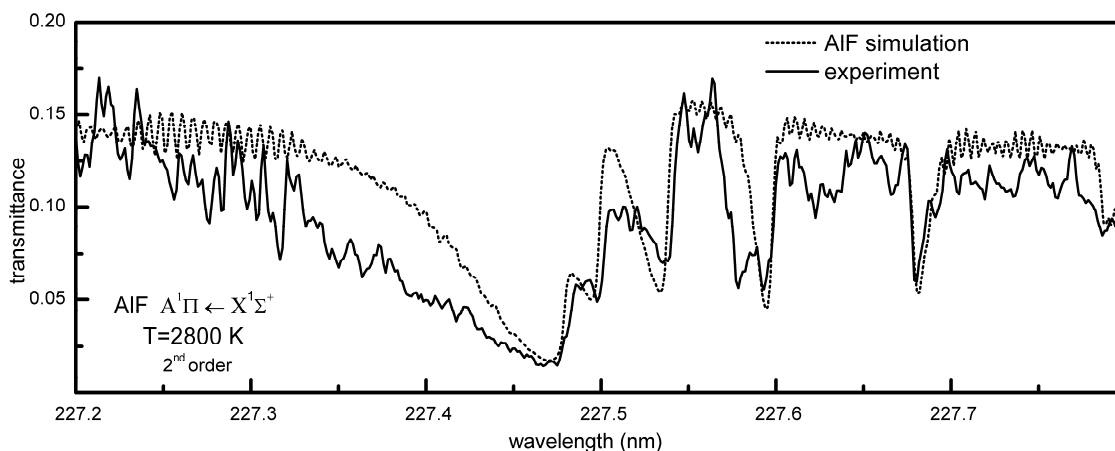


Figure 32. Second order spectrum of AIF with a simulation at 2800 K.

### *Absorption saturation*

High pulse intensities can optically pump the absorption medium so that sufficient population in the excited state may cause non-linear absorption effects. Full saturation is considered when the excited state population is driven by the laser radiation to match the ground state. In this scenario, the medium becomes effectively transparent to the laser light and no absorption will take place.

The limiting pulse energy is determined for NO  $A^2\Sigma^+ \leftarrow X^2\Pi (0,0)$  absorption as an example. The spectral range of the laser is considered from 226 nm to 229 nm. A beam radius of 2.5 mm and a pulse width of 5 ns are assumed. The calculated maximum pulse energy at which the excited state population reaches 25% is found to be approximately 0.4 mJ. In cases of higher pulse energy, an increase in the beam radius can reduce the overall beam intensity allowing for greater pulse energy at a small expense of spatial resolution in the measurement.

## 4. CONCLUSIONS

The use of a modeless dye laser as a spectral source for an absorption measurement is extended into the UV beyond the limitations of pumped dye beams by using broadband SHG. Absorption measurements of the NO  $A^2\Sigma^+ \leftarrow X^2\Pi (0,0)$  transition and atomic lines in aluminum EBWs are used to calibrate the diagnostic showing convergence in the optically thin limit over multiple pulses and to demonstrate microsecond time resolution in a series of experiments. The diagnostic is used to probe the fireballs of flash powders dispersed by EBWs to examine the optically thick AlF  $A^1\Pi \leftarrow X^1\Sigma^+$  transition, and the MgF  $B^2\Sigma^+ \leftarrow X^2\Sigma^+$  transition. A single temperature is derived by fitting simulations of the diatomic transitions to the experimental data. A simple analysis of the laser intensity where saturation effects may not be negligible is given for a two level system for wavelengths near NO and AlF transitions.

It is found in this setup that the pulse noise and pulse variation do not degrade the absorption measurement significantly. The average standard deviation in amplitude over the laser pulse spectrum for a sample of ten pulses is found to be 15-20%. The noise level of a single pulse, however, is estimated to be 5-10%. Improvements in the measurement can be made by splitting the beam before the combustion chamber and acquiring a simultaneous reference measurement using an array detector as demonstrated by Glumac.<sup>9</sup> Other broadband laser sources such as femtosecond lasers may offer superior noise characteristics, though currently, these tend to be more expensive than the dye based approach.

A strong focusing condition of the fundamental dye beam onto the crystal is found to be sufficient to produce approximately 1-3 nm of bandwidth. The SHG beam is able to saturate the detector in a single pulse and provides enough signal to be used for a single shot measurement in the second order of a grating. This diagnostic provides a simple tool for obtaining a path averaged measurement and overcoming the difficulties of absorption spectroscopy in explosive fireballs and other optically thick combustion systems as shown in previous studies using the visible spectrum of dyes.<sup>9</sup> Several atomic and diatomic species can be accessed for measurement by careful selection of dyes and crystals. Following the

assumption of approximately a 2 cm attenuation length from previous studies of optical depth in fireballs<sup>6</sup> and assuming a pulse energy around 10 mJ max, the technique is estimated to be able to scale up to a 20 cm path length.

## 5. REFERENCES

1. Lynch, P., H. Krier, and N. Glumac, *Emissivity of Aluminum-Oxide Particle Clouds: Application to Pyrometry of Explosive Fireballs*. Journal of Thermophysics and Heat Transfer, 2010. **24**(2): p. 301-308.
2. Goroshin, S., et al., *Optical Pyrometry of Fireballs of Metalized Explosives*. Propellants, Explosives, Pyrotechnics, 2006. **31**(3): p. 169-181.
3. Gaydon, A.G., *The spectroscopy of flames*. 1974, London: Chapman and Hall.
4. Lewis, W.K. and C.G. Rumchik, *Measurement of apparent temperature in post-detonation fireballs using atomic emission spectroscopy*. J. Appl. Phys., 2009. **105**(5): p. 056104.
5. Peuker, J.M., et al., *On AIO Emission Spectroscopy as a Diagnostic in Energetic Materials Testing*. Propellants Explos. Pyrotech., 2013: p. 577-585.
6. Peuker, J.M., et al., *Optical depth measurements of fireballs from aluminized high explosives*. Optics and Lasers in Engineering, 2009. **47**(9): p. 1009-1015.
7. Lewis, W.K., C.G. Rumchik, and M.J. Smith, *Emission spectroscopy of the interior of optically dense post-detonation fireballs*. J. Appl. Phys., 2013. **113**(2): p. 024903.
8. Carney, J.R., et al., *Water temperature and concentration measurements within the expanding blast wave of a high explosive*. Meas. Sci. Technol., 2011. **22**(4): p. 045601.
9. Glumac, N., *Absorption Spectroscopy Measurements in Optically Dense Explosive Fireballs Using a Modeless Broadband Dye Laser*. Appl. Spectrosc., 2009. **63**(9): p. 1075-1080.
10. Koch, E.-C., *Metal-fluorocarbon based energetic materials*. 2012: John Wiley & Sons.
11. Sippel, T.R., S.F. Son, and L.J. Groven, *Altering Reactivity of Aluminum with Selective Inclusion of Polytetrafluoroethylene through Mechanical Activation*. Propellants Explos. Pyrotech., 2013. **38**(2): p. 286-295.
12. Hahn, J.W., C.W. Park, and S.N. Park, *Broadband coherent anti-Stokes Raman spectroscopy with a modeless dye laser*. Appl. Opt., 1997. **36**(27): p. 6722-6728.

13. Glumac, N., *Absorption Spectroscopy Measurements in Optically Dense Explosive Fireballs Using a Modeless Broadband Dye Laser*. Appl. Spectrosc., 2009. **63**(9): p. 1075-1080.
14. Saikan, S., *Automatically tunable second-harmonic generation of dye lasers*. Opt. Commun., 1976. **18**(4): p. 439-443.
15. Saikan, S., D. Ouw, and F.P. Schäfer, *Automatic phase-matched frequency-doubling system for the 240-350-nm region*. Appl. Opt., 1979. **18**(2): p. 193-196.
16. Cheville, R.A., M.T. Reiten, and N.J. Halas, *Wide-bandwidth frequency doubling with high conversion efficiency*. Opt. Lett., 1992. **17**(19): p. 1343-1345.
17. Szabó, G. and Z. Bor, *Broadband frequency doubler for femtosecond pulses*. Appl. Phys. B, 1990. **50**(1): p. 51-54.
18. Boyd, G.D. and D.A. Kleinman, *Parametric Interaction of Focused Gaussian Light Beams*. J. Appl. Phys., 1968. **39**(8): p. 3597-3639.
19. Weiner, A.M., A.M. Kan'an, and D.E. Leaird, *High-efficiency blue generation by frequency doubling of femtosecond pulses in a thick nonlinear crystal*. Opt. Lett., 1998. **23**(18): p. 1441-1443.
20. Luque, J. and D. Crosley, *LIFBASE: Database and spectral simulation program (Version 1.5)*. SRI international report MP, 1999. **99**(009).
21. Kramida, A., et al., *NIST Atomic Spectra Database*, 2012, National Institute of Standards and Technology: Gaithersburg, MD.
22. Arnold, J.O., E.E. Whiting, and G.C. Lyle, *Line by line calculation of spectra from diatomic molecules and atoms assuming a voigt line profile*. Journal of Quantitative Spectroscopy and Radiative Transfer, 1969. **9**(6): p. 775-798.
23. Rowlinson, H.C. and R.F. Barrow, *The Band-Spectrum of Aluminium Monofluoride*. Proc. Phys. Soc. London, Sect. A, 1953. **66**(5): p. 437.
24. Liszt, H.S. and W.H. Smith, *RKR Franck-Condon factors for blue and ultraviolet transitions of some molecules of astrophysical interest and some comments on the interstellar abundance of CH, CH<sup>+</sup> and SiH<sup>+</sup>*. J. Quant. Spectrosc. Radiat. Transfer, 1972. **12**(5): p. 947-958.
25. Huber, K.-P. and G. Herzberg, *Constants of diatomic molecules*. Vol. 4. 1979: Van Nostrand Reinhold New York.
26. Maheshwari, R.C., I.D. Singh, and M.M. Shukla, *Franck-Condon factors and *r* centroids for the B-X and C-X systems of the MgF molecule*. J. Phys. B: At. Mol. Phys., 1968. **1**(5): p. 993.

27. Kovács, I. and L. Nemes, *Rotational structure in the spectra of diatomic molecules*. 1969: Hilger London.
28. Glumac, N., et al., *Temperature Measurements of Aluminum Particles Burning in Carbon Dioxide*. *Combustion Science and Technology*, 2005. **177**(3): p. 485-511.

# **SECTION 4. MODELLING OF FLAMES IN METAL SUSPENSIONS AND IN HYBRID SUSPENSIONS OF METALS AND HYDROCARBONS**

## **Chapter 1. Flame Propagation and Quenching in Binary Fuel Mixtures**

### **1. INTRODUCTION**

Many combustion systems involve more than one type of fuel. For example, in mixtures containing solid particle suspensions, combustion properties vary considerably with the size of particles [1] as well as with the presence of combustible gases in so-called hybrid flames. This variation often lead to staged combustion in flames and the appearance of multiple fronts. These have been observed, among others, in the combustion of metallized propellants [2] or in systems undergoing self-propagating high-temperature synthesis [3]. In the case of solid-gas fuel mixtures, experimental tests have studied the structure of flames in well-defined suspensions of micron-sized aluminum in methane-air mixtures [4]. A stabilized methane-air Bunsen flame was loaded with increasing concentrations of aluminum particles. At low concentrations, only a gas flame seeded with particles exists. As the concentration reaches a critical value, the aluminum reaction is sufficient to create and stabilize a second front in the products of the methane-air flame. Both flames appear somehow coupled and no visible change is observed for higher powder concentrations. The brightness of the aluminum flame, however, prevents a direct observation of its structure. A visual assessment was possible in the case of iron suspension in methane-air [5]. Here, the flame exhibits a similar behavior to the aluminum case and the presence of two interacting fronts can be clearly observed for concentrations above a critical value.

Stabilized Bunsen flames can nevertheless give only limited information on the nature of this interaction and on the conditions of formation of the second (metal) fuel front. The flame structure can be better probed by observing what happens as it approaches its propagation limits when it is subjected to heat losses. An experimentally easy way to achieve this is to measure the quenching distances of the flame, a fundamental quantity linked to heat losses. Tests, performed by our group on freely propagating flames in tubes [6], examined the quenching distances for the same aluminum suspensions in methane-air mixtures as in [4] over a large range of powder concentrations. Quenching was monitored by observing the flame propagation through narrow channels formed by a set of parallel

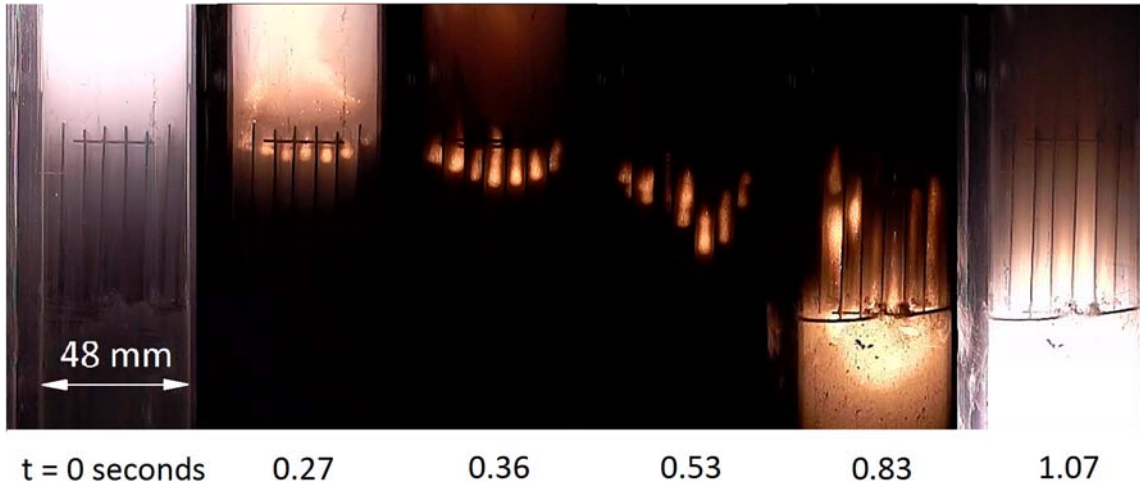


Figure 33: Caption of a flame propagating through the set of equally spaced quenching plates (reprinted from [6]). The disappearance of the bright aluminum front and its reforming once the dimmer methane flame has reached the end of the plates attests flame decoupling.

equidistant metal plates placed in the tube. The existence of two fronts was observed only above a critical powder concentration. Below this value, the flame consisted only of one methane-air front whose quenching distances increased with increasing powder concentration, similar to background tests performed with suspensions of inert SiC particles in the same methane-air gas mixture. Above the critical concentration, a coupled aluminum-methane flame, similar to the one in [4], formed in the tube. Depending on the powder concentration, two quenching behaviors were observed. Upon reaching the narrow channels, the flame first decoupled, i.e. the aluminum front extinguished while the methane flame propagated through the channels. As illustrated by Fig.1., once the methane flame emerged from the narrow channels, the aluminum front sometimes reappeared. This decoupled gas flame exhibited a similar dependence on powder concentration as the one loaded with inert SiC particles. At even higher concentrations, the flame stayed coupled and either propagated through the channels or completely quenched.

A qualitative interpretation of the experiments was based on the role of the aluminum powder, depending on whether it formed a front, enhancing the heat release rate of the flame, or only increased the heat capacity of the mixture. The explanation was supported by the results of an existing analytical model [7] which considers the combustion of two chemically distinct fuels in a binary mixture. The different predicted flame configurations

(Fig. 2), based on varying proportions of reactive phases in the mixture, explained the main features observed in the experimental tests, i.e. the absence of the second front at low and its formation at a critical aluminum concentration, as well as the flame coupling/decoupling behaviors. An analogy has been drawn with similar analyses of successive reactions in gas flames [8, 9].

The aim of the present work is to extend the aforementioned model [6, 9] to include the effects of heat losses to the channel walls, obtained from a previous work on single front solid-gas mixtures [10] to explain the different quenching modes observed and thus to obtain a qualitative understanding of flame propagation in binary fuel mixtures.

## 2. EXPERIMENTAL APPARATUS

The present model, based closely on previous work [7, 10], examines the combustion of two chemically independent fuels in a steady-state stationary flame which are represented as two reactive fractions of a binary mixture. The model neglects any chemical effects and considers only the heat equation. The combustion of each fraction is assumed to occur in the diffusive regime and can be therefore approximated as a step function triggered as soon as the temperature reaches an ignition temperature associated with each fraction. A recent publication [11] suggests that this representation may be in fact extended well beyond such considerations and may pertain to gas combustion with Arrhenius kinetics under certain circumstances. Moreover, to simplify the calculations of the analytical model, the mixture is fuel-lean, so that each reaction is limited only by the fuel which burns for a preset combustion time, associated to each fraction ( $\tau_1$  and  $\tau_2$ ), at a constant heat release rate.

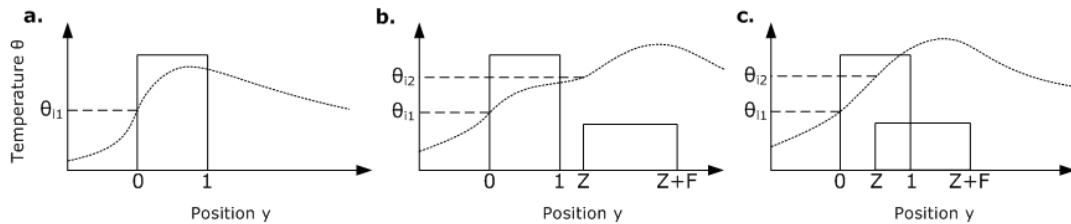


Figure 34: Three configurations the flame may adopt along with temperature profiles. a) one-front with corresponding ignition temperature, b) two separated fronts, c) two merged fronts, with corresponding ignition temperatures  $\theta_{11}$  and  $\theta_{12}$

Combining the previous considerations, the individual fronts, associated with the combustion of each fraction can be modeled by means of Heaviside step functions. In the present paper, the three flame configurations under study are depicted in Fig. 2. In the first case (2.a.), the second fraction does not form a front and the flame is represented by only one heat release zone. In the second flame (2.b), both fractions react with the oxidizer and form separate combustion zones. In the third case (2.c), the second fraction reacts before the end of combustion of the first one and both fronts are overlapped.

The present analysis is based on the previous work of one of the authors of this paper [7, 10]. Through the same derivation logic, a stationary flame subjected to the flow of fresh gas at a steady-state velocity  $\kappa$  can be described solely through the following heat equation:

$$\frac{d^2\theta}{dy^2} - \kappa^2 \frac{d\theta}{dy} = -R + \kappa^2\eta(\theta - 1) \quad (1)$$

The expressions relating the spatial coordinate  $y$ , the dimensionless temperature  $\theta$ , the flame speed  $\kappa$ , the heat loss term  $\eta$  and the heat source term  $R$  to their physical counterparts are described in details in [10]. The spatial origin is set at the beginning of the combustion zone corresponding to the reaction of the first fraction. In light of the model description, the heat release term, corresponding to the combustion zones, can therefore be expressed as:

$$R = \begin{cases} 0, & y < 0, 1 < y < Z \text{ and } y > Z + F \\ S_1\kappa^2, & 0 < y < 1 \\ S_2\kappa^2, \text{ with } S_2 = \zeta\phi & Z < y < Z + F \end{cases} \quad (2)$$

Where  $Z$  is the position of the ignition of the second front and  $F = \tau_2/\tau_1$  corresponds to the width of the second combustion zone. Here,  $\phi$  is the concentration of the second fraction,  $S_1$  and  $\zeta$  are scalars related to the heat of reaction of the respective fractions.

The boundary conditions and 2 more equations, linking the ignition temperatures  $\theta_{i1}$  and  $\theta_{i2}$  with the combustion zones of fuel 1 and 2 respectively, are:

$$\begin{aligned} \theta(-\infty) = 1, \quad \frac{d\theta}{dy}(-\infty) = 0, \quad \theta(+\infty) = 1, \quad \frac{d\theta}{dy}(+\infty) = 0. \\ \theta(0) = \theta_{i1}, \quad \theta(Z) = \theta_{i2}. \end{aligned} \quad (3)$$

### *Solution Procedure*

The step nature of the heat release term lead to the necessity to subdivide the integration domain into regions corresponding to the different values of  $R$  (Fig. 2.), and to solve equation (1) analytically over each sub-domain, giving:

$$\theta(y) = c_i e^{r_1 y} + c_j e^{r_2 y} + \frac{R}{\kappa^2(1 + \nu\phi)} y \quad (4)$$

With

$$r_1 = \frac{1}{2} \left[ \kappa^2 a - \sqrt{\kappa^4 a^2 + 4\kappa^2 \eta} \right] \quad \text{and} \quad r_2 = \frac{1}{2} \left[ \kappa^2 a + \sqrt{\kappa^4 a^2 + 4\kappa^2 \eta} \right] \quad \text{with } a = (1 + \nu\phi) \quad (5)$$

Then, in order to obtain a continuous temperature profile, both the temperature  $\theta$  and the rate of change  $d\theta/dy$  were matched at the boundaries of each region. Along with the boundary conditions, this provided a set of twelve equations. Ten of these equations were used to obtain the coefficients  $c_i$  and  $c_j$ . The remaining two equations featured nonlinear expressions of the two unknowns of the current problem, namely the burning velocity,  $\kappa$ ,

and the position of the second front,  $Z$ . Thus, the problem was transformed from a linear ODE with step forcing functions to a system of coupled algebraic transcendental equations.

In the case of the one front model, the solution were obtained in [10] . For the double front model, write expression of  $Z$  and the two non-linear equations of  $\kappa$ :

$$Z = \frac{1}{r_2} \ln \left( \frac{S_2 (1 - e^{-r_2 F})}{[2\eta + a](\theta_{i,1}) - S_1 (1 - e^{-r_2})} \right) \quad (6)$$

$$(2\eta + ar_2)(\theta_{i,2} - 1) = \left[ (2\eta + ar_2)(\theta_{i,1} - 1) - S_1 (1 - e^{-r_2}) \right] e^{r_2 Z} + S_1 \left( 1 + \frac{a}{\eta} r_2 \right) (e^{-r_1} - 1) e^{r_1 Z} \quad (7)$$

$$(2\eta + ar_2)(\theta_{i,2} - 1) = \left[ (2\eta + ar_2)(\theta_{i,1} - 1) - S_1 \right] e^{r_2 Z} - S_1 \left[ \left( 1 + \frac{a}{\eta} r_1 \right) (e^{r_1 Z} - 1) + 1 \right] \quad (8)$$

### 3. RESULTS AND DISCUSSION

The roots of the transcendental equations above have been obtained numerically and the corresponding flame speeds  $\kappa$  are plotted with respect to the 2<sup>nd</sup> fraction concentration  $\phi$  on Fig. 3.a. The individual curves represent the flame speed dependence on concentration for a given heat loss ( $\eta$ ). For the adiabatic case ( $\eta=0$ ), all the three flame configurations have at maximum one speed solution for a given concentration. It is a well-known fact in combustion that in the case of heat losses, a flame may have at least two speed solutions. Usually, one is a physical solution, i.e. its change with respect to a given parameter is physically sound, while the other, non-physical, exhibits an opposite, unrealistic behavior. For the one-front case, where the 2<sup>nd</sup> fraction is modelled as an inert component with the sole effect of increasing the heat capacity of the mixture, the flame speed is expected to decrease with concentration. On the other hand, for the two-front case, the 2<sup>nd</sup> fraction actively contributes to the heat generation of the flame and its addition should have a positive impact on the speed. Therefore, the physical solution for all configurations is associated with the upper branches of the double-valued curves and the non-physical speed will be neglected from further discussion. It has also been known for a long time [12] that the meeting of both branches at a finite speed value represents the quenching point of the flame. Fig. 3.b., directly obtained from Fig. 3.a., highlights the various changes in flame behavior. Along with the adiabatic flame speeds (solid curves), the quenching curves for both the one-front and two-front cases were obtained. Another important curve follows the boundary ( $Z=1$ ) between the merged- and separated-front configurations.

**Effect of concentration:** As can be seen on both Figs 3.a. and 3.b., raising the concentration of the 2<sup>nd</sup> fraction  $\phi$  for constant heat losses leads to changes in the flame configuration. This can be illustrated on the adiabatic case ( $\eta=0$ ) by the path 1-3 (Fig. 3 b.). At  $\phi=0$ , a one-front flame (from the reaction of the 1<sup>st</sup> fraction) exists. As the concentration is raised (1-2), the 2<sup>nd</sup> fraction increases the heat capacity of the mixture and

forces the flame speed to decrease. For these low concentrations, the flame can have only one front. Above a critical value of  $\phi$ , the flame can exist in two forms. Either the 2<sup>nd</sup> fraction is inert (as in the case of SiC in [6]) and the flame still exists as a one front, whose speed decreases with concentration until it quenches, or it acts as a fuel and can form its own front separated from the first one. In this case, raising the concentration leads to a decrease in the value of  $Z$ , i.e. the fronts approach, and the speed increases (2-3). At a particular concentration, the 2<sup>nd</sup> front reaches the 1<sup>st</sup> one ( $Z=1$ ). A further increase leads to the merging of the fronts (3-4).

**Effect of heat losses:** The flame configuration is also observed to change with increasing heat losses, as illustrated by paths a-d and e-g in Fig. 3.b. Both processes happen at a constant concentration,  $\phi=0.11$  and  $\phi=0.24$  respectively. In the first case, the adiabatic flame is composed of two separated fronts. As the heat losses are increased (a-b), the flame speed decreases and the fronts move further away, i.e.  $Z$  increases, until the second front completely vanishes (b). At this point, the flame speed suddenly drops (b-c) and only the primary flame can exist (c). Further increases in heat losses (c-d) lead to the quenching of this primary flame (d). The second example shows a flame at higher concentrations of the second fuel, where two merged fronts exist in the adiabatic case (e). Increasing the heat losses (e-f) leads to the decrease in flame speed and to a gradual increase in  $Z$  up to the point where  $Z=1$  (f). At this point, a further increase in heat losses (f-g) leads to the unmerging and separation of the fronts, and later, to the quenching of the merged flames (g). For higher heat losses at this concentration, the primary flame cannot exist without the heat release from the second front and the entire flame structure quenches in unison.

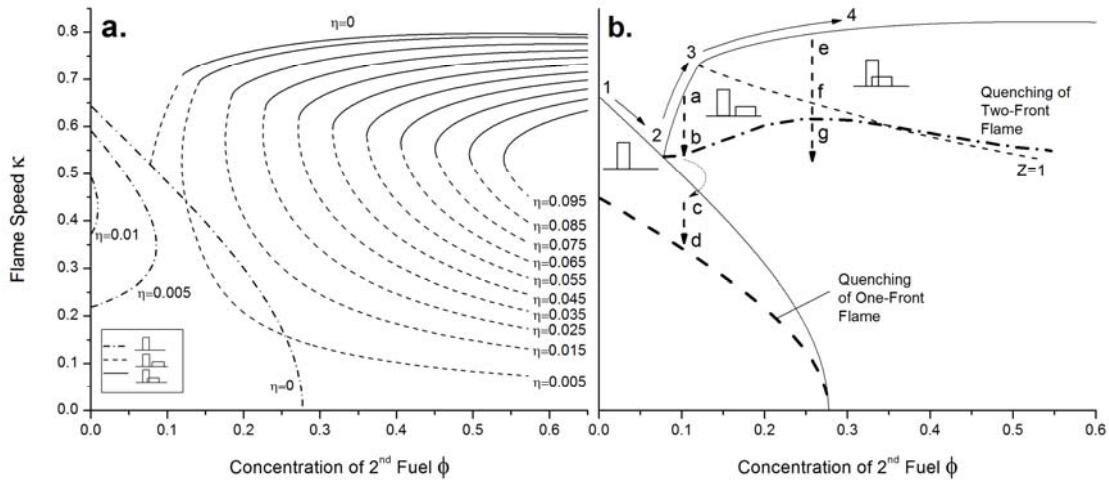


Figure 35: a. Flame speed dependence on 2<sup>nd</sup> fuel concentration for increasing heat losses ( $\eta=0$  to 0.095) for the three flame configurations showing physical and non-physical speeds. Parameters:  $S_1=7$ ,  $\nu=0.8$ , and  $S_2/\phi=10$ . b. Corresponding quenching curves for one-front and two-front flames, and the  $Z=1$  curve showing the change in flame structure at quenching for increasing concentrations. Also shown, the change in flame speed for the adiabatic case ( $\eta=0$ ) with increasing concentration (path 1-3) and two examples of change for increasing heat losses at constant concentration (path a-d and e-h).

**Comparison with experiments:** The analytical results for quenching from Fig. 3.b. were qualitatively compared to the experimental plot (Fig. 4.a.), obtained in [6]. From the definition in [10], values of  $1/\sqrt{\eta}$ , directly proportional to the quenching distances, were plotted with respect to the 2<sup>nd</sup> fraction concentration (Fig. 4.b.). Both plots are divided into two regions. The upper one shows the flame structure within the main tube (diameter of 48 mm) and the lower one illustrates the flame behavior in the narrow channels.

The appearance of an aluminum front at about 320 g/m<sup>3</sup> (Fig. 4.a.), observed in the main tube, virtually adiabatic compared to the narrow channels, is explained by considering the effect of concentration on flames, already illustrated by the path (1-3) in Fig. 3.b. and again shown in Fig. 4.b for different parameters chosen for better illustration of discussed concepts.

A clear qualitative correspondence between the two plots leads to a physical interpretation of the quenching behavior of the aluminum-methane-air flames in terms of the binary mixture of two reactive fractions. First, at low concentrations, only a methane-air flame, seeded with aluminum particles forms in the main tube and propagates through the narrow channels before it quenches. As more slowly reacting aluminum is added, its main effect is to raise the heat capacity of the mixture, thus lowering its flame speed and heat release, and making it susceptible to quench at higher channel widths. At a critical concentration, the aluminum reaction is sufficient to form a front in the main tube. As the model shows, the two fronts are at first separated and it is relatively easy to quench the secondary front through heat loss, corresponding to path a-d in Fig. 3.b. As was observed in Fig. 3.b., as the aluminum concentration further increases, the fronts in the main tube merge (3). The response of such flame to heat losses is first a front separation, and then a quenching of the second front, with the primary front still propagating, followed by the quenching of the primary flame with even higher heat loss values (path e-g in Fig. 3.b.). This logic matches with the experimental observations of the sudden aluminum flame extinction at the entrance of narrow channels, the sole propagation of the methane flame between the parallel plates, or its quenching for very narrow channels. As the primary methane flame emerges from the plates into the main tube, the decrease in heat loss allows the secondary front to re-couple to the primary flame [6]. As the heat release from the aluminum reaction increases with powder concentration, the coupled flame improves its resistance to extinction and propagates through narrower channels. This trend is opposite to the behavior of a single methane-air flame loaded with higher levels of non-reacting particles, which keeps increasing with concentration. At some point, these two quenching points cross and the flames cannot decouple and must propagate or quench in unison. . Again, a clear parallel can be drawn to the cases where the aluminum-methane flame cannot decouple, and either propagates through the channels or quenches as a whole in unison.

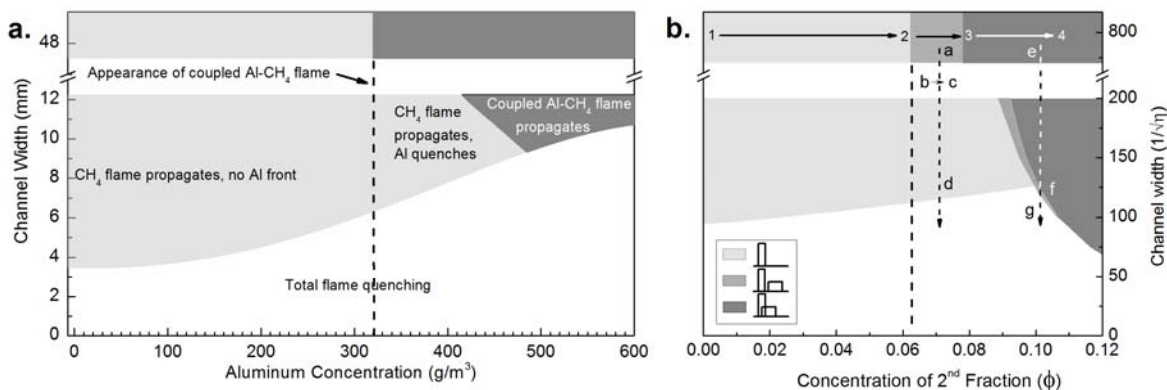


Figure 36: Comparison of experimental results from [6] (a.) with analytical findings of the model ( $S_1=7$ ,  $\nu=0.3$ ,  $S_2/\phi=10$ ) in the tube and the narrow channels. The colored regions correspond to respective flame configurations. The dotted line indicates the first appearance of the two-front flame in the main tube.

At such high concentrations, however, the model must be considered with caution, as one of its initial assumption, namely the fuel-lean nature of the mixture is no longer valid. Therefore, a more complex analysis, considering, among others, the depletion of oxidizer limiting the reaction rate and heat release for both of the fractions, should be developed.

#### 4. CONCLUSIONS

A simple analytical model, based solely on thermal considerations, is used to qualitatively explain some of the main features associated with the steady-state propagation and quenching of heterogeneous flames in binary fuel mixtures. Qualitative agreement between previously obtained experiments on flames of aluminum suspensions in methane-air mixtures was achieved in both the structure and quenching behavior of the flame. The effect of the key parameters, the secondary fuel concentration and the rate of heat losses, was examined. Both the flame existence and its structure were determined by whether the second fuel, aluminum in the experiments, enhanced the heat production of the primary methane-air front by its exothermic reaction, or hindered it by acting as an inert that simply increased the heat capacity of the mixture and reduced the temperature of the primary flame. This simple model predicts a wide range of flame configurations, including: a primary front whose propagation speed decreases with increasing concentrations of an effectively-inert second fuel; the formation of a secondary flame front at a critical concentration at a large separation distance; a reduction in separation distance between the two fronts as the concentration of the second fuel, and therefore its flame speed, are increased; and a merging of the two fronts into a flame structure with overlapping heat release zones. This simple model explains why, for some intermediate concentrations, the flame thermal coupling is not strong enough to withstand heat losses and the secondary front quenches while at higher concentrations the merged flame fronts become indivisible and must propagate or quench in unison. The results of the simple model do not capture

the full picture, as many effects are purposefully neglected, but allows the complex quenching behavior of flames burning binary fuel mixtures to be understood.

## 5. REFERENCES

- [1] T. Bazyn, H. Krier, and N. Glumac, "Evidence for the transition from the diffusion-limit in aluminum particle combustion," *Proceedings of the Combustion Institute*, vol. 31, pp. 2021-2028, 2007.
- [2] A. G. Merzhanov, "Self-propagating high-temperature synthesis: twenty years of search and findings," *Combustion and plasma synthesis of high-temperature materials*, pp. 1-53, 1990.
- [3] R. L. Geisler, R. A. Frederick, and M. Giarra, "Historical Overview and Solid Rocket Motor Fundamentals Model and Assumptions," *Encyclopedia of Aerospace Engineering*, 2010.
- [4] P. Julien, M. Soo, S. Goroshin, D. Frost, J. Bergthorson, N. Glumac, and F. Zhang, "Combustion of Aluminum Suspensions in Hydrocarbon Flame Products," *Journal of Propulsion and Power*, vol. 30, pp. 1047-1054, 2014.
- [5] P. Julien, S. Whiteley, S. Goroshin, M. J. Soo, D. L. Frost, and J. M. Bergthorson, "Flame structure and particle-combustion regimes in premixed methane–iron–air suspensions," *Proceedings of the Combustion Institute*, vol. 35, pp. 2431-2438, 2015.
- [6] J. Palecka, P. Julien, S. Goroshin, J. M. Bergthorson, D. L. Frost, and A. J. Higgins, "Quenching distance of flames in hybrid methane–aluminum mixtures," *Proceedings of the Combustion Institute*, vol. 35, pp. 2463-2470, 2015.
- [7] S. Goroshin, M. Kolbe, and J. H. Lee, "Flame speed in a binary suspension of solid fuel particles," *Proceedings of the Combustion Institute*, vol. 28, pp. 2811-2817, 2000.
- [8] I. B. Zeldovich, G. I. Barenblatt, V. B. Librovich, and G. M. Makhviladze, *Mathematical theory of combustion and explosions*, 1985.
- [9] B. I. Khaikin, A. K. Filonenko, and S. I. Khudyaev, "Flame propagation in the presence of two successive gas-phase reactions," *Combustion, Explosion and Shock Waves*, vol. 4, pp. 343-348, 1968/10/01 1968.
- [10] S. Goroshin, M. Bidabadi, and J. Lee, "Quenching distance of laminar flame in aluminum dust clouds," *Combustion and Flame*, vol. 105, pp. 147-160, 1996.
- [11] I. Brailovsky, P. V. Gordon, L. Kagan, and G. Sivashinsky, "Diffusive-thermal instabilities in premixed flames: Stepwise ignition-temperature kinetics," *Combustion and Flame*.

- [12] D. B. Spalding, *A Theory of Inflammability Limits and Flame-Quenching* vol. 240, 1957.

## Chapter 2. Reaction of a Particle Suspension in a Rapidly-Heated Oxidizing Gas

### NOMENCLATURE

$\alpha$	thermal diffusivity [ $\text{m}^2\text{s}^{-1}$ ]
$\beta$	mass transfer coefficient [ $\text{m}^1\text{s}^{-1}$ ]
$\gamma$	stoichiometric index
$\lambda$	thermal conductivity [ $\text{W}^1\text{m}^{-1}\text{K}^{-1}$ ]
$\rho_g$	gas density [ $\text{kg}^1\text{m}^{-3}$ ]
$\rho_s$	solid density [ $\text{kg}^1\text{m}^{-3}$ ]
$A$	particle surface area [ $\text{m}^2$ ]
$B$	particle concentration [ $\text{kg}^1\text{m}^{-3}$ ]
$c_g$	gas specific heat capacity [ $\text{J}^1\text{kg}^{-1}\text{K}^{-1}$ ]
$c_s$	solid specific heat capacity [ $\text{J}^1\text{kg}^{-1}\text{K}^{-1}$ ]
$C_s$	oxidizer concentration at surface [ $\text{kg}^1\text{m}^{-3}$ ]
$C$	oxidizer concentration [ $\text{kg}^1\text{m}^{-3}$ ]
$C_0$	initial oxidizer concentration [ $\text{kg}^1\text{m}^{-3}$ ]
$D$	mass diffusivity [ $\text{m}^2\text{s}^{-1}$ ]
Da	Damköhler number
$h$	heat transfer coefficient [ $\text{W}^1\text{m}^{-2}\text{K}^{-1}$ ]
$h_w$	cooling coefficient [ $\text{s}^{-1}$ ]
$k$	Arrhenius rate [ $\text{m}^1\text{s}^{-1}$ ]
$k_0$	pre-exponential factor [ $\text{m}^1\text{s}^{-1}$ ]
$m$	oxidizer mass [kg]
Nu	Nusselt number
$q$	heat of reaction [ $\text{J}^1\text{kg}^{-1}$ ]
$r$	particle radius [m]
$r_0$	initial particle radius [m]
Sh	Sherwood number
$T_a$	activation temperature [K]
$T_g$	gas temperature [K]
$T_s$	particle (solid) temperature [K]
$T_0$	ambient temperature [K]

### 1. INTRODUCTION

A suspension of reactive solid fuel particles dispersed within hot oxidizing gases may be formed, for example, following the detonation or deflagration of a metalized energetic material or during an accidental explosion in a coal mine or the process industries [1]. In the first example, the reaction time for the energetic material is typically much shorter than the characteristic time for heat exchange between the particles and the combustion products, hence the particle suspension may be treated as if it were suddenly exposed to a hot oxidizing atmosphere. Measures of the performance of the energetic material, such as the work done by the expanding products and blast wave for an explosive, or the specific

impulse of a propellant, will depend critically on the subsequent reaction delay and combustion time of the solid-fuel suspension. The overall system performance may be tailored by choosing appropriate particle sizes and other system parameters as guided by the available experimental data and predictions from theoretical models.

Historically, most of the information on solid-fuel reactivity has been obtained from laboratory experiments using relatively large single particles, with sizes ranging from tens to hundreds of microns. In the experiments, the particles are typically either injected into an oxidizing flow produced by a hydrocarbon flame [2], or heated by the gas behind a reflected shock within a shock tube [3]. The experimental results are then used to construct models that are extended to predict the combustion behavior of much smaller particles and of dense particulate suspensions that are common in practical particle-fuel systems. The underlying assumption made when extrapolating to practical energetic materials is that the combustion physics on which the models are built do not change with particle size or concentration. However, the validity of these assumptions is theoretically questionable and difficult to justify, especially in light of recent experiments using nano-sized particles [4, 5] and with large particle concentrations [6-8].

Experiments in which a small amount of aluminum powder was injected into a shock tube and heated by a reflected shock have indicated that the aluminum particle combustion regime shifts from being predominantly diffusion controlled to a kinetically-controlled reaction regime when the particle size is reduced to a value below about ten microns [9]. In contrast with isolated single particles, the reaction of a particle suspension modifies the ambient gas environment by reducing the concentration of oxidizer and increasing the temperature, which in turn influences the particle combustion rate [10]. The combustion regime for a particle suspension with a given initial particle size may change as the particles burn out and may also differ from the combustion regime of an isolated particle with the same size.

Recent experimental observations of flames in hybrid combustible gas-solid fuel mixtures have shown that the combustion physics of the solid suspension depends critically on the initial mass concentration of the solid fuel [7]. For the case of aluminum particles, the particle combustion regime within a methane-air-aluminum flame changes rapidly when the particle concentration reaches a critical threshold value of about  $150 \text{ g/m}^3$  [7], shifting from a relatively slow oxidation regime, characteristic of an isolated single particle within the same gaseous environment, to a relatively fast reaction regime associated with a flame front. An analogous transition is also observed in suspensions of iron powder in methane-air mixtures indicating that the phenomenon is of a general nature and is not fuel specific [8]. These results also suggest that the common practice of introducing externally-defined parameters, such as *ignition temperature*, *ignition delay*, and *burn time*, obtained from single-particle experiments into reaction models for metalized energetic compositions may be inadequate for cases in which a dense particle suspension is formed.

The goal of the present paper is to use a simple, transparent model to describe the characteristics of the combustion of fuel particle suspensions and to illustrate how distinct combustion phenomena may arise that do not occur during the combustion of a single

particle. The model does not represent a comprehensive description of the combustion of a specific fuel, but rather demonstrates in general terms how the mass concentration of a solid fuel can influence the reaction behavior and combustion regime of the particle suspension with different particle sizes. To accomplish this, it is assumed that the particles undergo a purely heterogeneous reaction with a gaseous oxidizer through one-step surface Arrhenius kinetics which avoids the complications introduced by phase transitions, multistage kinetics, and the complex thermodynamics typical of “real” systems [11]. Through this analysis, it is theoretically shown that the general terms *ignition temperature*, *combustion time*, and *ignition delay*, adapted from combustion models for large single particles, may be inadequate to describe the complex phenomena associated with the combustion of particle suspensions and for small particle sizes.

The present work illustrates the diverse combustion characteristics associated with adiabatic, constant-volume combustion of a stationary particle suspension for a particular choice of values for the reaction rate and other physical parameters associated with the solid and gaseous components. The effect of applying a rate of heat loss is also examined to illustrate how the combustion of a suspension might behave in a real system subject to, for example, expansion cooling. However, systematic parametric analysis of possible combustion phenomena that may arise in different experimental situations following detonation and deflagration events is beyond the scope of the present work.

## 2. MODEL AND RESULTS

### *Kinetic-Diffusion Reaction Rate*

The general treatment of heterogeneous reactions governed by the competition between transport and kinetic rates, and the associated thermal regimes and critical nature of regime change, is thoroughly investigated in the classical work of Frank-Kamenetskii [12] and further analyzed in Vulis [13]. A similar approach is applied here in a simplified form to analyze and interpret different reaction regimes for the case of a single particle and a particulate suspension.

As stated above, it is assumed that oxidizer consumption rate by chemical reaction on the particle surface is described by a single-step first-order Arrhenius reaction, i.e.,

$$\frac{dm}{dt} = C_s A k \quad (9)$$

$$k = k_0 \exp\left(\frac{-E_a}{RT_s}\right) \quad (10)$$

Here,  $C_s$  is the concentration of the oxidizer at the particle surface,  $A$  is the particle surface area, and  $k$  is the kinetic reaction rate, which depends on the activation energy  $E_a$  and the particle temperature  $T_s$ . Following the assumption made by Frank-Kamenetskii of quasi-static equilibrium [12], the concentration of the oxidizer at the particle surface  $C_s$  is found from the balance between the rate of consumption of the oxidizer by the chemical reaction in Eq. (9) and the rate of transport of the oxidizer to the particle surface by molecular diffusion and convection, i.e.,

$$AC_s k = A\beta(C_0 - C_s) \rightarrow C_s = C_0 \left( \frac{\beta}{k + \beta} \right) \quad (11)$$

where  $\beta$  is the mass-transfer coefficient between a particle and the gas, per surface area, and  $C_0$  is the volumetric concentration of the oxidizer in the flow. By introducing the expression for  $C_s$  from Eq. (11) into Eq. (9), the unified reaction rate, taking into account both the kinetic reaction and diffusion “resistances”, may be written as

$$\frac{dm}{dt} = AC_0 \beta Da^* \quad (12)$$

where  $Da^* = k/(k + \beta)$ . The normalized Damköhler parameter  $Da^*$  is related to the traditional Damköhler number,  $Da = k/\beta$ , by the expression  $Da^* = Da/(1 + Da)$ . The value of  $Da^*$  is close to unity when the reaction rate is controlled by the diffusion of the oxidizer (i.e., the diffusion regime where  $k \gg \beta$ ) and approaches zero when the rate of particle oxidation is determined by Arrhenius surface reaction rate (i.e., the kinetic regime where  $\beta \gg k$ ).

For the sake of simplicity, the contribution of the Stefan convective flow [12] to the heat and mass transfer between the particle and the gas is neglected. The Stefan flow is negligible when the concentration of the oxidizer in the flow is low and/or the volume of reacted gas oxidizing on particle surface is closely matched by the volume of the gaseous reaction products formed. In the absence of the Stefan flow, the mass and heat exchange coefficients between a particle and the gas take the following simple form:

$$\beta = \frac{Sh D}{2r} \quad (13)$$

$$h = \frac{Nu \lambda}{2r} \quad (14)$$

where the Nusselt (Nu) and Sherwood (Sh) numbers are calculated assuming spherical particles which are stationary relative to the gas (Nu=Sh=2). At Lewis numbers close to unity, and under the particle lumped-capacitance assumption, the profiles of the temperature field and oxidizer concentration around a particle are similar in all oxidation regimes, as shown in Figure 1.

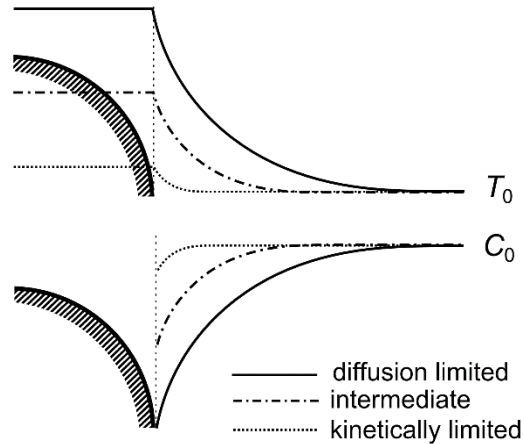


Figure 1. Temperature and oxidizer concentration profiles adjacent to the particle surface for different combustion regimes.

In the *diffusion-limited* stationary reaction regime, the concentration of the oxidizer at the particle surface is close to zero, and the particle temperature is close to the maximum adiabatic flame temperature of the stoichiometric mixture [13]. In the *kinetically-limited* regime, where diffusion is much faster than the rate of chemical reaction, the oxidizer concentration at the particle surface is close to the concentration within the bulk flow and the temperature difference between the particle and gas does not exceed one characteristic temperature interval,  $\Delta T \leq RT_{g0}^2 / E_a$  [13, 14].

### Ignition of a Single Particle

The transition from the kinetically-limited to the diffusion-limited reaction regime occurs as a discontinuous jump at a critical particle temperature and is the classic definition of the *ignition* of a particle. The corresponding critical gas temperature is denoted the *ignition temperature*. The reverse discontinuous transition from diffusion-limited to kinetically-limited reaction is called *extinction*. The Semenov thermal ignition diagram, shown in Fig. 2(left) adapted for the kinetic/diffusive particle reaction rate, qualitatively illustrates both the critical ignition and extinction points for a single particle and the subsequent transition into stable regimes. It is important to note that once *ignition* occurs (i.e., the jump to the diffusion-limited burning regime), the particle will also undergo extinction and return to the kinetically-limited burning regime when it reaches a critical size due to particle burnout. This is not reflected in the classical particle ignition theory which is only formulated to determine ignition temperatures and stationary states and ignores the changing particle mass with time [15]. With the inclusion of time-dependent particle burnout, for large initial particle sizes, the mass of the extinguished particle is negligibly small in comparison to the initial mass. However, for decreasing initial particle sizes, extinction occurs more rapidly after ignition, leading to a non-negligible mass of the extinguished particle which burns in the kinetically-limited regime.

There is a critical particle size for which the ignition and extinction temperatures coincide, illustrated in Fig. 2(right), leading to the existence of a limit where the particle is unable to *ignite* at any gas temperature. The breakdown of the ignition criticality is derived from the particle ignition conditions and reflects the dependence of the particle temperature

on the gas temperature for the classical stationary model for particle ignition. Below this critical size, there is no ignition temperature as the particle temperature is a monotonically increasing function of the gas-phase temperature and is not significantly different from the gas temperature which is expected in a purely kinetically-limited combustion regime.

The particular set of numerical values for the thermodynamic and transport constants of the gas and solid phase used to calculate the curves in Fig. 2(right) are shown in Table 1 and are also used in the subsequent examples in this paper. The values of the thermodynamic parameters are typical for metal fuels, and with the particular values of the reaction constants chosen, both the diffusion and kinetic combustion regimes occur with micron-sized particles, where the molecular mean free path is still much smaller than the particle radius and, therefore, Knudsen diffusion effects can be neglected.

Table 1. Numerical values of the gas and solid fuel parameters.

Property	Value	Property	Value
$\lambda$	$0.0238 \text{ W}^1\text{m}^-$	$T_0$	300 K
$c_g$	$1010.08 \text{ J}^1\text{kg}^-$	$c_s$	$978.56 \text{ J}^1\text{kg}^-$
$D$	$2.01 \times 10^{-5}$	$k_0$	$70 \text{ m}^1\text{s}^{-1}$
$\rho_g$	$1.172 \text{ kg}^1\text{m}^{-3}$	$\rho_s$	$2700 \text{ kg}^1\text{m}^{-3}$
$T_{g0}$	2100 K	$\gamma$	1.12
$C_0$	$0.27 \text{ kg}^1\text{m}^{-3}$	$q$	$3.10 \times 10^7$
$\alpha$	$2.01 \times 10^{-5}$	$E_a/R$	15000 K

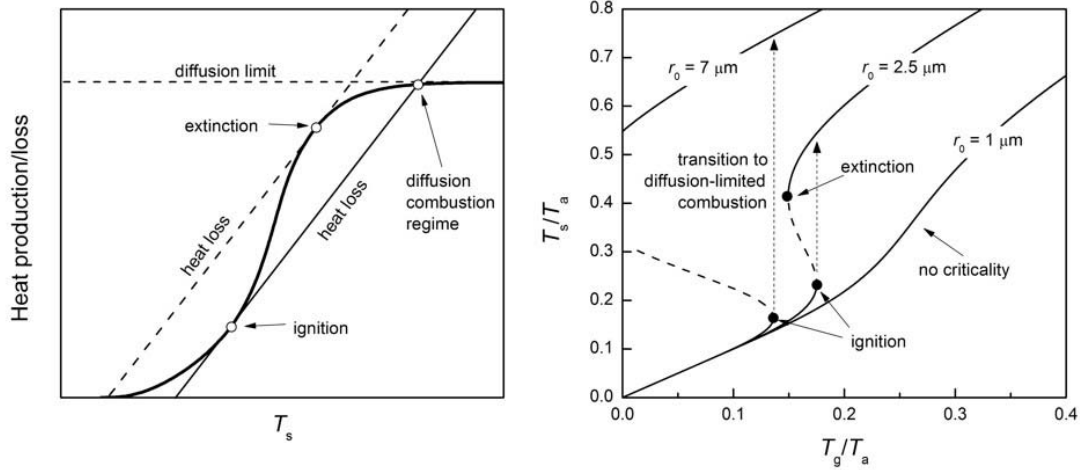


Figure 2. (left) Semenov diagram of the single particle ignition and extinction. (right) dependence of the particle temperature on gas temperature illustrating disappearance of the critical ignition and extinction points below some critical particle size (unstable regimes are marked with dashed lines). The temperatures are scaled by the activation temperature  $T_a = E_a/R$ .

The ignition temperature calculated from the balance between the rates of heat production and heat loss and their derivatives is plotted in Fig. 3 as a function of particle size. It is evident that the particle ignition temperature increases with decreasing particle size, reflecting the fact that the heat loss per unit particle surface area increases proportionally to  $1/r$ . For the set of numerical parameters chosen, the heat loss rate exceeds the heat production rate for any particle temperature when the particle size is below a critical size of about  $1.9 \mu\text{m}$ , and ignition, or a transition to diffusion-limited combustion, becomes impossible.

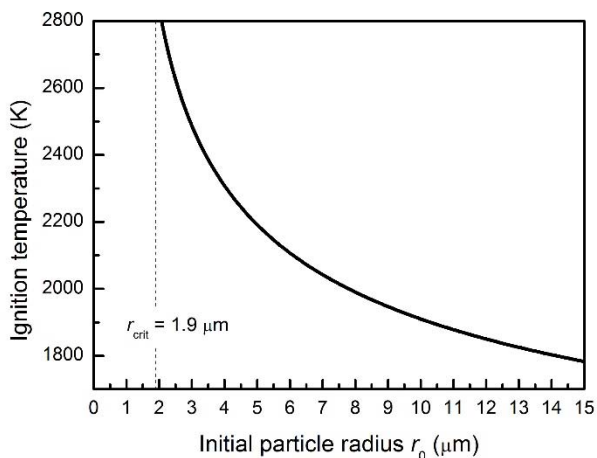


Figure 3. Dependence of the ignition temperature on particle size. Note that below a critical value of the particle radius of  $1.9 \mu\text{m}$  ignition is impossible.

If a particle below this limiting size is injected into a hot oxidizing gas it will heat slightly above the gas temperature and will undergo oxidation within the kinetic reaction regime without igniting. The time history of the temperature and radius of a single particle is plotted in Fig. 4 for three different particle sizes corresponding to different combustion regimes. The smallest particle undergoes a stable kinetically-limited oxidation process (Fig. 4A). The largest particle ignites leading to a stable diffusive combustion regime with  $\text{Da}^*$  near to unity, which then quenches when the particle size is less than 10% of the initial value (Fig. 4C). For an intermediate particle diameter, an intermediate transient regime occurs in which the particle ignites, but extinguishes prior to reaching a fully-developed diffusive-combustion regime (Fig. 4B).

The length of the kinetically-limited reaction “tail” depends exponentially on the ambient gas temperature and, thus, is usually very long for single particles or for a dilute suspension in which the self-heating of the mixture is negligible. In the transient combustion regime observed in Fig. 4B, the time for complete oxidation of the particle in the kinetic regime is usually much longer than for larger particles.

It should be noted that the particle size defining the border between the diffusion- and kinetically-limited combustion regimes is not only a function of the reaction parameters but also depends on the heat exchange coefficient between the particles and gas. As an example, the detonation of metalized explosives typically results in much larger gas-

particle slip velocities, in comparison with metalized propellants that undergo deflagration, resulting in a shift of the border between the two regimes towards larger particle sizes [16].

#### *Reaction of a Dense Particulate Suspension*

The dynamics of the solid-fuel reaction change completely if the initial concentration of the solid fuel is sufficient to significantly influence the gas temperature through the particle heating and subsequent heat release by the particle reaction. The effective reaction rate derived in the previous section is given in Eq. (7). The algebraically reduced conservation of energy equations describing the change of the particle temperature  $T_s$  by heat from the reaction and convective heat loss to the gas is given in Eq. (8) and its changing radius  $r$  due to mass consumption is given in Eq. (9). These must be supplemented with equations describing the time dependent temperature of the gas  $T_g$  heated convectively by the particles shown in Eq. (10) and the depletion of the oxidizer mass concentration  $C$  due to the reaction shown in Eq. (11).

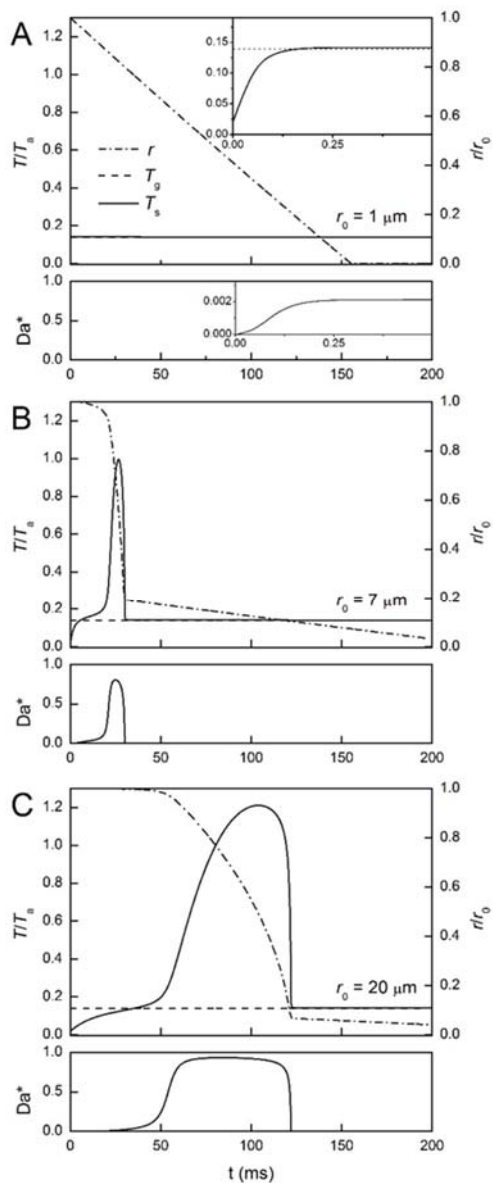


Figure 4. Time histories of the temperature (scaled to the activation temperature  $T_a$ ), radius and normalized Damköhler parameter for a single particle with different sizes injected into a hot oxidizing gas flow illustrating the different possible reaction regimes: a) a small particle ( $1 \mu\text{m}$  radius) that oxidizes within the kinetic regime, b) an intermediate sized ( $7 \mu\text{m}$ ) particle that ignites and quenches, and c) a large particle ( $20 \mu\text{m}$ ) that ignites and burns within the diffusive regime.

$$k_{eff} = \frac{k\beta}{k + \beta} = \frac{\text{Sh} \frac{D}{2r} k_o \exp(\frac{-E_a}{RT})}{k_o \exp(\frac{-E_a}{RT}) + \text{Sh} \frac{D}{2r}} \quad (15)$$

$$\frac{dT_s}{dt} = 3 \frac{\gamma q}{c_s \rho_s} k_{eff} \frac{C}{r} - 3 \frac{T_s}{r} \frac{dr}{dt} - \frac{3}{2} \frac{\lambda}{c_s \rho_s} \text{Nu} \frac{(T_s - T_g)}{r^2} \quad (16)$$

$$\frac{dr}{dt} = - \frac{\gamma}{\rho_s} k_{eff} C \quad (17)$$

$$\frac{dT_g}{dt} = \frac{3}{2} \frac{B\alpha}{\rho_s r_o^3} \text{Nu} (T_s - T_g) r \quad (18)$$

$$\frac{dC}{dt} = - \frac{3B}{r_o^3 \rho_s} k_{eff} r^2 C \quad (19)$$

The governing equations are written with a constant volume approximation and the assumption that the pressure increase does not change the reaction kinetics or the heat and mass transfer constants. The exclusion of the gas-dynamic effects that are specific to a particular experimental situation allows us to focus primarily on the effect of particle mass concentration  $B$  in the combustion dynamics of the suspension.

The time histories of the particle temperature, radius, concentration and the normalized Damköhler parameter are determined by numerically integrating equations 7–11 with the assumption that the initially cold particle suspension is suddenly exposed to a hot gas. The results are shown in Fig. 5 for the same three different particle sizes considered for the reaction of a single particle in Fig. 4. For the purposes of this illustration, we assume that the fuel suspension is lean with a mass concentration of 200 kg/m<sup>3</sup>, corresponding to about two-thirds of the stoichiometric value and with an initial gas temperature of 2100 K, which is characteristic of hydrocarbon flames.

As seen from Fig. 5A for a small particle size, in contrast with a single particle, the dense suspension of kinetically-reacting particles undergoes a rapid reaction onset and a corresponding sharp temperature increase. Although this behavior has the appearance of an ignition event, the rapid rise of the reaction rate of the small particles within the suspension lacks criticality as the value of the Damköhler parameter does not exceed 0.2 and, thus, the combustion process remains close to the kinetically-limited reaction regime. The nature of the sharp reaction onset in this case is analogous to that of a reactive gas mixture heated under adiabatic conditions. After a certain delay time during which the mixture slowly oxidizes, the reaction proceeds rapidly in an explosion-like manner reflecting the self-accelerating nature of Arrhenius kinetics at high activation energies and large heats of reaction. The adiabatic reaction delay time in this case can be estimated using the same well-known formula for gaseous mixtures if the reaction delay time is significantly longer than the particle heating time [14].

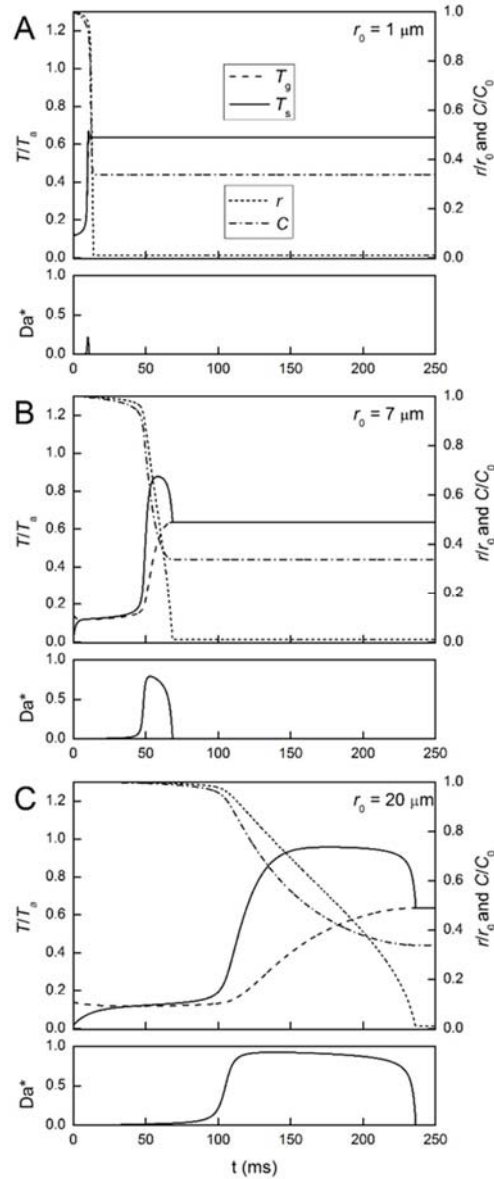


Figure 5. Reaction of an instantaneously heated suspension of solid fuel particles with a solid fuel concentration of  $200 \text{ g/m}^3$  with three different particles sizes, resulting in combustion regimes that are a) kinetically-limited, b) intermediate, and c) diffusively-limited.

For large particles, which have the ability to ignite and burn within the diffusion-limited regime, there is a complex interplay between the onset of the reaction due to the particle cloud effect and the individual particle ignition (Fig. 5C). The calculations indicate that, for any given particle concentration, the cloud effect leading to a reduction in the reaction delay diminishes with increasing initial particle size, where eventually the single particle combustion will behave in a similar fashion as the suspension. For suspensions of intermediate-sized particles, the diffusive-combustion regime is followed by extinction and kinetically-controlled combustion of the remaining fuel similar to the case of a single

particle (Fig. 5B). However, unlike a single particle, the transition to the kinetically burning branch of the suspension does not result in a long kinetic reaction particle burnout “tail” but proceeds rapidly due to much higher gas temperatures.

An important parameter for practical particle combustion applications is the sum of the delay and reaction times which indicates how rapidly the solid fuel energy is released for a particular energetic system. This is denoted for sake of brevity as the “combustion time”. The combustion time calculation is limited to the point when 90% of the particle mass is consumed in order to exclude the disproportional contribution of the long, kinetic-reaction “tail” during which a relatively small amount of fuel is consumed after particle extinction. The dependence of the combustion time on particle size is plotted in Fig. 6 for different solid fuel concentrations.

From Fig. 6, the overall combustion time of a single particle initially rises with particle radius, but then sharply drops after the initial particle size crosses a critical threshold at which point the particle does not extinguish and instead burns primarily in a diffusion-limited regime. After this drop, the combustion time slowly increases for increasing particle sizes although this is not readily apparent on the semi-log vertical scale on Fig. 6. The fraction of the particle mass that burns in the fast diffusive regime increases with particle size within this size range, compensating for both the increased heating and reaction times. With an increase in fuel concentration within the suspension (and therefore gas temperature), the advantage of the diffusion-combustion regime diminishes and, for high particle concentrations, the overall combustion time increases monotonically with particle size.

The same interplay between kinetically- and diffusively-limited combustion regimes at different fuel concentrations explains why the combustion time dependence with respect to concentration intersects for two different particle sizes, as shown in Fig. 7. At low fuel concentrations and, thus, lower gas temperatures, the large particles have an advantage. They can ignite and burn faster in the diffusion regime than kinetically-reacting particles at lower temperatures. At high fuel concentrations and, thus, high gas temperatures, the advantage of the diffusive combustion disappears and small particles react more rapidly due to their higher specific surface area.

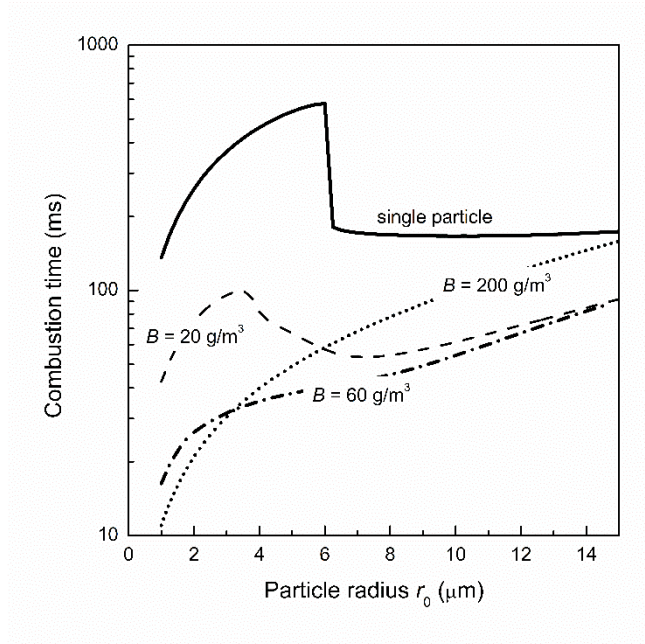


Figure 6. Dependence of combustion time on particle size at different solid fuel concentrations.

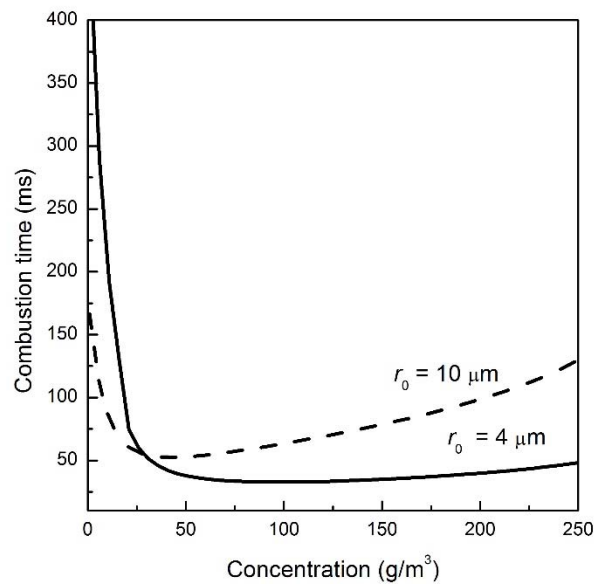


Figure 7. Dependence of combustion time on concentration of the solid fuel for particle sizes of 4 and 10  $\mu\text{m}$ .

Figure 7 also exhibits an initial sharp drop in the overall combustion time with an increase in the fuel concentration for both particle sizes. The combustion time for a suspension of 4  $\mu\text{m}$  particles reacting primarily in the kinetic mode decreases by about an order of magnitude in contrast with a single particle. The exponential dependence of the reaction delay time on the gas temperature, which is proportional to the fuel concentration,

is a clear demonstration of the “cloud” or “collective” effect on the combustion process. The drop in combustion time will be even stronger if the increase of the heat and mass transfer coefficients with temperature and pressure are taken into account. Accounting for the “cloud effect” may explain the extremely low combustion times observed experimentally for aluminum particles burning within the products of metalized explosives that are difficult to reconcile with the much longer times derived from experiments with single particles [17]. The recently proposed hypothesis [18, 19] that the short reaction times are due to the cracking of the protective alumina shell by a shock wave resulting in faster oxidation kinetics cannot explain why combustion times of the same order are observed during the detonation of aluminum suspensions in air where the shock pressure is lower by almost three orders of magnitude [20]. In addition, it is well known that protective oxide films can swiftly re-establish on the metal surface if the conditions are not optimum for the particle ignition [21].

### *Reaction of a Suspension in a Cooling Gas*

In a real experimental situation, the system is non-adiabatic and the temperature of the gas decreases with time due to heat loss or may fall sharply due to the expansion of the gas products as in the case of a detonation event. Modeling the complex flow dynamics of explosive formulations is outside the scope of this paper but, in the context of the present model, the general considerations of what may occur during the combustion of a suspension in such a system can be examined through the addition of a simple convective cooling rate of the gas phase as shown in equation (12) which is a modified form of equation (10), i.e.,

$$\frac{dT_g}{dt} = \frac{3}{2} \frac{B\alpha}{\rho_s r_0^3} \text{Nu}(T_s - T_g)r - h_w(T_g - T_0) \quad (20)$$

Here, the  $h_w$  is an arbitrary heat transfer coefficient, and  $T_0$  is the ambient temperature. The addition of the cooling rate in this simple form is not connected to any particular experimental situation, but serves to qualitatively demonstrate the type of analysis that can be performed to find optimum particle sizes for a given particle loading. The introduction of the cooling rate affects the ability of the particles to react to completion before the gas temperature drops below the point at which the reaction rate is negligible. The cooling of the gas may also lead to a longer reaction onset time in which case the particles will never react within the given time frame. Among several parameters, including the initial gas temperature and reaction constants, the major factors affecting the reaction completeness within a given time are the particle size and mass concentration of the fuel within the suspension. Although the particle size has long been recognized as a critical parameter, the fuel concentration within the suspension is typically neglected. To analyze this situation, a criterion is set such that if burnout of 90% of the particle mass does not occur within the assigned time frame, then it is considered to be unburned. The resulting combinations of particle size and concentration for which particle burnout occurs (shaded regions) are plotted in coordinates of particle size vs. mass concentration in Fig. 7 for three different cooling rates. Particle sizes below 1  $\mu\text{m}$  were not considered in the calculation.

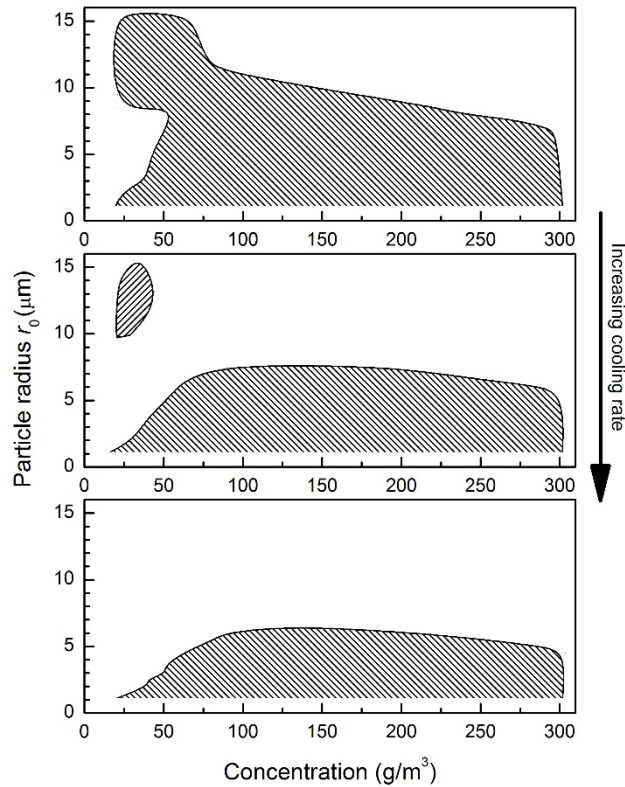


Figure 8. The transformation of the range of particle sizes and concentrations (shaded area) where 90% of the solid fuel mass is burned within 500 ms with a 20% and 40% increase of the cooling rate.

This is by no means a comprehensive analysis of the model as the set reaction time window and cooling rates are arbitrary, but it does show that the outcomes are not necessarily intuitive. The resulting particle size/concentration combinations for both the lowest and intermediate cooling rates indicate that at lower concentrations, it is actually more beneficial to use larger particle sizes since the smaller, more kinetically-limited particles do not burn to completion. In the intermediate case, at low concentrations, there is an isolated “island” of large particle sizes that burnout. This island continually shrinks with increasing cooling rate until, for a certain range of concentrations, there will only be a very small range of optimum particle sizes. In the case of the highest cooling rate, it is seen that only relatively small particle sizes have the ability to react to completion.

### 3. CONCLUSIONS

The primary conclusion of the present work is that the onset of the chemical reaction in a rapidly heated particulate suspension may occur by two different physical mechanisms. The first mechanism, realized in a dilute suspension of particles, is defined by the ignition of a single particle, i.e., by the critical phenomenon associated with the rapid transition from a kinetically- to diffusively-limited reaction regime. The second mechanism dominates the reaction onset in a dense particulate suspension and occurs in a similar

manner to the reaction onset in a rapidly-heated homogeneous gas mixture, where the highly-activated reaction occurs in an explosion-like manner after some delay and self-heating. Unlike the ignition phenomenon, the second mechanism lacks criticality and is not limited to particles above a certain size. The interplay between these two reaction onset mechanisms leads to a nontrivial dependence of the total reaction time on the particle size and fuel concentration within the suspension.

#### 4. REFERENCES

- [1] R. Eckhoff, *Dust Explosions in the Process Industries*. Gulf Professional Publishing, Boston **2003**.
- [2] R. Friedman and A. Maček, Ignition and Combustion of Aluminium Particles in Hot Ambient Gases. *Combust. Flame* **1962**, *6*, 9-19.
- [3] T.A. Roberts, R.L. Burton, and H. Krier, Ignition and Combustion of Aluminum/Magnesium Alloy Particles in O<sub>2</sub> at High Pressures. *Combust. Flame* **1993**, *92*, 125-143.
- [4] C. Kong, Q. Yao, D. Yu, and S. Li, Combustion Characteristics of Well-Dispersed Aluminum Nanoparticle Streams in Post Flame Environment. *Proc. Combust. Inst.* **2014**, DOI: 10.1016/j.proci.2014.06.127.
- [5] G. Young, K. Sullivan, M.R. Zachariah, and K. Yu, Combustion Characteristics of Boron Nanoparticles. *Combust. Flame* **2009**, *156*, 322-333.
- [6] M. Soo, P. Julien, S. Goroshin, J.M. Bergthorson, and D.L. Frost, Stabilized Flames in Hybrid Aluminum-Methane-Air Mixtures. *Proc. Combust. Inst.* **2013**, *34*, 2213-2220.
- [7] P. Julien, M. Soo, S. Goroshin, D.L. Frost, J.M. Bergthorson, N. Glumac, and F. Zhang, Combustion of Aluminum Suspensions in Hydrocarbon Flame Products. *J. Propul. Power* **2014**, *30*, 1047-1054.
- [8] P. Julien, S. Whiteley, S. Goroshin, M.J. Soo, D.L. Frost, and J.M. Bergthorson, Flame Structure and Particle-Combustion Regimes in Premixed Methane-Iron-Air Suspensions. *Proc. Combust. Inst.* **2014**, DOI: 10.1016/j.proci.2014.05.003.
- [9] T. Bazyn, H. Krier, and N. Glumac, Evidence for the Transition from the Diffusion-Limit in Aluminum Particle Combustion. *Proc. Combust. Inst.* **2007**, *31*, 2021-2028.
- [10] H.M. Cassel and I. Liebman, The Cooperative Mechanism in the Ignition of Dust Dispersions. *Combust. Flame* **1959**, *3*, 467-475.
- [11] B.T. Bojko, P.E. DesJardin, and E.B. Washburn, On Modeling the Diffusion to Kinetically Controlled Burning Limits of Micron-Sized Aluminum Particles. *Combust. Flame* **2014**, *161*, 3211-3221.
- [12] D.A. Frank-Kamenetskii, *Diffusion and Heat Transfer in Chemical Kinetics*. Plenum Press, New York **1969**.
- [13] L.A. Vulis, *Thermal Regimes of Combustion*. McGraw-Hill, New York **1961**.
- [14] Y.B. Zeldovich, G.I. Barenblatt, V.B. Librovich, and G.M. Makhviladze, *Mathematical Theory of Combustion and Explosions*. Consultants Bureau, New York **1985**.
- [15] L.P. Yarin and G. Hetsroni, *Combustion of Two-Phase Reactive Media*. Springer-Verlag, Berlin **2004**.

- [16]V. Tanguay, S. Goroshin, A.J. Higgins, and F. Zhang, Aluminum Particle Combustion in High-Speed Detonation Products. *Combust. Sci. Technol.* **2009**, *181*, 670-693.
- [17]M. Beckstead, Correlating Aluminum Burning Times. *Combust. Explo. Shock.* **2005**, *41*, 533-546.
- [18]S.K. Chan, Reaction Delay of Aluminum in Condensed Explosives. *Propellants Explos. Pyrotech.* **2014**, *39*, 897 DOI: 10.1002/prop.201400093.
- [19]R.C. Ripley, F. Zhang, and F.-S. Lien, Acceleration and Heating of Metal Particles in Condensed Matter Detonation. *Proc. R. Soc. A* **2012**.
- [20]F. Zhang, K. Gerrard, and R.C. Ripley, Reaction Mechanism of Aluminum-Particle-Air Detonation. *J. Propul. Power* **2009**, *25*, 845-858.
- [21]B. Delmon, *Introduction À La Cinétique Hétérogène*. Editions Technip, Paris **1969**.

## Chapter 3. Thermal Structure of Flames in Non-Volatile Fuel Suspensions

### 1. INTRODUCTION

Understanding the mechanisms controlling flame propagation in suspensions of non-volatile fuels is crucial to obtaining efficient combustion of metallized propellants [1], slurry fuels [2], pulverized coal [3], and powdered metals as carbon-free chemical energy carriers [4]. It is also necessary for the mitigation of catastrophic explosions in coal mines or in process industries that involve handling metallic dusts and other combustible solid powders [5].

Like gas flames, flames in particulate suspensions at the laboratory scale are primarily driven by molecular heat diffusion and have comparable burning velocities [4]. Nevertheless, they exhibit several significant differences in their structure and behavior from homogeneous flames due to their multiphase nature.

The main distinctive feature of a flame in a solid suspension is the ability of particles to ignite, that is, to transition from a combustion regime limited by reaction kinetics to a regime limited by diffusion of the oxidizing gas towards the particle surface, or in the case of evaporating particles, towards the micro-flame enveloping each individual particle.

After ignition, the temperature of the particle or micro-flame can exceed the gas temperature by several hundred degrees, often surpassing the adiabatic flame temperature for fuel-lean mixtures. The particle combustion rate in the diffusion combustion regime is a weak, non-Arrhenius, function of gas temperature. Unlike gas flames, the width of the flame reaction zone in the particle suspension can span a large temperature change and can be comparable to, or even exceed, the width of the preheat zone [6]. The existence of diffusion micro-flames within a global flame front (in effect, flames within the flame), which are insensitive to the bulk gas temperature, makes dust flames resistant to heat loss [7]–[9] and also serves to maintain a constant burning velocity with increasing fuel concentration in fuel-rich mixtures [10]. The ability of particles to ignite, in conjunction with low ignition temperatures, may result in much wider flame propagation limits in particle suspensions than for gaseous fuels [10].

Despite the overall qualitative understanding of the crucial role of the particle combustion regime on dust flame speed and thermal structure, the theoretical description of flames in particulate suspensions has been limited to simple semi-empirical models that postulate either purely diffusion or purely kinetic modes of particle combustion [10], [11]. The diffusive combustion models presume that particles within the suspension ignite and transit to the diffusion regime instantaneously when they reach the ignition temperature of a single, isolated particle. The common assumption is that, after ignition, the particle within the suspension will have a combustion time equal to that of an isolated single particle. Using this approach, particle ignition temperature and combustion time are considered to be external parameters that are independent of the flame-propagation mechanism. As such,

they often are taken from experiments with individual particles or calculated using theoretical models for single particle combustion. These assumptions are useful for estimation, but are, in general, not justified and may lead to erroneous predictions. In reality, the particle ignition temperature in the flame, particle reaction time, and the actual regime of particle combustion are all characteristic values of the flame propagation problem directly linked to the burning velocity eigenvalue. Moreover, the particle combustion regime may alternate throughout the flame. For example, the particle may start to react in a kinetically limited regime, then transit to a combustion mode partially limited by diffusion, before returning to a predominantly kinetically limited combustion mode [7]. As a result, a non-negligible fraction of the particle mass may be consumed during both diffusive and kinetic combustion, leading to a complex dependence of the flame speed on particle size and concentration, as demonstrated in this study.

In this paper, the thermal structure of a flame in a particulate suspension is investigated using a simplified, transparent model that assumes that non-volatile solid fuel particles react via a single-step Arrhenius surface reaction with gaseous oxidizer delivered to the particle surface by diffusion. Besides incorporating heterogeneous reaction kinetics, the model does not impose *a priori* the particle combustion mode or any other external combustion parameters. The flame propagation problem is solved numerically in a non-stationary formulation initially proposed by Spalding [12]. This approach avoids the difficulties inherent with a steady-state formulation and permits the investigation of flame stability, which has led to the discovery of a new type of oscillating flame in a heterogeneous mixture.

## 2. MODEL FORMULATION

### *Combined Kinetic-Diffusive Reaction Rate*

Following the quasi-stationary approach of Frank-Kamenetskii [8], the overall reaction rate per unit surface area of a particle in an oxidizing gas, accounting for both kinetic and diffusion “resistances” can be written as

$$\dot{\omega} = \gamma \frac{\kappa\beta}{\kappa + \beta} C_0 \quad (21)$$

where  $\dot{\omega}$  is the particle mass consumption rate per unit surface area,  $\gamma$  is the stoichiometric coefficient, and  $C_0$  is the concentration of oxidizer in the bulk gas far from the particle surface [ ]. The kinetic term,  $\kappa$ , is the overall Arrhenius surface reaction rate,  $\kappa = k_0 \exp(-E_a / RT_s)$ , where  $k_0$  is the pre-exponential factor,  $E_a$  is the activation energy, and  $R$  is the universal gas constant. The term  $\beta$  is the mass transfer coefficient between a particle and the gas.

For simplicity, the contribution of Stefan flow to the heat and mass transfer between the particle and the surrounding gas is assumed to be negligible. Stefan flow is small when the molecular weight of the reaction products is close to that of the consumed oxidizer or when the initial oxidizer concentration is relatively low [8]. In the absence of Stefan flow,

the mass transfer coefficient takes the simple form,  $\beta = \text{Sh}D_l/2r$ . Here  $D_l$  denotes the oxidizer diffusivity at the particle-gas interface, and  $r$ , the particle radius. For a spherical particle that is stationary relative to the gas, the exact solution to the steady-state diffusion equation yields a Sherwood number (Sh) equal to 2.

The reaction rate in Eq. (1) can then be written in terms of the normalized Damköhler number  $\text{Da}^*$ , which is related to the traditional Damköhler number,  $\text{Da} = \kappa / \beta$  by  $\text{Da}^* = \text{Da}/(1+\text{Da})$  [13]. The resulting expression for the heat release rate per unit of particle surface area is:

$$Q_r = q\dot{\omega} = q\gamma\beta\text{Da}^*C_0 \quad (22)$$

where  $q$  is the heat of reaction.

This formulation naturally incorporates the two limiting kinetic and diffusive regimes. In a kinetically controlled regime ( $\beta \ll \kappa$ ),  $\text{Da}^*$  approaches zero ( $\text{Da}^* \approx 0$ ). In the diffusion limit ( $\kappa \ll \beta$ ), the reaction rate is primarily governed by diffusive transport of oxidizer and  $\text{Da}^*$  approaches unity ( $\text{Da}^* \approx 1$ ).

#### *Ignition and Combustion of a Single Particle*

The reaction of a suspension of particles within the flame is fundamentally different from the reaction of an isolated single particle [13]. However, mapping the reaction regimes for a single particle is crucial to understanding this difference and interpreting the flame structure in a suspension. The interplay between kinetic and diffusion reaction rates of heterogeneous chemical reactions leading to the processes of ignition and extinction was first investigated by Frank-Kamenetskii [8] and then analyzed further by Vulis [9]. Their analyses are adapted here in a simplified form to interpret the reaction behavior of a single particle injected into a hot oxidizing gas.

The modified Semenov diagram shown in Fig. 1 plots the reaction heat release rate that accounts for both kinetic and diffusive rates as a function of the particle temperature,  $T_s$ . At low temperatures, the reaction rate increases exponentially with  $T_s$  due to Arrhenius kinetics. At high temperatures,  $\text{Da}^*$  approaches unity and the reaction rate in Eq. (2) becomes practically independent of temperature. If the heat loss from radiation is negligible, as is the case for moderate temperatures and small particles, then the heat loss rate is proportional to the temperature difference between the particle and gas and is plotted in Fig. 1 as straight lines:  $Q_l = h(T_s - T_g)$ . Here  $h$  is the heat transfer coefficient  $h = \text{Nu}\lambda_l/2r$ , where  $\lambda_l$  is the thermal conductivity of the gas at the gas-solid interface. The Nusselt number (Nu) is equal to 2 for a spherical particle that is stationary relative to the gas.

At some critical gas temperature, known as the ignition temperature, the heat loss and the heat release curves become tangent (point *I* on Fig. 1). The particle starts to accumulate heat and promptly transitions from a predominantly kinetic combustion regime to a predominantly diffusive regime with temperatures close to the adiabatic temperature

of the stoichiometric mixture (point  $D$  on the Semenov diagram). Once ignited, the burning particle inevitably extinguishes when its radius reduces to the point ( $r_1$ ) where the heat loss and heat release curves become tangent again, albeit at a higher particle temperature (point  $E$ ). After extinction, the particle will transit to a kinetic burning regime (point  $K$ ). For large particles, the extinction radius is small in comparison to the initial particle size and thus the residual particle mass at extinction is negligible since  $m \sim r^3$ . For smaller particles, the mass of the extinguished particle may not be negligible relative to the initial particle mass. If the initial particle size is reduced even further, the slope of the heat loss curve becomes so steep that tangency of the heat release and heat loss curves becomes impossible. Below this critical radius, the particle cannot ignite at any gas temperature (see inset in Fig. 1) [ ].

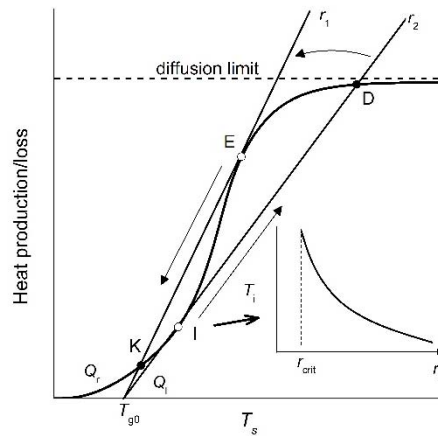


Figure 37. Modified Semenov diagram illustrating particle ignition (I) at some critical temperature and transition to near the diffusion limit (D). Extinction (E) occurs as the particle shrinks and undergoes the reverse transition to the kinetic limit (K). Stable states are shown by (●) while unstable states are denoted by (○). Inset: ignition temperature as a function of particle size showing critical radius below which ignition is impossible.

The particle temperature history for three different initial sizes injected into a hot oxidizing gas is illustrated in Fig. 2. The first case corresponds to a large particle that undergoes heating, then ignites and reacts to completion almost entirely in the diffusive regime. The second case corresponds to an intermediate-sized particle that ignites but extinguishes soon afterwards without achieving full-fledged diffusive combustion. After extinction, the particle continues to react in the kinetic regime at a temperature close to the gas temperature. The third case ( $r_0 < r_{crit}$ ) illustrates reaction of a particle with a size below the critical value. Here, the particle reacts entirely in the kinetic regime without ignition.

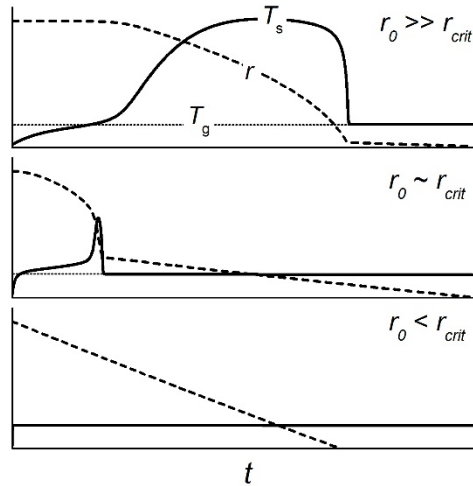


Figure 38. Particle temperature  $T_s$  and radius history of a particle injected into a hot oxidizing gas at temperature  $T_g$  burning in a predominantly diffusive combustion regime ( $r_0 \gg r_{crit}$ ), an intermediate regime ( $r_0 \sim r_{crit}$ ), and a kinetic combustion regime ( $r_0 < r_{crit}$ ).

This analysis shows that the particle reaction regime is a strong function of the particle radius as well as the surrounding temperature and oxidizer concentration. In a flame, a reacting particle with constantly changing radius is exposed to rising temperature and falling oxidizer concentration fields that are functions of the flame speed. Therefore, a priori postulation of the particle reaction regime and "ignition temperature" and "combustion time" parameters is, generally, unjustified in flame modelling. Only by solving the flame propagation problem as a whole can the particle combustion regime, along with other fundamental flame parameters, be determined.

#### *Governing equations and numerical method*

The flame propagation problem is cast in a time-dependent formulation, based on the method developed by Spalding [12], and solved numerically. This method has been used to analyze gas phase flames [14], [15]. Smoot *et al* also used this method to model flames in coal dust-air mixtures [16], but no attempt was made to draw general conclusions beyond the specifics of coal combustion.

The model presented here employs several simplifying assumptions: (i) the solid fuel is treated as a continuum with zero diffusivity, (ii) the velocity slip between particles and gas is negligible, (iii) the molecular weight and the heat capacity of the products are assumed to be close to those of the oxidizer, and (iv) the solid particles do not undergo any phase transitions [17]. All of these are second-order effects.

The governing equations for the flame can be simplified by introducing a density-weighted coordinate  $x$  which is related to the physical coordinate  $x'$  by the following relation [12],

$$[18]: x = \int_0^{x'} \rho_g / \rho_{g0} dx' .$$

In this coordinate system, the continuity equation is automatically satisfied, and advection effects induced by thermal expansion of the gas are absent. Once found, the solution in  $x$ -space can be transformed back to  $x'$ -space as described by Margolis [14].

For simplicity, the temperature dependence of transport and kinetic properties are chosen to eliminate the dependence of various parameter groupings on thermal expansion. With these assumptions, the governing equations can be algebraically reduced to the following expressions for the gas phase temperature in Eq. (3), particle temperature  $T_s$  in Eq. (4), particle mass  $m_s$  in Eq. (5) and normalized oxidizer mass fraction  $Y = Y_{ox} / Y_{ox,0}$  in Eq. (6). The combined kinetic-diffusion reaction rate  $\dot{\omega}$  corresponds to Eq. (1), and is given by Eq. (7).

$$\rho_{g0} c_g \frac{\partial T_g}{\partial t} = \lambda_0 \frac{\partial^2 T_g}{\partial x^2} + N_0 A h (T_s - T_g) \quad (23)$$

$$c_s \frac{\partial}{\partial t} (m_s T_s) = A q \dot{\omega} - A h (T_s - T_g) \quad (24)$$

$$\frac{\partial m_s}{\partial t} = -A \dot{\omega} \quad (25)$$

$$\frac{\partial Y}{\partial t} = D_0 \frac{\partial^2 Y}{\partial x^2} - \frac{N_0 \dot{\omega} A}{\gamma C_0 \rho_{g0}} \quad (26)$$

$$\dot{\omega} = \gamma \beta \text{Da}^* C_0 Y \quad (27)$$

Here  $A$  is the instantaneous surface area,  $c_s$  and  $c_g$  are the solid and gas phase specific heats,  $D_0$  and  $\lambda_0$  are the bulk mass diffusivity and thermal conductivity,  $\rho_{g0}$  is the initial gas density, and  $N_0$  is the initial particle number density. The evolution of the flame is observed in an effectively semi-infinite domain with an adiabatic and impermeable hot boundary. The numerical values for the thermodynamic, transport and reaction properties used are given in Table 1. These correspond to a typical metal fuel.

The equations are numerically integrated in MATLAB by the method of lines [19] using a second-order finite difference formulation and a multi-step, variable order, implicit time integration method [20].

Table 3. Numerical values of the gas and solid-fuel parameters.

$\lambda$	$0.02 \text{ W}^1\text{m}^{-1}\text{K}^{-1}$	$T_0$	$300 \text{ K}$
$c_g$	$1010 \text{ J}^1\text{kg}^{-1}\text{K}^{-1}$	$c_s$	$979 \text{ J}^1\text{kg}^{-1}\text{K}^{-1}$
$D$	$2.0 \times 10^{-5} \text{ m}^2\text{s}^{-1}$	$k_0$	$70 \text{ m}^1\text{s}^{-1}$
$\rho_{g0}$	$1.17 \text{ kg}^1\text{m}^{-3}$	$\rho_s$	$2700 \text{ kg}^1\text{m}^{-3}$
$\gamma$	$1.12$	$q$	$3.10 \times 10^7 \text{ J}^1\text{kg}^{-1}$
$C_0$	$0.27 \text{ kg}^1\text{m}^{-3}$	$E_a/R$	$15 \text{ 000 K}$
$\alpha$	$2.0 \times 10^{-5} \text{ m}^2\text{s}^{-1}$	$\lambda_I$	$0.02 \text{ W}^1\text{m}^{-1}\text{K}^{-1}$
$D_I$	$2.0 \times 10^{-5} \text{ m}^2\text{s}^{-1}$		

### 3. RESULTS AND DISCUSSION

#### *Flame Thermal Structure*

After an initial transient period, a steady-state flame, propagating at a constant speed, typically develops. As discussed below, for some values of  $\phi$  and  $r_0$ , no steady-state solution is observed. The resulting steady-state flame profiles of gas and particle temperatures, oxidizer mass fraction and particle radius are shown for the fuel-lean case (fuel equivalence ratio  $\phi = 0.5$ ) in Fig. 3 for three different initial particle sizes corresponding to overall kinetic ( $r_0 = 1 \mu\text{m}$ ), diffusive ( $r_0 = 10 \mu\text{m}$ ) and intermediate ( $r_0 = 4 \mu\text{m}$ ) particle combustion regimes.

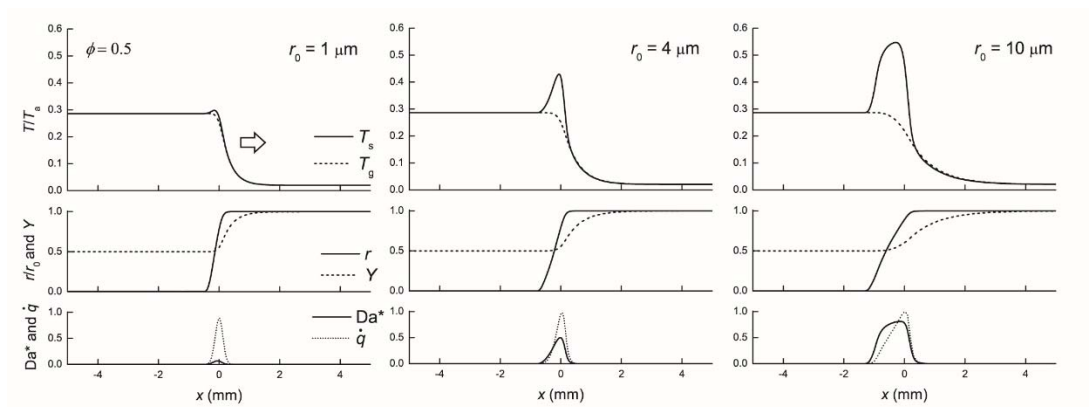


Figure 39. Flame structure profiles. Top: of gas and particle temperature  $T_g$ ,  $T_s$  (normalized with  $T_a = E_a / R$ ); Middle: normalized oxidizer mass fraction  $Y$ , and particle radius  $r$ ; Bottom: reaction heat release rate  $\dot{q}$  and  $Da^*$ , for three different particle sizes in a fuel-lean flame ( $\phi = 0.5$ ). The arrow indicates direction of propagation.

For small particle sizes, the flame structure is similar to that of a homogeneous gaseous flame. The gas and particle temperatures remain close to each other throughout the flame and the reaction zone is thin, with its location near the point where the temperature reaches the adiabatic flame temperature of the mixture.

In contrast, the flame structure for large particles is significantly different. After ignition, the particles attain a temperature close to the adiabatic flame temperature of the stoichiometric mixture, which greatly exceeds that of the fuel-lean mixture. In addition, the reaction zone is wide, encompassing a large gas temperature range. There is also a slight lag of the particle temperature profile behind the gas temperature in the flame preheat zone.

In the case of intermediate particle sizes, particles ignite, but then extinguish before achieving a full-fledged diffusive combustion regime. Thus, the particle temperature surpasses the adiabatic flame temperature of the mixture, but does not reach that of the stoichiometric mixture. In contrast to the reaction of a single particle of the same size, the kinetic reaction time after the transition back to the kinetic combustion mode, or extinction, is relatively short due to the high flame temperatures and, thus, does not significantly increase the overall combustion time.

Flames in fuel-rich suspensions, as shown in Fig. 4, have a different structure to that of fuel-lean mixtures, since the limiting reactant changes from the solid fuel, which has a negligible mass diffusivity, to the oxidizing gas, which readily diffuses across the flame. The primary difference is that the temperature of the particles after ignition does not exceed the adiabatic flame temperature of the mixture. The reason for this is that the temperature separation between particles and gas in the diffusive combustion regime is proportional to the concentration of the oxidizer in a particular location, which falls to zero as the temperature rises. Due to complete oxidizer consumption at the end of the combustion zone and, therefore, a negligibly small reaction rate, the value of  $Da^*$  remains constant after the oxidizer is depleted.

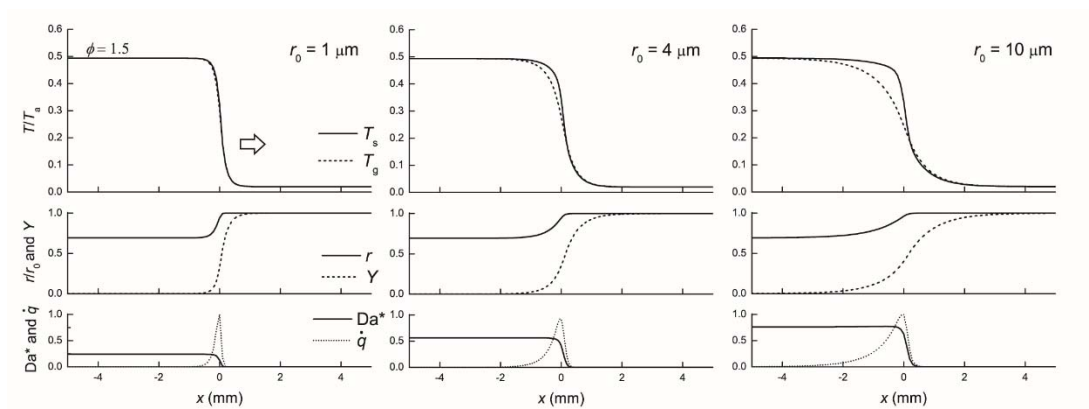


Figure 40. Flame structure profiles for three different particle sizes in a fuel-rich mixture ( $\phi = 1.5$ ). The same variables are shown as in Fig. 3.

## Burning Velocity

The burning velocity is calculated based on the displacement of the flame front as a function of time. The burning velocity is plotted in Fig. 5 as a function of initial particle size for different equivalence ratios. The general trend for stoichiometric and rich equivalence ratios, as well as flames that are not exceedingly fuel-lean, is that the burning velocity increases monotonically with decreasing particle size. This is simply due to the increasing specific reaction surface area with decreasing particle size. However, the dependence of burning velocity on particle size becomes non-monotonic for very lean mixtures. For equivalence ratios below  $\phi = 0.4$ , there is also a region where the burning velocity curves split into two separate branches between which no steady solution exists.

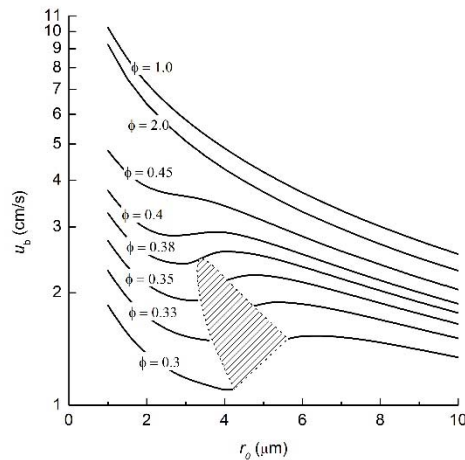


Figure 41. Burning velocity  $u_b$  as a function of particle size for different equivalence ratios. Hatched area corresponds to regions where unstable flame propagation is observed.

The nontrivial dependence of the burning velocity on particle size in lean mixtures is the result of the intricate interplay between the kinetic and diffusive particle combustion modes. Because of the relatively low flame temperatures in lean mixtures, the combustion time of a larger particle reacting diffusively can be shorter than that of a smaller particle reacting kinetically. This behavior is counter-intuitive, but is a direct consequence of the ability of large particles to ignite and burn with temperatures much higher than the adiabatic flame temperature of the lean mixture. The appearance of “hot spots” or “flames within the flame” results in a higher reaction rate for suspensions of larger particles that offsets, and potentially even overcomes, the reduced specific reaction surface area as compared to finer suspensions. This behavior can be seen first as a plateau in the dependence of burning velocity on particle radius (Fig. 5,  $\phi = 0.4$ ) and then a decline as particle size decreases (Fig 5.  $\phi < 0.4$  ). It can also be seen in Fig. 6 as intersections of the burning velocity versus equivalence ratio curves for different particle sizes. As the particle size is increased, eventually the effect of decreasing specific reaction surface area again dominates, and the burning velocity decreases with increasing particle size. These trends

have been observed experimentally in the combustion of coal suspensions [16] and liquid sprays [21], although no clear physical explanation was given at that time.

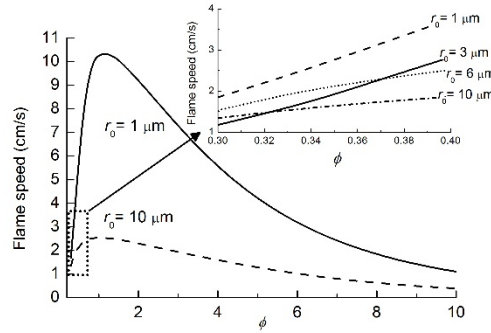


Figure 42. Burning velocity as a function of equivalence ratio for different particle sizes. The expanded view shows the intersections of burning velocities for lean equivalence ratios for various particle sizes.

### *Kinetic-Diffusive Instabilities*

For equivalence ratios below  $\phi = 0.4$ , there is a region where no steady-state flame propagation occurs. Instead, these flames oscillate both in terms of burning velocity and flame structure. An example of instantaneous particle and gas temperature profiles at different phases of the cycle are shown in Figure 7 for an equivalence ratio of  $\phi = 0.325$  and initial particle size of  $r_0 = 4.0 \mu\text{m}$ .

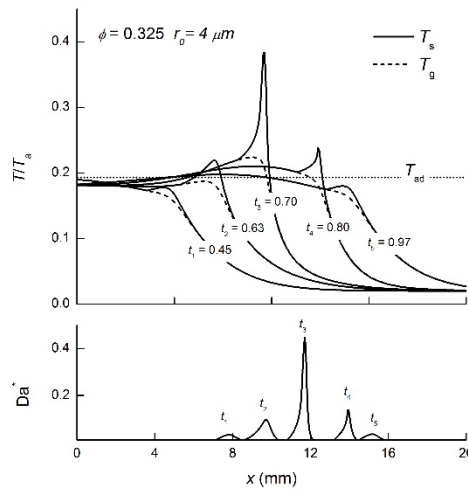


Figure 43. Instantaneous profiles of gas and particle temperatures and  $Da^*$  at different phases of an oscillating flame at  $\phi = 0.325$  and  $r_0 = 4 \mu\text{m}$ .

The gas temperature is observed to oscillate about the adiabatic flame temperature, while the particle temperature oscillates with a much wider amplitude than that of the gas. At first glance, these oscillations resemble the well-known thermo-diffusive flame

instability often observed in homogeneous gas [22] and quasi-homogeneous solid mixtures [23], and also recently observed in aluminum dust flames [24]. The physical mechanisms behind the thermo-diffusive instability and the heterogeneous pulsating flame shown here are, however, fundamentally different. Unlike in homogeneous mixtures, the pulsations observed here are not caused by changes in the gas molecular transport properties (i.e.,  $Le$  number) or overall heat production as required by the thermo-diffusive instability criteria formulated by [25], [26]. The fuel has zero diffusivity, and the gas-phase transport and kinetic parameters in the flame do not change with particle size. Instead, the cause of the observed instability is evidently rooted in the processes of particle ignition and extinction that are, indeed, very sensitive to particle size. Thus, it may be called a kinetic-diffusive instability, reflecting the fact that the particle combustion regime in the pulsating flame oscillates between diffusive and kinetic combustion modes. This interesting new phenomenon will be studied in detail in subsequent work.

### Comparison to Semi-Empirical Flame Models

Most existing models for flames in suspensions are semi-empirical and postulate either a purely kinetic or purely diffusive regime of particle combustion. Plots of the normalized burning velocity versus particle size predicted by such models are compared with the result of the current numerical computations in Fig. 8 for the lean mixture with an equivalence ratio of 0.3. For the case of the purely kinetic regime, the burning velocity is calculated using an analytical expression formulated by Zel'dovich and Frank-Kamenetskii modified for a combustible mixture with a single-step first order heterogeneous surface reaction [11]. The result is normalized to match the numerical simulations for small particles.

The burning velocity in the case of the purely diffusive regime is calculated using a simple expression given in [6], [10] that requires two externally defined combustion parameters: ignition temperature and combustion time of the single particle. Ignition temperatures at different particle sizes are calculated using the Semenov ignition criterion as shown in Fig. 1 and have a dependence with particle size similar to that shown inset in Fig. 1. The particle combustion time is calculated using a simple diffusive reaction model that predicts a  $t_c \sim r_0^2$  dependence [27]. The result of the purely diffusive model is normalized to match the numerical simulations for large particles.

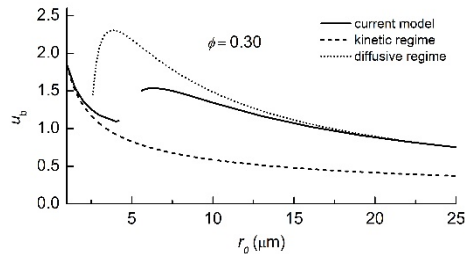


Figure 44. Comparison of computed burning velocity to semi-empirical asymptotic Zel'dovich and Frank-Kamenetskii (kinetic) and modified Mallard-Le Chatelier (diffusive) flame models. The semi-empirical models are normalized to the numerical model at  $r_0 = 1 \mu\text{m}$  for the kinetic model and  $r_0 = 25 \mu\text{m}$  size for the diffusive model.

As can be seen in Fig. 8, these semi-empirical models only qualitatively predict the asymptotic behavior of burning velocity on particle size where the combustion regimes are either purely kinetic or diffusive. Over a wide particle size range, where diffusion and kinetic rates are comparable, these models cannot capture the physics of the flame propagation and yield erroneous results.

#### 4. CONCLUSIONS

The comprehensive analysis of flame propagation in non-volatile particle suspensions presented in this paper has a historical parallel. It can be compared with the replacement of the semi-empirical Mallard-Le Chatelier flame model, based on the notion of ignition temperature and reaction time as external parameters, to flame models developed in the 20<sup>th</sup> century based on the Arrhenius reaction law. Here, it is similarly shown that the particle reaction onset temperature, particle reaction time, and regime of particle combustion are, in general, characteristic values of the flame problem that must be solved for together with the burning velocity. Moreover, this analysis demonstrates that the thermal structure of flames in suspensions is defined primarily by the interplay between kinetic and diffusive reaction modes that also yields non-trivial dependence of the burning velocity on particle size. This interplay leads to the emergence of a new type of pulsating instability that is related to the process of ignition and extinction of particles within the flame.

#### 5. REFERENCES

- [1] E. Price, "Combustion of Metalized Propellants," in *Fundamentals of Solid Propellant Combustion*, 1984, pp. 479–514.
- [2] P. R. Choudhury, "Slurry fuels," *Prog. Energy Combust. Sci.*, vol. 18, pp. 409–427, 1992.
- [3] D. Pratt and L. Smoot, *Pulverized-coal Combustion and Gasification*. 1979.
- [4] J. M. Bergthorson, S. Goroshin, M. J. Soo, P. Julien, J. Palecka, D. L. Frost, and D. J. Jarvis, "Direct combustion of recyclable metal fuels for zero-carbon heat and power," *Appl. Energy*, vol. 160, pp. 368–382, Dec. 2015.
- [5] R. Eckhoff, *Dust Explosions in the Process Industries: Identification, Assessment and Control of Dust Hazards*. Gulf Professional Publishing, 2003.
- [6] S. Goroshin, M. Bidabadi, and J. H. S. Lee, "Quenching distance of laminar flame in aluminum dust clouds," *Combust. Flame*, vol. 105, no. 1–2, pp. 147–160, 1996.
- [7] F.-D. Tang, S. Goroshin, and A. J. Higgins, "Modes of particle combustion in iron dust flames," *Proc. Combust. Inst.*, vol. 33, no. 2, pp. 1975–1982, 2011.
- [8] D. A. Frank-Kamenetskii, *Diffusion and Heat Transfer in Chemical Kinetics*. New York: Plenum Press, 1969.
- [9] L. A. Vulis, G. C. Williams, and M. D. Friedman, *Thermal Regimes of Combustion*. New York: McGraw-Hill, 1961.

- [10] S. Goroshin, I. Fomenko, and J. H. S. Lee, "Burning velocities in fuel-rich aluminum dust clouds," *Proc. Combust. Inst.*, vol. 26, no. 2, pp. 1961–1967, 1996.
- [11] Y. Zeldovich and D. Frank-Kamenetskii, "A theory of thermal propagation of flame," *Zh. Fiz. Khim.*, 1938.
- [12] D. B. Spalding, "The Theory of Flame Phenomena with a Chain Reaction," *Philos. Trans. R. Soc. A Math. Phys. Eng. Sci.*, vol. 249, no. 957, pp. 1–25, Mar. 1956.
- [13] M. Soo, S. Goroshin, D. Frost, and J. Bergthorson, "Reaction of a Particle Suspension in a Rapidly-Heated Oxidizing Gas," *Propellants, Explos. Pyrotech.*, 2015.
- [14] S. B. Margolis, "Time-dependent solution of a premixed laminar flame," *J. Comput. Phys.*, vol. 27, no. 3, pp. 410–427, Jun. 1978.
- [15] Y. B. Zeldovich and G. I. Barenblatt, "Theory of flame propagation," *Combust. Flame*, vol. 3, pp. 61–74, Jan. 1959.
- [16] L. Douglas Smoot and M. Duane Horton, "Propagation of laminar pulverized coal-air flames," *Prog. Energy Combust. Sci.*, vol. 3, no. 4, pp. 235–258, Jan. 1977.
- [17] S. N. G. S. V. S. Y. . Zolotko, "Modes of Combustion and Flame Velocity in Gas Suspensions.pdf." Doklady Akademii Nauk SSSR, Odessa, 1991.
- [18] K. Seshadri, A. L. Berlad, and V. Tangirala, "The structure of premixed particle-cloud flames," *Combust. Flame*, vol. 89, no. 3–4, pp. 333–342, Jun. 1992.
- [19] W. E. Schiesser and G. W. Griffiths, *A Compendium of Partial Differential Equation Models: Method of Lines Analysis with Matlab*. Cambridge University Press, 2009.
- [20] L. F. Shampine and M. W. Reichelt, "The MATLAB ODE Suite," *SIAM J. Sci. Comput.*, vol. 18, no. 1, pp. 1–22, Jan. 1997.
- [21] K.-K. Chan and S.-R. Wu, "An experimental and theoretical investigation of the transition phenomenon in fuel spray deflagration," *Fuel*, vol. 68, no. 2, pp. 139–144, Feb. 1989.
- [22] E. W. Christiansen, C. J. Sung, and C. K. Law, "Pulsating instability in near-limit propagation of rich hydrogen/air flames," *Symp. Combust.*, vol. 27, no. 1, pp. 555–562, Jan. 1998.
- [23] H. Yi and J. Moore, "Self-propagating high-temperature (combustion) synthesis (SHS) of powder-compacted materials," *J. Mater. Sci.*, 1990.
- [24] P. Julien, J. Vickery, S. Goroshin, D. L. Frost, and J. M. Bergthorson, "Freely-propagating flames in aluminum dust clouds," *Combust. Flame*, p. (accepted), 2015.
- [25] B. J. Matkowsky and G. I. Sivashinsky, "Propagation of a Pulsating Reaction Front in Solid Fuel Combustion," *SIAM J. Appl. Math.*, vol. 35, no. 3, pp. 465–478, Nov. 1978.

- [26] B. J. Matkowsky and D. O. Olagunju, "Propagation of a Pulsating Flame Front in a Gaseous Combustible Mixture," *SIAM J. Appl. Math.*, vol. 39, no. 2, pp. 290–300, Oct. 1980.
- [27] F.-D. Tang, S. Goroshin, A. Higgins, and J. H. S. Lee, "Flame propagation and quenching in iron dust clouds," *Proc. Combust. Inst.*, vol. 32, no. 2, pp. 1905–1912, 2009.

# SECTION 5. EXPLOSIVE DISPERSAL OF POWDERS

## Chapter 1. Blast mitigation by granular materials and liquids in spherical geometry

### 1. INTRODUCTION

Blast waves generated by high explosives are serious hazards for human health as well as for structures, hence the mitigation of blast waves is an important concern. One technique for reducing the strength of a free-field air blast is to surround a high explosive charge with liquid, granular material, and/or porous cellular material. A variety of blast energy dissipation mechanisms have been proposed, and the relative importance of the different mechanisms for blast wave mitigation depends on the particular media used.

The effects of blast attenuation by a surrounding liquid layer or multiphase liquid system has been previously investigated. Numerical predictions of blast mitigation with water surrounding a spherical charge indicate that a reduction in peak overpressure by up to 80% is possible [7]. Experimental studies using water and glycerine in a bulk form have confirmed the possibility of such a reduction [1, 27], with similar mitigation observed for the two liquids. The blast wave attenuation implies an energy loss to the mitigant layer, which has been attributed to the acceleration of the liquid and subsequent fragmentation of the liquid into fine droplets as well as thermal effects related to liquid vaporization [7, 27]. Several studies have investigated mitigation with two-phase media such as bubbly liquids [6, 13] or a liquid droplet mist [27, 28]. Within such compressible two-phase media, the propagation of waves is considerably modified due to impedance mismatching between the phases and collapse of pores. Recent studies have investigated the mitigation properties of aqueous foams within a confined area [9, 16, 18, 26]. A reduction of the peak overpressure by an order of magnitude, relative to that of a bare high explosive charge, was observed [9]. The attenuation is attributed to the momentum loss in the complex 3D multiphase structure of these media and is related to the number of gas cells found within the foams [18]. The high heat capacity of the liquid phase and the compressibility of the gas bubbles also play a significant role in the mitigation process [4].

The mitigation performance of granular materials has likewise been investigated. Sand has been proposed as a potential candidate and a peak overpressure attenuation of 5–40% has been demonstrated [18, 25]. A mixture of sand and cement has also shown the capacity to significantly mitigate the effects of blast waves [14]. Glass, steel, and ceramic [3], porcelain, plastic, claydite, and polyethylene spheres [21], and also perlite and pumice [19] have been studied. However, it is not clear, *a priori*, which properties of the granular media are most important for mitigation performance. Material density has been cited as a relevant parameter, suggesting that the transfer of momentum is an important source of energy dissipation [1]. Porosity of the granular medium is also significant, and the energy loss during the mitigation process has been attributed to the complex interaction of the blast wave with the compacting, impedance-mismatched medium [1, 10]. Particle size and the

length of the granular layer [3] have been cited as potential mitigation parameters and the collapse of voids, and particle crushing and rearrangement during wave propagation have been proposed as another mechanism of blast attenuation [19]. The configuration of the granular medium around the high explosive charge, including the addition air gaps, also influences mitigation efficiency [3, 7]. Finally, the energy dissipation via acceleration of the mitigant bed can also be related to the ratio of the mitigant mass to charge mass (denoted  $M/C$ ), which is correlated with the velocity of the explosively dispersed material according to classical Gurney analysis, as discussed in a companion paper [20].

The present study further examines the blast wave mitigation performance of granular material, liquids, and liquid-saturated particle beds surrounding an explosive charge in spherical geometry using a comprehensive array of mitigants. The link between the particle/liquid motion and the blast wave attenuation was also investigated. A variety of different mitigant materials were tested, including powders with a range of particle sizes, density, and packed bed porosity. The tests cover a wide range of mitigant to charge mass ratios. For select experiments, the blast wave peak overpressure and impulse were obtained from several fast-response pressure transducers located at various locations from the charge. The decay of the peak blast overpressure in the near field was inferred by extracting the blast wave trajectories from high-speed video images. The blast wave trajectory was then used to extract a Mach number, which can then be used to estimate a peak pressure via the Rankine-Hugoniot relations.

A general mechanism for the explosive dispersal of a granular mitigant can be described in terms of shock compaction and then dynamic fragmentation upon release and expansion of the compacted layer. When a high explosive charge surrounded by a layer of inert material is detonated, a shock wave propagates into the material, compacting the material to a degree which depends on the initial bed porosity, particle compressive strength and local strength of the shock wave. When the shock wave reaches the surface of the material layer, a blast wave is transmitted into the surroundings and an expansion wave propagates back into the compacted material, causing it to expand radially outwards. The tension induced within the compacted bed of material causes it break up into fragments that have a size on the order of the thickness of the compacted layer when the expansion waves reaches the inner surface of the layer [22]. The fragments move radially outwards, shedding fine fragments in their wake and leading to the formation of jet-like structures. Explosive dispersal of liquids also, in general, leads to the formation of jets, although other phenomena, such as cavitation within the liquid layer behind the expansion wave, govern jet formation. Due to the different mechanisms governing jet formation, the scaling of the number of jets with the mitigant mass to explosive mass ratio differs for liquids, dry granular materials and granular materials saturated with liquids [23]. Fig. 1 shows an example of the jet formation during the explosive dispersal of solid particles (glass particles, on the left), and a liquid layer (vegetable oil, on the right). In both cases, the number of jets formed is primarily dependent on the  $M/C$  ratio. In the case of liquid jets, the maximum travel distance of the jets depends on the initial jet velocity, the liquid volatility (i.e., the evaporation rate), and the aerodynamic shedding rate of the liquid, which depends on the liquid surface tension. For solid particle jets, the maximum travel distance depends on the jet velocity, rate of shedding and areal density of the jet tip.

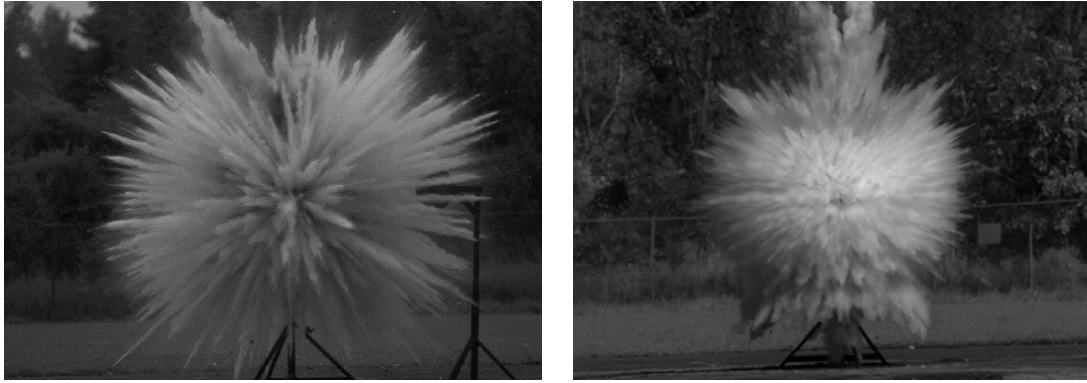


Fig. 1 Example of jet formation during explosive dispersal of solid particles (glass particles, on the right;  $M/C = 17.7$ ) and liquids (vegetable oil, on the right;  $M/C = 29.5$ ).

## 2. EXPERIMENTAL APPARATUS

The charge casings used in the present study consisted of thin-walled (1 mm thick) commercial bulb light bulbs with the filaments removed. Either G40 (nominal dia of 12.7 cm) or G25 (nominal dia of 9.5 cm) bulbs were used. A spherical ball of C4 (28–82 g) was placed in the middle of the glass sphere with a plastic tube attached to allow the insertion of an electric detonator into the C4 prior to the test. For liquid dispersals, the C4 was placed within a hollow polyethylene sphere (mass 12 g) to isolate it from the liquid. The PE sphere was cut in half, filled with C4, then reassembled. The sphere was drilled and glued to the detonator tube and a cross-piece at the top of bulb was used to center the charge in the bulb. In the case of solid particles, bare C4 charges were used. The charge was prepared by filling the sphere half full of powder, then placing the C4 ball, with attached tube, in the center of the sphere, then filling the remainder of the powder such that the C4 was held in place by the powder. The charges were placed on a section of plastic tube attached to the end of a wooden rod, with a height of burst of 1.5 m, as shown in Fig. 2.



Fig. 2 Photographs of charges consisting of spherical glass casings containing either water (left) or iron powder (right). The C4 charge in the center of the sphere is visible in the charge on the left. The tube protruding from the C4 charge is used to insert the detonator into the C4.

For some trials, the blast overpressure was recorded with piezoelectric pressure transducers (PCB 113A24) mounted in lollipop-style gauges (lollipop dia. 30 cm) at various distances from the charge, as shown schematically in Fig. 3 and in the photograph in Fig. 4. The distance for the farthest transducer was chosen such that the ground-reflected wave arrived at the transducer location after the end of the positive phase of the blast wave signature so that the positive-phase impulse measurement is not influenced by the reflected wave.

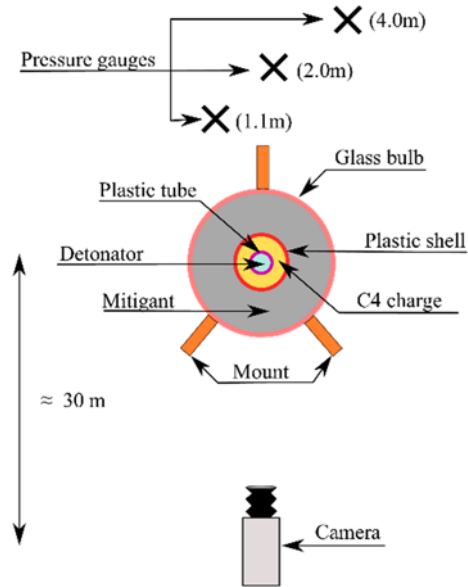


Fig. 3 Schematic of charge and test site (top view)

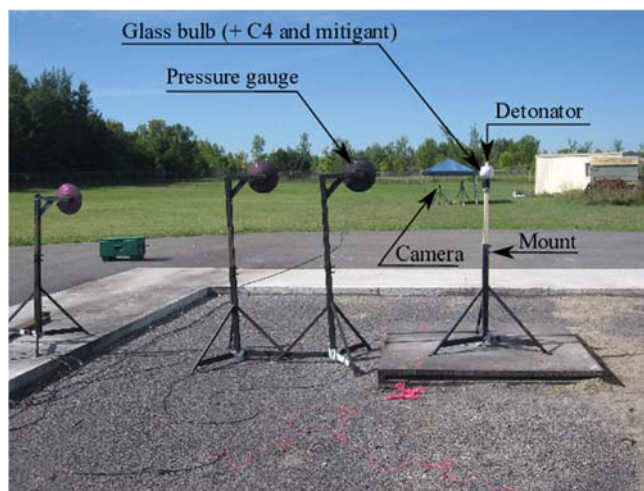


Fig. 4 Experimental test site

The explosive dispersal was recorded with two high-speed cameras: a Photron SA-5 recording at 10,000 fr/s and a NAC GX-8 recording at 5,000 fr/s. Prior to a test, a photograph of a checkboard scale or graded yard stick was taken to establish an absolute length scale. A resolution of 1024 x 744 pixels was used, leading to a physical distance ranging from 3.1–4.5 mm depending on the distance to the charge and the magnification.

A variety of mitigant materials were tested. Solid particles included: Chronital S-30 stainless steel shot (Vulkan), SAE J827 standard S-110 steel shot, pure iron (FE-112, Atlantic Equipment Engineers), glass (Potters Ballotini impact glass beads, #10 and #13), brass (BR-102, Atlantic Equipment Engineers), aluminum (Valimet H-95), silicon carbide (240 grit), sand (commercial toy box sand), granulated sugar, and icing sugar (commercial products). The liquids used include water, glycerol, ethanol, and vegetable oil. In a subset of tests, a bed of solid particles was fully saturated with water. In total, blast wave properties were extracted from 70 trials spanning a range of mitigant-mass to explosive-mass ratios ( $M/C$ ) of 3.8 to 168.0. A total of 39 trials were conducted with dry powders, 19 trials were conducted with neat liquids, and 12 trials were conducted with water-saturated particles.

#### *Video analysis procedure*

Two different methods are used to extract the position of the spherical blast wave as a function of time and involve the use of several image processing techniques. If the blast wave peak overpressure is sufficiently high, it is possible to observe the wave front directly from the raw video images as a result of the diffraction of the background light by the density gradient across the blast wave. Once the location of the wave front has been determined, a circle may be fit manually to the most spherical portion of the blast front. Due to a lack of symmetry of the blast wave for certain trials, the center of the circle does not necessarily correspond to the exact location of the charge but is typically very close. This procedure is repeated for each video image (for a framing rate of 10,000 fr/s, consecutive images are separated by 100  $\mu$ s in time) maintaining the same center for all the images. If the circle does not perfectly match the wave front in all directions, the edge of the circle is arbitrarily placed to precisely coincide with the left side of the blast wave. This method has the advantage of being relatively fast, taking into account the sphericity of the blast front and also avoiding the addition, or removal, of information associated with any image processing technique.

Above a mass ratio of around 50, the blast wave is weak enough that it is difficult to discern the blast wave front against the uneven pixel grayscale level of the background in individual video frames. To enhance the visibility of the blast front in these cases it is necessary to perform inter-frame image processing. The choice of image processing scheme depends on the brightness, contrast and pixel intensity of the particular trial. However, the basic procedure is to compare consecutive images so that only portions of the image that are moving (such as a blast wave) are retained. At this point, various routines are used to enhance the image contrast, apply a thresholding function, filter the image, and despeckle the image until the blast wave front is distinctly visible. An overview of the typical sequence of image processing routines used is shown in Fig. 5. First, a Matlab Bit-xor transformation is applied to two consecutive frames. The Bit-xor function compares bits of the same pixel in the two different images and returns 0 if bits are equal and 1 otherwise. Pixels which have the same value (from 0 to 256) are converted to black and

others are become more and less grey. Then, the contrast of the resulting image is enhanced (imadjust function) and a threshold is set to 4, 5 or 6 depending on the magnification ratio and the image properties. As a consequence, only pixels with a value above this threshold become visible. The next steps consist of removing the noise from the images. In the first instance, images are converted to binary, i.e., black and white. Then, several loops (about 10) of applications of the speckle removal algorithm is used to remove the smallest noise structures. This algorithm consists of a small 2D-median filter (3 x 3) which replaces an input pixel at a specific location by the median value of the input pixel and its 8 neighbours. If most of the pixels surrounding the input pixel are black the output pixel will be black and if it is not, the output pixel will be white. In the end, to get rid of the largest noise structures, a larger median filter (10 x 10) is applied. The size of this filter depends also on the image properties. One drawback of image processing techniques is that inevitably some information is either added to or removed from the image. After applying the various image processing techniques, care must be taken to distinguish the front of the particle cloud, which may appear as a front similar to a shock wave, from the blast wave front itself. Once the trajectory of the blast wave has been unambiguously identified, the procedure for fitting a circle to the blast wave described in the previous paragraph is applied.

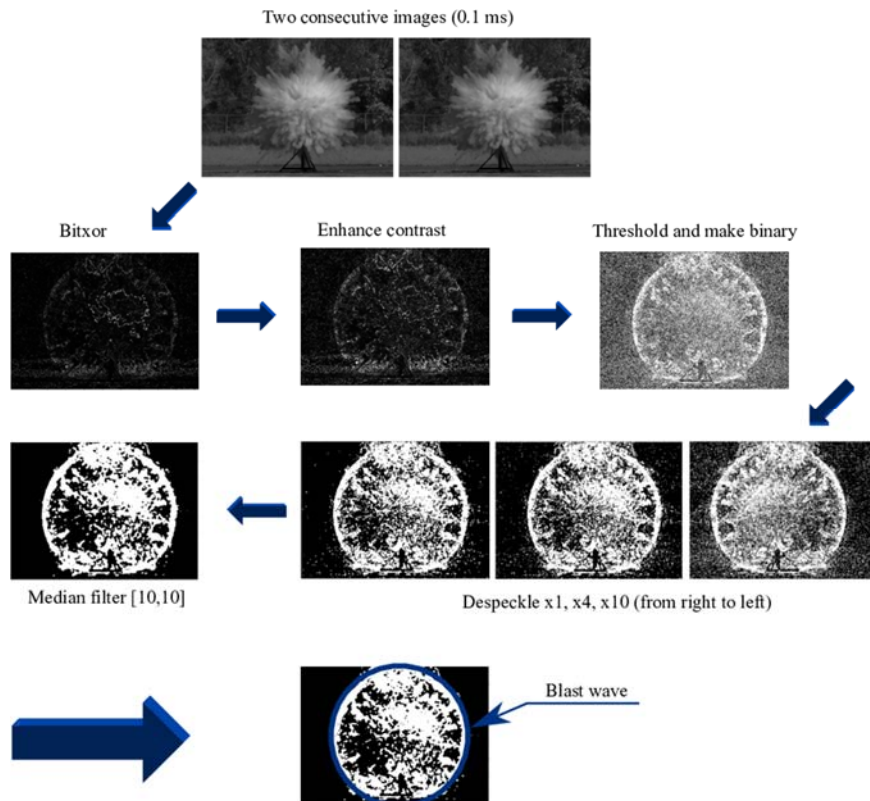


Fig. 5 Sequence of video processing techniques applied to video images to extract the location of blast wave in order to determine shock trajectory and velocity.

With the image analysis procedure described above, the spherical blast radius can be determined. Pixel counts are converted to distance via the pre-trial scale image. Intra-frame positions and times are used to determine the shock trajectory, and the shock velocity is extracted by differentiating a polynomial line of best fit to the position-time data points. Fig. 6 shows an example of a radius-time history plotted for a trial in which aluminum particles were explosively dispersed.

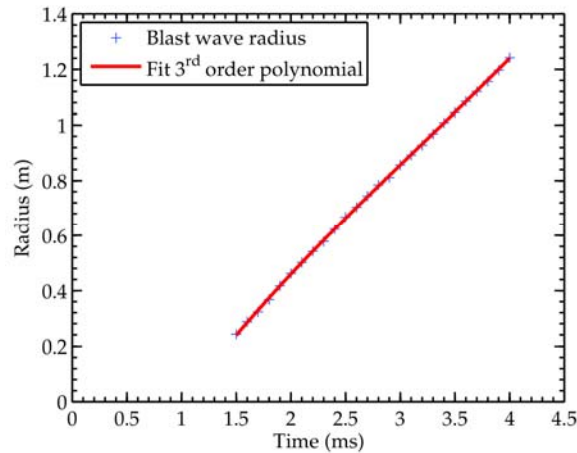


Fig. 6 Blast wave radius as a function of time for explosive dispersal of aluminum particles with  $M/C = 48.4$ . Blue crosses refer to the blast radius extracted at a specific instant. The red line corresponds to a 3<sup>rd</sup> order polynomial fit. To obtain the velocity profile this fit is differentiated.

Several methods can be used to obtain the history of the blast wave velocity. First, the instantaneous velocity can be determined at a specific instant based on the change in position between two frames:

$$V(i) = \frac{R(i + 1) - R(i - 1)}{t(i + 1) - t(i - 1)} \quad (1)$$

Where:

- $i$  = image number
- $R(i)$  = position of the blast in image number  $i$
- $T(i)$  = time of the image number  $i$
- $V(i)$  = blast velocity in image number  $i$

An example of the velocities calculated in this way is shown by the blue crosses in Fig. 7. The small changes in distance of the blast from one video frame to the next leads to large fluctuations in the velocity due to the lack of precision in determining the shock front location. To obtain a smoother variation in the blast front velocity, the shock wave trajectory is fit with a 3<sup>rd</sup> order polynomial, as shown in Fig. 6. The polynomial is then differentiated to get the velocity history, which is shown as the solid red curve in Fig. 7.

This fitting function works well for trials with a mass ratio above 11. However, for mass ratios below this value the fit is not accurate enough, especially at early times. As a result, in the range of mass ratio between 3.7 and 11, a rational mode fit, i.e., a ratio of a linear function and a second order polynomial, is chosen instead. A comparison between the two fitting functions for a low value of  $M/C$  is shown in Fig. 8. Note that at later times, the velocity fitting function starts to increase and diverge from the instantaneous velocity values. This is a non-physical behaviour and hence the velocity values to the right of the vertical dashed lines, at which point the velocity starts to increase, is discarded.

The Mach number and the pressure ratio across the shock is then determined from the velocity profile. The Mach number  $M$  is calculated using the ratio of the velocity over the speed of sound (Eq. 2) of the air assumed as an ideal gas:

$$c = \sqrt{\gamma RT} \quad (2)$$

Where:

$c$  = speed of sound (m/s)

$\gamma = 1.405$

$R = 286.9 \text{ J/kg}\cdot\text{K}$

$T$  = temperature in Kelvins

Depending on the trial, temperatures ranged from 5–25°C. Once the speed of sound is determined, the pressure ratio across the blast can be determined using the Hugoniot jump relation (Eq. 3) assuming that the shock front is relatively thin:

$$\frac{P}{P_0} = \frac{2\gamma}{\gamma + 1} M^2 - \frac{\gamma - 1}{\gamma + 1} \quad (3)$$

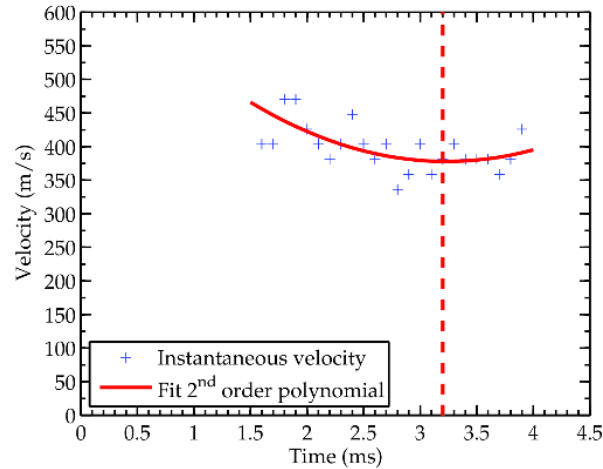


Fig. 7 Velocity profile for aluminum at  $M/C = 48.4$ . Solid red line corresponds to a 2<sup>nd</sup> order polynomial fit (derivative of the 3<sup>rd</sup> order polynomial fit of the position vs. time curve). At the right of the dashed line, data are not taken into account in the overpressure calculations.

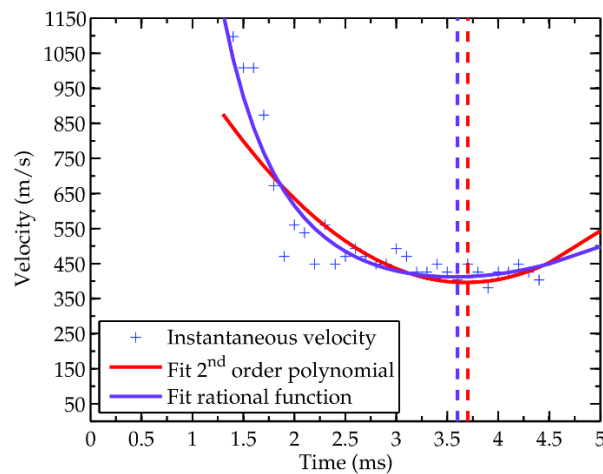


Fig. 8 Velocity profile for ethanol at  $M/C = 3.76$ . Solid red line corresponds to a 2<sup>nd</sup> order polynomial fit. Solid purple line corresponds to a rational mode fit (derivative of the rational fit of the position vs. time curve). To the right of the dashed lines, the velocity begins to increase and is not considered reliable.

### 3. RESULTS AND DISCUSSION

In addition to the estimation of peak blast overpressure using image analysis of the blast wave trajectories, overpressure measurements were obtained with piezoelectric pressure transducers in selected trials. The pressure gauge data were limited to measurements at only three or five specific locations and were placed relatively far from the charge so that the pressure field very near the charge was not obtained. Fig. 9 illustrates the typical overpressure measurements obtained with the gauges at three different locations for the

dispersal of glass particles saturated with water, with  $M/C = 62.3$ , recorded with a time resolution of  $5 \mu\text{s}$ . To reduce the noise in the signals due to impact of the particles with the gauge or gauge stand, a Savitzki-Golay filter with a first order polynomial and a frame size of 21 was applied to the curves. Note that for each curve, the second pressure spike due to the arrival of the ground-reflected wave occurs after the completion of the primary positive phase of the signal. These signals were used to determine the positive-phase impulse of the blast wave at various locations.

The peak overpressures derived from videography results are plotted as a function of scaled distance,  $Z$ , defined in Eq. 4, for all trials in subsequent sections. Following Kinney and Graham [17], the equivalent TNT charge mass,  $W$ , is equal to the mass of C4 multiplied by an effectiveness factor,  $\varepsilon$ , equal to 1.39 for C4 is used. The overpressure is defined by  $\frac{\Delta P}{P_0}$ , with  $\Delta P = P - P_0$ , and  $P_0 = 1 \text{ atm}$ . Thus:

$$Z = \frac{R}{W^{1/3}} \quad (4)$$

Where:

$Z$  = scaled distance ( $\text{m}/\text{kg}^{1/3}$ )

$R$  = dimensional distance (m)

$W$  = (charge mass in equivalent TNT) = mass of C4 (kg)  $\times$   $\varepsilon$  (effectiveness factor)

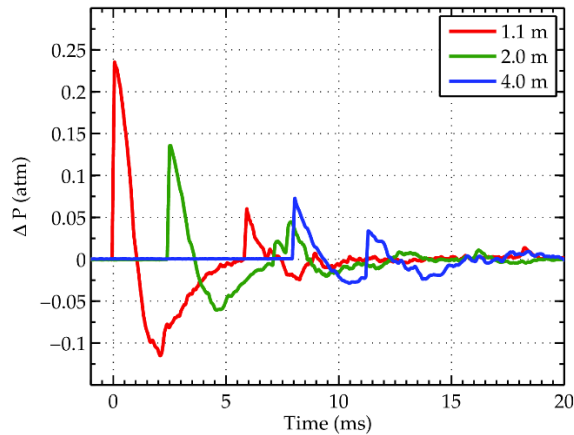


Fig. 9 Overpressure as a function of time captured with pressure gauges for glass (Ballotini #13 impact) beads saturated with water with a mass ratio of 62.3.

### Overpressure Results Granular Mitigants

Fig. 11 shows the peak overpressure as a function of scaled distance in a log-log plot for different dry granular mitigants for mass ratios ranging from 3.9 to 57.1. The solid red line corresponds to the peak overpressure of a bare C4 charge based on the Kinney and Graham database [17]. The peak overpressures for the eight different materials, and a mixture of silicon carbide and glass particles are shown. The curves extracted from the videos are spread over a range of scaled distances from  $Z = 0.5$  to  $Z = 4.0$ . At scaled distances less

than one, the peak overpressure is reduced by about one order magnitude with the pressure reduction increasing with increasing  $M/C$ , regardless of the mitigant material, as expected. Also, for all the materials, it is interesting to note that the decay rates of the mitigated overpressure curves do not follow the decay of a bare charge in air. In particular, in the near field, the blast overpressure from a mitigated charge decays significantly slower than for a representative homogeneous high explosive charge described by the Kinney and Graham curve. However, after  $Z = 2$ , indicated by the vertical dashed line on the graph in Fig. 11, the mitigated overpressure decays similarly to the baseline bare charge in air.

To facilitate the comparison between the peak overpressure of the mitigated charges with a bare charge, the ratio of the mitigated overpressure to that of the baseline case for a bare charge from Kinney and Graham is shown in Fig. 12 for all reported trials. The greatest degree of mitigation occurs at small scaled distances, and the pressure mitigation decreases monotonically with distance from the charge. Furthermore, adding more material mass for a given explosive mass increases the mitigation effect, with mitigated pressures normalized with the baseline case ranging from a low value (i.e., greatest pressure mitigation) of 2.6% at  $Z = 0.7$  for a mixture of SiC and glass with  $M/C = 56$ , to a high value of 83% at  $Z = 2.33$  for granulated sugar with  $M/C = 3.93$ .

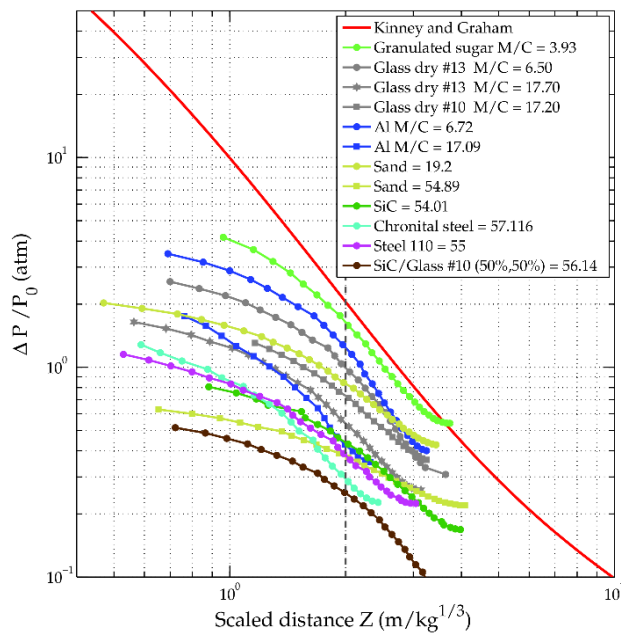


Fig. 11 Blast wave peak overpressure as a function of scaled distance,  $Z$ , for dry powders.

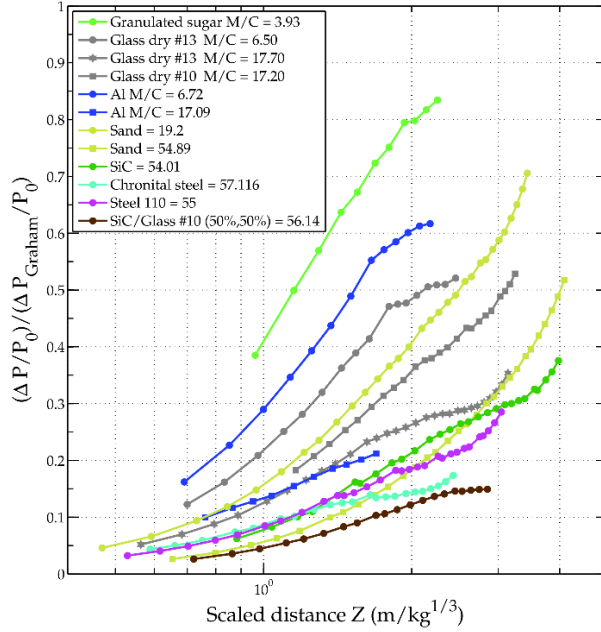


Fig. 12 Ratio of the mitigated blast wave peak overpressure over the peak overpressure of a blast wave for a bare HE charge in air (Kinney and Graham database) as a function of the scaled distance for dry powders.

To illustrate the dependence of pressure mitigation on  $M/C$ , 3 values of scaled distance were arbitrarily chosen ( $Z = 0.8, 1.5,$  and  $3.24$ ) and then at these values of  $Z$ , the corresponding mitigated overpressure values and normalized values were extracted from Fig. 11 and Fig. 12, respectively. Fig. 13 shows the results for the mitigated overpressure as a function of  $M/C$  for  $Z$  values of 0.8 and 3.2 (the data for  $Z = 1.5$  is omitted for clarity). At each scaled distance, the overpressures are reduced with increasing  $M/C$ . This relation can be represented by the following power law fits:

$$\frac{\Delta P}{P_0} = \alpha \times \left(\frac{M}{C}\right)^{-\beta} \quad (5)$$

Where:

$$(\alpha, \beta) = (9.2, 0.615) \text{ for } Z = 0.8$$

$$(\alpha, \beta) = (5.29, 0.584) \text{ for } Z = 1.5$$

$$(\alpha, \beta) = (1.62, 0.578) \text{ for } Z = 3.24$$

In a similar manner, the ratio of the mitigated overpressure to the overpressure for an unmitigated charge is plotted as a function of  $M/C$  at  $Z = 0.8$  and  $Z = 2.33$  in Fig. 14 based on the data from Fig. 12. Similar to Fig. 13, the normalized overpressure diminishes with increasing  $M/C$ , and the data for the different materials are clustered within a broad band. The  $M/C$  ratio appears to be the primary factor in determining the mitigation effect for a given  $Z$  value, and the solid particle material properties play a secondary role. In the near field, for  $Z = 0.8$ , for  $M/C$  values greater than about 20, the blast overpressure is highly

attenuated, with values less than 10% of the value for a bare charge based on the Kinney and Graham data.

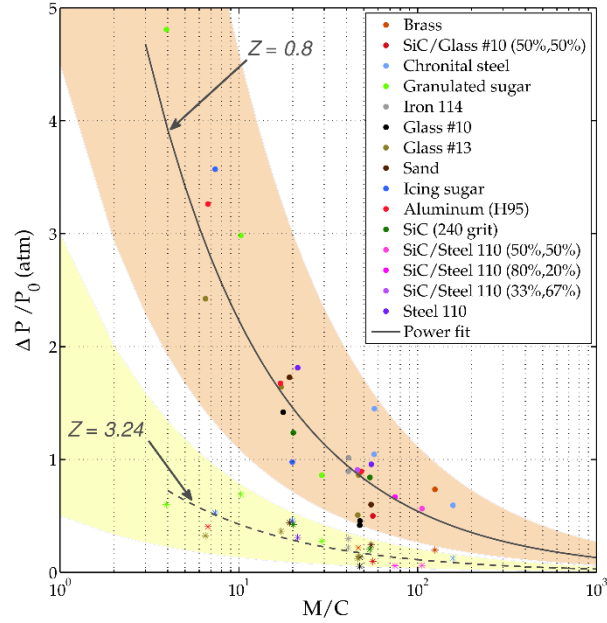


Fig. 13 Blast wave peak overpressure as a function of  $M/C$  at two different scaled distances in the case of solid powders. (●)  $Z = 0.8$ , (\*)  $Z = 3.24$ .

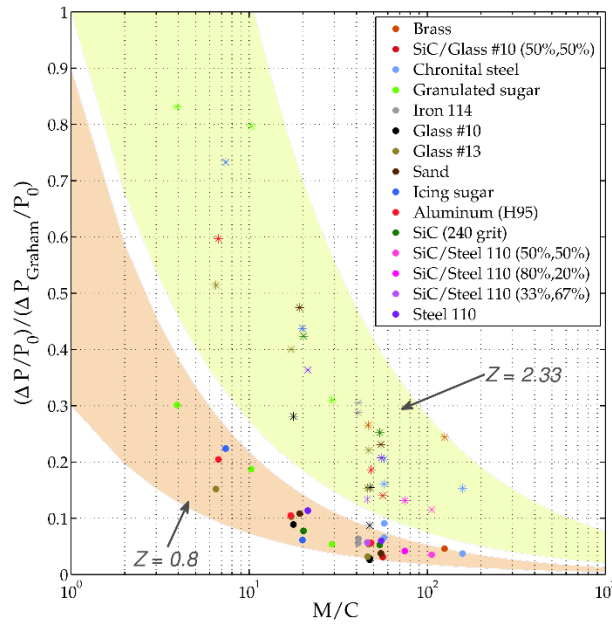


Fig. 14 Ratio of the mitigated blast wave peak overpressure over the peak overpressure of a blast wave in the air as a function of  $M/C$  for solid powders. (●)  $Z = 0.8$ , (\*)  $Z = 2.33$ .

### Overpressure Results for Liquids and Saturated Particle Beds

In the same manner as in Fig. 11, Fig. 15 presents the decay of peak blast overpressure as a function of scaled distance for mitigants consisting of pure liquids or powders fully saturated with water. Fig. 16 presents the normalized results for the liquid trials. The reduction in peak overpressures with liquids and powders saturated with water surrounding the charge follow the same trend as for solid powders with large pressure reductions at small scaled distances and with the pressures approaching more closely to that of a bare charge for  $Z > 2$ , except for the case of the largest values of  $M/C$ . A similar analysis is presented for the liquid experiments, where the peak overpressure and normalized overpressure is plotted as a function of  $M/C$  for three values of scaled distance. These results follow a similar power law decay as with the solid powders, but with different coefficients for Eq. 5:  $(\alpha, \beta) = (24.6, 0.82)$  for  $Z = 0.8$ ,  $(\alpha, \beta) = (10.56, 0.684)$  for  $Z = 1.5$ , and  $(\alpha, \beta) = (1.07, 0.352)$  for  $Z = 3.24$ . The reduction in peak overpressure for these scaled distances as a function of  $M/C$  is shown in Fig 17.

Fig. 18 represents the ratio of the liquid/saturated powder mitigated blast wave peak overpressure over the peak overpressure of a blast wave in the air as a function of  $M/C$ . To facilitate the comparison of the blast overpressure attenuation performance of particles versus liquids (or particles saturated with water) for a given  $M/C$  ratio, the power law fits to the data shown in Figs. 13 and 17 are replotted in Fig. 19. Note that in the near field ( $Z = 0.8$ ), for small  $M/C$  values, powders are about twice as effective at mitigating blast pressure. As  $M/C$  increases, the differences are reduced and also at large distances ( $Z = 3.24$ ), all materials show the same mitigation performance, irrespective of  $M/C$  value.

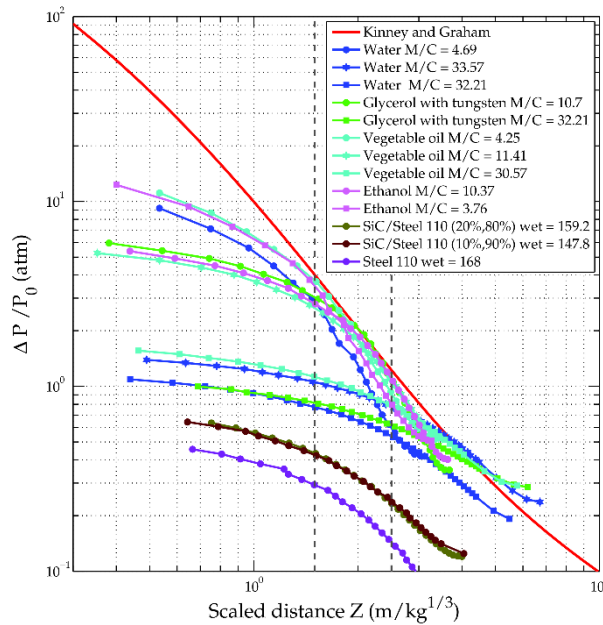


Fig. 15 Blast wave peak overpressure as a function of the scaled distance in the case of liquids/powders saturated with water.

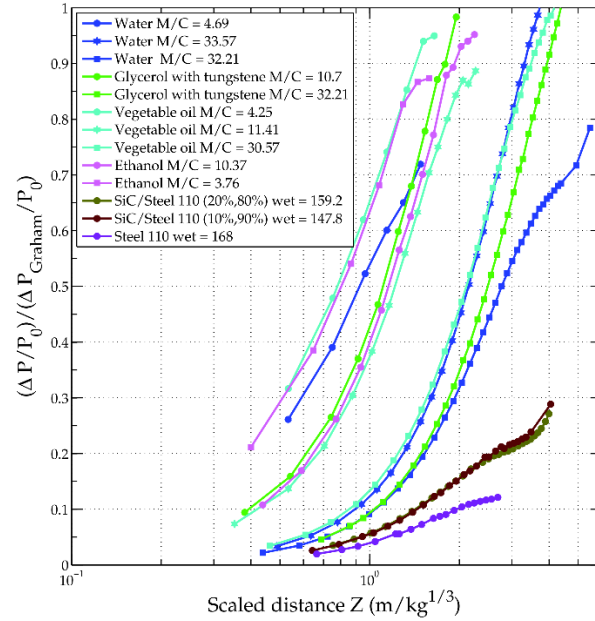


Fig. 16 Normalized blast wave peak overpressure versus scaled distance for liquids and powders saturated with water.

### Positive-Phase Impulse

The positive phase blast impulse is an important parameter when assessing structural damage due to blast waves. The positive phase impulse  $I^+$  is defined as the area under the curve of the first positive section of the overpressure curve, i.e.,

$$I^+ = \int_{t_a}^{t_f} \frac{\Delta P}{P_0} dt \quad (6)$$

with  $t_f = t_a + t_d$ ,  $t_a$  being the time of arrival of the blast wave, and  $t_d$  being the duration time of positive overpressure. For the convenience of comparing results from experiments with different explosive masses, it is convenient to define a scaled impulse as follows:

$$I_s^+ = \frac{I^+}{W^{1/3}} \quad (7)$$

Where:

$I_s^+$  = Blast wave scaled impulse (bar·ms/kg<sup>1/3</sup>)

$I^+$  = Blast wave positive impulse (bar·ms)

$W$  (charge mass in equivalent TNT) = mass of C4 (kg) ×  $\varepsilon$  (effectiveness factor)

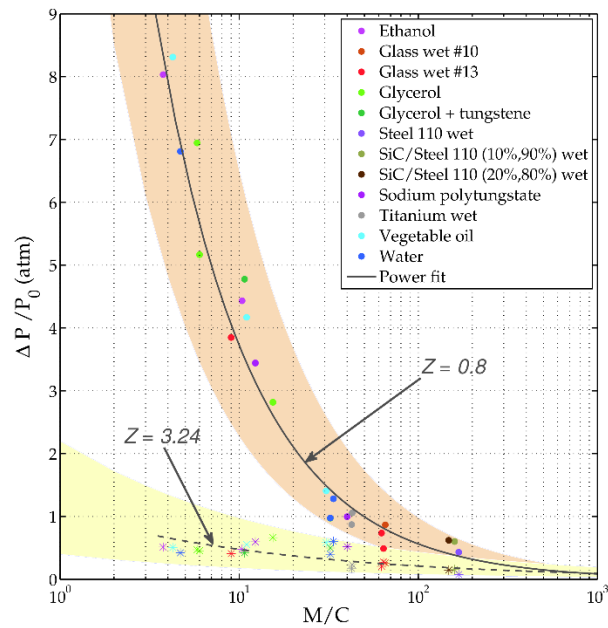


Fig. 17 Blast wave peak overpressure as a function of  $M/C$  at two different scaled distances in the case of liquids/powders saturated with water. (●)  $Z = 0.8$ , (\*)  $Z = 3.24$ .

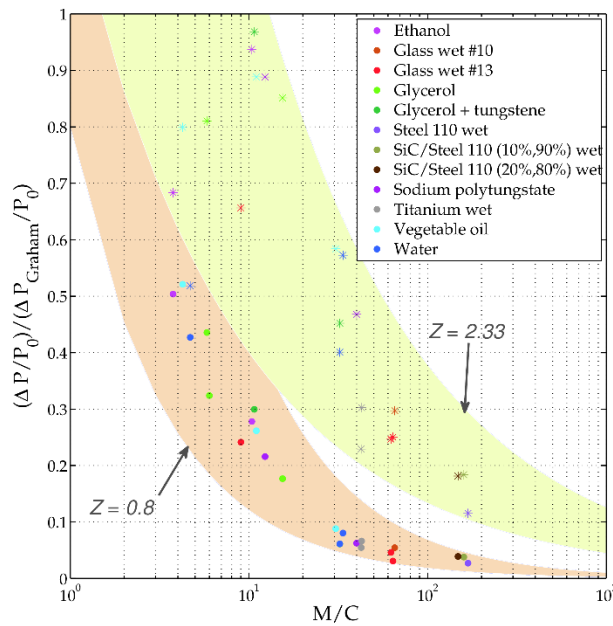


Fig. 18 Ratio of the mitigated blast wave peak overpressure over the peak overpressure of a blast wave in the air as a function of  $M/C$  in the case of liquids/powders saturated with water. (●)  $Z = 0.8$ , (\*)  $Z = 2.33$ .

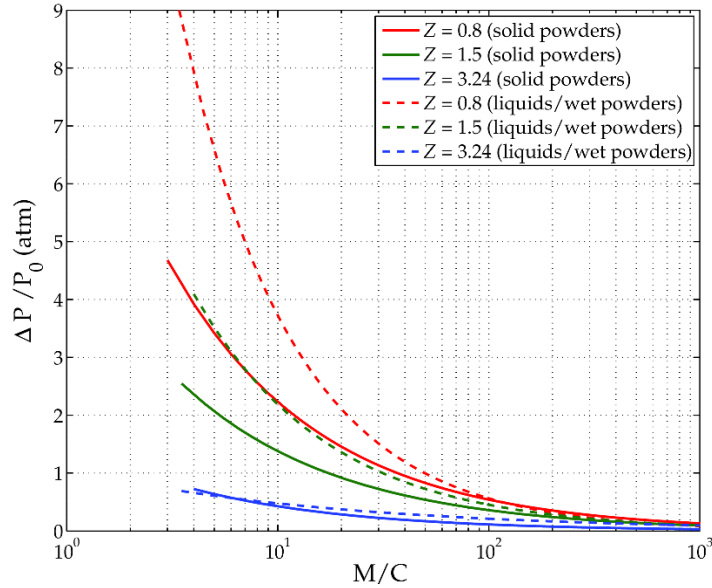


Fig. 19 Comparison of the power law fits to the blast overpressure data vs.  $M/C$  ratio for particles and liquids/wet powders.

The impulse data for all trials obtained by integrating the blast overpressure-time history obtained with the side-on piezoelectric pressure transducers. Another method for determining blast impulse using optical data to characterize density gradients within the flow field has been reviewed by Biss and McNesby [2]. This method is not practical in the present situation due to the presence of a non-static background and the presence of compacted fragments that perturb the local pixel intensity.

#### *Impulse from Dry Powder Mitigants*

Fig. 20 presents the scaled impulse results for 5 different types of powders. In all cases, the blast impulse falls below the values for a homogeneous explosive from Kinney and Graham, by up to a factor of 5. The spread in the results is the result of variations in the  $M/C$  value. Fig. 21 shows the dependence of scaled impulse with  $M/C$  for 3 different  $Z$  values. For a given  $Z$  value, the impulse results for different powders collapse somewhat, indicating that the material properties do not play an important role in the blast mitigation, and the data can be fit once again with power law fits according to Eq. 5 with the following coefficients:

$$\begin{aligned}
 (\alpha, \beta) &= (1.27, 0.517) \text{ for } Z = 3.24 \\
 (\alpha, \beta) &= (0.73, 0.494) \text{ for } Z = 5.9 \\
 (\alpha, \beta) &= (0.445, 0.543) \text{ for } Z = 11.8
 \end{aligned}$$

#### *Impulse from Liquid and Water-Saturated Powder Mitigants*

In a similar manner, the scaled impulse for liquids and liquid-saturated powders, is plotted as a function of  $Z$  and  $M/C$  (for given  $Z$  values) in Figs. 22 and 23, respectively. In contrast with powders, liquid mitigants unexpectedly have virtually no influence on the decay of

the scaled positive-phase impulse with distance, in comparison with a bare HE charge. Furthermore, from Fig. 23, the scaled impulse does not depend on  $M/C$ .

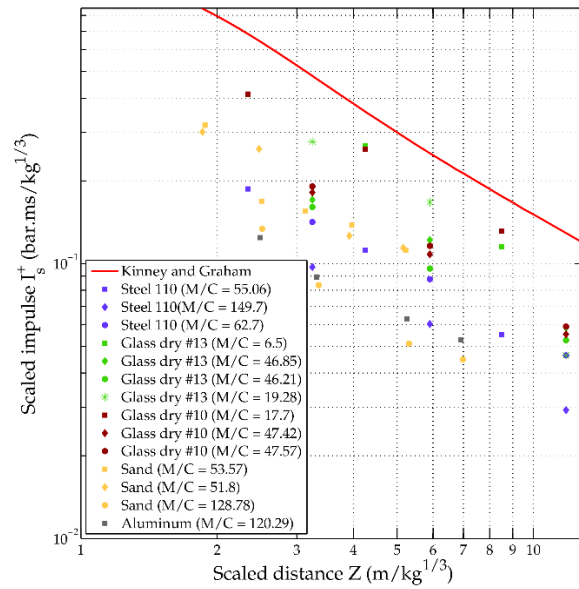


Fig. 20 Scaled blast wave impulse as a function of scaled distance for the case of solid powder mitigants.

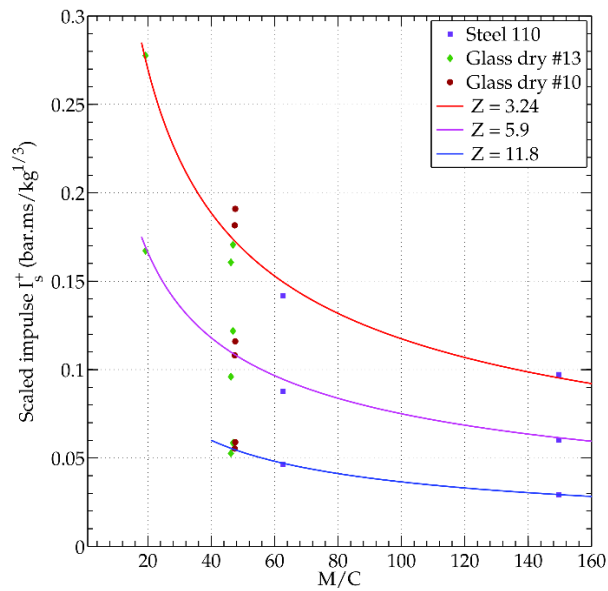


Fig. 21 Scaled impulse as a function of  $M/C$  at three different fixed scaled distances for solid powders. (Red)  $Z = 3.24$ , (magenta)  $Z = 5.9$ , (blue)  $Z = 11.8$ .

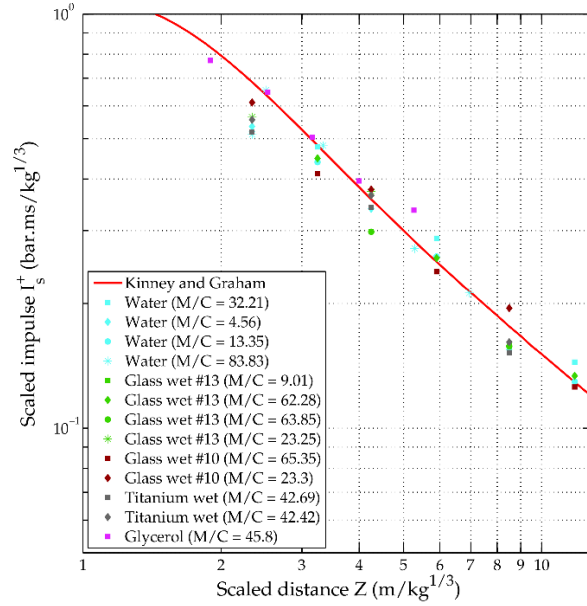


Fig. 22 Scaled blast wave impulse as a function of scaled distance for the case of liquid (or liquid-saturated powders) mitigants.

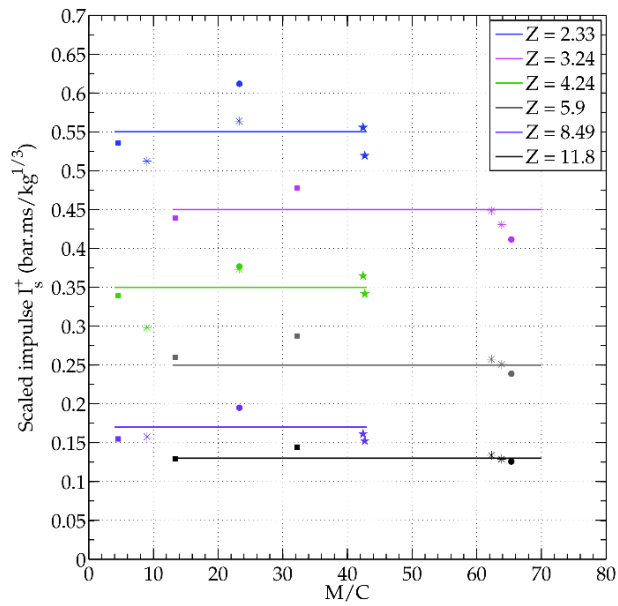


Fig. 23 Scaled impulse as a function of  $M/C$  at five different fixed scaled distance for liquids/powders saturated with water: (■) Neat water, (●) Glass wet #13, (\*) Glass wet #10, (★) Titanium wet.

### *discussion*

The present results demonstrate that the peak blast overpressure from a high explosive charge may be reduced by up to more than one order of magnitude by surrounding the charge with a layer of mitigating powder providing that the mass of mitigant is sufficiently large, relative to the explosive mass. The mitigation effect is most effective in the near field, particularly for scaled distances of  $Z < 2$ . The attenuation of the peak overpressure is primarily dependent on the  $M/C$  ratio, for a given scaled distance. Since the mitigant mass (or mass ratio) is the key parameter controlling the effectiveness of blast mitigation, it is likely that the transfer of momentum and energy from the detonation product expansion to the particles is the primary reason that the pressure is reduced in the far field. Once the particles begin to decelerate due to drag with the surrounding gas, the kinetic energy of the particles will be converted back to internal energy of the gas and the pressure mitigation effect is reduced at farther distances from the charge.

Plotted versus  $M/C$ , there are small differences in overpressure reduction for different powders, although it is not clear which material properties play the most important role in distinguishing the performance of different powders as there is no clear trend of particular materials providing superior mitigation on a per-mass basis. It should be noted that there are small differences in the solid volume fraction (or void fraction) for the different powders, and this may explain some of the differences in the results. It is interesting to note that while some particles form jets when explosively dispersed, and others are much less susceptible to jetting (such as heavy particles like steel shot), the pressure mitigation does not seem to be strongly dependent on the presence, or not, of particle jets. Further insight into the dependence of pressure mitigation on material properties may be gained by carrying out hydrocode simulation of the explosive dispersal process, with the material properties varied systematically, and work is currently underway in this area.

The rate of decay of the overpressure in the near field for powder mitigants is less than for an unmitigated homogeneous explosive charge in the near field ( $Z < 2$ ). One possible explanation for this observation is that since the particles follow closely behind the blast wave in the near field, the particle front is effectively acting as a porous piston, which generates pressure disturbances that support the blast wave. Effectively each particle, or particle jet in the case of some particles, will drive a bow shock ahead of it, which locally perturbs the pressure field. The cumulative effect of these micro-bow shocks is to support the blast wave and reduce its rate of decay. As the particles move radially outwards, the local particle density is reduced and the piston effect will be reduced. When the blast wave separates spatially from the particle front, this piston effect will be eliminated since the pressure disturbance caused by the particles will not be able to catch up to and influence the blast wave, although they will still influence the pressure field behind the blast wave and hence the blast impulse.

Powders are more effective at mitigating blast overpressure, particularly for small  $M/C$  ratios and in the near field, in comparison to liquids or liquid-saturated powders. It is likely that the energy dissipation during compaction of dry powders plays a key role in attenuation of the blast wave overpressure. In a recent publication, Milne [24] used hydrocode calculations to develop an empirical correlation for the particle velocity obtained during explosive dispersal and showed that the velocity deficit, in comparison with the conventional Gurney velocity, is largely due to losses during the powder

compaction stage. A similar argument likely explains the pressure mitigation effect of powders. Liquid, in contrast with powders, have no initial porosity, and hence energy dissipation due to pore collapse does not play a role during shock propagation through the liquid. Other phenomena play a role during explosive dispersal of liquids, including cavitation behind the inward expansion wave generated when the shock wave reaches the liquid surface. Re-compaction of the bubbly liquid generated by cavitation by the expanding explosive products, and breakup of the liquid into droplets and subsequent droplet evaporation will also occur, as discussed in a recent publication on the dynamics of liquid dispersal [23]. The lack of porosity in a liquid also likely contributes to the observation that liquid mitigants have virtually no effect on the positive phase blast impulse. Further elucidation of this surprising observation will require detailed hydrocode calculations to explore the dependence of various parameters as well as the effect of liquid cavitation, liquid fragmentation, and droplet evaporation.

#### 4. CONCLUSIONS

The mitigation of a blast wave created by the detonation of a high explosive was investigated experimentally. Various types of mitigants such as particles (iron, steel, brass, aluminum, sand, glass, sugar, silicon carbide) as well as liquids (water, glycerol, ethanol, vegetable oil) have been tested. The blast peak overpressure was inferred from the analysis of the blast wave motion from the high-speed video records and the positive-phase blast impulse was determined from side-on pressure transducers at several distances from the charge. The primary results of this study are as follows:

- 1) Solid powders, liquids, or powders saturated with a liquid can be used as blast wave mitigants. However, solid powders outperform liquids with respect to mitigating the blast wave overpressure. The difference in mitigation performance is likely due to the energy loss during the compaction of solid powders at early times which indicates that initial porosity is a beneficial factor for mitigation.
- 2) The decay in peak blast overpressure for both granular solid and liquid mitigants as a function of the mass of mitigant to the charge ratio ( $M/C$ ) follows a weak power law function. The decay in blast impulse as a function of  $M/C$  for the solid powders also exhibits a power law decay. However, in the case of the liquids or liquid-saturated powders, blast impulses are virtually the same as an unmitigated charge with the same explosive mass and does not depend on the mass ratio.
- 3) It is hypothesized that the slower rate of decay of the blast wave overpressure in the near field for a mitigated charge versus an equivalent bare charge is due to partial blast wave support from the higher inertia mitigant acting as a porous/imperfect piston.

Current work is underway to gain insight into the blast wave mitigation during explosive dispersal of material surrounding a charge as well as to explore the dependence of the blast wave properties on the  $M/C$  ratio and particle or liquid properties using the multiphase hydrocode EDEN in collaboration with scientists at Fluid Gravity Ltd. [23].

#### 5. REFERENCES

- [1] Allen, R.M., Kirkpatrick, D.J., Longbottom, A.W., Milne, A.M. and Bourne N.K., 2004, Experimental and Numerical Study of Free-Field Blast Mitigation, AIP Conference Proceedings, Vol. 706 (1), 823-826.
- [2] Biss, M.M. and McNesby, K.L., 2014, Optically Measured Explosive Impulse, Experiments in Fluids, Vol. 55 (6), 1749.
- [3] Britan, A., Ben-Dor, G., Igra, O. and Shapiro, H., 2001, Shock Waves Attenuation by Granular Filters, International Journal of Multiphase Flow, Vol. 27 (4), 617-634.
- [4] Britan, A., Shapiro, H. and Ben-Dor, G., 2012, Foams for Blast Mitigation, Foam Engineering: Fundamentals and Applications (Paul Stevenson), Ch. 19, 477-512.
- [5] Brode, H.L., 1959, Blast Wave from a Spherical Charge, Physics of Fluids, Vol. 2 (1959), 217-229.
- [6] Campbell, I.J. and Pitcher, A.S., 1957, Shock Waves in a Liquid Containing Gas Bubbles, Proceedings of the Royal Society of London. Series A. Mathematical and Physical Sciences, Vol. 243 (1235), 534-545.
- [7] Cheng, M., Hung, K.C. and Chong, O.Y., 2005, Numerical Study of Water Mitigation Effects on Blast Wave, Shock Waves, Vol. 14 (13), 217-223.
- [8] Cooper, P.W., 1996, Explosives Engineering, Wiley-VCH, USA.
- [9] Del Prete, E., Chinnayya, A., Domergue, L., Hadjadj A. and Haas, J.F., 2013, Blast Wave Mitigation by Dry Aqueous Foams, Shock Waves, Vol. 23 (1), 39-53.
- [10] Endo, K., Kitagawa, K. and Yasuhara, M., 2009, Diffusion Effect of Blast Pressure in Porous Complex Media, 39th AIAA Fluid Dynamics Conference, San Antonio, Texas, June 22-25, 2009.
- [11] Frost, D.L., Loiseau, J., Marr, B.J. and Goroshin, S., Particle Segregation during Explosive Dispersal of Binary Particle Mixtures, 19th Biennial Conference of the APS Topical Group on Shock Compression of Matter, Tampa, Florida, June 14-19, 2015.
- [12] Frost, D.L., Grégoire, Y., Petel, O., Goroshin, S. and Zhang, F., 2012, Particle Jet Formation during Explosive Dispersal of Solid Particles, Physics of Fluids, Vol. 24.
- [13] Gelfand, B.E., Blast Waves Attenuation in Two-Phase Media, Symposium on Interdisciplinary Shock Wave Research, Sendai, Japan, March 22-24, 2004.
- [14] Golub, V.V., Lu, F.K., Medin, S.A., Mirova, O.A., Parshikov, A.N., Petukhov, V.A. and Volodin, V.V., Blast Wave Attenuation by Lightly Destructable Granular Materials, Proc. 24th International Symposium on Shock Waves, Beijing, China, July 11-16, 2004.
- [15] Gurney, R.W., 1943, The Initial Velocities of Fragments from Bombs, Shells, and Grenades, BRL-405, Maryland.
- [16] Hartman, W.F., Boughton, B.A. and Larsen, M.E., 2006, Blast Mitigation Capabilities of Aqueous Foam, Sandia report, SAND2006-0533, Sandia National Laboratories.

- [17] Kinney, G.F. and Graham, K.J., 1985, Explosive Shocks in Air, Second Edition, Springer Science, New York.
- [18] Kitagawa, K., Yamashita, S., Takayama, K. and Yasuhara, M., 2009, Attenuation Properties of Blast Wave through Porous Layer, Proceedings of the 26th International Symposium on Shock Waves, Shock Waves, Vol. 1, Part II, 73-78.
- [19] Langhorst, B., Cook, C., Schondel J. and Chu, H.S., Material Systems for Blast-Energy Dissipation Mechanism, Proceedings of the IMPLAST 2010 Conference, Rhode Island, USA, October 12-14, 2010.
- [20] Loiseau, J., Pontalier, Q., Milne, A., Goroshin, S. and Frost, D.L., Terminal Velocity of Liquids and Granular Materials Accelerated by a High Explosive, 24th International Symposium on Military Aspects of Blast and Shock (MABS), Halifax, Canada, September 18-23, 2016.
- [21] Medvedev, S.P., Frolov, S.M. and Gelfand, B.E., 1990, Attenuation of Shock Waves by Screens of Granular Material, Journal of Engineering Physics, Vol. 58 (6), 714-718.
- [22] Milne, A.M., Floyd, E., Longbottom, A.W. and Taylor, P., 2014, Dynamic Fragmentation of Powders in Spherical Geometry, Shock Waves, Vol. 24 (5), 501-513.
- [23] Milne, A.M., Longbottom, A.W., Frost D.L., Grégoire, Y., Loiseau J. and Goroshin S., 2016, Explosive Fragmentation of Liquids in Spherical Geometry, Shock Waves, 1-11.
- [24] Milne, A.M., 2016, Gurney Analysis of porous shells, Propellants, Explosives, Pyrotechnics.
- [25] Nesterenko, V.F., 2003, Shock (Blast) Mitigation by Soft Condensed Matter, MRS Symposium Proceedings, Vol. 759 (1), MM4.3.1-4.3.12.
- [26] Raspet, R., Powers, J.M., Panczak, T.D., Butler, P.B. and Jahani, F., 1989, Attenuation of Blast Waves using Foam and Other Materials, U.S. Army Construction Engineering Research Laboratory report, AD-A203, USA.
- [27] Resnyansky, A.D. and Delaney, T.G., 2006, Experimental Study of Blast Mitigation in a Water Mist, Weapons Systems Division, Defense Science and Technology Organisation Technical (DSTO) report, DSTO-TR-1944, Edinburgh South Australia, Australia.
- [28] Schwer, D. and Kailasanath, K., 2006, Blast Mitigation by Water Mist (3) Mitigation of Confined and Unconfined Blasts, Naval Research Laboratory Report, NRL/MR/6410-06-8976, Washington DC 20375-5320, USA.

## SECTION 6. BIOCIDAL AGENT DETECTION IN FIELD CONDITIONS

### Chapter 1. CuCl Experiments

#### 1. INTRODUCTION

Large scale experiments were performed with biocidal material to investigate the potential concentration of biocidal material released in the air during the combustion of the aluminum cloud.

#### 2. EXPERIMENTAL APPARATUS

Large-scale experiments were performed at the Canadian Explosives Research Laboratory (CERL) in Nepean, Ontario. The apparatus used is identical to the one used in the previous years of this grant. Figure 8 shows the apparatus used to generate a large-scale aluminum cloud measuring roughly 4m in height and 2m in width. Figure 1 also shows a picture of the apparatus and an image of the cloud itself.

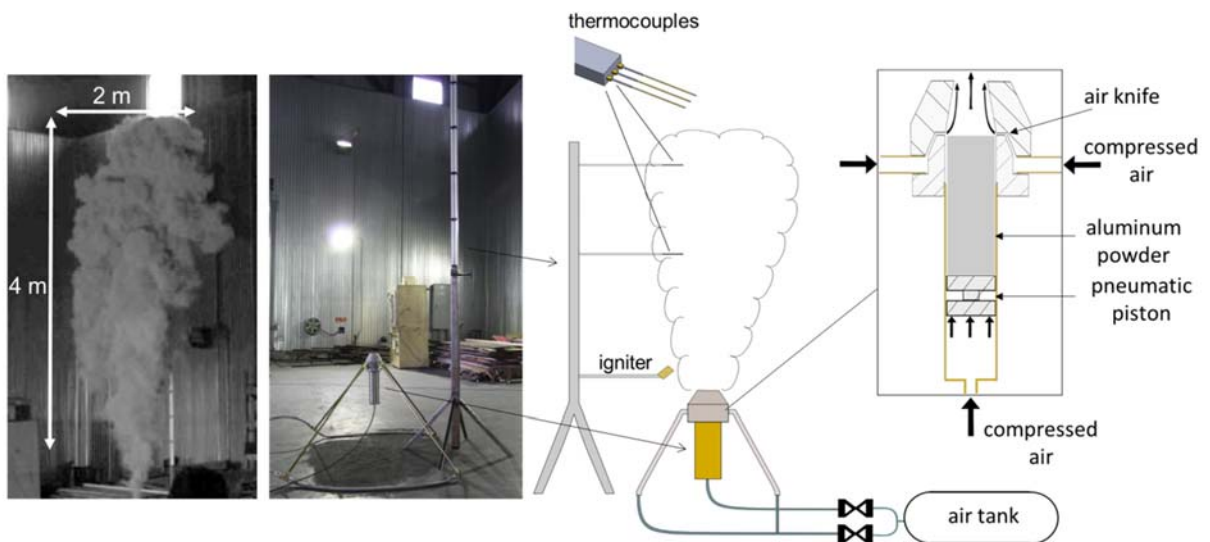


Figure 1. Schematics and photograph of the experimental rig for the large-scale dust cloud combustion tests.

### 3. RESULTS AND DISCUSSION

Figure 2 shows still frames of the flame propagation for two ignition delay times. Flame propagation is imaged with a Photron SA-5 at 2000 frames per second. Figure 3 shows color still-frames of the flame propagation.

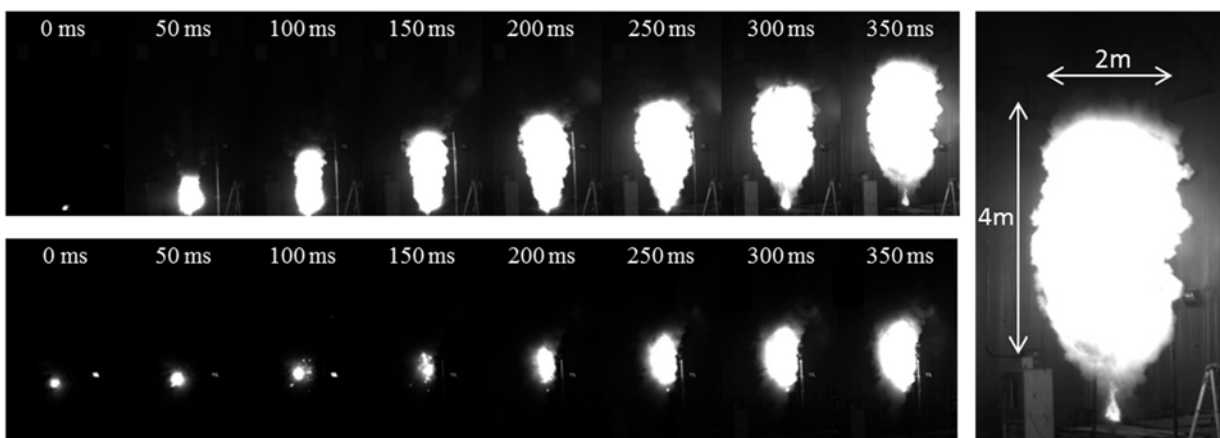


Figure 2. Still frames of flames ignited without delay (top) and with 0.4 seconds delay (bottom) after the end of the dust dispersion process.



Figure 3. Visible radiation from a flame propagating through a large-scale aluminium (12  $\mu\text{m}$  Valimet H-10 powder)-air dust cloud. Time between frames is 125 ms.

A biocidal material, copper chloride ( $\text{CuCl}$ ), in powder form, was added to the aluminum powder. The concentration ranged from 1% to 20% and was thoroughly mixed. During combustion of aluminum,  $\text{CuCl}$  decomposes into copper and chloride and “releases” the biocidal material. The biocidal effects come from the biocidal halogen, from the high temperature of an aluminum flame (3400 K) and from the UV radiation emitted from alumina particles in the post-flame region.

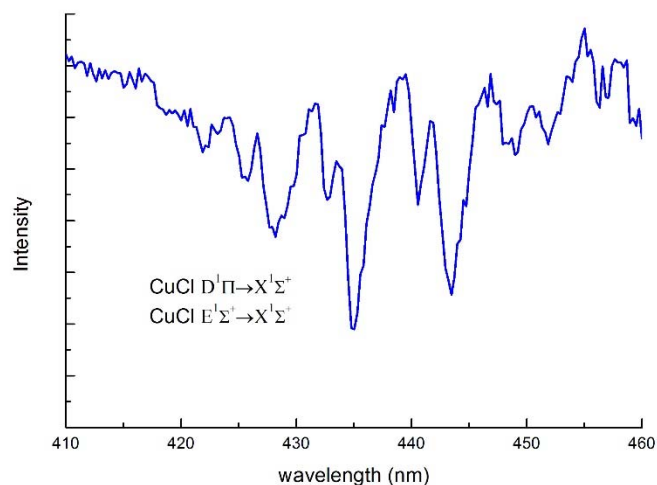


Figure 4. Emission spectra of CuCl inside the aluminum flame.

The two copper chloride bands can be seen in the wavelength region between 420 nm and 460 nm on Fig. 11. This information can be used to obtain the temperature of copper chloride molecules and also determine its concentration.

Emission spectroscopy was also used to measure the gas phase temperature using AlO. AlO is a sub-oxide present in the gas phase in the combustion zone. AlO molecules quickly form Al<sub>2</sub>O<sub>3</sub> through chemical condensation after the flame. The molecule AlO is therefore short lived and is present in the gas phase close to the burning particles. Figure 12 shows the emission spectra of AlO in an aluminum flame at three different times during the event.

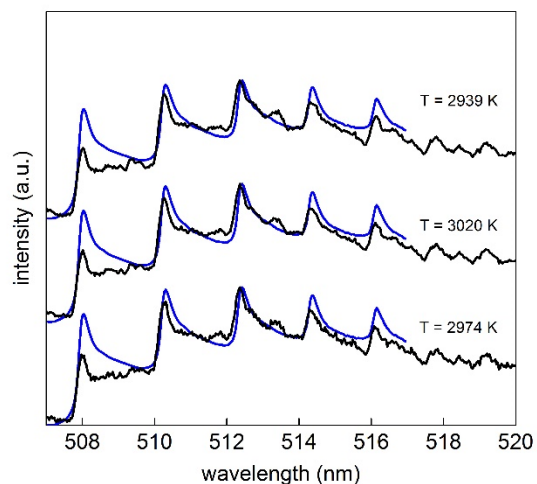


Figure 5. Experimental and fitted theoretical AlO spectra at a single temperature from a single fiber for different points in time after dispersion, each 5 ms apart.

The temperature of the aluminum flame was derived from AlO molecular spectra by fitting the experimentally measured shape with the shape derived from theoretical calculations (Goroshin et al., 2007). Light from three equidistant locations 0.5 m apart, perpendicular to the incoming flame front, was transmitted by multimode fibers (0.4 mm dia) to the entrance slit of a customized f/5 imaging, Czerny-Turner spectrometer. The fibers were coupled along the slit such that the light from each fiber was spatially separated on the spectrometer image plane. The spectrometer was coupled to a high speed SA-5 Photron digital videocamera filming spectra at 2000 frames/s. Using a 300 gr/mm grating, the spectrometer resolution was about 0.15 nm with a spectral range of about 130 nm covering the entire AlO emission band. The resulting integrated spectrum signal from a fiber and the corresponding theoretically calculated spectrum corresponding to a temperature for several different frames is shown in Fig. 10.

The measured flame temperatures are in the range of 2900 – 3000 K which is about 300 K lower than temperatures measured from a Bunsen aluminum flame by the same method. The difference can be attributed to the experimental uncertainty of the measurement, which is on the order of a few hundred Kelvin.

**DISTRIBUTION LIST  
DTRA-TR-18-8**

**DEPARTMENT OF DEFENSE**

DEFENSE THREAT REDUCTION  
AGENCY  
8725 JOHN J. KINGMAN ROAD  
STOP 6201  
FORT BELVOIR, VA 22060  
ATTN: A. DALTON

DEFENSE TECHNICAL  
INFORMATION CENTER  
8725 JOHN J. KINGMAN ROAD,  
SUITE 0944  
FT. BELVOIR, VA 22060-6201  
ATTN: DTIC/OCA

**DEPARTMENT OF DEFENSE  
CONTRACTORS**

QUANTERION SOLUTIONS, INC.  
1680 TEXAS STREET, SE  
KIRTLAND AFB, NM 87117-5669  
ATTN: DTRIAC